POLITECNICO DI MILANO
MOX - DEPARTMENT OF MATHEMATICS
DOCTORAL PROGRAMME IN
MATHEMATICAL MODELS AND METHODS IN ENGINEERING

FINITE VOLUME METHODS AND DISCONTINUOUS GALERKIN METHODS FOR THE NUMERICAL MODELING OF MULTIPHASE GAS–PARTICLE FLOWS

Doctoral Dissertation of:
Susanna Carcano

Supervisor:
Dott. Luca Bonaventura, Dott. Augusto Neri

Tutor:
Prof. Fabio Nobile

The Chair of the Doctoral Program:
Prof. Roberto Lucchetti

2014 – XXVI Cycle

Abstract

THE thesis is devoted to the numerical modeling of multiphase gas–particle flows. This work has been originally motivated by the need of developing numerical tools for the simulation of explosive volcanic eruptions. Due to the complexity of volcanic phenomena, that does not allow to reproduce them at the laboratory scale, mathematical and numerical models are achieving an essential role.

Several theoretical and numerical challenges arise in the field of the simulation of explosive volcanic eruptions. The mathematical description of the real multiphase fluid is not trivial, due to the presence of a wide spectrum of solid components and a large number of chemical gaseous components that interact with each other. Concerning the numerical modeling of explosive volcanic eruptions, the main difficulties are related to the multiscale nature of the phenomena and to the wide variety of flow regimes involved. Further difficulties are related to the rigorous model verification and validation. In conclusion, the accurate and efficient simulation of realistic eruptive scenarios still represents a challenge for computational fluid dynamics.

After a discussion on different approaches to the mathematical modeling of multiphase gas–particle flows, a model based on the Eulerian-Eulerian approach is presented for a mixture of a gaseous phase and N classes of solid particles, able to handle the widest range of physical phenomena. The mathematical model consists in a set of balance equations representing the mass, momentum and energy conservation. Appropriate closure equations are introduced, based on literature review.

The dimensional analysis of the multiphase equations is carried out for significant test problems, both on the volcanic scale and the laboratory scale. The relative importance of different physical phenomena that take place in the volcanic jet and in the pyroclastic density current are assessed. In the volcanic jet problem, we show that the ejected multiphase mixture can be well approximated as inviscid. Gravitational effects and dissipation due to viscous and drag forces are negligible. Compressibility effects are important and a transonic regime can be expected. Moreover, the hypothesis of equilibrium between different phases is not valid and a fully multiphase mathematical model is needed to investigate the non-equilibrium dynamics between different phases. After the volcanic column collapse, in the pyroclastic current gravitational effects be-

come dominant. When reproducing a multiphase jet on the laboratory scale, particle dynamics is strongly decoupled from gas dynamics. Moreover, viscous dissipation and the work done by the drag force may play a key role in the thermodynamics of the mixture. As a consequence, the thermodynamics processes that influence the jet dynamics on the laboratory scale may differ from those characterizing the volcanic jet dynamics.

Two distinct numerical approximations of the multiphase flow equations are presented and validated, based on the finite volume and the discontinuous Galerkin approach. The proposed finite volume scheme achieves second order accuracy in space and time and it is validated against experimental and numerical results in both supersonic and subsonic regimes. The underexpanded jet problem on the laboratory and volcanic scale, the particle-laden gravity current and the collapsing jet problem are taken as benchmark tests. Supersonic and subsonic regimes are well described by the finite volume scheme. The multidimensional second order spatial discretization is essential to accurately capture the shock wave pattern observed in underexpanded jets and to reduce numerical diffusion. Validation against experiments and comparison against numerical results is satisfactory.

The alternative p-adaptive discontinuous Galerkin approach allows to achieve higher accuracy, while keeping a small computational stencil and a relatively limited computational cost thanks to a p-adaptivity approach. In the present work, the discontinuous Galerkin scheme is applied to solve multiphase gas–particle equations that accounts for drag and heat exchange coupling between different phases. Appropriate flux limiting and slope limiting techniques are applied to the proposed discontinuous Galerkin approximation of the multiphase flow equations. The discontinuous Galerkin approach is tested on several benchmark problems in the one-dimensional case. In particular, monophase and multiphase shock tube test cases are considered in order to assess the accuracy, the limiting techniques properties and the computational efficiency obtained thanks to the p-adaptive approach. We show that slope limiting and flux limiting techniques are essential in multiphase shock tube problems to guarantee the positivity of physical quantities and the stability of the numerical solution. The p-adaptive approach is able to reduce the computational cost up to 50 % by keeping a good accuracy on the numerical solution.

In the last part of the work, the finite volume numerical model is applied to study the effect of gas–particle non-equilibrium on underexpanded volcanic jets by assuming monodisperse, bidisperse and polydisperse mixtures. By means of a scaling analysis based on particle Stokes numbers St, i.e., the ratio between the particle relaxation time and the Mach disk formation time of the underexpanded jet, we classify solid particulate into two categories, namely fine and coarse particles. Fine particles are tightly coupled with the gas phase and do not modify the structure of the shock wave pattern in the jet. On the contrary, coarser particles are decoupled from the gas phase and strongly influence the jet decompression structure, including the intensity, shape and position of the Mach disk. Depending on the mass ratio between fine ($St \ll 1$) and coarse ($St \gg 1$) particles, the jet flow pattern can dramatically change, leading to the obliteration of the Mach disk structure.

On the basis of the results of the time scale analysis, an hybrid pseudogas-multiphase model is proposed, in which fine particles and the gas phase are modeled together as a pseudogas with average thermodynamics properties, whereas coarse particles are

grouped together into a representative class of solid particles with average properties. Numerical results confirm the validity of the hybrid approach for the simulation of monodisperse, bidisperse and polydisperse underexpanded jets and highlight the key effect of the total grain size distribution on the underexpanded jet and on the overall stability properties of the eruptive column.

The developed methodology and techniques are general and can be extended to the many different multiphase gas–particle flows that can be encountered in geophysical and industrial applications.

Contents

CHAPTER 1

Introduction

THE object of the present thesis is the investigation of numerical modeling approaches for multiphase gas–particle flows, with a special focus on the application to explosive volcanic eruptions. Volcanic eruptions are complex phenomena that involve many physical processes. A significant progress towards understanding these phenomena has been done in the last years thanks to the synthesis of mathematical and laboratory models with data and observations. However, due to intrinsic danger that makes direct measurement of volcanic processes rather difficult and due to the complexity of these phenomena, that does not allow to reproduce them at the laboratory scale, mathematical and numerical models are achieving an essential role in the study of volcanic eruptions. This is especially important in view of the growing need to quantify and map the hazards associated to future explosive eruptions in known active areas, such as the Vesuvian area and the Campi Flegrei area in Italy.

Volcanoes display a wide range of eruption styles, from the effusion of lava flows to explosive eruptions. The difference in the eruption style can be associated with the fluid mechanics governing magma ascent inside the volcano. Examples of interacting factors, that can determine the eruption style, are the ascent rate of magma, the magma rheology and the interaction of magma with external sources of water [55]. Magma, stored in the magma chamber, is composed by a silicate melt with solid crystals and dissolved volatile species, primarily water. During a volcanic eruption, magma is driven to the surface by buoyancy and/or by overpressure in the magma chamber. The liquid magma starts rising in the volcanic conduit and the decompression during the ascent causes dissolved gases to exsolve from the melt and to form bubbles, thus providing an additional driving force for the eruption. Gaseous components can derive from the exsolved magmatic volatiles in magmatic eruptions, vaporized free water or hydrother-

mal fluids in hydromagmatic and phreatomagmatic eruptions [102]. As gas is exsolved, bubbles form and rapidly expand inside the magma until the liquid film around them breaks up and a fragmented mixture of ash and volatiles ascends along the volcanic vent and is decompressed into the atmosphere. If the gas trapped in the growing bubbles is lost during the magma ascent by permeable gas flow or by outgassing, magma tends to erupt effusively. This happens typically for low viscosity and slowly ascending magmas. On the other hand, if outgassing is inefficient on the time scale of the eruption, the bubbly magma can fragment forming a gas–pyroclast dispersion. In this process the potential and thermal energy of the melt and the gas phases are converted to kinetic energy, causing an explosive eruption.

In the first stages of the explosive eruption, the hot, dense mixture expands and begins to entrain and heat ambient air, thereby lowering the mixture density, but it also decelerates under gravity. If the eruption velocity is sufficiently high, then the material can become buoyant and will generate a buoyant ash plume, called eruption column, which rises above the vent (see Figure 1.1). In contrast, if the eruption velocity is small or the mass flux is very large, then the material will typically collapse back toward the vent and form a dense, laterally spreading flow (see Figure 1.2). Buoyant eruption columns are able to transport the material high into the atmosphere, since they provide an efficient means of converting the initial thermal energy of the mixture into potential energy through entrainment and heating of ambient air. Dense, hot ash flows, generated by collapsing columns, transport ash and clasts laterally from the vent, sedimenting many of the larger clasts and entraining ambient air. As a result, the density of the mixture may fall below that of the atmosphere, and the finer-grained solid material may thereby become buoyant and rise from the flow.

Several theoretical and numerical challenges arise in the field of the simulation of explosive volcanic eruptions. Explosive eruptions involve the ejection of dense mixtures of gas and ashes from the volcanic vent at high pressures and speeds. The mathematical description of the real multiphase fluid is not trivial, due to the presence of a wide spectrum of solid components and a large number of chemical gaseous components that interact with each other. A general understanding of the dynamics of the multiphase pyroclast flow in the atmosphere was first achieved by describing the eruptive mixture as homogeneous, i.e. by assuming kinetic and thermal equilibrium between gas and particles, and inert, i.e. by neglecting chemical reactions and phase transitions [95, 96, 128]. Mathematical models based on multiphase flow formulation have been proposed starting from the late 1980s [34, 138] and have become more popular in the last decade [32, 42, 71, 104]. However, further work is still necessary to test their adequacy in describing volcanic multiphase flows.

Concerning the numerical simulation of explosive volcanic eruptions, one of the main difficulties is related to the multiscale nature of the phenomena and on the wide variety of flow regimes involved. Large volcanic eruptions can generate a buoyant ash plume (Plinian eruption column) that rises above the vent and is able to transport material high into the upper part of the atmosphere, up to tens of kilometers in height [147]. There, pyroclasts can be transported by winds for thousands of kilometers. On a shorter time scale, they can cause disruption of air traffic, see e.g. [59]. On longer time scales, they can even influence global climate, see e.g. [74]. At the same time dense and hot

Figure 1.1: Spectacular explosive eruption at Mount St. Helens volcano (Washington, U.S.) occurred on July 22nd, 1980. This eruption sent pumice and ash up to 18 kilometers into the air, and was visible in Seattle, Washington, 160 kilometers to the north. Image by USGS.

Figure 1.2: Pyroclastic flow at Mount St. Helens volcano (Washington, U.S.), after the explosive event on August 7th, 1980. Image by USGS.

ash flows can be generated by the lateral collapsing of the column. These pyroclastic flows transport ash laterally from the vent, sedimenting many of the larger clasts and entraining air. The distance traveled by a pyroclastic flow can reach several kilometers, depending on the mixture composition and on the ground topography. Concerning the temporal scale, eruptions can last even for several days. While the spatial and temporal scales involved in the eruptions are really large, thus requiring the computational domain to be large and the computation to be long enough, the characteristic lengths and times of the physical phenomena that have to be reproduced can be very small. As an example, large explosive eruptions are characterized by highly efficients fragmentation processes that produce particulate of few micrometers in diameter. Moreover, characteristic time scales of such particles are of the order of fractions of a second. In conclusion, the efficient simulation of realistic eruptive scenarios still represents a challenge for computational fluid dynamics.

Numerical models also have to be robust enough to reproduce supersonic and subsonic regimes that coexist during an explosive eruption. In fact, it has been proven that the erupted multiphase mixture, under some conditions at the vent, can be accelerated up to supersonic speeds, generating shock waves inside the flow. At the same time, the pyroclastic flows, that form after the collapse of the volcanic column, are stratified by gravity and almost subsonic and granular regimes can be observed [16, 147].

The last difficulty in the mathematical and numerical approach to the study of volcanic phenomena is related to the rigorous model verification and validation, which is perhaps impossible [99]. The validation of numerical results against empirical observation of well-documented eruptions, together with the congruence of numerical benchmarks with experimental and theoretical results are at present the only available instruments to asses the "empirical adequacy" [99] of models to simulate eruptive scenarios.

Several examples of numerical simulation of volcanic processes can be found in the literature. Typically, the numerical approach applied to solve the pseudogas or the multiphase flow equations is based on low order finite volume schemes [97, 98, 104]. Moreover, simplified conditions are assumed (i.e. cylindrical symmetry, point source, steady state conditions [125, 144, 146]) and simplified models are introduced with the aim to focus on well-defined phenomena, e.g. highlighting the key roles of environmental atmospheric conditions [57], large-eddy turbulence [127], vent overpressure [97], boundary layer processes [35] and ash deposition [70].

In the first part of this work, different approaches to the mathematical modeling of multiphase gas–particle flows are reviewed and the instruments that allow to select the most appropriate multiphase model in the framework of volcanological application are introduced. In particular, the multiphase conservation equations based on the two-fluid model and the pseudogas model are described in detail for a mixture of a gaseous phase and N classes of solid particles, together with appropriate closure relationships. The dimensional analysis of the multiphase gas–particle equations is presented, with application to significant regimes, representative of different application areas.

In the second part of the thesis, two distinct approaches are presented and investigated for the numerical approximation of multiphase conservation laws. First, the

numerical discretization of the multiphase gas–particle equations based on the finite volume method is presented. The finite volume method is derived from the conservative formulation of the balance laws and guarantees that the conservation properties of the continuous formulation are satisfied by the discrete formulation. The approach proposed in [42, 91] is described and an original extension of the IMF algorithm to achieve full second order accuracy in space and time is presented. Furthermore, fully multidimensional advection fluxes are introduced, following [83], in the framework of the model proposed in [42, 91].

It is well known that achieving higher order of accuracy in the finite volume framework implies an increasing computational cost related to the extension of the computational stencil, in particular when a parallel implementation has to be employed. As an alternative, a novel discontinuous Galerkin approach is proposed for the discretization of the multiphase gas–particle equations. Discontinuous Galerkin methods can be interpreted as an extension of finite volume methods to arbitrary order of accuracy. Unlike finite volume methods, in discontinuous Galerkin methods the increasing of accuracy is achieved by increasing the order of the polynomial approximation locally on each control volume, without extending the computational stencil. In addition, in this work the discontinuous Galerkin approximation for multiphase equations is coupled for the first time with a p-adaptivity algorithm, that allows to reduce the computational cost while maintaining the accuracy of the numerical approximation. Appropriate flux limiting and slope limiting techniques, originally introduced in the framework of scalar and linear equations, are applied to the proposed discontinuous Galerkin approximation of the multiphase flow equations. The present work represents the first attempt to apply discontinuous Galerkin methods to multiphase gas–particle equations with drag and heat exchange interphase coupling.

The system of ordinary differential equations resulting from the spatial discretization by either finite volume or discontinuous Galerkin scheme can be solved by means of explicit or implicit time advancing schemes with different orders of accuracy. In both cases, however, an implicit treatment of the interphase coupling terms in the multiphase flow equations is needed to guarantee the physical coupling of the phases also at the discrete level. In the implicit approach, an iterative solver based on an approximate Newton method and on the implicit multifield (IMF) method is applied, in order to solve the non linear coupling between the equations [42, 63]. A second order semi-implicit extension of the original implicit scheme introduced in [42] is proposed. In the explicit approach, a linearization of the interphase terms is proposed, in order to partly decouple the multiphase equations.

In the third part of the work, the finite volume numerical model is validated against experimental results at the laboratory scale, as well as empirical laws and numerical results presented in the literature both in the supersonic and subsonic regimes that can be observed in realistic volcanic scenarios. In particular, the numerical schemes is applied to reproduce supersonic jets, see i.e. [19], and density currents in two dimensions. Analogously, a validation of the discontinuous Galerkin numerical model is carried out in the one dimensional case against significant benchmark test cases, in order to assess the accuracy of the scheme, the capability of limiting techniques to prevent the formation of spurious oscillations in the numerical solution and the performances of the p-adaptive approach.

Finally, the finite volume numerical method is applied to the simulation of multiphase underexpanded jets on the volcanic scale. The aim of the investigation is to assess the importance of the non equilibrium regime between the gas phase and the solid phase in supersonic jets. Moreover, the interactions between solid particles and shock waves in underexpanded jets are analyzed by means of characteristic time scales. The comparison between the characteristic time scales of the multiphase jet allows to split a given granulometric structure in finer particles, i.e. small particles that are coupled with the gas phase and cannot influence the shock wave structure in the underexpanded jet, and coarser particles, i.e. particles that modify the internal shock wave pattern of the jet. On the basis of the results of the analysis, an hybrid pseudogas-multiphase approach is proposed, in which fine particles and the gaseous phase are described as a unique pseudogas phase and coarse particles are grouped together into a unique representative class of solid particles with average properties. Numerical simulations for monodisperse, bidisperse and polydisperse flows support the validity of the hybrid approach in the underexpanded jet regimes. The proposed approach allows to reduce drastically the computational cost of the multiphase flow simulation.

CHAPTER 2

Mathematical modeling of multiphase dusty flows

MULTIPHASE flow is the motion of a continuous medium in which more than one physical state of matter is present. Multiphase flows can be classified according to the state of the different phases. Therefore, we refer to gas/solid flows (e.g. gas–particle flows or fluidized beds), liquid/solid flows (e.g. slurry flows or sediment transport), or liquid/gas flows (e.g. aerosols, bubbly or cavitating flows) and so on. Moreover, two general categories of multiphase flow can be identified, namely dispersed flows and separated flows [15]. *Dispersed flows* are those in which one phase consists of finite and discrete elements, such as droplets in a gas or bubbles in a liquid, distributed in a connected volume of the continuous phase. The discrete elements are not connected. In dispersed multiphase flows, the evolution of the interface between the phases is considered of secondary importance. On the other hand, in a *separated flow*, the two phases are divided by a line of contact. This means that in a separated flow it is possible to pass from one point to another in the same phase by remaining in the same medium. In both dispersed and separated flows, those cases in which the components are well mixed above the molecular level are excluded. Consequently, the flow has some level of phase separation at a scale well above the molecular level.

The focus of this work is on *multiphase gas–particle flows*, a type of dispersed flow which involves a gas with suspended solid particles. Examples of multiphase gas–particle flows can be found in industrial devices such as in the exhaust products of solid propellant rockets, in the combustion of coal in fossil fuel power systems or in cyclonic separation devices that are used to remove particulates from an air stream. Multiphase gas–particle flows are also a common feature of our environment and can be found for example in explosive volcanic eruptions and in the cometary atmosphere.

When particle–particle and particle–wall interactions are much more important than the forces due to the interstitial gas, multiphase gas–particle flows are known as *gran-*

ular flows. If the particles become motionless, the problem reduces to *flow through a porous medium*, in which the viscous force on the particle surface is the primary mechanism affecting the gas flow. Even though granular flows and flows through porous media can be formally considered as multiphase gas–particle flows, their treatment goes beyond the scope of this work.

In this chapter, we introduce the fundamental quantities that describe multiphase gas–particle flows. In the second part, a review of different approaches to the mathematical modeling of multiphase gas–particle flows is presented, with special attention to the application regimes. In the present work, the Eulerian approach is adopted and the conservation equations for a mixture of a gaseous phase and N classes of solid particles are described in details. The mathematical model is completed by a set of closure relationships. In the last part, the dimensional analysis of the multiphase equations is presented to get insight into the fundamental properties of the system. Finally, the dimensional analysis is applied to study a few significant regimes.

2.1 Fundamental definitions

To describe multiphase gas–particle flows, some fundamental quantities should be introduced. We consider a multiphase gas–solid system in which the solid phase is a granular material that is dispersed in the gaseous phase. The solid material is finely divided into small separate grains in such a way that the volume of each grain is small in comparison to the total volume of the solid. The *volume fraction* ϵ_s of the phase s is defined as [30]

$$\epsilon_s = \lim_{V \to V_0} \frac{V_s}{V}, \tag{2.1}$$

where V_s is the volume occupied by the phase s in the total volume V. V_0 is the limiting volume, defined as the volume in which flow properties do not vary significantly from point to point [15]. Indeed the volume fraction can not be defined at a point. By definition, the sum of the volume fractions must be unity, i.e.,

$$\sum_{s=1}^{N} \epsilon_s = 1. \tag{2.2}$$

The bulk density, or *macroscopic density*, of the phase s is the mass of the phase s per unit volume of mixture, that is [30]

$$\bar{\rho}_s = \lim_{V \to V_0} \frac{M_s}{V}, \tag{2.3}$$

where M_s is mass of the phase s in the volume V. The bulk density can be computed from the material, or *microscopic density*, ρ_s as

$$\bar{\rho}_s = \epsilon_s \rho_s. \tag{2.4}$$

2.1.1 Particle properties

Solid particles are incompressible and are supposed to maintain their original size. In the most general case, the solid phase is composed by a continuous distribution of

particles; however, here we suppose that particles can be classified into N classes, denoted by the subscript $s = 1, \ldots, N$. Each class is characterized by the values of diameter d_s, microscopic density ρ_s, specific heat $c_{p,s}$, thermal conductivity k_s and viscosity μ_s. The state of the solid phase s is described by its volume fraction ϵ_s, velocity $\mathbf{v}_s$ and total specific energy E_s (or as an alternative specific enthalpy h_s or temperature T_s), defined at each point $\mathbf{x} \in \mathbb{R}^3$ and time $t \in \mathbb{R}^+$.

2.1.2 Gas phase properties

The gas phase is considered as compressible and inert, i.e. not chemically reactive, and it obeys the ideal gas law. The gas phase can be composed of M different chemical components, such as water vapor H_2O, carbon dioxide CO_2, oxygen O_2, hydrogen H_2 and atmospheric air, considered as a single chemical component. In the following sections we indicate with the subscript g the gas phase and with $l = 1, \ldots, M$ the chemical components. We denote with y_l the mass fraction of the l-th gas chemical component, that is

$$y_l = \frac{M_l}{M_{gas}} = \frac{M_l}{\sum_{l=1}^{M} M_l}. \tag{2.5}$$

It results that

$$\sum_{l=1}^{M} y_l = 1. \tag{2.6}$$

Each component is characterized by its specific heat at constant pressure $c_{p,l}$ and constant volume $c_{v,l}$, whereas thermal conductivities k_g and viscosities μ_g are supposed to be equal for all the gas species. The state of the gas phase is described by its volume fraction ϵ_g, density ρ_g, pressure P_g, velocity $\mathbf{v}_g$ and total specific energy E_g (or as an alternative specific enthalpy h_g or temperature T_g), defined at each point $\mathbf{x} \in \mathbb{R}^3$ and time $t \in \mathbb{R}^+$.

2.1.3 Mixture properties

The multiphase mixture has certain mixture properties that can be evaluated from the properties of each phase. As an example, the *mixture density* is defined as the sum of the bulk densities, that is

$$\rho_{mix} = \epsilon_g \rho_g + \sum_{s=1}^{N} \epsilon_s \rho_s. \tag{2.7}$$

Analogously, given the quantities Q_g and Q_s, for all $s = 1, \ldots, N$, the corresponding mixture quantity Q_{mix} can be computed as mass-weighted average of the phases' properties, that is

$$\rho_{mix} Q_{mix} = \epsilon_g \rho_g Q_g + \sum_{s=1}^{N} \epsilon_s \rho_s Q_s. \tag{2.8}$$

2.1.4 The particulate loading

The *particulate loading*, or mass loading, is defined as the mass density ratio of the dispersed solid phase to that of the carrier gaseous phase [30], that is

$$\beta = \frac{\epsilon_s \rho_s}{\epsilon_g \rho_g}. \tag{2.9}$$

We can introduce also the *density ratio*

$$\eta = \frac{\rho_s}{\rho_g} \tag{2.10}$$

which is usually greater that 1000 for gas/solid flows [30]. Using these parameters it is possible to estimate the average distance L between the individual particles of the solid phase. An estimate of this distance is given by [30]

$$\frac{L}{d_s} = \left(\frac{\pi}{3} \frac{1+\kappa}{\kappa} \right)^{\frac{1}{3}} \tag{2.11}$$

where $\kappa = \beta/\eta$. The value of this parameter allows to understand whether the particles can be treated as isolated, i.e. $L \gg d_s$, or whether interactions between particles can not be neglected, i.e. $L \sim 1$. In conclusion, the particulate loading allows to understand which is the appropriate multiphase flow model to be used to solve a specific problem.

2.1.5 The Stokes number

The *Stokes number* can be defined as the ratio between the particle response time and the fluid characteristic time [30, 86]:

$$St = \frac{\tau_s}{\bar{t}} \tag{2.12}$$

where $\tau_s = \frac{\rho_s d_s^2}{18 \mu_g}$ and $\bar{t}$ is based on the characteristic length $\bar{L}$ and the characteristic velocity $\bar{U}$ of the system, that is $\bar{t} = \bar{L}/\bar{U}$. The Stokes number allows to characterize the degree of coupling between the different phases. As the particulate loading, the Stokes number helps to select the correct modeling approach.

2.2 Mathematical modeling of multiphase gas–particle flows

The volume fraction occupied by the solid phase, the particulate mass loading and the Stokes number introduced in the previous section are the critical parameters that determine the level of interaction between the phases and allow to distinguish between different modeling approaches [15, 37].

Three types of models are usually adopted for the description of dispersed gas–particle flows: trajectory models, two-fluid models and mixture models.

Trajectory models are also known as discrete or Lagrangian models. The motion of the dispersed phase is assessed by tracking either the motion of the actual particles or the motion of larger, representative particles through the flow field. The effects of the flow around each of the particles are included into assumed drag, lift and moment forces acting on and altering the trajectory of those particles.

Trajectory models consider a one-way coupling between the phases, that is the carrier phase has a dominant effect on the dynamics of the dispersed phase, which in turn can not influence the dynamics of the carrier phase [15, 33]. The solution is obtained by solving a single phase flow for the continuous phase and applying this flow field into the equations of motion for the particles to compute their trajectory. The fundamental assumptions made in this kind of model are that the dispersed phase occupies a low volume fraction and that the particle mass loading is small. Indeed, this approach is valid in very dilute flows, where particle–particle interactions and the effects of the particle volume fraction on the gas phase are negligible. As the concentration of the dispersed phase increases, more complex phenomena can arise both in the continuous phase flow and the dispersed phase motions and a two-way coupling should be modeled. Trajectory models are appropriate for the description of sprays, coal and liquid fuel combustion, but they cannot be applied when the second phase volume fraction is not negligible, e.g. fluidized beds or liquid/liquid mixtures. Finally, since the particle trajectories are computed individually, the number of particles that can be actually simulated with a Lagrangian model is usually limited by computational resources.

The alternative approach, the *two-fluid model*, is also known as continuum or Eulerian-Eulerian model. The dispersed particles are treated mathematically as a continuous phase, interpenetrating and interacting with the gas phase [3, 30]. Conservation equations are introduced for each considered phase. These equations include interaction terms modeling the exchange of mass, momentum and energy between the two phases, accounting for the back influence that the dispersed phase has on the carrier phase dynamics (two-way coupling). The model is closed by providing constitutive relations obtained from empirical information or by application of kinetic theory. Essentially, the two-fluid model neglects the discrete nature of the dispersed phase and approximates its effects on the continuous phase.

In this approach, averaging methods are needed to characterize the properties of the dispersed phase [30]. In particular, the averaging process is based on the underlying hypothesis that there exists an infinitesimal volume of dimension V_0 such that V_0 is much smaller than the typical distance over which the phase properties vary significantly, but much larger than the size of the individual phase elements. These conditions are necessary to define derivatives of the flow properties and to guarantee that the averaging volume contains representative samples of each of the components. However, it is not always possible to define the averaging volume V_0. In particular, this approach is valid when a large number of small particles is considered. A significant advantage of the Eulerian approach is that the equations for both phases have the same form, so the same solution techniques can be used for each phase. Applications of the two-fluid model include particle suspensions and fluidized beds.

In *mixture models*, or homogeneous equilibrium models, equations that are generalizations of single-phase ones are postulated. As proposed in [21] and [86], the two-phase mixture is regarded as a single phase with modified properties. It is assumed that the velocity and the temperature are equal for all the phases. For example, when one phase is finely dispersed in another phase generating large interfacial area, this assumption is often valid. The resulting equations resemble those for a pseudofluid with mixture properties and an equation of state which links the phases to obtain these thermodynamic mixture properties is needed. The mixture model is preferable if there is a

wide distribution of the dispersed fine particles, i.e. if the particles vary in size and the largest particles do not separate from the primary flow field, because it is less computationally expensive than the full Eulerian model.

The choice of the most appropriate model depends on the applications considered. In general, we need to determine the flow regime of the multiphase system that we want to describe in order to select properly the appropriate multiphase model. In general, for very dilute flows containing large particles the Lagrangian model is appropriate. On the contrary, when the particle volume fraction increases, mixture or Eulerian models should be used.

In order to identify the appropriate multiphase model, in addition to the particle volume fraction, also the particulate loading β should be considered. Depending on the particulate loading, the degree of interactions between different phases can be divided into three categories. For very low loading, the coupling between the phases is one-way, i.e. the continuous phase influences the particles via drag force and turbulence, but the particles have no influence on the fluid. The mixture, the Lagrangian and the Eulerian model can all handle this type of regime correctly, but the mixture and the Lagrangian models are less expensive.

For high loading, the two-way coupling between gas and particles plus their influence on the pressure and viscous stresses has to be described (four-way coupling). Usually, only the Eulerian model can handle this type of problem correctly, although recently also Lagrangian models have been extended to include particle–particle interactions [139, 148].

For intermediate loading, the coupling is two-way, that is the particles influence the fluid flow by means of reduction of momentum and turbulence. In this case, to choose between the Lagrangian, the mixture and the Eulerian models we need to look at the Stokes number St. When the Stokes number is much lower than one, the particles will follow the flow closely and any of the three models can be applied. In most cases the mixture model is used due to the lower computational cost. On the other hand, when the Stokes number is larger than one, particles dynamics decouples from gas dynamics and trajectory models or Eulerian models should be used.

In this work the focus is on gas–particle flows in which mechanical and thermal equilibrium between different phases can not be assumed, so that mixture models are in general not valid. Moreover, this work is not restricted to the analysis of dilute regimes: since the number of solid particles could become large, discrete particle-tracking approaches could become computationally too much expensive. Thus, in this work the Eulerian-Eulerian two-fluid or multifluid approach will be adopted to describe multiphase gas–particle flows, in order to be able to handle the widest range of physical phenomena.

2.3 Conservation equations

The averaging approach is adopted to derive the conservation equations for each phase that compose the mixture. Variables are averaged over a region that is large compared with the particle spacing but smaller than the flow domain, as discussed in the previous

section. The Eulerian approach leads to a model that is composed by a set of coupled partial differential equations for the independent variables ρ_g, P_g, y_l, ϵ_s, $\mathbf{v}_s$, E_s (or h_s, or T_s), with $s = g, 1, \ldots, N$ and $l = 1, \ldots, M$.

2.3.1 Conservation of mass

The mass conservation equations for the gas phase g, the s-th solid phase and the l-th gas chemical component are

$$\frac{\partial}{\partial t}(\epsilon_g \rho_g) + \nabla \cdot (\epsilon_g \rho_g \mathbf{v}_g) = 0, \tag{2.13a}$$

$$\frac{\partial}{\partial t}(\epsilon_s \rho_s) + \nabla \cdot (\epsilon_s \rho_s \mathbf{v}_s) = 0, \tag{2.13b}$$

$$\frac{\partial}{\partial t}(\epsilon_l \rho_l y_l) + \nabla \cdot (\epsilon_l \rho_l y_l \mathbf{v}_g) = 0, \tag{2.13c}$$

for all $s = 1, \ldots, N$ and $l = 1, \ldots, M$. The first term on the left side accounts for the rate of mass accumulation per unit volume and the second term is the net rate of advective mass flux. The last equation, in particular, represents the species conservation for the gas phase in terms of mass fractions y_l. All types of mass transfer between different phases are neglected, e.g. chemical reactions, phase changes, fragmentation and aggregation, sedimentation processes, and pure transport equations for each component of the mixture are obtained.

2.3.2 Conservation of momentum

The momentum balance equations for the gas phase and the s-th solid phase, for all $s = 1, \ldots, N$ with $p \neq s$, can be written as

$$\frac{\partial}{\partial t}(\epsilon_g \rho_g \mathbf{v}_g) + \nabla \cdot (\epsilon_g \rho_g \mathbf{v}_g \mathbf{v}_g) = -\nabla P_g + \nabla \cdot \mathbf{T}_g + \epsilon_g \rho_g \mathbf{g} + \mathbf{D}_g, \tag{2.14a}$$

$$\frac{\partial}{\partial t}(\epsilon_s \rho_s \mathbf{v}_s) + \nabla \cdot (\epsilon_s \rho_s \mathbf{v}_s \mathbf{v}_s) = \nabla \cdot \mathbf{T}_s + \epsilon_s \rho_s \mathbf{g} + \mathbf{D}_s. \tag{2.14b}$$

In the left-hand-side we can recognize the accumulation and advection terms, whereas the right-hand-side of the two equations accounts for viscous effects, gravitational force and drag forces between the phases. $\mathbf{T}_g$ and $\mathbf{T}_s$ are the stress tensors and $\mathbf{D}_s$ represents the total drag force acting on the phase s. Finally, $\mathbf{g}$ is the gravitational acceleration. Pressure gradient is included only in the gas momentum equation, whereas granular pressure effects are neglected in the particle momentum equation [69, 115].

2.3.3 Conservation of energy

The energy balance equations for the gas phase and the solid phases are written in terms of total energy [15, 30], for all $s = 1, \ldots, N$:

$$\frac{\partial}{\partial t}(\epsilon_g \rho_g E_g) + \nabla \cdot (\epsilon_g \rho_g E_g \mathbf{v}_g) = -\nabla \cdot (P_g \mathbf{v}_g) + \nabla \cdot (\mathbf{T}_g \cdot \mathbf{v}_g) + \nabla \cdot (k_{ge} \epsilon_g \nabla T_g) + \epsilon_g \rho_g \mathbf{g} \cdot \mathbf{v}_g + \mathbf{D}_g \cdot \mathbf{v}_g + \mathrm{Q}_g, \tag{2.15a}$$

$$\frac{\partial}{\partial t}(\epsilon_s \rho_s E_s) + \nabla \cdot (\epsilon_s \rho_s E_s \mathbf{v}_s) = \nabla \cdot (\mathbf{T}_s \cdot \mathbf{v}_s) + \nabla \cdot (k_s \epsilon_s \nabla T_s) + \epsilon_s \rho_s \mathbf{g} \cdot \mathbf{v}_s + \mathbf{D}_s \cdot \mathbf{v}_s + \mathrm{Q}_s, \tag{2.15b}$$

where k_{ge} is the effective thermal conductivity of the gas phase, Q_g and Q_s is the heat transferred from the surrounding phases to the phases g and s, respectively. Diffusive transport is expressed in the form of Fourier law.

For the gas phase, the reversible rate of energy change due to compression or expansion has been taken into account, since it is important in transient, compressible flows. The viscous dissipation and the work done by the gravitational and the drag forces are included in the energy balance equations, even if in volcanological applications they could be neglected, as discussed in Section 2.6.

The energy balance can also be written in terms of the specific enthalpies h_g, h_s, for all $s = 1, \ldots, N$:

$$\frac{\partial}{\partial t}(\epsilon_g \rho_g h_g) + \nabla \cdot (\epsilon_g \rho_g h_g \mathbf{v}_g) = \epsilon_g \left(\frac{\partial P_g}{\partial t} + \mathbf{v}_g \cdot \nabla P_g \right) + \nabla \cdot (\mathbf{T}_g \cdot \mathbf{v}_g) + \nabla \cdot (k_{ge} \epsilon_g \nabla T_g) + \epsilon_g \rho_g \mathbf{g} \cdot \mathbf{v}_g + \mathbf{D}_g \cdot \mathbf{v}_g + \mathrm{Q}_g, \tag{2.16a}$$

$$\frac{\partial}{\partial t}(\epsilon_s \rho_s h_s) + \nabla \cdot (\epsilon_s \rho_s h_s \mathbf{v}_s) = \nabla \cdot (\mathbf{T}_s \cdot \mathbf{v}_s) + \nabla \cdot (k_s \epsilon_s \nabla T_s) + \epsilon_s \rho_s \mathbf{g} \cdot \mathbf{v}_s + \mathbf{D}_s \cdot \mathbf{v}_s + \mathrm{Q}_s. \tag{2.16b}$$

The first term on the right-hand-side of Equation (2.16a) accounts for the expansion and compression of the gas phase. In general, enthalpies conservation equations are preferred when reactions and phase transitions are introduced in the multiphase model.

2.3.4 Mathematical model in cylindrical coordinates

In the previous sections, the mathematical model describing the dynamics of multiphase gas–particle flows has been presented referring to a Cartesian coordinate system (x, y, z). However, in the application of the model to phenomena that have some symmetry about the longitudinal axis, it is often useful to write and solve it using cylindrical coordinates, i.e. (r, φ, z) where r is the radial distance, φ is the angular position and z is the symmetry axis. In this presentation, the cylindrical axis coincides with the Cartesian z-axis and the correspondence between cylindrical and Cartesian coordinate systems is given by

$$\begin{aligned} x &= r \cos \varphi \\ y &= r \sin \varphi. \end{aligned} \tag{2.17}$$

Equations (2.13a), (2.13b), (2.13c), (2.14a), (2.14b), (2.15a) and (2.15b) can be written in cylindrical coordinates by appling differential operators in the new coordinate sys-

tem. The divergence operator in cylindrical coordinates applied to the vectorial function $\mathbf{f} = (f_r, f_\varphi, f_z)^T$ is defined as

$$\nabla_r \cdot \mathbf{f} = \frac{1}{r}\frac{\partial (r f_r)}{\partial r} + \frac{1}{r}\frac{\partial f_\varphi}{\partial \varphi} + \frac{\partial f_z}{\partial z}. \tag{2.18}$$

Analogously, the gradient of the scalar function f is defined as

$$\nabla_r f = \begin{bmatrix} \dfrac{\partial f}{\partial r} \\ \dfrac{1}{r}\dfrac{\partial f}{\partial \varphi} \\ \dfrac{\partial f}{\partial z} \end{bmatrix}. \tag{2.19}$$

In the hypothesis of axisymmeric flow in $\mathbb{R}^3$, the derivative along the axial coordinate is assumed to be null, i.e. $\frac{\partial}{\partial \varphi} = 0$, and the spatial dimension of the problem is reduced by one.

2.4 Constitutive equations

The mathematical model presented in the previous section is completed by a set of closure relationships.

2.4.1 Volumetric and mass fraction closures

The averaging operation applied to derive the balance equations for the multiphase flow leads to the introduction of new field variables, the volume fractions ϵ_s for all $s = g, 1, \ldots, N$, which are assumed to be continuous functions of space and time. Volumetric and mass fractions closures represent the fact that phases are treated as interpenetrating continua and by definition it results that

$$0 \leq \epsilon_g \leq 1, \quad 0 \leq \epsilon_s \leq 1, \tag{2.20a}$$

$$\epsilon_g + \sum_{s=1}^{N} \epsilon_s = 1. \tag{2.20b}$$

2.4.2 Equations of state

The gas phase is compressible and we suppose that the relation between the thermodynamic quantities is given by the ideal gas law:

$$\rho_g = \frac{P_g}{R_g T_g}, \tag{2.21}$$

where R_g is the specific gas constant of the mixture of gaseous components:

$$R_g = \frac{R}{M_{mol}}. \tag{2.22}$$

Here, R is the universal gas constant, which is equal to 8.314 J/K·mol, and M_{mol} is the molar mass of the gaseous mixture. Particulate solid phases are considered as incompressible, consequently their microscopic density is constant

$$\rho_s = const, \quad \forall\ s = 1 \dots N, \tag{2.23}$$

and an equation of state for the solid phase is not needed. The total energy per unit mass (or total specific energy) of the phase s is defined as

$$E_s = e_s + \frac{1}{2}|\mathbf{v}_s|^2 \tag{2.24}$$

where e_s is the specific internal energy

$$e_s = c_{v,s}(T_s)T_s. \tag{2.25}$$

The coefficient $c_{v,s}$ is the specific heat at constant volume, which is a function of temperature for the gaseous components and approximately a constant for the solid phases. Analogously, the specific enthalpy is related to the temperature by

$$h_s = c_{p,s}(T_s)T_s \tag{2.26}$$

where coefficient $c_{p,s}$ is the specific heat at constant pressure. For solid particles, we assume that $c_{p,s} = c_{v,s}$, whereas for the gas phase it results that $c_{p,g} = c_{v,g} + R_g$. For the gas phase, using Equation (2.21), the total specific energy is computed as

$$E_g = \frac{P_g}{(\gamma_g - 1)\rho_g} + \frac{1}{2}|\mathbf{v}_g|^2 \tag{2.27}$$

where γ_g is the heat capacity ratio for the gas phase, that is

$$\gamma_g = \frac{c_{p,g}}{c_{v,g}}\,. \tag{2.28}$$

Due to their minor dependence on temperature, the specific heats for particles $c_{p,s}$ are assumed to be constant and to correspond to average values. The specific heat of the gas phase depends on temperature and it is computed as a function of the specific heats of the M chemical components:

$$c_{p,g}(T_g) = \sum_{l=1}^{M} y_l C_{p,l}(T_g). \tag{2.29}$$

Finally, the speed of sound waves of the gas is defined as

$$c = \sqrt{\gamma \frac{P_g}{\rho_g}}. \tag{2.30}$$

2.4.3 Stress tensors

The gas phase stress tensor is divided into a viscous component $\boldsymbol{\tau}_{g,\mu}$ and a turbulent component $\boldsymbol{\tau}_{g,t}$. It takes the following form:

$$\mathbf{T}_g = \boldsymbol{\tau}_{g,\mu} + \boldsymbol{\tau}_{g,t}. \tag{2.31}$$

The viscous tensor is given by

$$\boldsymbol{\tau}_{g,\mu} = \epsilon_g \mu_g \left(\nabla \mathbf{v}_g + \nabla \mathbf{v}_g^T - \frac{2}{3} (\nabla \cdot \mathbf{v}_g) \mathbf{I} \right). \tag{2.32}$$

The turbulent term is modeled by adopting a turbulent subgrid scale model and following the Large Eddy Simulation (LES) approach. An eddy turbulent viscosity $\mu_{g,t}$ is introduced:

$$\boldsymbol{\tau}_{g,t} = \epsilon_g \mu_{g,t} \left(\nabla \mathbf{v}_g + \nabla \mathbf{v}_g^T \right). \tag{2.33}$$

Different expressions for the turbulent viscosity $\mu_{g,t}$ have been introduced in the literature. The simplest one is the Smagorinsky model [122]

$$\mu_{g,t} = l^2 \rho_g \left[2 \; tr \left(\frac{\boldsymbol{\tau}_{g,\mu} \cdot \boldsymbol{\tau}_{g,\mu}}{(\epsilon_g \mu_g)^2} \right) \right]^{1/2}, \tag{2.34}$$

where l represents the subgrid length scale of turbulent motions and is a parameter for the model. More complex models have been proposed later, such as the Germano dynamic model [48], the localized dynamic model [76] or the dynamic global-coefficient model [149].

The stress tensor of the s-th particulate phase is described in terms of a viscous component $\boldsymbol{\tau}_{s,\mu}$ and a Coulombic repulsive component $\boldsymbol{\tau}_{s,c}$. The tensor can be expressed by

$$\mathbf{T}_s = \boldsymbol{\tau}_{s,\mu} + \boldsymbol{\tau}_{s,c}, \quad \forall \; s = 1, \ldots, N, \tag{2.35}$$

where the viscous tensor is

$$\boldsymbol{\tau}_{s,\mu} = \epsilon_s \mu_s \left[\nabla \mathbf{v}_s + \nabla \mathbf{v}_s^T - \frac{2}{3} (\nabla \cdot \mathbf{v}_s) \mathbf{I} \right], \tag{2.36}$$

and the Coulombic component is given by

$$\boldsymbol{\tau}_{s,c} = -\tau_{s,c} \mathbf{I}. \tag{2.37}$$

The Coulombic coefficient $\tau_{s,c}$ is defined implicitly through its gradient by

$$\nabla \tau_{s,c} = G(\epsilon_s) \nabla \epsilon_s, \qquad G(\epsilon_s) = 10^{-a\epsilon_s + b}, \tag{2.38}$$

with $a < 0$. $G(\epsilon_s)$ is the solid elastic modulus able to account for repulsive forces when high values of particle volume fraction are reached in the mixture [49, 50].

It can be observed that the Coulombic component of the solid stress tensor plays the role that the pressure gradient has in the gas momentum equation. This is the reason why the Coulombic term $\tau_{s,c}$ is often called *solid pressure*. This term has to be specified in order to ensure that void fraction does not become unphysically small. This solid pressure term is then specified as an arbitrary function of solid volume fraction that becomes very large when the solid fraction approaches the packed-bed void fraction. An alternative approach, which avoids the need to specify a solid pressure function, is to treat the granular media as an incompressible fluid at a certain critical void fraction. With this method, the solid pressure has to be computed as a function of the granular temperature of the solid phase [132].

Concerning the solid viscosity value, semi-empirical correlations based on experimental works and on kinetic theory studies can be adopted [51]. As an example, it is possible to assume that

$$\mu_s = c_s, \tag{2.39}$$

with $c_s \in [0.5, 2.0]$ Pa·s, where larger values apply to coarser particles.

2.4.4 Effective conductivity

The effective gas conductivity is determined through the turbulent Prandtl number Pr_t as

$$k_{ge} = k_g + k_{gt}, \qquad k_{gt} = \frac{c_{p,g}\,\mu_{g,t}}{Pr_t}. \tag{2.40}$$

Here, the turbulent gas conductivity quantifies the conduction enhancement due to turbulence.

2.4.5 Drag forces

The drag force that the solid dispersed particles exert on the gas phase can be computed by superimposing the contributions from different classes of particles. Moreover, it is well known that the drag force is proportional to the difference between the velocities of the two considered phases. Thus, the drag force acting on the gas phase can be defined as

$$\mathbf{D}_g = \sum_{s=1}^{N} D_{g,s}(\mathbf{v}_s - \mathbf{v}_g). \tag{2.41}$$

Analogously, the drag force acting on a selected particle class is given by the sum of the drag force exerted by the gas phase and the drag force exerted by other particles, that is

$$\mathbf{D}_s = D_{s,g}(\mathbf{v}_g - \mathbf{v}_s) + \sum_{p=1}^{N} D_{s,p}(\mathbf{v}_p - \mathbf{v}_s). \tag{2.42}$$

The interphase exchange coefficients $D_{g,s}$ and $D_{s,p}$ are derived from semi-empirical correlations.

Gas–particle drag coefficients

Different expressions for the interphase exchange coefficient between gas and particles can be found in the literature. In [141], the following expression, valid in dilute regimes, i.e. $\epsilon_g > 0.8$, has been proposed:

$$D_{g,s} = \frac{3}{4} C_{d,s} \frac{\epsilon_g \epsilon_s \rho_g |\mathbf{v}_s - \mathbf{v}_g|}{d_s}\, \epsilon_g^{-2.7}, \quad \forall\, s = 1, \ldots, N, \tag{2.43}$$

with [118]

$$C_{d,s} = \begin{cases} \dfrac{24}{Re_s}\left[1 + 0.15 Re_s^{0.687}\right], & \text{if } Re_s < 1000, \\ 0.44, & \text{if } Re_s \geq 1000, \end{cases} \tag{2.44}$$

where the particle Reynolds number is defined as

$$Re_s = \frac{\epsilon_g \rho_g d_s |\mathbf{v}_s - \mathbf{v}_g|}{\mu_g}. \tag{2.45}$$

In the dense regime, for $\epsilon_g < 0.8$, the drag expression by [40] can be used:

$$D_{g,s} = 150\frac{\epsilon_s^2 \mu_g}{\epsilon_g d_s^2} + 1.75\frac{\epsilon_s \rho_g |\mathbf{v}_s - \mathbf{v}_g|}{d_s}, \quad \forall\ s = 1, \dots, N, \tag{2.46}$$

By definition it results that $D_{g,s} = D_{s,g}$.

This two expressions have been widely validated by experiments. However, the two asymptotic regimes do not analytically match at $\epsilon_g = 0.8$, so that other continuous formulations have been proposed. However, in this work we will only deal with dilute regimes and will not investigate in detail the effect of the drag coefficient formulation.

Particle–particle drag coefficient

To define the particle–particle interphase coefficient, in [130] the following semi-empirical correlation is proposed:

$$D_{p,s} = F_{p,s}\alpha(1+e)\rho_s\epsilon_s\rho_p\epsilon_p\frac{(d_s+d_p)^2}{\rho_s d_s^3 + \rho_p d_p^3}|\mathbf{v}_p - \mathbf{v}_s|, \quad \forall\ s = 1 \dots N, p \neq s, \tag{2.47}$$

where α is an empirical coefficient accounting for non-head-on collisions, e is the restitution coefficient for a collision and $F_{p,s}$ is a complex function of the volume fraction of the two phases and of the maximum volume fraction of a random closely packed mixture $\epsilon_{p,s}$:

$$F_{p,s} = \frac{3\epsilon_{p,s}^{1/3} + (\epsilon_s + \epsilon_p)^{1/3}}{2\left(\epsilon_{p,s}^{1/3} - (\epsilon_s + \epsilon_p)^{1/3}\right)}. \tag{2.48}$$

In order to define $\epsilon_{p,s}$, the following quantities are introduced:

$$\begin{aligned} a &= \left(\frac{d_s}{d_p}\right)^{1/2}, \quad \text{with } d_s \leq d_p, \\ X_s &= \frac{\epsilon_s}{\epsilon_s + \epsilon_p}, \end{aligned} \tag{2.49}$$

and $\Phi_s = 0.63$, representing the solid volume fraction at maximum packing in a single particle system for the s-th phase. Then we define

$$\epsilon_{p,s} = \begin{cases} [(\Phi_s - \Phi_p) + (1-a)(1-\Phi_s)\Phi_p]\dfrac{[\Phi_s + (1-\Phi_p)\Phi_s]}{\Phi_s}X_s + \Phi_p, \\ \qquad\qquad \text{if } X_s \leq \dfrac{\Phi_s}{\Phi_s + (1-\Phi_s)\Phi_p}, \\ (1-a)[\Phi_s + (1-\Phi_s)\Phi_p](1-X_s) + \Phi_s, \\ \qquad\qquad \text{if } X_s \geq \dfrac{\Phi_s}{\Phi_s + (1-\Phi_s)\Phi_p}. \end{cases} \tag{2.50}$$

By definition it results that $D_{p,s} = D_{s,p}$.

The empirical expressions for gas–particle and particle–particle drag coefficient reported in this section as an example deal with uniform, smooth, hard spherical particles. More complex drag definitions, starting from the original proposal by [100], have been proposed in the literature accounting for rough, non-spherical or soft particles. As an example, soft spherical particles have been considered in [31]; effects of Van der Waals interactions in dense regimes have been described in [62]; finally, several drag models have been proposed for non spherical particles, e.g. [87, 88, 136, 140] Finally, it may be necessary to explicitly account for the effect of particle interactions on the gas–solid interaction force. For example, the averaging required to approximate the particles as a granular continuum renders the hydrodynamic equations incapable of resolving the wake dominated flow near the particles that under certain favorable conditions cause the particles to form clusters. The effect of such aggregates can be explicitly accounted for in the fluid–solid interaction constitutive relation. In any case, all the mathematical and numerical issues presented in this work do not depend on the drag expressions introduced in the model.

2.4.6 Heat transfer

The heat transfer between different phases is given by the product of a transfer coefficient Q_s and a driving force, which is the temperature difference between the two phases. The heat transferred from the solid phase to the gas phase is

$$\mathrm{Q}_g = \sum_{s=1}^{N} Q_s(T_s - T_g). \tag{2.51}$$

Analogously, for solid particles the heat transfer term is given by

$$\mathrm{Q}_s = Q_s(T_g - T_s). \tag{2.52}$$

The heat transfer term between different classes of solid particles can been neglected, if we assume not to be closed to the granular regime.

The coefficient Q_s represents the volumetric interphase heat transfer coefficient which can be computed as the product of the specific exchange area and the fluid-particle heat transfer coefficient written in terms of an empirical expression for the Nusselt number Nu_s [60], that is:

$$Q_s = Nu_s \frac{6 k_g \epsilon_s}{d_s^2}, \tag{2.53a}$$

$$Nu_s = \left(2 + 5\epsilon_s^2\right)\left(1 + 0.7 Re_s^{0.2} Pr^{1/3}\right) + \left(0.13 + 1.2\epsilon_s^2 Re_s^{0.7} Pr^{1/3}\right), \tag{2.53b}$$

with

$$Pr = \frac{c_{p,g}\mu_g}{k_g}, \tag{2.54}$$

where k_g is the thermal conductivity of the gas phase. Other expressions for the Nusselt number have been proposed in the literature, e.g. [46, 107, 143].

2.5 Pseudogas model approximation

As discussed in Section 2.2, when the ratio between the particle response time scale, i.e. the particle relaxation time τ_s, and the system characteristic time scale $\bar{t}$ is small, the

multiphase mixture can be described using a mixture model, that is by describing the dynamics of a unique phase, called *pseudogas* or *dusty gas*, with averaged properties.

Suppose that the mixture composed by the gas phase g and one class of solid particles s satisfies the pseudogas hypothesis. Then, if we indicate with the subscript ps the properties of the pseudogas, the mixture model takes the following form:

$$\frac{\partial}{\partial t}(\rho_{ps}) + \nabla \cdot (\rho_{ps}\mathbf{v}_{ps}) = 0, \tag{2.55a}$$

$$\frac{\partial}{\partial t}(\rho_{ps}\mathbf{v}_{ps}) + \nabla \cdot (\rho_{ps}\mathbf{v}_{ps}\mathbf{v}_{ps}) = -\nabla P_{ps} + \nabla \cdot \mathbf{T}_{ps} + \rho_{ps}\mathbf{g}, \tag{2.55b}$$

$$\frac{\partial}{\partial t}(\rho_{ps}E_{ps}) + \nabla \cdot (\rho_{ps}E_{ps}\mathbf{v}_{ps}) = -\nabla \cdot (P_{ps}\mathbf{v}_{ps}) + \nabla \cdot (k_{ps}\nabla T_{ps}). \tag{2.55c}$$

By definition, the mixture model is derived from multiphase gas–particle equations by assuming that

$$\begin{aligned} \mathbf{v}_{ps} &= \mathbf{v}_g = \mathbf{v}_s, \\ T_{ps} &= T_g = T_s. \end{aligned} \tag{2.56}$$

Moreover, the pseudogas density is defined by relation (2.7), whereas the mixture total energy is defined by relation (2.8). The pseudogas pressure is computed by means of a modified equation of state, that accounts for the presence of solid particles in the gas phase:

$$P_{ps} = \rho_{ps}R_{ps}T_{ps} \tag{2.57}$$

where

$$R_{ps} = \frac{R}{M_{ps}} \simeq \frac{R_g}{1+\beta} \tag{2.58}$$

and M_{ps} is the molar mass of the pseudogas mixture. Appropriate corrections have to be introduced also for the thermodynamic coefficients of the gas phase that appear in the constitutive equations, i.e. gas kinematic viscosity ν_{ps} and specific heats $c_{v,ps}$, $c_{p,ps}$. They can be adjusted by means of the particulate loading β, defined in (2.9), as proposed by [86]:

$$\nu_{ps} = \frac{\nu_g}{1+\beta} = \frac{\mu_g}{\rho_g(1+\beta)}, \tag{2.59a}$$

$$c_{v,ps} = \frac{c_{v,g} + \beta c_{v,s}}{1+\beta}, \tag{2.59b}$$

$$c_{p,ps} = \frac{c_{p,g} + \beta c_{p,s}}{1+\beta}, \tag{2.59c}$$

$$\gamma_{ps} = \frac{c_{p,g} + \beta c_{p,s}}{c_{v,g} + \beta c_{v,s}}. \tag{2.59d}$$

For dilute mixture the dynamic viscosity μ_{ps} and the conductivity k_{ps} of the pseudogas can be approximated with the one of the pure gas [86, 145], that is

$$\mu_{ps} \simeq \mu_g, \tag{2.60a}$$

$$k_{ps} \simeq k_g. \tag{2.60b}$$

In general, however, as proposed in [17, 145], the pseudogas dynamic viscosity can be corrected with a factor proportional to the particle loading that accounts for the effects

of particle–particle collisions. In the present work, following [145], the pseudogas dynamic viscosity is computed as:

$$\mu_{ps} = \mu_g(1+\beta)^2. \tag{2.61}$$

Finally, according to [15, 86], the mixture speed of sound is computed as follows

$$c_{mix} = \sqrt{\gamma_g R_g T_g \frac{1+\beta\frac{c_{p,s}}{c_{p,g}}}{(1+\beta)\left(1+\beta\frac{c_{v,s}}{c_{v,g}}\right)}}. \tag{2.62}$$

A simplified expression can be derived for high values of particulate loading, i.e. $\beta \gg 1$, typical of gas–particle flows:

$$c_{mix} = \sqrt{\frac{R_g T_g}{1+\beta}}. \tag{2.63}$$

Relation (2.62) highlights how the presence of solid particle causes the speed of sound waves to decrease with respect to the pure gas speed of sound.

The extension of the pseudogas model to a mixture with more than one classes of solid particles is straightforward.

2.6 Dimensional analysis

The objective of dimensional analysis is to get insight into the fundamental properties of a complex system. The equations are rescaled in order to assess the relative importance of each term. Through this analysis, non-dimensional parameters are derived to quantify the relative importance of the various physical phenomena that are considered in the model. The comparison between these parameters allows to understand the physical mechanisms that dominate in a complex situation, to check the plausibility of the mathematical model and to identify possible simplifications [80].

In thermo-fluid dynamics, the dimension of any physical quantity can be expressed in terms of four independent fundamental dimensions: mass M, length L, time T and temperature $\mathbf{\Theta}$, as shown in Table 2.1. However, this is not the only possible choice. In this work, the set of independent dimensions is given by length L, velocity U, density $\boldsymbol{\rho}$ and temperature $\mathbf{\Theta}$, where velocity and density will play the role of time and mass respectively. Adopting this approach, the following fundamental quantities, characterizing the initial and boundary conditions of the system, are introduced

- $\bar{L}$ = characteristic length,
- $\bar{U}$ = characteristic velocity,
- $\bar{\rho}$ = characteristic density,
- $\bar{\Theta}$ = characteristic temperature.

and the following non-dimensional quantities are defined

- non-dimensional length $\tilde{x} = \dfrac{x}{\bar{L}}$,

- non-dimensional velocity $\tilde{\mathbf{v}} = \dfrac{\mathbf{v}}{\bar{U}}$,
- non-dimensional density $\tilde{\rho} = \dfrac{\rho}{\bar{\rho}}$,
- non-dimensional temperature $\tilde{\Theta} = \dfrac{T}{\bar{\Theta}}$.

Secondary non-dimensional quantities can be derived by products of the fundamental ones, e.g.

- non-dimensional time $\tilde{t} = t\,\dfrac{\bar{U}}{\bar{L}}$,
- non-dimensional pressure $\tilde{P}_g = \dfrac{P_g}{\bar{\rho}\bar{c}^2}$, where $\bar{c}$ is the speed of sound in the fluid,
- non-dimensional total energy $\tilde{E} = \dfrac{E}{c_p\bar{\Theta}}$.

2.6.1 Dimensionless form of the equations

Let us consider the Equations (2.13a), (2.13b), (2.14a), (2.14b), (2.15a), (2.15b) for the gas phase g and only one solid phase s:

$$\frac{\partial}{\partial t}(\epsilon_g\rho_g) + \nabla\cdot(\epsilon_g\rho_g\mathbf{v}_g) = 0, \tag{2.64a}$$

$$\frac{\partial}{\partial t}(\epsilon_s\rho_s) + \nabla\cdot(\epsilon_s\rho_s\mathbf{v}_s) = 0, \tag{2.64b}$$

$$\frac{\partial}{\partial t}(\epsilon_g\rho_g\mathbf{v}_g) + \nabla\cdot(\epsilon_g\rho_g\mathbf{v}_g\mathbf{v}_g) = -\nabla P_g + \nabla\cdot\mathbf{T}_g + \epsilon_g\rho_g\mathbf{g} + D_{g,s}(\mathbf{v}_s - \mathbf{v}_g) \tag{2.64c}$$

$$\frac{\partial}{\partial t}(\epsilon_s\rho_s\mathbf{v}_s) + \nabla\cdot(\epsilon_s\rho_s\mathbf{v}_s\mathbf{v}_s) = \nabla\cdot\mathbf{T}_s + \epsilon_s\rho_s\mathbf{g} + D_{s,g}(\mathbf{v}_g - \mathbf{v}_s) \tag{2.64d}$$

$$\begin{aligned}\frac{\partial}{\partial t}(\epsilon_g\rho_g E_g) + \nabla\cdot(\epsilon_g\rho_g E_g\mathbf{v}_g) = {}& -\nabla\cdot(P_g\mathbf{v}_g) + \nabla\cdot(\mathbf{T}_g\cdot\mathbf{v}_g) + \nabla\cdot(k_{ge}\epsilon_g\nabla T_g)\\ & + \epsilon_g\rho_g\mathbf{g}\cdot\mathbf{v}_g + D_{g,s}(\mathbf{v}_s - \mathbf{v}_g)\cdot\mathbf{v}_g + Q_s(T_s - T_g),\end{aligned} \tag{2.64e}$$

$$\begin{aligned}\frac{\partial}{\partial t}(\epsilon_s\rho_s E_s) + \nabla\cdot(\epsilon_s\rho_s E_s\mathbf{v}_s) = {}& \nabla\cdot(\mathbf{T}_s\cdot\mathbf{v}_s) + \nabla\cdot(k_{se}\epsilon_s\nabla T_s) + \epsilon_s\rho_s\mathbf{g}\cdot\mathbf{v}_s\\ & + D_{s,g}(\mathbf{v}_g - \mathbf{v}_s)\cdot\mathbf{v}_s + Q_s(T_g - T_s).\end{aligned} \tag{2.64f}$$

Introducing the non-dimensional quantities in the Equation (2.64a) we obtain the non-dimensional continuity equation for the gas phase:

$$\frac{\partial}{\partial\tilde{t}}\,(\epsilon_g\tilde{\rho}_g) + \tilde{\nabla}\cdot(\epsilon_g\tilde{\rho}_g\tilde{\mathbf{v}}_g) = 0. \tag{2.65}$$

In the same way, the non-dimensional mass conservation equation for solid particles is derived from Equation (2.64b), obtaining

$$\frac{\partial}{\partial\tilde{t}}\,(\epsilon_s\tilde{\rho}_s) + \tilde{\nabla}\cdot(\epsilon_s\tilde{\rho}_s\tilde{\mathbf{v}}_s) = 0. \tag{2.66}$$

In order to derive the non-dimensional form of the momentum equations, the non-dimensional stress tensor is defined as

$$\tilde{\mathbf{T}}_g = \frac{\mathbf{T}_g \bar{L}}{\mu_g \bar{U}}. \tag{2.67}$$

Starting from Equation (2.64c), we obtain

$$\begin{aligned} \frac{\partial}{\partial \tilde{t}} (\epsilon_g \tilde{\rho}_g \tilde{\mathbf{v}}_g) + \tilde{\nabla} \cdot (\epsilon_g \tilde{\rho}_g \tilde{\mathbf{v}}_g \tilde{\mathbf{v}}_g) = & -\frac{1}{Ma^2} \tilde{\nabla} \tilde{P}_g + \frac{1}{Re_g} \tilde{\nabla} \cdot \tilde{\mathbf{T}}_g \\ & + \frac{1}{Fr^2} \epsilon_g \tilde{\rho}_g \mathbf{k} + \frac{1}{St} (\tilde{\mathbf{v}}_s - \tilde{\mathbf{v}}_g) \end{aligned} \tag{2.68}$$

where $\mathbf{k} = \frac{\mathbf{g}}{|\mathbf{g}|}$ and the non-dimensional parameters Mach number Ma, Reynolds number Re, Froude number Fr and Stokes number St are defined in Table 2.2. Analogously, the non-dimensional form of the momentum equation for the solid phase (2.64d) is derived:

$$\begin{aligned} \frac{\partial}{\partial \tilde{t}} (\epsilon_s \tilde{\rho}_s \tilde{\mathbf{v}}_s) + \tilde{\nabla} \cdot (\epsilon_s \tilde{\rho}_s \tilde{\mathbf{v}}_s \tilde{\mathbf{v}}_s) = & \frac{1}{Re_s} \tilde{\nabla} \cdot \tilde{\mathbf{T}}_s \\ & + \frac{1}{Fr^2} \epsilon_s \tilde{\rho}_s \mathbf{k} + \frac{1}{St} (\tilde{\mathbf{v}}_g - \tilde{\mathbf{v}}_s). \end{aligned} \tag{2.69}$$

Introducing the non-dimensional variables in the Equation (2.64e), we obtain:

$$\begin{aligned} \frac{\partial}{\partial \tilde{t}} (\epsilon_g \tilde{\rho}_g \tilde{E}_g) + \tilde{\nabla} \cdot (\epsilon_g \tilde{\rho}_g \tilde{E}_g \tilde{\mathbf{v}}_g) = & -\frac{Ec}{Ma} \tilde{\nabla} \cdot (\tilde{P}_g \tilde{\mathbf{v}}_g) + \frac{Ec}{Re_g} \tilde{\nabla} \cdot (\tilde{\mathbf{T}}_g \cdot \tilde{\mathbf{v}}_g) \\ & + \frac{1}{Pe_g} \tilde{\nabla} \cdot (\epsilon_g \tilde{\nabla} \tilde{T}_g) + \frac{Ec}{Fr^2} \epsilon_g \tilde{\rho}_g \mathbf{k} \cdot \tilde{\mathbf{v}}_g + \frac{Ec}{St} (\tilde{\mathbf{v}}_s - \tilde{\mathbf{v}}_g) \cdot \tilde{\mathbf{v}}_g \\ & + \frac{Nu_g}{Pe_g} (\tilde{T}_s - \tilde{T}_g). \end{aligned} \tag{2.70}$$

The non-dimensional parameters, i.e. Eckert number Ec, Péclet number Pe and Nusselt number Nu, are defined in Table 2.2. Analogously, we derive the non-dimensional form of the energy conservation equation for solid particles (2.64f):

$$\begin{aligned} \frac{\partial}{\partial \tilde{t}} (\epsilon_s \tilde{\rho}_s \tilde{E}_s) + \tilde{\nabla} \cdot (\epsilon_s \tilde{\rho}_s \tilde{E}_s \tilde{\mathbf{v}}_s) = & \frac{Ec}{Re_s} \tilde{\nabla} \cdot (\tilde{\mathbf{T}}_s \cdot \tilde{\mathbf{v}}_s) + \frac{1}{Pe_s} \tilde{\nabla} \cdot (\epsilon_s \tilde{\nabla} \tilde{T}_s) \\ & + \frac{Ec}{Fr^2} \epsilon_s \tilde{\rho}_s \mathbf{k} \cdot \tilde{\mathbf{v}}_s + \frac{Ec}{St} (\tilde{\mathbf{v}}_g - \tilde{\mathbf{v}}_s) \cdot \tilde{\mathbf{v}}_s + \frac{Nu_s}{Pe_s} (\tilde{T}_g - \tilde{T}_s). \end{aligned} \tag{2.71}$$

Quantity	Symbol	Dimension
Mass	m	M
Length	x	L
Time	t	T
Temperature	T	$\mathbf{\Theta}$
Volume fraction	ϵ	$\mathsf{1}$
Density	ρ	ML^{-3}
Velocity	$\mathbf{v}$	LT^{-1}
Pressure	P	$\mathsf{ML}^{-1}\mathsf{T}^{-2}$
Gravity	$\mathbf{g}$	LT^{-2}
Stress tensor	$\mathbf{T}$	$\mathsf{ML}^{-1}\mathsf{T}^{-2}$
Drag coefficient	$D_{g,s}$	$\mathsf{ML}^{-3}\mathsf{T}^{-1}$
Total specific energy	E_{tot}	$\mathsf{L}^2\mathsf{T}^{-2}$
Thermal conductivity	k	$\mathsf{MLT}^{-3}\,\mathbf{\Theta}^{-1}$
Heat trasfer coefficient	Q_s	$\mathsf{ML}^{-1}\mathsf{T}^{-3}\,\mathbf{\Theta}^{-1}$
Viscosity	μ	$\mathsf{ML}^{-1}\mathsf{T}^{-1}$
Specific heat	c_p	$\mathsf{L}^2\mathsf{T}^{-2}\,\mathbf{\Theta}^{-1}$

Table 2.1: Dimensional form of the main physical quantities

We can now summarize the non-dimensional form of the multiphase gas–particle model, where the symbol $\tilde{}$ has been removed for the sake of simplicity:

$$\frac{\partial}{\partial t}\left(\epsilon_g\rho_g\right) + \nabla\cdot\left(\epsilon_g\rho_g\mathbf{v}_g\right) = 0 \tag{2.72a}$$

$$\frac{\partial}{\partial t}\left(\epsilon_s\rho_s\right) + \nabla\cdot\left(\epsilon_s\rho_s\mathbf{v}_s\right) = 0 \tag{2.72b}$$

$$\begin{aligned}\frac{\partial}{\partial t}\left(\epsilon_g\rho_g\mathbf{v}_g\right) + \nabla\cdot\left(\epsilon_g\rho_g\mathbf{v}_g\mathbf{v}_g\right) = &-\frac{1}{Ma^2}\,\nabla P_g + \frac{1}{Re_g}\,\nabla\cdot\mathbf{T}_g \\ &+ \frac{1}{Fr^2}\,\epsilon_g\rho_g\mathbf{k} + \frac{1}{St}(\mathbf{v}_s - \mathbf{v}_g)\end{aligned} \tag{2.72c}$$

$$\frac{\partial}{\partial t}\left(\epsilon_s\rho_s\mathbf{v}_s\right) + \nabla\cdot\left(\epsilon_s\rho_s\mathbf{v}_s\mathbf{v}_s\right) = \frac{1}{Re_s}\,\nabla\cdot\mathbf{T}_s + \frac{1}{Fr^2}\,\epsilon_s\rho_s\mathbf{k} + \frac{1}{St}(\mathbf{v}_g - \mathbf{v}_s) \tag{2.72d}$$

$$\begin{aligned}\frac{\partial}{\partial t}\left(\epsilon_g\rho_g E_g\right) + \nabla\cdot\left(\epsilon_g\rho_g E_g\mathbf{v}_g\right) = &-\frac{Ec}{Ma}\,\nabla\cdot\left(P_g\mathbf{v}_g\right) + \frac{Ec}{Re_g}\nabla\cdot\left(\mathbf{T}_g\cdot\mathbf{v}_g\right) \\ &+ \frac{1}{Pe_g}\,\nabla\cdot\left(\epsilon_g\nabla T_g\right) + \frac{Ec}{Fr^2}\,\epsilon_g\rho_g\mathbf{k}\cdot\mathbf{v}_g + \frac{Ec}{St}(\mathbf{v}_s - \mathbf{v}_g)\cdot\mathbf{v}_g \\ &+ \frac{Nu_g}{Pe_g}\,(T_s - T_g)\end{aligned} \tag{2.72e}$$

$$\begin{aligned}\frac{\partial}{\partial t}\left(\epsilon_s\rho_s E_s\right) + \nabla\cdot\left(\epsilon_s\rho_s E_s\mathbf{v}_s\right) = &\frac{Ec}{Re_s}\nabla\cdot\left(\mathbf{T}_s\cdot\mathbf{v}_s\right) + \frac{1}{Pe_s}\,\nabla\cdot\left(\epsilon_s\nabla T_s\right) \\ &+ \frac{Ec}{Fr^2}\,\epsilon_s\rho_s\mathbf{k}\cdot\mathbf{v}_s + \frac{Ec}{St}(\mathbf{v}_g - \mathbf{v}_s)\cdot\mathbf{v}_s + \frac{Nu_s}{Pe_s}\,(T_g - T_s).\end{aligned} \tag{2.72f}$$

Non-dimensional number	Definition
Reynolds number	$Re = \frac{\bar{\rho}\bar{U}\ \bar{L}}{\mu}$
Mach number	$Ma = \frac{\bar{U}}{\bar{c}}$
Froude number	$Fr = \frac{\bar{U}}{\sqrt{g\bar{L}}}$
Stokes number	$St = \frac{\bar{\rho}\bar{U}}{D_{g,s}\bar{L}}$
Péclet number	$Pe = \frac{\bar{U}\ \bar{L}\bar{\rho}c_p}{k}$
Eckert number	$Ec = \frac{\bar{U}^2}{c_p\bar{\Theta}}$
Nusselt number	$Nu = \frac{Q_s\bar{L}^2}{k}$

Table 2.2: Definition of non-dimensional parameters.

2.6.2 Physical meaning of the non-dimensional parameters

The non-dimensional parameters allow to identify different physical regimes that can arise for the gas–particle mixture, as discussed in [7].

The *Reynolds number* is defined as the ratio of inertial forces and viscous forces. When $Re \to \infty$, the viscous forces are negligible and the flow can be approximated as inviscid. In fluid dynamics, this hypothesis allows to reduce the Navier-Stokes system of equations to the Euler equations. On the other hand, when $Re \ll 1$, inertial and advective forces are small compared to the viscous forces and the Stokes equations can provide an accurate solution to the problem.

The *Froude number* represents the ratio between inertial and gravitational forces. When $Fr \to \infty$, i.e. the velocity of the flow is high, the gravitational force cannot influence the dynamics of the flow and can be neglected. As the the velocity decreases, gravity starts playing a significant role in the dynamics of the fluid by accelerating it downward.

The *Mach number* compares the flow velocity with the speed of sound in the medium. It allows to understand the importance of the compressibility effects in the flow. When $Ma \to 0$, the fluid can be approximated as incompressible. Moreover, the Mach number allows to distinguish between different flow regimes, i.e. subsonic ($Ma < 1$), transonic $Ma \sim 1$ and supersonic $Ma > 1$.

The dynamics of a particle suspended in a fluid flow is described by the *Stokes number*. It compares the drag force acting on the particles with the inertial forces. When the Stokes number decreases, i.e. $St \to 0$, the friction between the two phases is large and particles follow the fluid streamlines closely. When the Stokes number is small, the gas phase and the solid phase dynamics are coupled and could be approximated as a unique

medium with average properties. On the contrary, as the Stokes number increases, the dispersed phase can manifest significant non-equilibrium phenomena.

The *Eckert number* is defined as the ratio between the kinetic energy and the enthalpy and it is used to characterize dissipation. For small Eckert numbers, the effects of pressure changes on the energy balance of the system can be neglected with respect to conduction and convection phenomena.

The *Péclet number* represents the ratio between advection and the thermal diffusion (conduction). When the flow velocity is very high ($Pe \to \infty$), the time scale of the thermal diffusion process is much bigger than the transport time scale, thus the heat diffusion can be neglected.

Finally, the *Nusselt number* compares the convective heat transfer with the conductive heat transfer (diffusion). When the Nusselt number is large, thermal diffusion is negligible with respect to the heat transfer between gas and particles.

2.6.3 Application of dimensional analysis to significant test cases

The value of the non-dimensional parameters introduced in the previous section has to be computed using the characteristic quantities and the physical coefficients typical of the application we are interested in. In this section we are going to apply the dimensional analysis to study a few significant regimes, representative of different application areas of this kind of multiphase models.

Volcanic jet

During an explosive volcanic eruption, a mixture of gas and solid particles is ejected from the volcanic vent into the atmosphere. The multiphase equations (2.13a), (2.13b), (2.14a), (2.14b), (2.15a), (2.15b) can be used to describe the jet that forms in the first stages of the eruption and the non-dimensional form of the equations allows to better understand the main processes that take place in this geophysical phenomena.

The only length that can influence the jet dynamics is the exit diameter, i.e. the vent diameter $\bar{L} = D_v$. The characteristic velocity of the jet is the exit velocity of the mixture, that is $\bar{U} = |\mathbf{v}_{v,mix}|$. Analogously, the characteristic density is equal to the exit mixture density, $\bar{\rho} = \rho_{v,mix}$, whereas the characteristic temperature is given by the difference between the exit mixture temperature and the atmospheric temperature, that is $\bar{\Theta} = |T_{v,mix} - T_{atm}|$. Due to the complexity of the physical problem, the introduced variables cannot always be quantified exactly by means of experimental data. Thus, in the computation of the non-dimensional parameters only the approximate order of magnitude will be introduced. In particular we refer to [45, 91, 93, 134] for the values of the volcanological parameters, that are shown in Tables 2.3 and 2.4.

From the value of the computed non-dimensional parameters in Table 2.5 it is possible to observe that the Reynolds numbers are much larger than 1, so that the viscous effects in the momentum equations are negligible with respect to the inertial forces for both the gas and the particles. Analogously, the values of the Péclet numbers demonstrate that the conductive heat transfer is negligible with respect to other heat transfer processes. Consequently, the viscous terms in the momentum equations, the diffusion and the viscous dissipation terms in the energy equations can be neglected in the considered regime. For these regimes, the gas can be considered inviscid. Furthermore, the gravitational force plays a secondary role in the jet dynamics ($Fr > 1$), due to

Parameter	Reference value	Unit
ϵ_s	10^{-2}	
ϵ_g	1	
d_s	10^{-4}	m
μ_g	10^{-5}	Pa·s
μ_s	10^{-2}	Pa·s
$D_{g,s}$	10^{3}	kg/m^3·s
$c_{p,g}$	10^{3}	J/Kg·K
$c_{p,s}$	10^{3}	J/Kg·K
k_g	10^{-3}	W/m·K
k_s	1	W/m·K
Q_s	10^{6}	W/m^3·K
$\bar{c}$	10^{2}	m/s

Table 2.3: Approximate order of magnitude of physical parameters for volcanological applications

Quantity	Reference value	Unit
$\bar{L}$	10	m
$\bar{U}$	10^{2}	m/s
$\bar{\Theta}$	10^{3}	K
$\bar{\rho}$	10	kg/m^3

Table 2.4: Characteristic quantities for the volcanic jet test case

the high velocity of the mixture in the vertical direction. In particular, the work done by the gravitational force can be neglected in the energy balance equations. The order of magnitude of the Mach number is one, so the gas phase cannot be approximated as incompressible. Compressibility effects are important in the jet test problem and a transonic regime can be expected. Finally, we can observe that both the Stokes number and the ratio between the Péclet number and the Nusselt number are of the order of 0.1. They are not so small to justify the hypothesis of equilibrium between different phases. Consequently, the work done by the drag force may have some effect on the thermodynamics of the volcanic jet, although it would be negligible compared to the interphase heat exchange. It is possible to conclude that, in the jet dynamics, non-equilibrium effects between gas and solid particles can arise and that the pressure, advection and interphase exchange terms influence the global behavior of the jet.

Pyroclastic density current

On the long time scale, after the volcanic jet has expanded into the atmosphere, the volcanic column can collapse under the effect of gravitational forces. The collapsing mixture feeds a pyroclastic density current that flows along the volcanic flank.

To characterize the process of the density current, we need to introduce the characteristic length. In volcanological applications, it can be approximate with the height from which the mixture is collapsing, i.e. the height of the collapsing volcanic column H_c. The characteristic velocity is not easy to define. It can be roughly approximated with the velocity that a fluid reaches when falling from an height H_c under gravitational

Parameter	Reference value
Re_g	10^9
Re_s	10^6
Ma	1
Fr	10
Ec	10^{-2}
Pe_g	10^{10}
Pe_s	10^7
St	10^{-1}
Nu_g	10^{11}
Nu_s	10^8

Table 2.5: Non-dimensional parameters for the volcanic jet test case

acceleration, $\bar{U} = \sqrt{2g'H_c}$, where g' is the reduced gravity, i.e.

$$g' = \left| \frac{\rho_{mix} - \rho_{atm}}{\rho_{atm}} \, \mathbf{g} \right|. \tag{2.73}$$

As in the previous test case, the characteristic density is the density of the mixture, i.e. $\bar{\rho} = \rho_{mix}$ and the characteristic temperature is the difference between the mixture and the atmospheric temperature, i.e. $\bar{\Theta} = |T_{mix} - T_{atm}|$. As in the previous section, we refer to [45, 91, 93, 134] to obtain the approximate order of magnitude of physical parameters, see Tables 2.3 and 2.6.

The computed non-dimensional parameters for the pyroclastic current test case are shown in Table 2.7. As in the jet test case, it is possible to observe how viscous effects in the momentum equations, as well as diffusive and viscous dissipation temrs in the energy equations, are negligible with respect to advection ($Re, Pe \gg 1$). However, we expect that these terms will become relevant in the boundary layer, where the velocities approaches zero and the characteristic length is the roughness of the solid boundary. Gravitational force is important and influences the dynamics of the density current ($Fr \simeq 1$): it tends to stratify the mixture into layers with decreasing density moving away from the boundary layer. At the same time, the work done by the gravitational force can be neglected if we assume that the density current is moving in the horizontal direction mainly, i.e. $\mathbf{v} \cdot \mathbf{k} \simeq 0$. The Mach number is of the order of one and compressibility effects are not negligible, due to the presence of solid particles that reduce the speed of sound in the mixture. We observe how the Stokes number and the ratio between the Péclet number and the Nusselt number are of the order of 10^{-3}. These values, which are representative of the large scale dynamics of the density current, imply that the solid phase tends to approach equilibrium with the gas phase in the horizontal direction, i.e. $\mathbf{v} \cdot \mathbf{i} \simeq \bar{U}$. In the vertical direction, where $\mathbf{v} \cdot \mathbf{k} \ll \bar{U}$, the coupling between gas and particles is governed by small scale dynamics and turbulence. Finally, in the density current regime, the work done by the drag force is comparable to the heat exchange between different phases, thus it can not be neglected.

Laboratory experiments on multiphase gas–particle jets

Supersonic and high speed free jets of particle-laden gas are of great interest for a number of practical problems, e.g. solid propellant rocket engines in space technology

Quantity	Reference value	Units
$\bar{L}$	10^3	m
$\bar{U}$	10^2	m/s
$\bar{\Theta}$	10^2	K
$\bar{\rho}$	10	kg/m^3

Table 2.6: Characteristic quantities for the pyroclastic density current test case

Parameter	Reference value
Re_g	10^{11}
Re_s	10^8
Ma	1
Fr	1
Ec	10^{-1}
Pe_g	10^{12}
Pe_s	10^9
St	10^{-3}
Nu_g	10^{15}
Nu_s	10^{12}

Table 2.7: Non-dimensional parameters for the pyroclastic density current test case

or for two-phase combustion systems. Detailed experiments have been carried out to give further insight into the multiphase flow behaviour, see e.g. [84, 124].

The test facility employed in the laboratory to reproduce multiphase jets is typically composed by a high pressure chamber which includes a mixing chamber connected to the particle feeding system in order to ensure good mixing of the particles with the gas flow. A variable speed screw feeder is used to adjust the particle mass flow rate. The high pressure chamber is connected to a low pressure chamber through a converging nozzle. A vacuum pump is used to maintain a steady state pressure on the low pressure side. Optical devices and methods are used to collect measurements during the experiments, e.g. shadowgraph or schlieren method to study the free jet structure, lased light sheet method to study the particle-laden region and laser-Doppler anemometer to measure the particle velocity at the nozzle exit.

To carry out the dimensional analysis of the laboratory multiphase jet, we refer to the experimental setup described and adopted in [124]. Here, the exit diameter of the nozzle is 3 mm and the low pressure chamber has a inner diameter of 300 mm. The pressure in the low pressure chamber is equal to 10^4 Pa. Solid particles have a diameter of the order of 10 μm and density equal to 2500 kg/m^3. The particle volumetric concentration is low, of the order of 10^{-4}. The gas and solid exit velocities are equal to the sonic speed of the pure gas, whereas the gas exit pressure is 30 times the low chamber pressure. A summary of the experimental parameter values is reported in Table 2.8. The characteristic scales of the phenomena are reported in Table 2.9, whereas the resulting non dimensional parameter are shown in Table 2.10. It can be observed that advection is dominant with respect to viscous effects and gravitational forces, even in spite of the small spatial scale. Compressibility effects cannot be neglected. The Stokes number and the ratio between the Péclet and the Nusselt number are large, thus meaning the dynamics of solid particles is strongly decoupled from the the dynamics

Parameter	Reference value	Unit
ϵ_s	10^{-4}	
ϵ_g	1	
d_s	10^{-5}	m
μ_g	10^{-5}	Pa·s
μ_s	10^{-2}	Pa·s
$D_{g,s}$	10^{2}	kg/m^3·s
$c_{p,g}$	10^{3}	J/Kg·K
$c_{p,s}$	10^{3}	J/Kg·K
k_g	10^{-3}	W/m·K
k_s	1	W/m·K
Q_s	10^{5}	W/m^3·K
$\bar{c}$	10^{2}	m/s

Table 2.8: Experimental parameters for the multiphase jet on the laboratory scale.

Quantity	Reference value	Units
$\bar{L}$	10^{-3}	m
$\bar{U}$	10^{2}	m/s
$\bar{\Theta}$	1	K
$\bar{\rho}$	1	kg/m^3

Table 2.9: Characteristic quantities for the multiphase jet on the laboratory scale.

of the gas phase, as observed also in [124]. Finally, the viscous dissipation term and the work done by the drag force are comparable to the heat exchange term in the energy balance equations, thus they have an important role in the thermodynamics of the jet. By comparing the results obtained for the jet on the laboratory scale in Table 2.10 to the ones obtained on the volcanic scale in Table 2.5, it is possible to assess that the experimental setup and the nozzle conditions proposed in [124] are not appropriate to reproduce the main thermodynamic processes that take place in the volcanic jet.

Parameter	Reference value
Re_g	10^{4}
Re_s	10
Ma	1
Fr	10^{3}
Ec	10
Pe_g	10^{5}
Pe_s	10^{2}
St	10^{3}
Nu_g	10^{2}
Nu_s	10^{-2}

Table 2.10: Non-dimensional parameters for the multiphase jet on the laboratory scale.

CHAPTER 3

Spatial discretization by finite volume methods

FINITE volume method (FVM) is a spatial discretization technique which is derived from the integral form of the general conservation law. The finite volume method is based on cell-averaged values, which are usually the most fundamental quantities in fluid dynamics. This property distinguishes the FVM from the finite difference and the finite element methods, where the main quantities are the local function values at the mesh points. FVM is one of the most widely applied methods in fluid dynamics, due to its generality and conceptual simplicity. With respect to other discretization approaches, FVM has the fundamental property that a locally conservative discretization is achieved automatically, through the direct discretization of the integral form of the conservation law.

The first step in the FVM is the tassellation of the computational domain into a collection of non overlapping control volumes that completely cover the domain. Let $\mathcal{T}_h$ denote the tassellation of the domain $\Omega \subset \mathbb{R}^d$, with $d = 1, 2, 3$. The control volumes, denoted with K, are such that $\bigcup_{K \in \mathcal{T}_h} \overline{K} = \overline{\Omega}$. The intersection between two distinct control volumes can be either an edge e or else a set of measure at most $d - 2$. In this work, we assume that the mesh is conforming, i.e. each edge e is shared by only two distinct control volumes. We denote with h_K a length scale associated with each control volume K, e.g. $h_K = \text{diam}(K)$, and with h a length scale associated with the tassellation $\mathcal{T}_h$, e.g. $h = \max_{K \in \mathcal{T}_h} h_K$.

Even if the FVM can be applied on an arbitrary mesh, in this work only Cartesian meshes, i.e. built up by Cartesian producty of intervals in the $x-$, $y-$ and $z-$ directions, will be considered. We enumerate by $i = 1, \ldots, N_x$, $j = 1, \ldots, N_y$ and $k = 1, \ldots, N_z$ the intervals in the $x-$, $y-$ and $z-$ directions, respectively. Finally, we denote by K_{ijk}

the grid cell with position i, j, k, defined as:

$$K_{ijk} = \left[x_{i-\frac{1}{2}}, x_{i+\frac{1}{2}}\right] \times \left[y_{j-\frac{1}{2}}, y_{j+\frac{1}{2}}\right] \times \left[z_{k-\frac{1}{2}}, z_{k+\frac{1}{2}}\right]. \tag{3.1}$$

The center of each control volume K_{ijk} is the point (x_i, y_j, z_k), whereas $x_{i+\frac{1}{2}}$, $y_{j+\frac{1}{2}}$ and $z_{k+\frac{1}{2}}$ denote the cell faces.

The finite volume approach assumes a piecewise constant solution representation in each control volume, with value equal to the cell average. We indicate with $u(t)|_K$ the average value of the quantity $u(x,t)$ on the cell K, which is defined as:

$$u(t)|_K = \frac{1}{|K|}\int_K u(x,t)dx. \tag{3.2}$$

On the tassellation $\mathcal{T}_h$, we introduce the space of piecewise constants V_h^0, i.e.

$$V_h^0 = \left\{v : v(x) \cdot \chi_K \in \mathcal{P}^0(K), \forall K \in \mathcal{T}_h\right\} \tag{3.3}$$

where χ_K is the characteristic function on K and $\mathcal{P}^0(K)$ is the space of constant polynomials on the control volume K.

The finite volume approximation is then obtained from the integral form of the equation, by integrating the differential equation over appropriate control volumes and applying the divergence theorem.

In this chapter, the finite volume approximation is presented for scalar conservation laws. The extension to systems of conservation laws is then introduced both on a colocated and on a staggered mesh arrangement. In the second part, a review on different numerical fluxes and flux limiting techniques that can be adopted is presented for scalar equations and systems of conservation laws. Finally, some details on the implementation of the finite volume discretization of multiphase gas–particle equations in the Pyroclastic Dispersal Analysis Code (PDAC) [42] are described.

3.1 General formulation

Let us consider the scalar conservation equation

$$\frac{\partial u}{\partial t} + \nabla \cdot \mathbf{f}(u) = s(u,t), \tag{3.4}$$

where $u(x,t) : \mathbb{R}^d \times [0,T] \to \mathbb{R}$ is the conserved variable, $\mathbf{f}(u) : \mathbb{R} \to \mathbb{R}^d$ is the flux vector and $s(u,t) : \mathbb{R} \times [0,T] \to \mathbb{R}$ is the source function.

3.1.1 Weak solution and entropy solution

It is well known that, if a function is discontinuous, it cannot be the solution of a partial differential equation in the conventional case, because derivatives are not defined at the discontinuity. Instead, the solution is required to satisfy a family of related integral equations. Multiplying the conservation law (3.4) in the homogeneous case by a test function $\varphi \in C_0^1(\mathbb{R}^d \times [0,\infty])$ and integrating over $\mathbb{R}^d \times [0,\infty]$, we obtain

$$\int_0^\infty \int_{\mathbb{R}^d} \left[u\frac{\partial \varphi}{\partial t} + \mathbf{f}(u) \cdot \nabla \varphi\right] dxdt + \int_{\mathbb{R}^d} u_0 \varphi(x,0)dx = 0, \tag{3.5}$$

with $u_0 = u(x,0) \in L^\infty(\mathbb{R}^d \times [0,\infty])$. Unlike the differential form (3.4), the integral form can be satisfied by piecewise continuous functions. If $u \in L^\infty(\mathbb{R}^d \times [0,\infty])$ and u satisfies the integral equation (3.5) for all $\varphi \in C_0^1(\mathbb{R}^d \times [0,\infty])$, then u is a *weak solution* of the conservation law. It can be shown that there exists at least one weak solution to (3.5) if the flux function $\mathbf{f}(u)$ is at least Lipschitz continuous [78]. Differentiable weak solutions are also solutions of the partial differential equation (3.4) and are uniquely determined by the initial data. However, the class of weak solutions is too large to guarantee uniqueness of solutions. An important class of solutions are piecewise classical solutions with discontinuities separating the smooth regions. In this case, the solution is a weak solution if and only if the following jump condition (Rankine-Hugoniot condition) across the discontinuity surface S is satisfied [4, 52, 77]:

$$\mathbf{c}\,[\![u]\!] \cdot \mathbf{n}_S = [\![\mathbf{f}(u)]\!] \cdot \mathbf{n}_S \tag{3.6}$$

where $\mathbf{n}_S$ is the unit vector normal to the discontinuity surface S, $[\![q]\!]$ represents the jump of the quantity q across the discontinuity surface when following the streamline and $\mathbf{c}$ is defined as the discontinuity propagation speed. Various form of discontinuities are physically possible: *shocks*, where all the flow variables undergo a discontinuous variation, *contact discontinuities* and *vortex sheets*, also called *slip lines*, across which density and tangential velocity may be discontinuous, although pressure and normal velocity remain continuous.

The Rankine-Hugoniot conditions are not sufficient to identify a unique weak solution, since they are not able to distinguish between positive and negative entropy variations across the discontinuity. Consequently, additional conditions must be introduced in order to single out one solution, i.e. the entropy weak solution, within the class of weak solutions [78]. A condition has to be imposed in order to ensure that the solutions of the inviscid problem are indeed limits, for vanishing viscosity, of the real fluid behaviour and that entropy does not unphysically decrease, thus violating the second principle of thermodynamics [4, 77, 78].

3.1.2 Spatial finite volume (semi) discretization

To obtain the finite volume approximation for Equation (3.4), formally polynomials of degree zero are chosen as test functions, e.g.

$$\varphi(x,t) = \begin{cases} 1 & \text{if } (x,t) \in K \times [t_1, t_2] \\ 0 & \text{otherwise.} \end{cases} \tag{3.7}$$

Notice that φ does not belong to the space C_0^1, but it can be approximated arbitrarily well by a smoothed-out version. Multiplying Equation (3.4) by φ and integrating on the domain we obtain:

$$\int_K \frac{\partial u}{\partial t}\, dx + \int_K \nabla \cdot \mathbf{f}(u)\, dx = \int_K s(u,t)\, dx \tag{3.8}$$

and integrating by parts the flux term:

$$\frac{d}{dt}\int_K u\, dx + \int_{\partial K} \mathbf{f}(u) \cdot \mathbf{n}\, dx = \int_K s(u,t)\, dx, \tag{3.9}$$

The semi-discrete finite volume approximation of Equation (3.4) using a piecewise solution representation in space is obtained by applying the definition (3.2). We look for an approximate solution $u_h(x,t) \in V_h^0$, which is defined on the computational mesh $\mathcal{T}_h$ by means of its mean values $u_K(t) = u_h(x,t)|_K$, for all the control volumes $K \in \mathcal{T}_h$. The degrees of freedom of the approximate solution are computed by integrating in time the following ordinary differential equation

$$\frac{d}{dt}u_K(t) + \frac{1}{|K|}\int_{\partial K} \mathbf{f}(u)\cdot\mathbf{n}\,dx = \frac{1}{|K|}\int_K s(u)\,dx, \tag{3.10}$$

with initial data

$$u_K(0) = \frac{1}{|K|}\int_K u_0(x)\,dx. \tag{3.11}$$

To complete the finite volume discretization of Equation (3.10), appropriate numerical approximation to the volume integral and to the boundary integral terms should be introduced.

The volumetric source term is integrated by means of a Gauss numerical quadrature rule on the control volume K, that is

$$\int_K s(u,t)\,dx \simeq \sum_{m\in\mathcal{I}_K} \omega_m\, s(u(x_m),t), \tag{3.12}$$

where the coefficients ω_m and the points $x_m \in \mathcal{I}_K$ are the weights and the quadrature points, respectively, of the integration rule on K. The values of the function u on the quadrature points have to be appropriately reconstructed by using interpolation techniques. As an example, if the second-order accurate midpoint integration rule is adopted, the approximate integral is computed as the product between the cell volume and the source function evaluated at the control volume center, where the variable is assumed to be equal to its mean value on K, that is

$$\int_K s(u,t)\,dx \simeq s(u_K,t)|K| = s_K(t)|K|. \tag{3.13}$$

Analogously, the boundary integrals are computed by means of a numerical quadrature rule on the edge e.

The use of piecewise constant functions on the control volumes K renders the numerical solution multivalued on the cell interfaces e, thus making the definition of a single valued flux at these interfaces ambiguous. The true flux has to be replaced by a numerical flux function $\tilde{f}$. Given the control volume K and its edge e, here we indicate with K_e the control volume that shares with K the edge e, i.e. $e = K \cap K_e$, and with $\mathbf{n}_e$ the vector normal to e, pointing from K to K_e. The numerical flux function can now be defined as

$$\int_e \mathbf{f}(u)\cdot\mathbf{n}_e\,dx \simeq \tilde{f}(u_K, u_{K_e}, \mathbf{n}_e), \tag{3.14}$$

where u_K and u_{K_e} are appropriate reconstructions of the function u on the edge e of the control volume K and K_e, respectively. The numerical flux is assumed to satisfy two fundamental properties:

- conservation

$$\tilde{f}(u,v,\mathbf{n}) = -\tilde{f}(v,u,-\mathbf{n}); \tag{3.15}$$

- consistency

$$\tilde{f}(u, u, \mathbf{n}) = \int_e \mathbf{f}(u) \cdot \mathbf{n}\, dx. \tag{3.16}$$

Under these hypothesis, the Lax-Wendroff theorem [81] guarantees that, when the numerical solution of the conservative scheme converges, it will converge to a solution of the continuous equations that satisfies the Rankine-Hugoniot relations in presence of discontinuities [66]. The final finite volume approximation of the problem (3.4) is given by

$$\frac{d}{dt} u_K(t) + \frac{1}{|K|} \sum_{e \in \partial K} \tilde{f}(u_K, u_{K_e}, \mathbf{n}_e) = \frac{1}{|K|} \int_K s(u,t)\, dx. \tag{3.17}$$

The system (3.17) allows to update in time the values of the mean quantities $u_K(t)$ in all the control volumes. It can be solved with a variety of explicit and implicit time integration methods, that will be presented in Chapter 5.

3.2 Extension to systems of conservation laws

Let us consider the system of M conservation equations

$$\frac{\partial \mathbf{U}}{\partial t} + \nabla \cdot \mathbf{F}(\mathbf{U}) = \mathbf{S}(\mathbf{U}, t), \tag{3.18}$$

where $\mathbf{U}(x,t) : \mathbb{R}^d \times [0,T] \to \mathbb{R}^M$ is the vector of conserved variables, $\mathbf{F}(\mathbf{U}) : \mathbb{R}^M \to \mathbb{R}^M \times \mathbb{R}^d$ is the flux function and $\mathbf{S}(\mathbf{U}, t) : \mathbb{R}^M \times [0,T] \to \mathbb{R}^M$ is the vector source function.

The finite volume scheme introduced in the previous section can be extended to systems of conservation laws by following two alternative approaches, the colocated method and the staggered method, depending on the arrangement of the dependent variables.

3.2.1 Colocated finite-volume scheme

In the *colocated mesh arrangement* all the unknowns and all fluid properties are identified with the values in the center of the computational cell K. In particular, the velocity components are located with the scalar variables at the cell centers, as shown in Figure 3.1.

We consider the system of conservation laws (3.18) and the tassellation $\mathcal{T}_h$ on the computational domain Ω. As in the previous section, each scalar equation that composes the system (3.18) is integrated over the control volume K

$$\int_K \frac{\partial \mathbf{U}}{\partial t}\, dx + \int_K \nabla \cdot \mathbf{F}(\mathbf{U})\, dx = \int_K \mathbf{S}(\mathbf{U}, t)\, dx \tag{3.19}$$

and the flux term is integrated by parts:

$$\frac{d}{dt} \int_K \mathbf{U}\, dx + \int_{\partial K} \mathbf{F}(\mathbf{U}) \cdot \mathbf{n}\, dx = \int_K \mathbf{S}(\mathbf{U}, t)\, dx \tag{3.20}$$

We introduce the space of piecewise constant vectorial function $\mathbf{V}_h^0$ on the tassellation $\mathcal{T}_h$, i.e.

$$\mathbf{V}_h^0 = \left\{ \mathbf{V} \in \mathbb{R}^M : V^{(i)} \in V_h^0, \forall i = 1, \ldots, M \right\}. \tag{3.21}$$

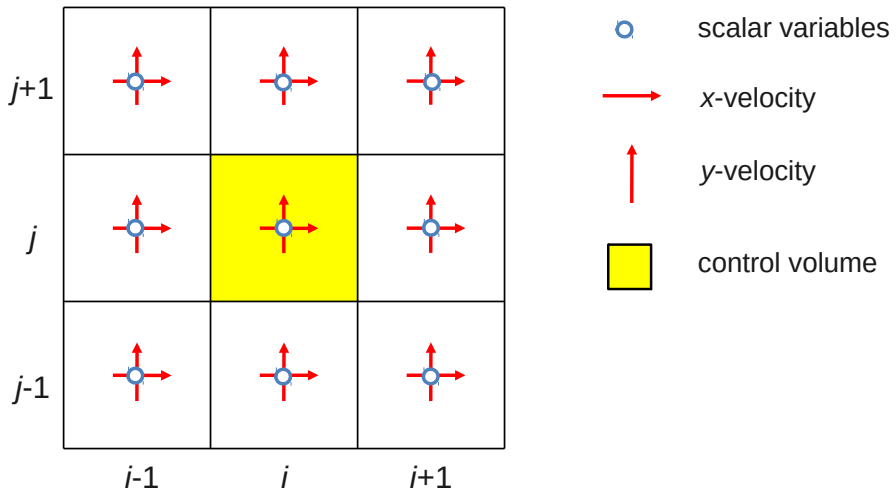

Figure 3.1: Sketch of the colocated mesh arrangement on a two dimensional Cartesian mesh. Both scalar variables and velocity components are defined at the cell center.

The mean value of the vector function $\mathbf{U}(x,t)$ over the control volume K is the vector $\mathbf{U}_K(t)$ whose components are the mean values of the components $U^{(i)}$ of $\mathbf{U}$, for all $i = 1, \ldots, M$. The semi-discrete finite volume approximation of equations (3.18) using a piecewise solution representation in space, that is $\mathbf{U}_h(t) \in \mathbf{V}_h^0$, with initial data

$$\mathbf{U}_K(0) = \frac{1}{|K|}\int_K \mathbf{U}_0(x)dx, \tag{3.22}$$

is given by the following system of ordinary differential equations

$$\frac{d}{dt}\mathbf{U}_K(t) + \frac{1}{|K|}\int_{\partial K} \mathbf{F}(\mathbf{U})\cdot\mathbf{n}\,dx = \int_K \mathbf{S}(\mathbf{U},t)\,dx. \tag{3.23}$$

The system (3.23) allows to update in time the values of the mean quantities $\mathbf{U}_K(t)$ in all the control volumes.

To approximate the volume and boundary integrals, the same steps introduced in the previous section can be adopted for each component of the system (3.23), i.e. see Equations (3.12) and (3.14). The final finite volume approximation of the system (3.18) on a colocated mesh is given by

$$\frac{d}{dt}\mathbf{U}_K(t) + \frac{1}{|K|}\sum_{e\in\partial K}\tilde{\mathbf{F}}(\mathbf{U}_K, \mathbf{U}_{K_e}, \mathbf{n}_e) = \frac{1}{|K|}\int_K \mathbf{S}(\mathbf{U},t). \tag{3.24}$$

Colocated methods have some advantages, in particular when unstructured or non-orthogonal grids are used. First, all variables are defined at the same locations, hence there is only one set of control volumes; furthermore, the advection term can be evaluated in the same way for all the variables. This kind of arrangement allows for a simple treatment of complex geometries and the straightforward application of multigrid techniques.

However, some disadvantages must be highlighted. The main drawback of the colocated mesh scheme is that, in the incompressible limit, a decoupling between the velocity and the pressure is generated [103]. This difficulty can be solved either using

appropriate interpolation strategies [68, 105, 111] or introducing a staggered arrangement of the variables on the computational mesh [64].

Another difficulty is related to the dispersion of linear waves. If we consider a simple advection equation, it is well known (see e.g. [36] for a complete analysis) that colocated schemes are not able to resolve wave phase-speed and group velocity correctly at all wave numbers. In particular, let us consider as an example the one-dimensional case advection equation: the least well-resolved wave on a grid with length Δx has wavelength $2\Delta x$ and wave number $k = \pi/\Delta x$. While in the continuous problem the phase speed and the group velocity are independent on the wave number (nondispersive waves), the discrete dispersion relation shows that both the discrete phase speed and the discrete group velocity depend on k, thus meaning that the numerical solution consists of dispersive waves. Moreover, the least well-resolved wave travels with phase speed equal to zero, thus introducing a considerable source of errors and numerical noise in the approximate solution. This problem can be solved either by adding numerical dissipation to the method or by adopting a staggered approach.

3.2.2 Staggered finite-volume scheme

In the *staggered-mesh arrangement* the velocity degrees of freedom are distributed on the cell faces $e \in \partial K$, whereas the pressure and other scalar quantities are defined at the cell centers, as shown in Figure 3.2. This feature, introduced in [64], results in fully coupled velocity and pressure fields.

In a Cartesian mesh, the pressure and all other scalar variables are located in the center of each control volume. The velocity components u, v and w are shifted in the $x-$, $y-$ and $z-$ directions, respectively. For each velocity component, a shifted control volume has to be introduced, too.

The equations are then formally integrated over the respective control volumes. Thus, conservation equations for scalar quantities, e.g. density and energy, are discretized on the volume centered on the point (x_i, y_j, z_k), that is K_{ijk}, while the $x-$momentum conservation is integrated over the volume centered on the location of u, that is $K_{i+\frac{1}{2}jk}$ with center $(x_{i+\frac{1}{2}}, y_j, z_k)$. Similarly, $y-$momentum and $z-$momentum equations are expressed for the volumes centered on the location of v and w, respectively.

Staggered-mesh arrangements have been successfully applied to a variety of systems of conservation laws, see e.g. [11, 58].

3.3 Numerical fluxes

3.3.1 Central schemes

The space-centred algorithms were historically the first to be derived. They are uniquely defined for linear equations, but many variants can be introduced for non-linear fluxes, even in one dimension. Among centred schemes, the most widely used are the Lax-Friedrichs and the Lax-Wendroff numerical fluxes.

The *Lax-Friedrichs flux* is a first-order centred scheme defined as

$$\tilde{f}(u_K, u_{K_e}, \mathbf{n}_e) = \frac{1}{2}\left[\mathbf{f}(u_{K_e}) \cdot \mathbf{n}_e + \mathbf{f}(u_K) \cdot \mathbf{n}_e - a\left(u_{K_e} - u_K\right)\right] \tag{3.25}$$

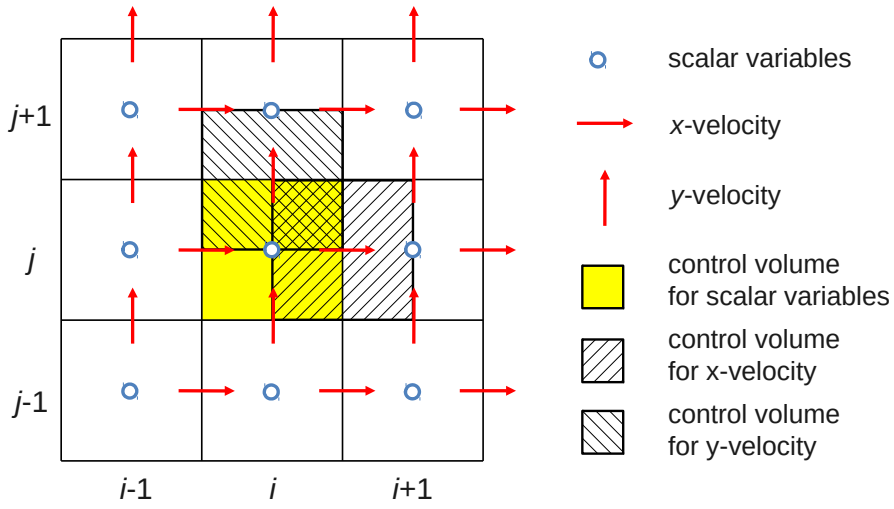

Figure 3.2: Sketch of the staggered mesh arrangement on a two dimensional Cartesian mesh. Scalar variables are defined at the cell center, whereas velocity component are defined at the cell faces. Staggered control volumes are introduced for the momentum equations.

where $a = |K|/\Delta t$, where Δt is the time-step. An improvement of the Lax-Friedrichs flux is obtained by replacing the value a with a locally determined value $a = \lambda_e$, where

$$\lambda_e = \max\left(\left|\frac{\partial \mathbf{f}}{\partial u}(u_K)\cdot\mathbf{n}_e\right|, \left|\frac{\partial \mathbf{f}}{\partial u}(u_{K_e})\cdot\mathbf{n}_e\right|\right). \tag{3.26}$$

The resulting method is the Rusanov's method, or Local Lax-Friedrichs method [116].

The extension to systems of conservation laws is straightforward. The numerical flux is computed as

$$\tilde{\mathbf{F}}(\mathbf{U}_K, \mathbf{U}_{K_e}, \mathbf{n}_e) = \frac{1}{2}\left[\mathbf{F}(\mathbf{U}_{K_e})\cdot\mathbf{n}_e + \mathbf{F}(\mathbf{U}_K)\cdot\mathbf{n}_e - a\left(\mathbf{U}_{K_e} - \mathbf{U}_K\right)\right] \tag{3.27}$$

where $a = |K|/\Delta t$, where Δt is the time-step. In the Rusanov's method, the coefficient a is replaced by $a = \lambda$, where

$$\lambda = \max\left(\left|eig\left(\frac{\partial \mathbf{F}}{\partial \mathbf{U}}(\mathbf{U}_{K_e})\cdot\mathbf{n}_e\right)\right|, \left|eig\left(\frac{\partial \mathbf{F}}{\partial \mathbf{U}}(\mathbf{U}_K)\cdot\mathbf{n}_e\right)\right|\right). \tag{3.28}$$

Here, $\frac{\partial \mathbf{F}}{\partial \mathbf{U}}$ represents the Jacobian matrix and eig are its eigenvalues.

A second order extension of the Lax-Friedrichs method is the *Lax-Wendroff scheme*. The Lax-Wendroff method differs from the Lax-Friedrichs method only for the definition of the coefficient a, which is given, for a scalar equation, by $a = \lambda_e^2 \Delta t/h$, with

$$\lambda_e = \frac{\partial \mathbf{f}}{\partial u}\left(\frac{u_K + u_{K_e}}{2}\right)\cdot\mathbf{n}_e. \tag{3.29}$$

The extension to systems of conservation laws is done in the same way as for the Lax-Friedrichs flux. The Lax-Wendroff flux is second-order accurate and yields much better approximations on smooth solutions than first order methods,, but fails near discontinuities, where oscillations are generated. A flux-limiting technique can be adopted to guarantee the monotonicity of the scheme, as discussed in Section 3.4.

3.3.2 Upwind schemes

The family of upwind schemes is directed towards the introduction of the physical properties of the flow equations into the discretized formulation. Constructing schemes which take into account the essential physical properties of the equations is aimed at preventing the creation of unwanted oscillations that appear in second-order central schemes.

Upwind methods are very simple to formulate for scalar advection equations, that is $\mathbf{f}(u) = \mathbf{a}u$, in which name they are also known as *donor-cell upwind methods*. The first order upwind flux through the edge $e = K \cap K_e$ is given by

$$\tilde{f}(u_K, u_{K_e}, \mathbf{n}_e) = (\mathbf{a} \cdot \mathbf{n}_e)^+ u_K + (\mathbf{a} \cdot \mathbf{n}_e)^- u_{K_e} \tag{3.30}$$

where $(\mathbf{a}\cdot\mathbf{n}_e)^+ = \max(\mathbf{a}\cdot\mathbf{n}_e, 0)$ and $(\mathbf{a}\cdot\mathbf{n}_e)^- = \min(\mathbf{a}\cdot\mathbf{n}_e, 0)$ indicate the positive and the negative parts of the velocity, respectively. The numerical flux is essentially computed by solving a Riemann problem across e, whose solution consists of a single wave carrying the jump in u between the neighboring two grid cells, propagating at speed $(\mathbf{a}\cdot\mathbf{n}_e)$. A first order correction to the donor-cell upwind method is the corner-transport upwind method [28], which includes the so-called transverse fluxes by considering the proper wave propagation speed $\mathbf{a}$ through the edge and not only the normal component. Several extensions of the basic donor-cell upwind method have been proposed in the literature to obtain second order accuracy and to account for systems of advection equations [28, 83, 117].

3.3.3 Numerical fluxes for system of conservation laws

In the discretization process of systems of conservation laws the introduction of the proper wave propagation speed is usually performed according to two main approaches. In the first approach, physical properties are accounted for by introducing information on the sign of the eigenvalues of the Jacobian matrix of the flux function, whereby the flux terms are split and discretized directionally according to the sign of the associated propagation speeds. This leads to the flux vector splitting methods. The second approach, referred to as flux difference splitting method or Godunov-type method, is based on the solution of the local Riemann problem at the interface e.

Flux vector splitting methods have been originally proposed for the system of Euler equations, in which the flux function can be written as an homogeneous function of the vector $\mathbf{U}$, that is $\mathbf{F}(\mathbf{U}) = \mathbf{A}(\mathbf{U})\mathbf{U}$. Under this hypothesis, the numerical flux can be computed by applying the Steger-Warming splitting

$$\tilde{\mathbf{F}}(\mathbf{U}_K, \mathbf{U}_{K_e}, \mathbf{n}_e) = \mathbf{A}^+(\mathbf{U}_K, \mathbf{n}_e)\mathbf{U}_K + \mathbf{A}^-(\mathbf{U}_{K_e}, \mathbf{n}_e)\mathbf{U}_{K_e} \tag{3.31}$$

with

$$\mathbf{A}^+ = \mathbf{R}\mathbf{\Lambda}^+\mathbf{R}^{-1} \tag{3.32a}$$

$$\mathbf{A}^- = \mathbf{R}\mathbf{\Lambda}^-\mathbf{R}^{-1} \tag{3.32b}$$

where the matrices $\mathbf{\Lambda}^+$ and $\mathbf{\Lambda}^-$ contains the positive and negative eigenvalues of $\mathbf{A}(\mathbf{U}, \mathbf{n}) = \mathbf{A}(\mathbf{U})\cdot\mathbf{n}$, respectively, and $\mathbf{R}$ is the matrix containing the right eigenvectors of $\mathbf{A}(\mathbf{U}, \mathbf{n})$.

The *Godunov method* [53] is obtained by solving the Riemann problem between the states $\mathbf{U}_K$ and $\mathbf{U}_{K_e}$ in order to determine the flux through e. It is defined as

$$\tilde{\mathbf{F}}(\mathbf{U}_K, \mathbf{U}_{K_e}, \mathbf{n}_e) = \mathbf{F}(\mathbf{U}^{Riemann}(0)) \cdot \mathbf{n}_e. \tag{3.33}$$

where $\mathbf{U}^{Riemann}(\xi/t)$, with $\xi = \mathbf{x}\cdot\mathbf{n}_e$, is the similarity solution of the Riemann problem evaluated at $\xi/t = 0$. The exact solution of the Riemann problem is often computationally expensive, depending on the complexity of the equation of state and the flux function, in particular in the multidimensional case. Thus, numerical fluxes based on approximations of the solution of the Riemann problem have been proposed, i.e. the HLL-type Riemann solver [38, 65, 135], the Roe-type Riemann solver [113, 114] and the Osher-type Riemann solver [39, 101].

The *Roe method* is based on the exact solution of an approximate Riemann problem. The approximate problem results from replacing the original non-linear conservation law (3.4) by a linearized equation with constant coefficients, given by the so called Roe matrix, and the initial data of the exact problem [113].

The approximate Riemann problem across the edge e is defined as

$$\frac{\partial \mathbf{U}}{\partial t} + \hat{\mathbf{A}}(\mathbf{U}_e, \mathbf{U}_{K_e}, \mathbf{n}_e)\frac{\partial \mathbf{U}}{\partial \xi} = 0 \tag{3.34}$$

with $\xi = \mathbf{x} \cdot \mathbf{n}_e$ and initial data $\mathbf{U}_0(\xi) = \mathbf{U}_K$ for $\xi < 0$ and $\mathbf{U}_0(\xi) = \mathbf{U}_{K_e}$ for $\xi \geq 0$. The Roe matrix $\hat{\mathbf{A}}(u_e, u_{K_e}, \mathbf{n}_e)$ is computed from a linearization of the flux function such that

- $\hat{\mathbf{A}}(\mathbf{U}, \mathbf{V}, \mathbf{n})$ is diagonalizable with real eigenvalues;
- $\hat{\mathbf{A}}(\mathbf{U}, \mathbf{U}, \mathbf{n}) = \mathbf{A}(\mathbf{U}, \mathbf{n}) = \sum_{i=1}^{d} \frac{\partial \mathbf{F}_i}{\partial \mathbf{U}} n_i$;
- $\hat{\mathbf{A}}(\mathbf{U}, \mathbf{V}, \mathbf{n})(\mathbf{U} - \mathbf{V}) = \mathbf{F}(\mathbf{U}) \cdot \mathbf{n}_e - \mathbf{F}(\mathbf{V}) \cdot \mathbf{n}_e$

Finally, the numerical flux is computed as

$$\begin{aligned} \tilde{\mathbf{F}}(\mathbf{U}_K, \mathbf{U}_{K_e}, \mathbf{n}_e) &= \mathbf{F}(\mathbf{U}_K) \cdot \mathbf{n}_e + \hat{\mathbf{A}}^+(\mathbf{U}_K, \mathbf{U}_{K_e}, \mathbf{n}_e)(\mathbf{U}_{K_e} - \mathbf{U}_K) \\ &= \mathbf{F}(\mathbf{U}_{K_e}) \cdot \mathbf{n}_e - \hat{\mathbf{A}}^-(\mathbf{U}_K, \mathbf{U}_{K_e}, \mathbf{n}_e)(\mathbf{U}_{K_e} - \mathbf{U}_K), \end{aligned} \tag{3.35}$$

with

$$\hat{\mathbf{A}}^+ = \mathbf{R}\mathbf{\Lambda}^+\mathbf{R}^{-1} \tag{3.36a}$$

$$\hat{\mathbf{A}}^- = \mathbf{R}\mathbf{\Lambda}^-\mathbf{R}^{-1} \tag{3.36b}$$

where the matrices $\mathbf{\Lambda}^+$ and $\mathbf{\Lambda}^-$ contains the positive and negative eigenvalues of $\hat{\mathbf{A}}$, respectively, and $\mathbf{R}$ is the matrix containing the right eigenvectors. In an alternative approach, proposed in [114], the computation of the average Jacobian matrix is not required.

3.4 Flux-limiting techniques

Flux-limiting techniques are used to avoid spurious oscillations that would occur with high-order spatial discretization near shocks or sharp gradients in the solution. These techniques are based on the computation of numerical fluxes using both an algorithm guaranteed not to violate the maximum principle (low order flux) and an algorithm that is formally of high accuracy in the smooth portions of the solution (high order fluxes). The final numerical flux is then constructed as weighted average of these two fluxes. The weighting is performed in a manner which ensures that the high order fluxes are used to the greatest extent possible without introducing unphysical values into the solution. This procedure is referred to as flux-correction or flux-limiting.

For the sake of simplicity, we consider the finite volume approximation of the conservation equation for the scalar variable u on the element K:

$$\frac{d}{dt}u_K + \frac{1}{|K|}\sum_{e\in\partial K}\tilde{f}(u_K, u_{K_e}, \mathbf{n}_e) = 0, \tag{3.37}$$

where $\tilde{f}(u_K, u_{K_e}, \mathbf{n}_e) = \tilde{f}_e$ is the numerical flux through the edge e. If we define with $\tilde{f}_e^L$ the low order flux and with $\tilde{f}_e^H$ the high order flux, the the numerical flux can be split into a low order diffusive flux and a limited antidiffusive flux as follows:

$$\tilde{f}_e = \tilde{f}_e^L + C_{\mathrm{lim},e}\tilde{a}_e \tag{3.38}$$

where the antidiffusive flux is defined as

$$\tilde{a}_e = \tilde{f}_e^H - \tilde{f}_e^L \tag{3.39}$$

and $C_{\mathrm{lim},e} \geq 0$. The computation of the coefficients $C_{\mathrm{lim},e}$ depends on the type of flux-limiter we want to apply.

3.4.1 Standard flux-limiter

A large number of different definitions for the limiting coefficients has been proposed in the literature [129]. The coefficient $C_{\mathrm{lim},e}$ is expressed as a function of a parameter r_e that represents a measure of the smoothness of the data near the edge e, that is $C_{\mathrm{lim},e} = C_{\mathrm{lim}}(r_e)$, with

$$r_e = \frac{\Delta u_{e,\mathrm{upw}}}{\Delta u_e}. \tag{3.40}$$

Here, Δu_e is the jump of the solution at the interface e and $\Delta u_{e,\mathrm{upw}}$ is the jump at the interface on the upwind side of e. Examples of computation of C_{lim} are

- minmod function
$$C_{\mathrm{lim}}(r) = \max\left(0, \min\left(1, r\right)\right); \tag{3.41}$$
- superbee
$$C_{\mathrm{lim}}(r) = \max\left(0, \min\left(2r, 1\right), \min\left(r, 2\right)\right); \tag{3.42}$$
- van Leer
$$C_{\mathrm{lim}}(r) = \frac{r + |r|}{1 + |r|}. \tag{3.43}$$

3.4.2 Flux-Corrected Transport algorithm

The theory of Flux-Corrected Transport (FCT) algorithms has been developed in several works [12–14, 150] in the framework of finite volume methods. Here, we present the details of the method proposed in [150]. For each element $K \in \mathcal{T}_h$:

- compute the low order solution $\tilde{u}_K$ with $\tilde{a}_e = 0$;
- compute the maximum and minumum allowable mean values $u_K^{\max}$ and $u_K^{\min}$ from the upstream neighbouring elements;
- compute P_K^+ and P_K^- as the sum of all antidiffusive fluxes into and away from K, respectively;
- compute

$$Q_K^+ = \left(u_K^{\max} - \tilde{u}_K\right)|K|, \quad Q_K^- = \left(\tilde{u}_K - u_K^{\min}\right)|K| \tag{3.44}$$

- set

$$R_K^+ = \begin{cases} \min\left(1, Q_K^+/P_K^+\right) & \text{if } P_K^+ > 0, \\ 0 & \text{if } P_K^+ = 0, \end{cases} \tag{3.45}$$

$$R_K^- = \begin{cases} \min\left(1, Q_K^-/P_K^-\right) & \text{if } P_K^- > 0, \\ 0 & \text{if } P_K^- = 0. \end{cases} \tag{3.46}$$

Finally, set for each edge $e = K \cap K_e$, with normal vector $\mathbf{n}_e$ directed from K to K_e compute

$$C_{\mathrm{lim},e} = \begin{cases} \min\left(R_{K_e}^+, R_K^-\right) & \text{if } \tilde{a}_e \geq 0 \\ \min\left(R_K^-, R_{K_e}^+\right) & \text{if } \tilde{a}_e < 0 \end{cases} \tag{3.47}$$

This algorithm allows to compute for each scalar equation i of the system of conservation laws the limiting coefficient $C_{\mathrm{lim},e}^{(i)}$. As observed in [85], the results available in the literature show that FCT allows to obtain excellent solutions for a single scalar conservation laws, but, when trying to extend the limiting procedure to systems of equations, no natural extension is available. The advection of each single wave and the limiting of each equation separately does not always give good results. It is necessary to introduce an alternative approach, by combining the limiters for all equations of the system. Many variations can be implemented, however the results strongly depend on the equations are being solved. In particular, for the Euler system, the minimum of the limiters obtained for the density and the energy equations is usually adopted. This choice, proposed in [85], produces acceptable results, although some undershoots for very strong shocks can be observed.

3.5 PDAC implementation

The present work has been partially devoted to the enhancement of the PDAC model (Pyroclastic Dispersal Analysis Code, Esposti Ongaro et al. [42]). PDAC is a parallel code that solves the multiphase flow equations presented in Chapter 2. The original implementation of the PDAC code was based on a first order donor-cell finite-volume scheme, extended to second order in each separate spatial direction by adopting the

one-dimensional MUSCL scheme [129], as is common practice in other multiphase flow codes, e.g. MFIX in [131, 133]. The resulting numerical method is effective, but its results still display significant numerical diffusion, especially in multidimensional simulations, which implies the need for very high spatial resolution and small time steps to achieve an accurate simulation. One of the objectives of this work has been to modify the numerical algorithm in order to increase the accuracy in the simulation of the near-vent decompression dynamics, potentially involving supersonic regimes and shock waves, and the transient dynamics of turbulent eddies that control, for example, the atmospheric air entrainment. More specifically, the fully multidimensional Corner Transport Upwind (CTU) advection scheme [83] is introduced to achieve second order accuracy in the finite volume spatial discretization, including minmod flux limiting to avoid the creation of spurious extrema in the solution. We implemented the enhanced finite volume approximation in the parallel PDAC code in the two dimensional and three dimensional case. The introduction of the new methods has required the extension of the computational stencil and the consequent increase of the information exchanged between different subdomains in the parallel implementation of the code.

Numerical simulations proposed in Chapter 6 and Chapter 8, when not specified explicitly, are all carried out using the enhanced version of the parallel PDAC code, i.e. applying the second order Corner Transport Upwind scheme to compute advective terms.

CHAPTER 4

Spatial discretization by discontinuous Galerkin methods

THE Discontinuous Galerkin (DG) method has been originally introduced as a Galerkin approximation of the continuous problem in conservative form in which discontinuous basis functions are adopted. At the same time, the DG method can be also interpreted as an extension of finite volume methods to arbitrary order of accuracy. In fact, as it happens in the finite volume approach, the discontinuous Galerkin approach is derived from the conservative form of the balance equations, but the solution is approximated with discontinuous polynomials of degree r on each control volume K.

Like finite volume methods, DG methods provide discrete conservation laws that reproduce on each control volume the fundamental physical balances characterizing the continuous problem. Thus, they both represent a good choice for the approximation of problems whose solution presents discontinuities, where classical solutions are not properly defined. However, unlike finite volume methods, with DG methods high order accuracy can be obtained without extending the computational stencil, thus allowing for a good scalability on parallel architectures. Moreover, DG schemes allow for an easy introduction of adaptivity techniques, regarding both the computational mesh and the degree of the local basis functions on each element of the mesh.

The DG method for the solution of steady state hyperbolic problems was first introduced in [108] for the solution of the neutron transport equation. The application of DG method to time dependent scalar conservation laws was first proposed in [22], where explicit forward Euler time stepping is stabilized with a local projection operator based on the monotonicity preserving projection [82]. The application is refined in [26], where Runge-Kutta explicit time integration schemes are introduced and extended to

systems of equations and multidimensional problems in [23–25, 27]. Finally, the DG method has been successfully applied to fluid dynamics problems in a great variety of flow regimes, see e.g. [5, 6].

In this chapter, the discontinuous Galerkin approximation for a general system of conservation laws is presented. Then, the p-adaptivity algorithm, originally proposed by Tumolo et al. [137] is described. One of the objectives of the work has been the implementation of the presented p-adaptive discontinuous Galerkin approximation of multiphase gas–particle equations in the one dimensional case in a Fortran code, starting from the original code by Tumolo et al. [137].

4.1 Discontinuous Galerkin approximation of conservation laws

We consider as model problem a general system of M nonlinear conservation laws. In compact notation, the system can be written defining the vector of conserved variables $\mathbf{U}$ and the flux vector $\mathbf{F}(\mathbf{U})$:

$$\frac{\partial \mathbf{U}}{\partial t} + \nabla \cdot \mathbf{F}(\mathbf{U}) = \mathbf{S}(\mathbf{U}, t). \tag{4.1}$$

Here $\mathbf{U}(x,t) : \mathbb{R}^d \times [0,T] \to \mathbb{R}^M$ is the vector of conserved variables, $\mathbf{F}(\mathbf{U}) : \mathbb{R}^M \times [0,T] \to \mathbb{R}^M \times \mathbb{R}^d$ is the flux function and $\mathbf{S}(\mathbf{U},t) : \mathbb{R}^M \times [0,T] \to \mathbb{R}^M$ is the vector source function. The system of conservation laws may also be written in quasilinear form:

$$\frac{\partial \mathbf{U}}{\partial t} + \sum_{i=1}^{d} \mathbf{A}_i(\mathbf{U}) \frac{\partial \mathbf{U}}{\partial x_i} = \mathbf{S}(\mathbf{U}), \tag{4.2}$$

where the coefficient matrices $\mathbf{A}_i(\mathbf{U}) \in \mathbb{R}^M \times \mathbb{R}^M$ are the Jacobian matrices of the flux components $\mathbf{F}_i$, that is

$$\mathbf{A}_i(\mathbf{U}) = \frac{\partial \mathbf{F}_i}{\partial \mathbf{U}}. \tag{4.3}$$

In this section we give a standard presentation of the DG spatial discretization for the general system of conservation laws (4.1). As described in Chapter 3, we consider a Cartesian mesh $\mathcal{T}_h$ on the domain $\Omega \subset \mathbb{R}^d$, with $d = 1, 2, 3$ and we denote with K the control volumes. Given the control volume K and its edge $e \in \partial K$, here we denote with K_e the control volume that shares with K the edge e, that is such that $e = K \cap K_e$, and with $\mathbf{n}_e$ the vector normal to e, pointing from K to K_e. Notice that, here and in the following sections, no assumptions on the conformity of the mesh are made and the DG scheme proposed in this chapter is equally valid for conforming and non conforming meshes.

We introduce for each element K the nonnegative integer $r(K)$ and the space $V^r(K) = \mathbb{P}^r(K)$, that denotes the space of polynomials of degree at most $r(K)$ on the element K. The space of elements of $L^\infty(\Omega)$ whose restriction on K belongs to $V^r(K)$ for all $K \in \mathcal{T}_h$ is denoted by V_h^r. Notice that functions in V_h^r can be discontinuous across the control volume edges $e \in \partial K$. Moreover, observe how the polynomial degree is not constant on the tassellation, but may change from element to element. We define the space $\mathbf{V}_h^r$ as the the space of vector functions such that their components belong to V_h^r.

For a given element $K \in \mathcal{T}_h$, edge $e \in \partial K$, point $\xi \in e$ and for any functions $\varphi \in V_h^r$ we define

$$\varphi_K(\xi) = \lim_{x \to \xi} \varphi(x), \quad \text{with } x \in K \tag{4.4a}$$

$$\varphi_{K_e}(\xi) = \lim_{x \to \xi} \varphi(x), \quad \text{with } x \in K_e. \tag{4.4b}$$

The extension to vector functions $\mathbf{v} \in \mathbf{V}_h^r$ is straightforward. The average and the jump of the scalar function $\varphi \in V_h^r$ across the edge $e \in \partial K$ are defined as

$$\{\varphi\}(\xi) = \frac{1}{2}\left(\varphi_K(\xi) + \varphi_{K_e}(\xi)\right) \tag{4.5a}$$

$$[\![\varphi]\!](\xi) = \varphi_K(\xi)\mathbf{n}_e - \varphi_{K_e}(\xi)\mathbf{n}_e. \tag{4.5b}$$

Analogously, for a vector function $\mathbf{v} \in \mathbf{V}_h^r$, the average and the jump are defined as

$$\{\mathbf{v}\}(\xi) = \frac{1}{2}\left(\mathbf{v}_K(\xi) + \mathbf{v}_{K_e}(\xi)\right) \tag{4.6a}$$

$$[\![\mathbf{v}]\!](\xi) = \mathbf{v}_K(\xi) \cdot \mathbf{n}_e - \mathbf{v}_{K_e}(\xi) \cdot \mathbf{n}_e. \tag{4.6b}$$

Notice that the jump of a scalar function is a vector parallel to the normal, whereas the jump of a vector function is a scalar quantity.

Following the standard procedure in the framework of finite element methods, we introduce a set of polynomial basis functions for the finite dimensional space $\mathbf{V}_h^r$ on the reference element $\hat{K}$. Concerning the choice of basis functions, two main alternatives are possible: nodal basis functions and modal basis functions. By using *nodal basis functions*, the unknown coefficients can be interpreted as the values of the variable at a set of grid nodes. On the one–dimensional reference element $\hat{K} = [-1, 1]$, for $\xi \in \hat{K}$, $\{L_k^n(\xi)\}_{k=1}^r$ is the Lagrangian nodal basis, where

$$L_k^n(\xi) = \prod_{i=0, i \neq k}^{r} \frac{\xi - x_i}{x_k - x_i} \tag{4.7}$$

where x_i are the interpolation nodes (i.e. the Legendre-Gauss-Lobatto points).

In this work, *modal basis functions* will be adopted [18]. Modal bases provide a hierarchical representation, where each basis function is associated with a given wavelength. On the reference element $\hat{K} = [-1, 1]$, for $\xi \in \hat{K}$, the k-th Legendre (i.e. modal) basis polynomial, i.e. $L_k^m(\xi)$, is defined by the following recurrence relation:

$$\begin{aligned} &L_{k+1}^m = \frac{2k+1}{k+1}\xi L_k^m(\xi) - \frac{k}{k+1}L_{k-1}^m(\xi), \quad k = 1, 2, \dots \\ &L_0^m(\xi) = 1, \\ &L_1^m(\xi) = \xi. \end{aligned} \tag{4.8}$$

The Legendre polynomials form an orthogonal basis for polynomials on $\hat{K}$ since

$$(L_p^m, L_q^m)_{L^2} = \int_{-1}^{1} L_p^m(\xi) L_q^m(\xi) d\xi = \frac{2}{2p+1}\delta_{pq}. \tag{4.9}$$

This orthogonality property of basis functions has important numerical implications in the Galerkin approximation, since it implies that the mass matrices are diagonal and gives improved conditioning to the resulting discretization [18]. In particular, we will use normalized basis functions $\varphi_{K,j}$ such that

$$(\varphi_{K,p}, \varphi_{K,q})_{L^2} = \int_K \varphi_{K,p}(x)\varphi_{K,q}(x)dx = |K|\delta_{pq}. \tag{4.10}$$

The extension to higher dimension over quadrilateral control volumes is relatively straightforward. As an example, in the two dimensional case, for $(\xi_1, \xi_2) \in \hat{K}$, a hierarchical basis can be constructed by taking tensor products of the Legendre polynomials introduced in the one-dimensional case. Two-dimensional basis functions will be of the form $L_k^m(\xi_1)L_l^m(\xi_2)$ for $0 \leq k, l, \leq r$. In the case of systems of conservation laws, we denote with $\boldsymbol{\varphi}_{K,k}$ the $k-$th basis polynomial, with components $\boldsymbol{\varphi}_{K,k}^{(i)} = \varphi_{K,k}$.

We look for an approximation $\mathbf{U}_h(x,t) \in \mathbf{V}_h^r$ of the solution $\mathbf{U}(x,t)$ of system (4.1). For each element $K \in \mathcal{T}_h$, the discrete degrees of freedom associated with the numerical solution at time t are denoted by $\{\mathbf{U}_{K,j}(t)\}_{j\in\mathcal{J}_K}$, with $\mathcal{J}_K = \{0, \ldots, N_r - 1\}$ and $N_r = dim(\mathbf{V}_r(K)) = (r(K)+1)^d$. The approximate solution can be reconstructed locally for all $K \in \mathcal{T}_h$ as

$$\mathbf{U}_h(x,t)\big|_K = \sum_{j\in\mathcal{J}_K} \mathbf{U}_{K,j}(t)\boldsymbol{\varphi}_{K,j}(x). \tag{4.11}$$

Here, j is a suitable multi-index relabelling the d-dimensional degrees of freedom in terms of the one-dimensional ones, i.e. $\boldsymbol{\varphi}_{K,j} = \prod_{i=1}^d \boldsymbol{\varphi}_{K,j_i}(x_i)$. In order to determine the degrees of freedom $\mathbf{U}_{K,j}(t)$, for all $K \in \mathcal{T}_h$ and $j \in \mathcal{J}_K$, of the numerical solution $\mathbf{U}_h$, we multiply each equation of the system by a test function $\boldsymbol{\varphi}_h \in \mathbf{V}_h^r$ and we integrate over control volume K:

$$\frac{d}{dt}\int_K \mathbf{U}(x,t)\boldsymbol{\varphi}_h(x)\,dx + \int_K \nabla\cdot\mathbf{F}(\mathbf{U}(x,t))\boldsymbol{\varphi}_h(x)\,dx = \int_K \mathbf{S}(\mathbf{U},t)\boldsymbol{\varphi}_h(x)\,dx. \tag{4.12}$$

By integrating by parts the flux term, we obtain

$$\begin{aligned} &\frac{d}{dt}\int_K \mathbf{U}(x,t)\boldsymbol{\varphi}_h(x)\,dx - \int_K \mathbf{F}(\mathbf{U}(x,t))\cdot\nabla\boldsymbol{\varphi}_h(x)\,dx \\ &+ \int_{\partial K} (\mathbf{F}(\mathbf{U}(x,t))\cdot\mathbf{n})\boldsymbol{\varphi}_h(x)\,dx = \int_K \mathbf{S}(\mathbf{U},t)\boldsymbol{\varphi}_h(x)\,dx \end{aligned} \tag{4.13}$$

As usual in the finite element framework, we introduce as test functions the basis functions $\varphi_{K,i}$, for all $i \in \mathcal{J}_K$, and we introduce the representation of the approximate solution (4.11), obtaining

$$\begin{aligned} &\frac{d}{dt}\sum_{j\in\mathcal{J}_K} \mathbf{U}_{K,j}(t)\int_K \boldsymbol{\varphi}_{K,j}(x)\boldsymbol{\varphi}_{K,i}(x)\,dx - \int_K \mathbf{F}(\mathbf{U}_h)\cdot\nabla\boldsymbol{\varphi}_{K,i}(x)\,dx \\ &+ \int_{\partial K} (\mathbf{F}(\mathbf{U}_h)\cdot\mathbf{n})\boldsymbol{\varphi}_{K,i}(x)\,dx = \int_K \mathbf{S}(\mathbf{U},t)\boldsymbol{\varphi}_{K,i}(x)\,dx. \end{aligned} \tag{4.14}$$

Thanks to the orthogonality property (4.10) of the basis functions, we obtain

$$\begin{aligned}&\frac{d}{dt}\mathbf{U}_{K,i}(t)|K| - \int_K \mathbf{F}(\mathbf{U}_h)\cdot\nabla\boldsymbol{\varphi}_{K,i}(x)\,dx \\ &+ \int_{\partial K}(\mathbf{F}(\mathbf{U}_h)\cdot\mathbf{n})\boldsymbol{\varphi}_{K,i}(x)\,dx = \int_K \mathbf{S}(\mathbf{U},t)\boldsymbol{\varphi}_{K,i}(x)\,dx.\end{aligned} \tag{4.15}$$

All the integrals appearing in the weak formulation are evaluated by means of Gauss numerical quadrature rules with a number of integration points consistent with the accuracy of the scheme, as introduced in the finite volume framework in Chapter 3.

Concerning the computation of flux terms, a distinction has to be done between convective and diffusive fluxes. The flux function is then splitted as follow

$$\mathbf{F}(\mathbf{U}) = \mathbf{F}^c(\mathbf{U}) + \mathbf{F}^v(\mathbf{U}), \tag{4.16}$$

where $\mathbf{F}^c(\mathbf{U})$ is the hyperbolic flux and $\mathbf{F}^v(\mathbf{U})$ is the diffusive flux.

The convective flux terms are computed with the same techniques applied in finite volume schemes, presented in Chapter 3. The flux function $\mathbf{F}(\mathbf{U})\cdot\mathbf{n}_e$ is in fact replaced by a numerical flux function $\tilde{\mathbf{F}}(\mathbf{U}_e, \mathbf{U}_{K_e}, \mathbf{n}_e)$ which depends on the internal interface state $\mathbf{U}_K$, on the neighbouring interface state $\mathbf{U}_{K_e}$ and on the face orientation $\mathbf{n}_e$.

Diffusive fluxes introduce in the equations second-order derivatives, i.e. $\mathbf{F}^v = \mathbf{F}^v(\nabla\mathbf{U})$, that require a special treatment in the DG approximation. Several methods have been proposed in the literature to deal with diffusion terms in a mathematically consistent way. The spatial discretization of the viscous term is constructed by resorting to a mixed finite element formulation, as proposed in [5]. Second-order derivatives, in fact, cannot be approximated directly in a weak formulation using a discontinuous function space. The gradient of the conservative variables is regarded as an auxiliary unknown, that is $\nabla\mathbf{U} = \mathbf{R}(\mathbf{U})$. The original system of conservation law is then riformulated as the following coupled system for the unknowns $\mathbf{U}$ and $\mathbf{R}$:

$$\mathbf{R} - \nabla\mathbf{U} = 0, \tag{4.17a}$$

$$\frac{\partial\mathbf{U}}{\partial t} + \nabla\cdot\mathbf{F}^c(\mathbf{U}) + \nabla\cdot\mathbf{F}^v(\mathbf{U},\mathbf{R}) = \mathbf{S}(\mathbf{U}). \tag{4.17b}$$

An approximation $(\mathbf{U}_h, \mathbf{R}_h)$ to the solution $(\mathbf{U}, \mathbf{R})$ is sought such that $(\mathbf{U}_h, \mathbf{R}_h) \in \mathbf{V}_h^r \times (\mathbf{V}_h^r)^d$. Integrating over the control volumes $K \in \mathcal{T}_h$ we get

$$\int_K \mathbf{R}\,\boldsymbol{\varphi}_h dx - \int_K \nabla\mathbf{U}\,\boldsymbol{\varphi}_h dx = 0 \tag{4.18a}$$

$$\int_K \frac{\partial\mathbf{U}}{\partial t}\,\boldsymbol{\varphi}_h dx + \int_K \nabla\cdot\mathbf{F}^c(\mathbf{U})\,\boldsymbol{\varphi}_h dx + \int_K \nabla\cdot\mathbf{F}^v(\mathbf{U},\mathbf{R})\,\boldsymbol{\varphi}_h dx = \int_K \mathbf{S}(\mathbf{U})\,\boldsymbol{\varphi}_h dx \tag{4.18b}$$

Method	C_{11}	$\mathbf{C}_{12}$	$\mathbf{C}_{21}$	C_{22}
SIPG	$-C_{IP}\frac{p^2}{h_e}$	0	0	0
NIPG	$-C_{IP}\frac{p^2}{h_e}$	0	$\mathbf{n}_e$	0
BO	0	0	$\mathbf{n}_e$	0

Table 4.1: Coefficients corresponding to different DG formulations of diffusive fluxes.

Then, formally integrating by parts, we obtain

$$\int_K \mathbf{R}\,\boldsymbol{\varphi}_h dx + \int_K \mathbf{U}\cdot\nabla\boldsymbol{\varphi}_h dx - \int_{\partial K}(\mathbf{U}\cdot\mathbf{n})\,\boldsymbol{\varphi}_h dx = 0 \tag{4.19a}$$

$$\begin{aligned}\int_K \frac{\partial \mathbf{U}}{\partial t}\,\boldsymbol{\varphi}_h dx &- \int_K \mathbf{F}^c(\mathbf{U})\cdot\nabla\boldsymbol{\varphi}_h dx + \int_{\partial K}\mathbf{F}^c(\mathbf{U})\cdot\mathbf{n}\,\boldsymbol{\varphi}_h dx \\ &- \int_K \mathbf{F}^v(\mathbf{U},\mathbf{R})\cdot\nabla\boldsymbol{\varphi}_h dx + \int_{\partial K}\mathbf{F}^v(\mathbf{U},\mathbf{R})\cdot\mathbf{n}\,\boldsymbol{\varphi}_h dx \\ &= \int_K \mathbf{S}(\mathbf{U})\,\boldsymbol{\varphi}_h dx\end{aligned} \tag{4.19b}$$

Finally, appropriate numerical fluxes have to be introduced to approximate the additional viscous flux terms, i.e. $\mathbf{U}\cdot\mathbf{n} \simeq \tilde{\mathbf{U}}$ and $\mathbf{F}^v(\mathbf{U},\mathbf{R})\cdot\mathbf{n} \simeq \tilde{\mathbf{F}}^v$. Depending on the choice of the numerical flux function, different DG discretization can be derived. In [6], Bassi and Rebay proposed

$$\tilde{\mathbf{U}}(\mathbf{U}_K,\mathbf{U}_{K_e},\mathbf{n}_e) = \frac{1}{2}\left(\mathbf{U}_K + \mathbf{U}_{K_e}\right)\mathbf{n}_e \tag{4.20}$$

and

$$\tilde{\mathbf{F}}^v(\mathbf{U}_K,\mathbf{R}_K,\mathbf{U}_{K_e},\mathbf{R}_{K_e},\mathbf{n}_e) = \frac{1}{2}\left[\mathbf{F}^v(\mathbf{U}_K,\mathbf{R}_K) + \mathbf{F}^v(\mathbf{U}_{K_e},\mathbf{R}_{K_e})\right]\cdot\mathbf{n}_e \tag{4.21}$$

for the compressible Navier-Stokes equations. In general, the viscous numerical fluxes can be expressed as a function of the averages and the jumps across the edge e as follow

$$\tilde{\mathbf{F}}^v = \{\mathbf{R}\} + C_{11}[\![\mathbf{U}]\!] + \mathbf{C}_{12}[\![\mathbf{R}]\!] \tag{4.22a}$$

$$\tilde{\mathbf{U}} = \{\mathbf{U}\} + \mathbf{C}_{21}[\![\mathbf{U}]\!] + C_{22}[\![\mathbf{R}]\!]. \tag{4.22b}$$

The free parameters allow to control the stability and accuracy of the scheme [2]. Some examples are reported in Table 4.1 [8, 112, 142].

4.2 p-adaptivity criterion

The numerical method described in the previous sections can be implemented taking a constant value for the degree of the polynomials defining the local basis on each element. However, our aim is to exploit the great flexibility of the DG spatial discretization by supplying the method with an automatic criterion to adapt the local number of degrees of freedom to the nature of the numerical solution.

Various approaches for $p-$adaptivity have been proposed in the literature, see e.g. [41,47,67,109]. The simple technique we employ was originally proposed in [137] and relies on the use of orthogonal hierarchical tensor-product basis functions. Consider the local (to the element K) representation of some dependent variable $u(x)$:

$$u(x)\big|_K = \sum_{j \in \mathcal{J}_K} u_{K,j} \varphi_{K,j}(x). \tag{4.23}$$

If a normalized hierarchical basis is employed, by Parseval's identity one will have

$$\mathcal{E}^{tot} = \|Pu\|^2 = \sum_{j \in \mathcal{J}_K} u_{K,j}^2 \tag{4.24}$$

where P is the L^2 projector onto the local polynomial subspace. Now combining (4.24) with the hierarchical property of the basis, for any integer $p = 1, \ldots, r(K)+1$, we can define the energy contained in the p-th modal component of $u|_K$ for a given element $K \in \mathcal{T}_h$ as

$$\mathcal{E}^p = u_{K,p}^2. \tag{4.25}$$

Therefore, for any integer $p = 1, \ldots, r(K)+1$, the quantity

$$w_p = \sqrt{\frac{\mathcal{E}^p}{\mathcal{E}^{tot}}} \tag{4.26}$$

will measure the relative weight of the p-th modal components of u with respect to the best approximation available for the L^2 norm of u. Assuming that u denotes a generic model variable at the beginning of the computation of a generic time step, the proposed adaptation criterion can be described as follows:

Given an error tolerance $\epsilon_K > 0$, for each element $K \in \mathcal{T}_h$ compute w_{p_K}. Then

(1) if $w_{r(K)} \geq \epsilon_K$, then

- *(1.a) set $r(K) = r(K) + 1$*
- *(1.b) set $u_{K,r(K)} = 0$, exit the loop and go the next element*

(2) if instead $w_{r(K)} < \epsilon_K$, then

- *(2.a) compute $w_{r(K)-1}$*
- *(2.b) if $w_{r(K)-1} \geq \epsilon_K$, exit the loop and go the next element*
- *(2.c) else if $w_{r(K)-1} < \epsilon_K$, set $r(K) = r(K) - 1$ and go back to (2.a)*

At the beginning of the simulation, all the variables are initialized with the maximum possible number of local degrees of freedom. The adaptation algorithm then runs preliminary to any computation in each new time step, including the first.

In order to assess the efficiency gain given by the adaptivity algorithm, the computational effort reduction is estimated as

$$\Delta_{dof} = \frac{\sum_{K \in \mathcal{T}_h} (r(K)+1)^d}{dim(\mathcal{T}_h)(r_{max}+1)^d} \tag{4.27}$$

where $dim(\mathcal{T}_h)$ is the number of elements in the tassellation and r_{max} is the maximum polynomial degree admitted in the computation. As analyzed in detail in [137], the computational saving achieved by the adaptation algorithm on different benchmark test cases is in general between 40% and 60%.

CHAPTER 5

Time discretization

FOLLOWING the method of lines, from the spatial discretization of a system of conservation laws by applying either finite volume of discontinuous Galerkin schemes, a system of ordinary differential equations is obtained, i.e.

$$\frac{d}{dt}\mathbf{U}(t) = \mathcal{L}_h(\mathbf{U}(t)) \tag{5.1}$$

with initial datum

$$\mathbf{U}(0) = \mathbf{U}_0. \tag{5.2}$$

Here $\mathbf{U}(t) : [0,T] \to \mathbb{R}^N$ and $\mathcal{L}_h(\mathbf{U}) : \mathbb{R}^N \times [0,T] \to \mathbb{R}^N$. The operator $\mathcal{L}_h$ represents the spatial approximation of the continuous problem

$$\frac{\partial \mathbf{U}}{\partial t} + \nabla \cdot \mathbf{F}(\mathbf{U}) = \mathbf{S}(\mathbf{U}). \tag{5.3}$$

on the tassellation $\mathcal{T}_h$, that is

$$\mathcal{L}_h(\mathbf{U}) \simeq -\nabla \cdot \mathbf{F}(\mathbf{U}) + \mathbf{S}(\mathbf{U}). \tag{5.4}$$

We introduce a partition of the time interval $[0,T]$ into N_T subintervals $[t^n, t^{n+1}]$. For the sake of simplicity we consider a constant time step Δt, such that $t^n = n\Delta t$ for all $n = 0, \ldots, N_T - 1$. However, in general, the time step can be adapted, i.e. $\Delta t = \Delta t^n$ in order to satisfy stability restrictions in transient problems. In the following sections, we denote with $\mathbf{U}^n$ the approximation of the solution at time t^n, i.e. $\mathbf{U}^n \simeq \mathbf{U}(t^n)$.

In this chapter, explicit and implicit methods for the approximate solution of systems of ordinary differential equations are presented. In the second part, time discretizations

adopted in this work in the framework of finite volume and discontinuous Galerkin spatial approximation of the multiphase gas–particle equations are described in details. One of the objectives of the this work has been the implementation of the second order time discretization techniques presented in Section 5.3 in the parallel PDAC code and in the discontinuous Galerkin code.

5.1 Explicit time advancing schemes

In the framework of discontinuous Galerkin approximations, the system (5.1) is usually solved by means of explicit Strong Stability Preserving (SSP) Runge-Kutta schemes, as proposed [121]. These methods were designed specifically for solving the ordinary differential equations coming from a semi-discrete, spatial discretization of time dependent problems, whose dimensions can be very large depending on the spatial discretization mesh size. Moreover, there are certain stability properties of the original problem, such as maximum norm stability, which are mainained by certain spatial discretizations with the first order explicit Euler time discretization that are desirable to maintain for high order time discretizations as well.

The SSP property guarantees that, if the first order forward Euler discretization of a semi-discrete scheme is stable under a certain norm, then a SSP high order time discretization maintains this stability, provided that appropriate restrictions on the time step value are satisfied.

It has been shown [56] that oscillations and non-linear instability can occur when a linearly stable but non-SSP method is applied. Thus, when solving problems with shocks, for which the traditional linear stability analysis is not applicable, the use of SSP methods is more appropriate.

5.1.1 Forward Euler scheme

By applying the first-order forward finite difference scheme to approximate the time derivative in (5.1), the forward or explicit Euler time-advancing scheme is obtained:

$$\mathbf{U}^{n+1} = \mathbf{U}^n + \Delta t \mathcal{L}_h(\mathbf{U}^n) \tag{5.5}$$

The scheme is first-order accurate in time and it is stable, e.g.

$$\|\mathbf{U}^{n+1}\| \leq \|\mathbf{U}^n\| \tag{5.6}$$

with a certain norm, under a suitable time step restriction, which depends on the discrete operator $\mathcal{L}_h$ and the mesh size h, that is

$$\Delta t \leq \Delta t_0(\mathcal{L}_h, h). \tag{5.7}$$

5.1.2 Runge-Kutta schemes

Runge-Kutta methods are time discretization which can be written in several different ways. A general Runge-Kutta method with m stages is written in the form:

$$\begin{aligned} &\mathbf{U}^{(i)} = \sum_{l=0}^{i-1} \alpha_{il}\mathbf{U}^{(l)} + \beta_{il}\Delta t \mathcal{L}_h(\mathbf{U}^{(l)}) \quad \forall i = 1, \ldots, m \\ &\mathbf{U}^{(0)} = \mathbf{U}^n, \qquad \mathbf{U}^{(m)} = \mathbf{U}^{n+1}. \end{aligned} \tag{5.8}$$

A necessary condition for the Runge-Kutta scheme to be SSP is that all the coefficients are nonnegative, i.e. $\alpha_{il} \geq 0$, $\beta_{il} \geq 0$ [120]. Notice that, under the same hypothesis, then (5.8) is just a convex combination of Euler forward operators. It can be proved that, it the forward Euler method (5.5) is stable in the sense of (5.6) under the time step restriction (5.7), then the Runge-Kutta method with nonnegative coefficients is SSP, i.e. its solution satisfies the same stability (5.6) under the time step restriction

$$\Delta t \leq c\Delta t_0(\mathcal{L}_h, h) \tag{5.9}$$

with

$$c = \min_{i,l} \frac{\alpha_{il}}{\beta_{il}}. \tag{5.10}$$

The coefficient c is called the Courant-Friedrichs-Lewy (CFL) coefficient of the SSP method. For a fixed number of stages m, the optimal choice of the coefficients α_{il}, β_{il} is the one that maximizes the order of accuracy and the value of the CFL coefficient.

For $m = 2$, the optimal second order nonlinear SSP Runge-Kutta scheme is given by [56, 121]

$$\begin{aligned} \mathbf{U}^{(1)} &= \mathbf{U}^n + \Delta t\mathcal{L}_h(\mathbf{U}^n), \\ \mathbf{U}^{n+1} &= \frac{1}{2}\mathbf{U}^n + \frac{1}{2}\mathbf{U}^{(1)} + \frac{1}{2}\Delta t\mathcal{L}_h(\mathbf{U}^{(1)}), \end{aligned} \tag{5.11}$$

with CFL coefficient $c = 1$. The optimal third order ($m = 3$) nonlinear SSP Runge-Kutta scheme is defined as

$$\begin{aligned} \mathbf{U}^{(1)} &= \mathbf{U}^n + \Delta t\mathcal{L}_h(\mathbf{U}^n), \\ \mathbf{U}^{(2)} &= \frac{3}{4}\mathbf{U}^n + \frac{1}{4}\mathbf{U}^{(1)} + \frac{1}{4}\Delta t\mathcal{L}_h(\mathbf{U}^{(1)}), \\ \mathbf{U}^{n+1} &= \frac{1}{3}\mathbf{U}^n + \frac{2}{3}\mathbf{U}^{(2)} + \frac{2}{3}\Delta t\mathcal{L}_h(\mathbf{U}^{(2)}), \end{aligned} \tag{5.12}$$

with CFL coefficient $c = 1$.

5.1.3 Slope-limiting techniques

Slope limiting techniques are based on the application of a limiting step (or reconstruction step) with the use of a non linear local projection operator $\Lambda\Pi_h$ with the aim to enforce nonlinear stability of the numerical solution and to prevent spurious oscillations near discontinuities. If applied to Runge-Kutta schemes, the numerical solution has to be adjusted at the end of each Runge-Kutta step as follow

$$\mathbf{U}^{(i)} = \Lambda\Pi_h\left(\mathbf{U}^{(i)}\right). \tag{5.13}$$

Different slope-limiter operators have been proposed in the literature. A simple slope limiting operator is introduced in [23, 25, 27] for scalar equations, assuming that spurious oscillations are present in the numerical solution $\mathbf{U}_h$ only if they are present in its linear component $\mathbf{U}_1$, which is its L^2-projection into the space of piecewise linear functions. Actually, under this hypothesis, the operator $\Lambda\Pi_h$ is defined only for piecewise linear functions. The limiting is performed on each element K by replacing the

linear component of the solution, i.e. $\mathbf{U}_{K,1}$, with its limited version $\mathbf{U}_{K,1}^{\lim}$ using the differences of the means between adjacent elements. In the one-dimensional case we obtain

$$\mathbf{U}_{i,1}^{\lim} = minmod\left(\mathbf{U}_{i,1}, \frac{\mathbf{U}_{i+1,0} - \mathbf{U}_{i,0}}{h}, \frac{\mathbf{U}_{i,0} - \mathbf{U}_{i-1,0}}{h}\right). \tag{5.14}$$

If spurious oscillations are present in the linear part of the solution, the higher order part of the numerical approximation is chopped off, thus reducing the solution accuracy near discontinuities.

Several extensions of the original method have been proposed in the literature. The extension to the multidimensional case is described in [27]. For systems of conservation laws, the limiting can be performed either on the conserved quantities or on the characteristic variables [24,27]. Finally, a slope-limiting technique acting on high order solution moments have been proposed in [9].

5.2 Implicit time-advancing schemes

Implicit schemes treat implicitly the operator $\mathcal{L}_h$, thus meaning that it is evaluated on the solution at time step $n+1$ when computing $\mathbf{U}^{n+1}$. If the operator $\mathcal{L}_h$ is non linear, some iterative algorithm has to be applied to solve the resulting non linear system of equations, e.g. Newton or quasi-Newton methods [106].

5.2.1 Time averaged implicit scheme

The time averaged implicit method, also known as off-centred Crank-Nicolson scheme or θ-method, was originally introduced in [29]:

$$\mathbf{U}^{n+1} - \theta\Delta t\mathcal{L}_h(\mathbf{U}^{n+1}) = (1-\theta)\Delta\mathcal{L}_h(\mathbf{U}^n) + \mathbf{U}^n \tag{5.15}$$

with parameter $\theta \in [0,1]$. The scheme is unconditionally stable when applied to linear problems with $\theta \geq 1/2$ and formally second order accurate with $\theta = 1/2$. In particular, for $\theta = 1$, the backward or implicit Euler time-advancing scheme is recovered.

Higher orders of accuracy can be achieved by applying Adams-Moulton, Backward Differentiation Formulas (BDF) or Implicit Runge-Kutta methods [106].

5.3 Time discretization of multiphase gas–particle equations

Let us consider the set of multiphase equations (2.13a), (2.13b), (2.14a), (2.14b), (2.16a) and (2.16b) and, for the sake of simplicity, let us consider only one class of solid particles. The system of ordinary differential equations, resulting from the spatial discretizations introduced in the previous chapters, can be written as

$$\frac{d\mathbf{U}}{dt} = \mathcal{L}_h(\mathbf{U}), \tag{5.16}$$

with

$$\mathbf{U} = \begin{bmatrix} \epsilon_g \rho_g \\ \epsilon_g \rho_g \mathbf{v}_g \\ \epsilon_g \rho_g E_g \\ \epsilon_s \rho_s \\ \epsilon_s \rho_s \mathbf{v}_s \\ \epsilon_s \rho_s E_s \end{bmatrix}. \tag{5.17}$$

or, as an alternative, with

$$\mathbf{U} = \begin{bmatrix} \epsilon_g \rho_g \\ \epsilon_g \rho_g \mathbf{v}_g \\ \epsilon_g \rho_g h_g \\ \epsilon_s \rho_s \\ \epsilon_s \rho_s \mathbf{v}_s \\ \epsilon_s \rho_s h_s \end{bmatrix}. \tag{5.18}$$

The operator $\mathcal{L}_h$ depends on the adopted spatial discretization. The system (5.16) can be solved with the explicit and implicit methods introduced in the previous sections.

5.3.1 Semi-implicit scheme for multiphase equations

Let us consider the system (5.16) with the unknows (5.18). The operator $\mathcal{L}_h(\mathbf{U})$ is first split in an implicit and an explicit component as follows

$$\frac{d\mathbf{U}}{dt} = \mathcal{L}_h(\mathbf{U}) = \mathcal{L}_h^{impl}(\mathbf{U}) + \mathcal{L}_h^{expl}(\mathbf{U}), \tag{5.19}$$

where $\mathcal{L}_h^{impl}(\mathbf{U})$ and $\mathcal{L}_h^{expl}(\mathbf{U})$ are the spatial approximations of the following continuous operators

$$\mathcal{L}^{impl}(\mathbf{U}) = \begin{bmatrix} -\nabla \cdot (\epsilon_g \rho_g \mathbf{v}_g) \\ -\omega_g \nabla P_g + \epsilon_g \rho_g \mathbf{g} + D_{g,s}(\mathbf{v}_s - \mathbf{v}_g) \\ Q_s(T_s - T_g) \\ -\nabla \cdot (\epsilon_s \rho_s \mathbf{v}_s) \\ -\omega_s \nabla P_g + \epsilon_s \rho_s \mathbf{g} + D_{g,s}(\mathbf{v}_g - \mathbf{v}_s) \\ Q_s(T_g - T_s) \end{bmatrix}. \tag{5.20}$$

and

$$\mathcal{L}^{expl}(\mathbf{U}) = \begin{bmatrix} 0 \\ -\nabla \cdot (\epsilon_g \rho_g \mathbf{v}_g \mathbf{v}_g) + \nabla \cdot \mathbf{T}_g \\ -\nabla \cdot (\epsilon_g \rho_g h_g \mathbf{v}_g) + \epsilon_g \left(\frac{\partial P_g}{\partial t} + \mathbf{v}_g \cdot \nabla P_g \right) + \nabla \cdot (k_g \epsilon_g T_g) \\ 0 \\ -\nabla \cdot (\epsilon_s \rho_s \mathbf{v}_s \mathbf{v}_s) + \nabla \cdot \mathbf{T}_s \\ -\nabla \cdot (\epsilon_s \rho_s h_s \mathbf{v}_s) + \nabla \cdot (k_s \epsilon_s T_s) \end{bmatrix}. \tag{5.21}$$

By applying the method (5.15) with time step Δt to the implicit operator $\mathcal{L}_h^{impl}(\mathbf{U})$ in system (5.19) we obtain

$$\mathbf{U}^{n+1} - \theta\Delta t\ \mathcal{L}_h^{impl}(\mathbf{U}^{n+1}) = \mathbf{U}^n + (1-\theta)\Delta t\ \mathcal{L}_h^{impl}(\mathbf{U}^n) + \Delta t\ \mathcal{L}_h^{expl}(\mathbf{U}^n). \quad (5.22)$$

Notice that the implicit term makes the equations nonlinearly coupled through the pressure gradient. Thus, an iterative algorithm has to be applied to compute the solution at each time step. One example is the implicit multifield (IMF) method, originally introduced in [63] in a version based on the implicit Euler method and extended here to the time averaged implicit method to increase accuracy. The IMF procedure consists in the iterative correction of the pressure until mass conservation is satisfied up to a residual. The iterative algorithm can be syntetized as follows

At each time step $n = 0, \ldots, N_T$

(1) compute temperature-dependent coefficients of the gas phase, e.g. viscosity, specific heat;

(2) compute the interphase coefficients $D_{g,s}$ *and* Q_s *and the explicit terms in (5.19);*

(3) solve the coupled continuity and momentum equations iteratively by the approximate Newton method to update velocity fields, pressure and volumetric fractions;

(4) compute gas mass fractions by solving the linear transport equations;

(5) solve the energy equations, which are linear in the temperatures and decoupled from the continuity and momentum equations.

Observe that, since the energy equations are solved explicitly after the solution of the momentum and continuity equations, the temperatures are kept constant during the iterative procedure. The effect of the temperature variation on the gas pressure and density are deferred to the next time step computation.

In this work, this implicit time advancing scheme is applied in the framework of the finite volume spatial discretization presented in Chapter 3.

5.3.2 Explicit scheme for multiphase equations

Let us consider the set of multiphase equations (5.16) with the unknowns (5.17). The system of ordinary differential equations derived from either a finite volume or a discontinuous Galerkin spatial approximation cannot be solved with a fully explicit time advancing scheme, due to the presence of the interphase coupling terms. As discussed in [63] and in Section 2.6, drag and heat exchange terms in disperse flows can be large, because of the physical coupling between the two phases. To guarantee the coupling among the fields also in the numerical solution, an implicit coupling between gas and particles fields has to be imposed, i.e. between gas and particles velocities and between gas and particles energies. This coupling is obtained by treating implicitly the interphase exchange terms.

Let us consider the following decomposition of the operator $\mathcal{L}_h(\mathbf{U})$:

$$\frac{d\mathbf{U}}{dt} = \mathcal{L}_h(\mathbf{U}) = \mathcal{L}_h^{impl}(\mathbf{U}) + \mathcal{L}_h^{expl}(\mathbf{U}), \quad (5.23)$$

with

$$\mathcal{L}^{impl}(\mathbf{U}) = \begin{bmatrix} 0 \\ D_{g,s}(\mathbf{v}_s - \mathbf{v}_g) \\ Q_s(T_s - T_g) \\ 0 \\ D_{g,s}(\mathbf{v}_g - \mathbf{v}_s) \\ Q_s(T_g - T_s) \end{bmatrix}. \tag{5.24}$$

and

$$\mathcal{L}^{expl}(\mathbf{U}) = \begin{bmatrix} -\nabla \cdot (\epsilon_g \rho_g \mathbf{v}_g) \\ -\nabla \cdot (\epsilon_g \rho_g \mathbf{v}_g \mathbf{v}_g) - \omega_g \nabla P_g + \epsilon_g \rho_g \mathbf{g} + \nabla \cdot \mathbf{T}_g \\ -\nabla \cdot (\epsilon_g \rho_g E_g \mathbf{v}_g) - \nabla \cdot (P_g \mathbf{v}_g) + \nabla \cdot (k_g \epsilon_g T_g) \\ -\nabla \cdot (\epsilon_s \rho_s \mathbf{v}_s) \\ -\nabla \cdot (\epsilon_s \rho_s \mathbf{v}_s \mathbf{v}_s) - \omega_s \nabla P_g + \epsilon_s \rho_s \mathbf{g} + \nabla \cdot \mathbf{T}_s \\ -\nabla \cdot (\epsilon_s \rho_s E_s \mathbf{v}_s) + \nabla \cdot (k_g \epsilon_g T_g) \end{bmatrix}. \tag{5.25}$$

The semi-discrete problem is solved by applying an operator splitting technique, i.e. Lie-Trotter splitting, and computing an intermediate solution $\mathbf{U}^*$ as follows

$$\frac{d\mathbf{U}^*}{dt} = \mathcal{L}_h^{expl}(\mathbf{U}^*) \tag{5.26a}$$

$$\frac{d\mathbf{U}}{dt} = \mathcal{L}_h^{impl}(\mathbf{U}) \tag{5.26b}$$

This simple operator splitting approach is first order accurate and it is exact when the operators $\mathcal{L}_h^{expl}$ and $\mathcal{L}_h^{impl}$ commute. As an alternative, the first order additive splitting or the second order Strang splitting can be considered [126]. By applying the explicit Runge-Kutta time advancing scheme (5.8) on the explicit part of problem (5.26a) and the implicit time advancing scheme (5.15) on the implicit part (5.26b), we obtain the following fully-discrete problem:

$$\begin{aligned} \mathbf{U}^* = \mathbf{U}^{(m)} \quad \text{with } \mathbf{U}^{(i)} &= \sum_{l=0}^{i-1} \alpha_{il} \mathbf{U}^{(l)} + \beta_{il} \Delta t \, \mathcal{L}_h(\mathbf{U}^{(l)}), \\ \mathbf{U}^{(0)} &= \mathbf{U}^n, \ \forall i = 1, \ldots, m, \end{aligned} \tag{5.27}$$

$$\mathbf{U}^{n+1} - \theta \Delta t \, \mathcal{L}_h^{impl}(\mathbf{U}^{n+1}) = \mathbf{U}^* + (1-\theta) \Delta t \, \mathcal{L}_h^{impl}(\mathbf{U}^*).$$

Notice in (5.24) that, if the interphase coefficients and the gas properties (i.e. viscosity and specific heat) are considered constant at each time step and they are computed using the solution at the previous step, the operator $\mathcal{L}_h^{impl}$ is linear with respect to the velocities and the temperatures, but not with respect to the conserved variables $\mathbf{U}$. In

this work, the operator $\mathcal{L}^{impl}$ is linearized as follows:

$$\mathcal{L}_L^{impl}(\mathbf{U}) = \begin{bmatrix} 0 \\ \frac{D^*_{g,s}}{\epsilon^*_s\rho^*_s}\epsilon_s\rho_s\mathbf{v}_s - \frac{D^*_{g,s}}{\epsilon^*_g\rho^*_g}\epsilon_g\rho_g\mathbf{v}_g \\ \frac{Q^*_s}{\epsilon^*_s\rho^*_s c^*_{v,s}}\left(\epsilon_s\rho_s E_s - \frac{1}{2}\epsilon^*_s\rho^*_s|\mathbf{v}^*_s|^2\right) - \frac{Q^*_s}{\epsilon^*_g\rho^*_g c^*_{v,g}}\left(\epsilon_g\rho_g E_g + \frac{1}{2}\epsilon^*_g\rho^*_g|\mathbf{v}^*_g|^2\right) \\ 0 \\ \frac{D^*_{g,s}}{\epsilon^*_g\rho^*_g}\epsilon_g\rho_g\mathbf{v}_g - \frac{D^*_{g,s}}{\epsilon^*_s\rho^*_s}\epsilon_s\rho_s\mathbf{v}_s \\ \frac{Q^*_s}{\epsilon^*_g\rho^*_g c^*_{v,g}}\left(\epsilon_g\rho_g E_g - \frac{1}{2}\epsilon^*_g\rho^*_g|\mathbf{v}^*_g|^2\right) - \frac{Q^*_s}{\epsilon^*_s\rho^*_s c^*_{v,s}}\left(\epsilon_s\rho_s E_s + \frac{1}{2}\epsilon^*_s\rho^*_s|\mathbf{v}^*_s|^2\right) \end{bmatrix}.$$

Observe that in the implicit step (5.26b) of the operator splitting procedure the momentum equations are decoupled from the energy equations. Moreover, thanks to the simple linearization approach, the two subsystems for the momentum and the energy decouple and can be solved without any iterative procedure.

If the set of unknowns (5.18) is considered, the linearization step simplifies as follows:

$$\mathcal{L}_L^{impl}(\mathbf{U}) = \begin{bmatrix} 0 \\ \frac{D^*_{g,s}}{\epsilon^*_s\rho^*_s}\epsilon_s\rho_s\mathbf{v}_s - \frac{D^*_{g,s}}{\epsilon^*_g\rho^*_g}\epsilon_g\rho_g\mathbf{v}_g \\ \frac{Q^*_s}{\epsilon^*_s\rho^*_s c^*_{p,s}}\epsilon_s\rho_s h_s - \frac{Q^*_s}{\epsilon^*_g\rho^*_g c^*_{p,g}}\epsilon_g\rho_g h_g \\ 0 \\ \frac{D^*_{g,s}}{\epsilon^*_g\rho^*_g}\epsilon_g\rho_g\mathbf{v}_g - \frac{D^*_{g,s}}{\epsilon^*_s\rho^*_s}\epsilon_s\rho_s\mathbf{v}_s \\ \frac{Q^*_s}{\epsilon^*_g\rho^*_g c^*_{p,g}}\epsilon_g\rho_g h_g - \frac{Q^*_s}{\epsilon^*_s\rho^*_s c^*_{p,s}}\epsilon_s\rho_s h_s \end{bmatrix}.$$

More complex linearized forms for the operator $\mathcal{L}^{impl}(\mathbf{U})$ can be introduced as an alternative. In this work, however, only the presented expression for $\mathcal{L}_L^{impl}(\mathbf{U})$ will be tested.

CHAPTER 6

Validation of the finite volume numerical model

In this chapter, the numerical validation of the Finite Volume approximation of the multiphase gas–particle conservation equations introduced in Chapter 2 and Chapter 3 is presented. The numerical model presented in Chapter 2 has been originally implemented in the Pyroclastic Dispersal Analysis Code, a Fortran code developed at the INGV (Istituto Nazionale di Geofisica e Vulcanologia) of Pisa and has been applied widely to simulate realistic eruptive scenarios [42–45, 91, 92]. In the present work, the original Finite Volume method presented in [42] has been improved by introducing a fully multidimensional second order spatial and time discretization, as described in Chapters 3 and 5. In the following sections, the improved FV scheme is tested on a number of classical benchmarks, in order to assess the accuracy in the computation of multiphase flow in both supersonic and subsonic regimes. The aim is to provide a further validation of the FV approximation of the multiphase gas–particle equations, showing that analogous results reported in the literature can be reproduced.

6.1 Supersonic regimes

In supersonic regimes, i.e. $Ma > 1$, we expect that the conservative formulation of the multiphase equations will allow to obtain an accurate computation of the shock wave position and speed. Thus, in this section, we focus on the supersonic jet problem, for which a discontinuous solution is foreseen, and we check if the numerical method is able to reproduce correctly the expected dynamics. In particular, we consider the *underexpanded jet* test problem. We consider a fluid which is ejected from a nozzle into the atmosphere. The fluid properties at the inlet are considered constant in time. Nozzle conditions are underexpanded, that is gas pressure at the inlet is larger than the ambient one. It has been proven theoretically and experimentally that nozzles with

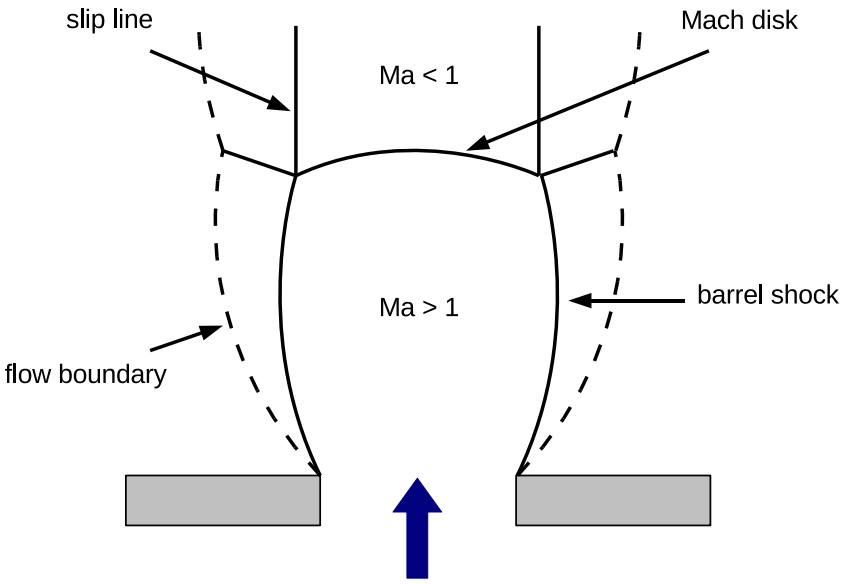

Figure 6.1: Sketch of the fluid dynamics in underexpanded jets. The overpressured fluid exits from the nozzle, expands and accelerates in the atmosphere. Supersonic velocities are reached in the expansion region ($Ma > 1$). Expansion waves that forms at the nozzle exit are reflected into compression waves at the flow boundary. Compression waves coalesce and form a barrel shock and a normal shock wave (Mach disk). The fluid crosses the normal shock, compresses and decelerates to subsonic speeds ($Ma < 1$) in the core of the jet. A slip line divides the slowly moving flow from the surrounding supersonic shell.

supersonic vertical velocity and gas pressure greater than the atmospheric one result in a rapid expansion and acceleration of the fluid to high Mach numbers, see e.g. [84, 98]. A series of expansion waves form at the vent exit (Prandtl-Meyer expansion), which are reflected as compression waves at the jet flow boundary. The compression waves coalesce to form a barrel shock and a standing normal shock wave (Mach disk), across which the vertical velocity is reduced and the pressure in the core of the jet increases. The fluid that crosses the Mack disk is rapidly compressed and decelerated to subsonic speeds, as shown in Figure 6.1. Above the Mach disk, the fluid moves slowly in the core of the jet and it is surrounded by a supersonic moving shell, with a tangential slip-line, which is eventually torn by turbulence. As discussed in Chapter 2, Reynolds and Prandtl numbers in the jet problem are large, so viscous term are neglected in the simulation proposed in the following sections. Comparison of the results obtained with the viscous and the inviscid model will demonstrate that, in the development of the jet above the inlet, the dynamics is controlled by inertial, pressure and drag terms (see results in Section 6.1.3).

In the following sections, the laboratory scale numerical results will be compared with experimental results and empirical relationships proposed in the literature. On larger spatial scales, such as the ones of volcanic phenomena, results obtained with the proposed FV approximation will be compared with numerical results proposed in the literature and obtained with different numerical approaches. Numerical validation is carried out for both homogeneous and multiphase test cases.

6.1.1 Homogeneous jet on laboratory scale

We consider an homogeneous fluid (dry air with standard chemical components), and we impose underexpanded sonic conditions at the inlet, as shown in Table 6.1. Four different values of the inlet pressure are considered, correspondig to four different values of the jump in the pressures, i.e. $K = \frac{P_v}{P_{atm}} = 2, 5, 10, 20$.

We assume that the problem is axisymmetric and we solve the multiphase equations in cylindrical coordinates. The computational domain is a box of size 0.1 m $\times 0.2$ m, whose left side coincides with the axis of the vent. The side and the bottom boundaries of the axisymmetric domain are impermeable and stress free. Two uniform meshes of 160×320 ($\Delta x = \Delta z = 6.25 \times 10^{-4}$ m) and 500×1000 ($\Delta x = \Delta z = 2 \times 10^{-4}$ m) cells have been employed, with time steps of $\Delta t = 10^{-7}$ s and $\Delta t = 5 \times 10^{-8}$ s, respectively. Simulations are carried out using a first order Upwind FV spatial discretization and its second order extension by applying the Corner Transport Upwind method. Time advancing is done by means of the semi-implicit scheme proposed in Section 5.3.1.

In order to assess the accuracy of the numerical scheme, the height of the Mach disk forming in the jet is evaluated and compared with the empirical law proposed in [84]

$$h_{Ma} = 0.69\, D_v\, Ma_v\, \sqrt{\gamma K}, \tag{6.1}$$

which relates the equilibrium position of the normal shock wave with the gas inlet conditions.

In Figure 6.2, the results obtained in terms of vertical velocity and temperature are shown for the case $K = 5$ at time $t = 10^{-3}$ s, when the Mach disk has reached its steady state position. The profiles of gas pressure along the axis of the jet are shown in Figure 6.3 for the four values of K. We observe how the numerical method is able to reproduce the dynamics of the underexpanded jet and to provide a good estimate of the position of the Mach disk, that fits with experimental results. In particular, better estimates are obtained with second order methods, as shown in Figure 6.4.

Numerical simulations have been repeated with different meshes, in order to check the dependence of the results on the grid resolution. Results in Figures 6.5 and 6.6 show the axial profiles of gas pressure for $K = 5$ obtained with $\Delta x = 1, 0.625, 0.5, 0.25, 0.2$ mm with second order FV approximation and the estimates of the Mach disk height, respectively. We observe that the Mach disk height estimate improves with grid resolution and that the numerical method is able to provide a reliable estimate of the Mach disk position even with coarse meshes.

Parameter		**Units**
D_{v}	0.01	m
K	2, 5, 10, 20	
P_{atm}	101325	Pa
T_{atm}	298	K
w_{v}	346	m/s
T_{v}	298	K
Ma_{v}	1.0	

Table 6.1: Inlet conditions for the homogeneous underexpanded jet at the laboratory scale.

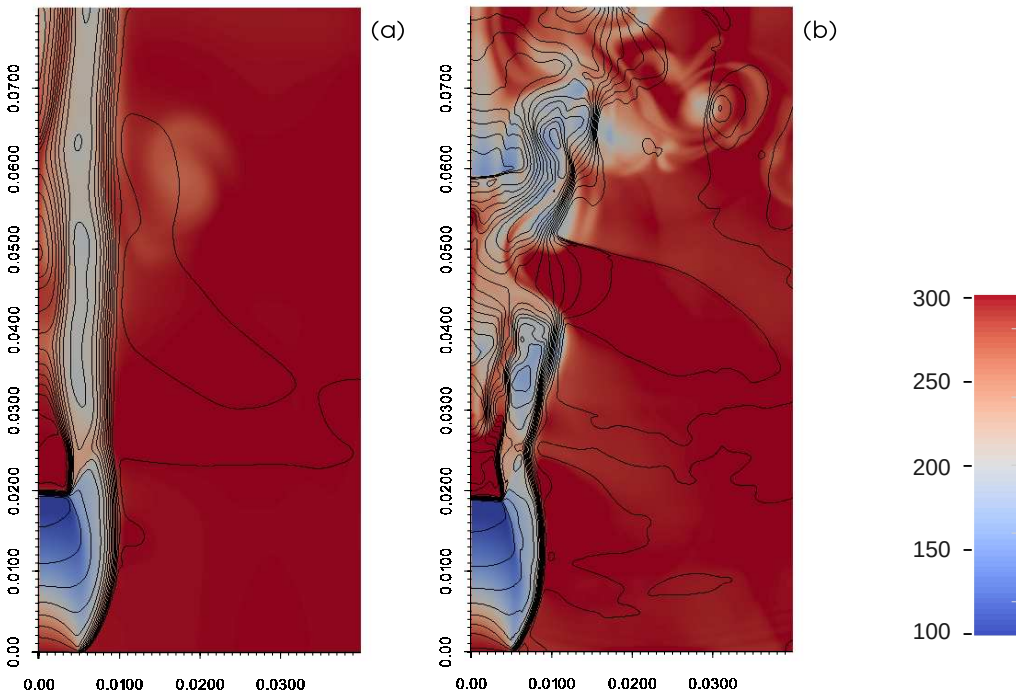

Figure 6.2: Homogeneous jet on laboratory scale. Temperature field from 100 to 300 K at $t = 10^{-3}$ s and isolines of gas vertical velocity [0:50:700] m/s, obtained with $K = 5$ on a 500×1000 mesh. Comparison between **(a)** first order upwind FV method and **(b)** second order FV method with Corner Transport Upwind scheme for advective fluxes.

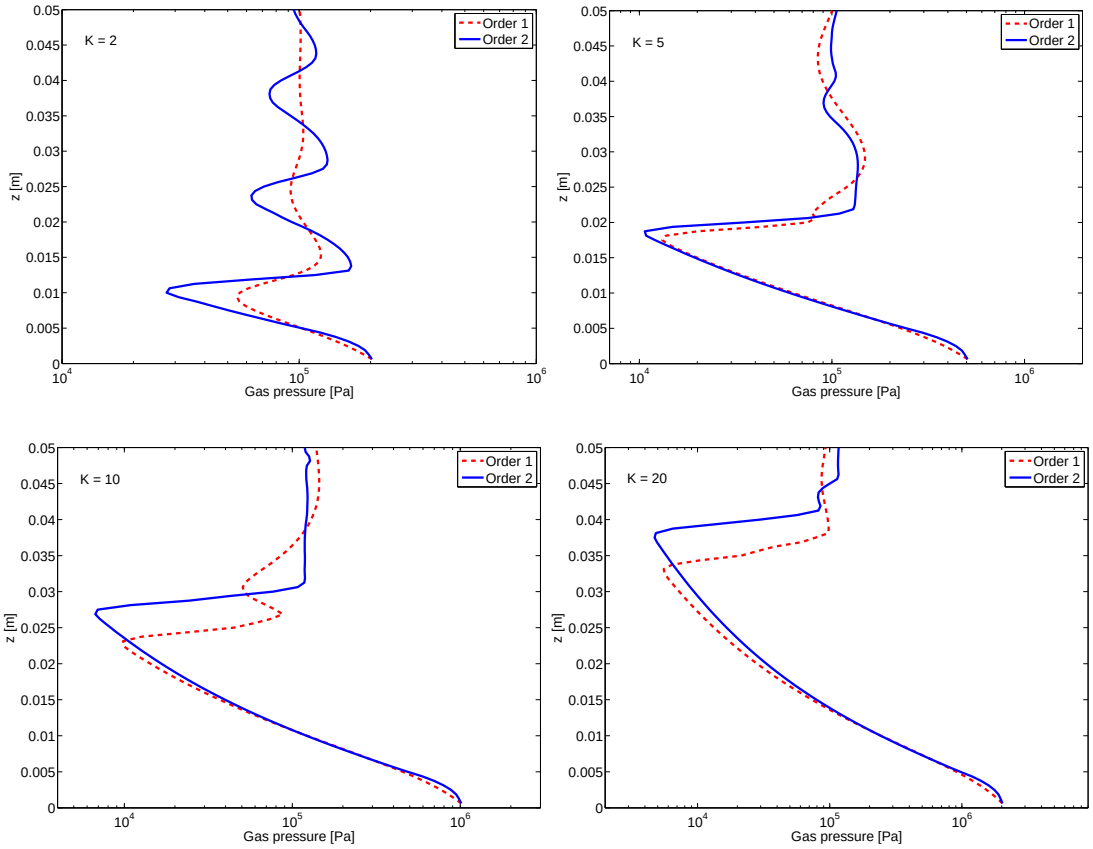

Figure 6.3: Homogeneous jet on laboratory scale. Gas pressure at $t = 2 \times 10^{-3}$ s. Axial profile for different values of the nozzle overpressure $K = 2, 5, 10, 20$ computed on a 160×320 mesh. Comparison between first order upwind FV method (Order 1) and second order FV method with Corner Transport Upwind scheme for advective fluxes (Order 2).

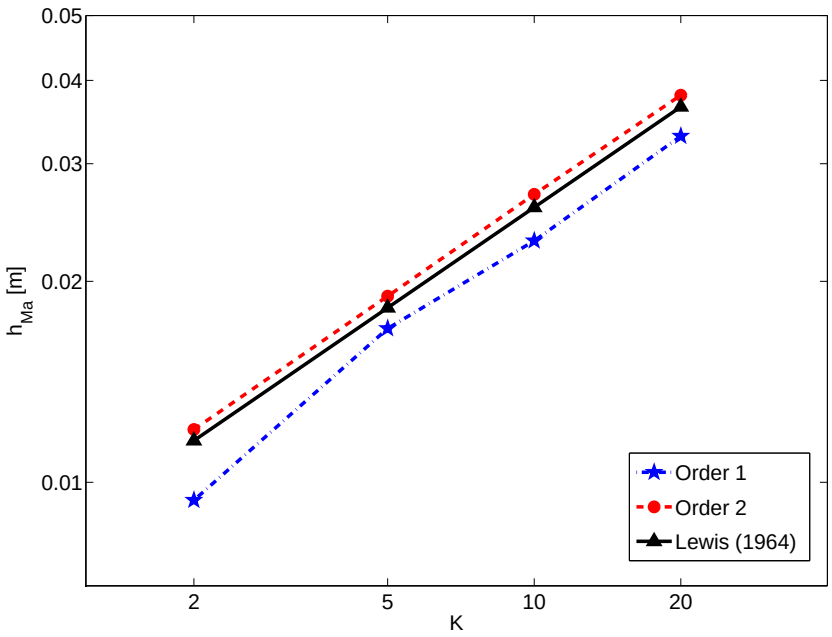

Figure 6.4: Homogeneous jet on laboratory scale. Comparison between experimental and numerical results in terms of Mach disk height h_{Ma} for different values of the nozzle overpressure $K = 2, 5, 10, 20$. The results obtained by Lewis and Carlson [84] are compared with numerical simulation applying first order upwind FV method with implicit time advancing scheme (Order 1) and second order Corner Transport Upwind FV method with θ-method time discretization (Order 2).

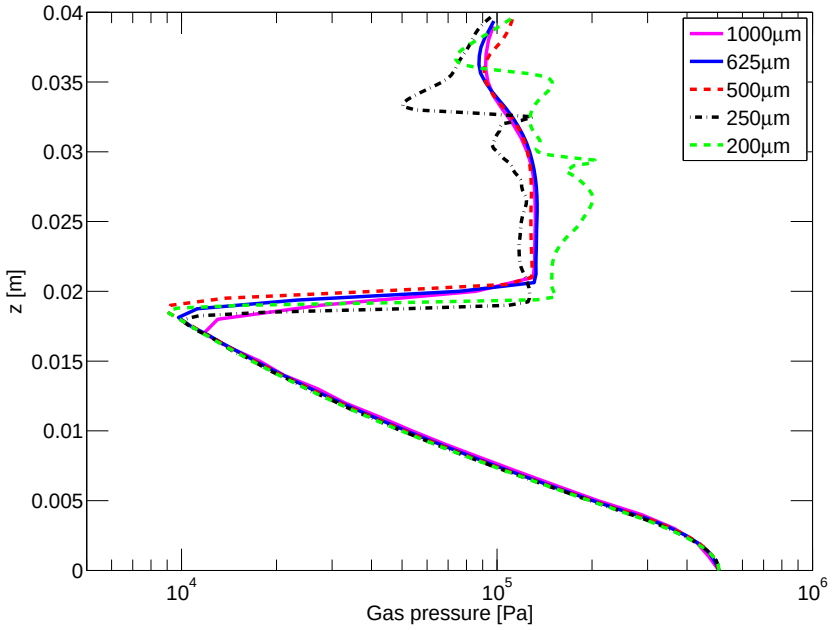

Figure 6.5: Homogeneous jet on laboratory scale. Gas pressure at $t = 2 \times 10^{-3}$ s. Axial profiles obtained with second order Corner Transport Upwind FV method and θ-method time discretization. Comparison between different grid resolutions $\Delta x = 1000, 625, 500, 250, 200$ μm.

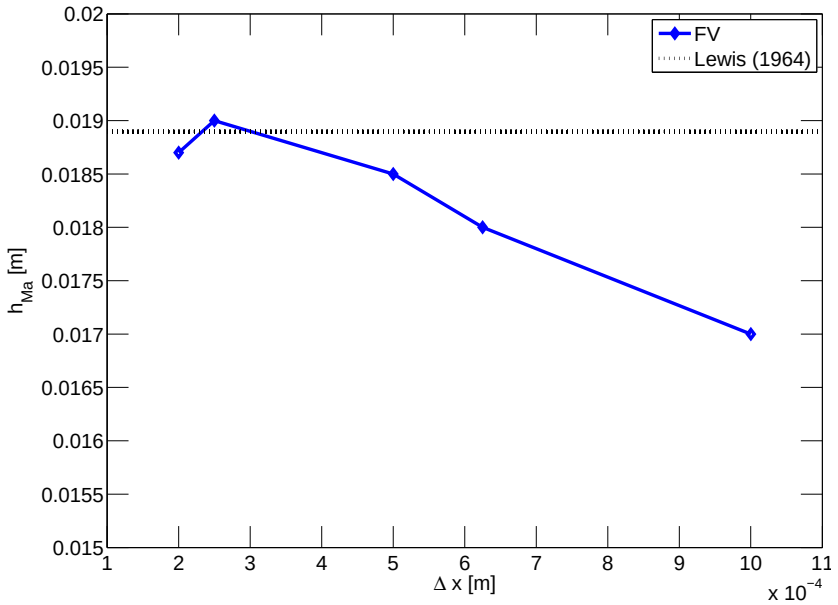

Figure 6.6: Homogeneous jet on laboratory scale. Estimate of the Mach disk height h_{Ma} obtained with second order Corner Transport Upwind FV method and θ-method time discretization with different grid resolution $\Delta x = 1000, 625, 500, 250, 200$ μm. Comparison between numerical results and theoretical estimate.

6.1.2 Multiphase jet on laboratory scale

When solid particles are added to the gas flow, new phenomena associated to kinetic and thermal non-equilibrium between the gas and particulate phases arise.

In this section, we consider a mixture of dry air and fine solid particles, with diameter equal to 10 μm and density equal to 2500 kg/m^3. Inlet flow parameters correspond to experimental and simulation conditions investigated by [124]. Gas and particle velocities are both equal to the speed of sound in the pure gas, whereas the overpressure of the gas phase is $K = 31$, producing supersonic underexpanded conditions at the inlet, as described in Table 6.2.

The computational domain is a box of size 0.15 m $\times 0.225$ m and, as in the previous test cases, the left side coincides with the axis of the vent, whereas the side and the bottom boundaries of the axisymmetric domain are impermeable and stress free. A non uniform mesh of 500×750 computational cells have been employed, with time step of $\Delta t = 2 \times 10^{-8}$ s. The maximum resolution is imposed above the inlet, where $\Delta x = \Delta z = 10^{-4}$ m. We consider different values of particle volume fractions ϵ_s at the inlet and we compare numerical results with experimental results in [124].

In Figure 6.7 we report the results of four different simulations of particle laden underexpanded jets with different particle concentrations. The gas phase expands radially as in the homogeneous case, thus increasing the final jet radius up to three times in correspondence to the Mach disk location.

On the other hand, as observed in laboratory [124], particles are almost unaffected by the rapid gas expansion and strongly decoupled from the gas phase, as expected from the dimensional analysis presented in Section 2.6.3. Particle trajectories remain nearly vertical, with some radial spreading which is almost independent of particle concen-

tration. In the expansion region, particles are only slightly and gradually accelerated by the gas phase (at most by 20 m/s, up to 368 m/s) where the Mach disk is located, and then slowly decelerated in the subsonic region, but they never reach an equilibrium condition with the gas phase. However, solid particles tend to deform the Mach disk, moving it towards the vent and making it as more concave as the particle loading increases. For initial particle volume fraction equal to 0.0005, the normal shock is located 14.5 mm from the inlet and the distance is reduced to 12.2 mm when $\epsilon_s = 0.004$. Moreover, increasing the particle loading, the expansion, the acceleration and the cooling of the gas phase are reduced, as shown in Figure 6.8. As regards particle distribution, the mixture density profile along the jet axis is not affected by the presence of the shock wave but remains almost constant and displays only a small reduction due to the radial spreading, that tends to increase with increasing particle loading, as observed also by [124].

6.1.3 Multiphase jet on volcanic scale

When studying physical processes on the natural scale of volcanic phenomena, it is not possible, or at least very difficult, to make direct comparisons with measurements and experimental results. Thus, to validate the numerical model on these spatial scales, we refer to numerical results on supersonic multiphase jets on the volcanic scale proposed in the literature. Most of them are based on the pseudogas assumption, in which mechanical and thermal equilibrium are assumed between the gas phase and solid particles. Under such assumption, Ogden et al. [97] described the eruptive mixture as an homogeneous pseudogas, characterized by average thermodynamic and rheologic properties. Two-dimensional numerical simulations of underexpanded volcanic jets were performed with CFDLib, a computational fluid dynamics library developed at Los Alamos National Laboratory, that uses a finite volume computational scheme with cell-centered state variables. CFDLib applies a variation of the Implicit Continuous-fluid Eulerian (ICE) method, proposed in [1] and [63], and a modified Godunov method [54] to solve shock waves.

Following [97], numerical simulations presented in this section are performed in absence of gravity, in order to focus on compressibility effects in the gas phase. Inlet conditions for numerical simulations are specified in Table 6.3. The mixture is composed by water vapor and solid particles that are injected in a standard atmosphere composed by dry air. We consider a single solid dispersed phase with particle diameter equal to 10 μm. Two different inlet pressure ratios of $K = 20$ (Case A) and $K = 5$

Parameter		**Units**
D_{v}	0.003	m
K	31	
w_v	347	m/s
T_v	300	K
ϵ_s	0.0005, 0.001, 0.002, 0.004	
d_s	10	μm
ρ_s	2500	kg/m^3

Table 6.2: Inlet conditions for the multiphase underexpanded jet on laboratory scale.

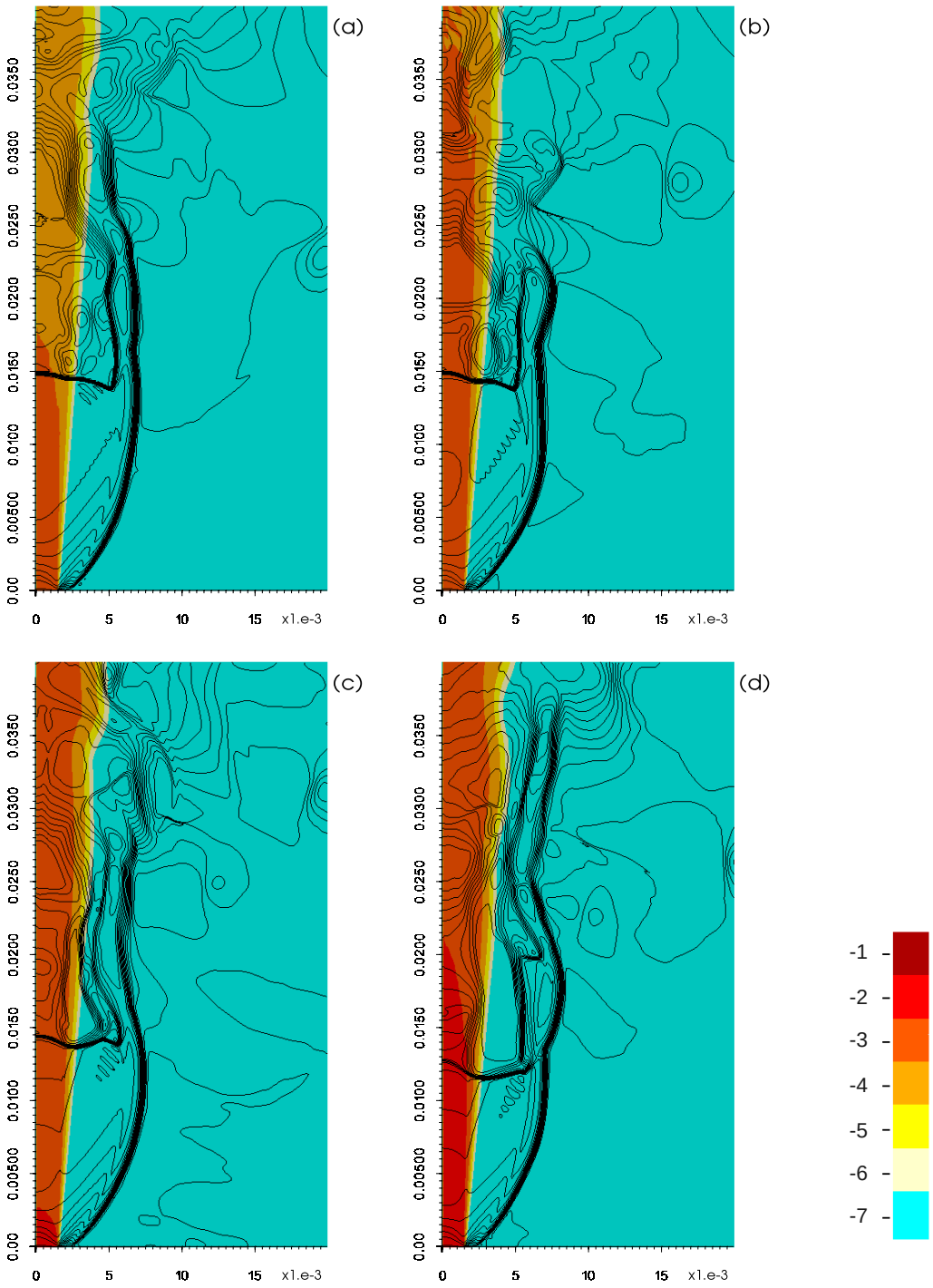

Figure 6.7: Multiphase jet on laboratory scale. Isolines of gas vertical velocity [0:50:750] m/s and logarithm to the base 10 of particle volume fraction from 10^{-7} to 10^{-1} at $t = 3 \times 10^{-4}$ s for different values of initial particle volume fraction: **(a)** $\epsilon_s = 0.0005$, **(b)** $\epsilon_s = 0.001$, **(c)** $\epsilon_s = 0.002$, **(d)** $\epsilon_s = 0.004$. Numerical results obtained with second order Corner Transport Upwind FV method and θ-method time discretization.

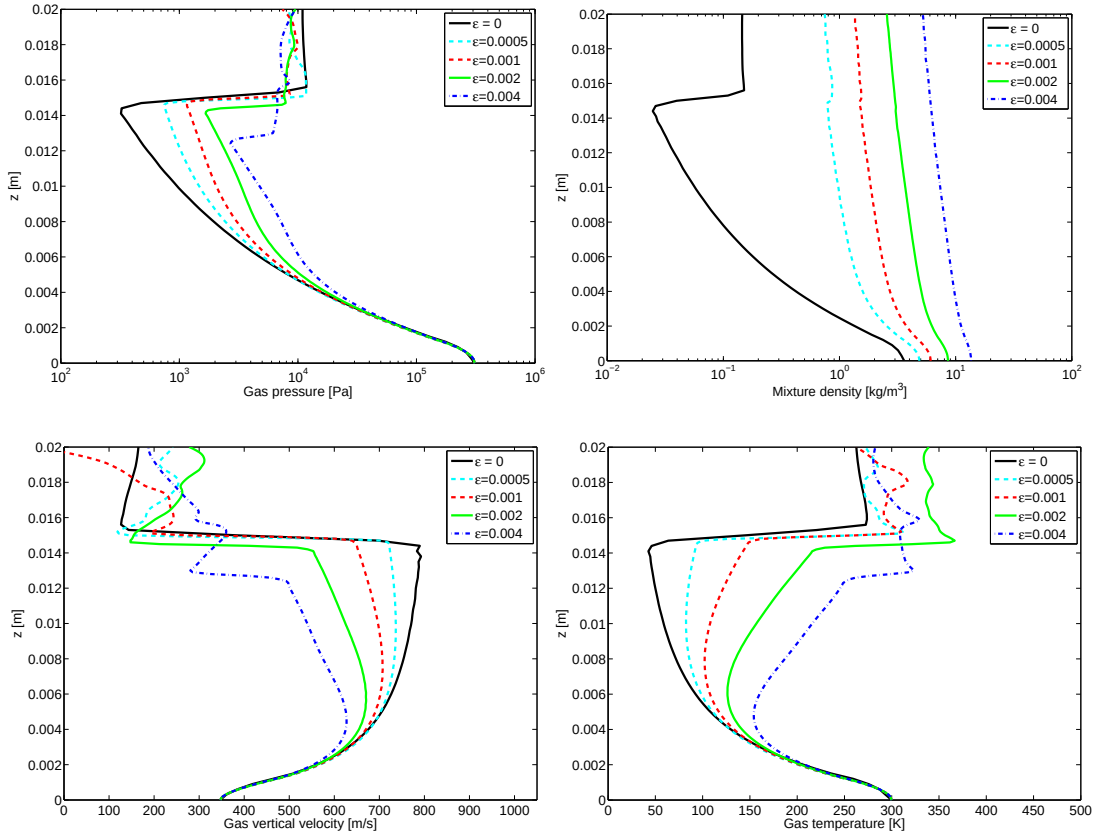

Figure 6.8: Multiphase jet on laboratory scale. Axial profile of gas pressure, mixture density, gas vertical velocity and gas temperature at $t = 3 \times 10^{-4}$ s. Comparison between homogeneous jet's profile ($\epsilon_s = 0$) and results obtained for different values of initial particle volume fraction: $\epsilon_s = 0.0005, 0.001, 0.002, 0.004$. Numerical results obtained with second order Corner Transport Upwind FV method and θ-method time discretization.

(Case B) are adopted.

In Case A, the computational domain is a box of size 800 m $\times 2400$ m and we use a uniform 200×600 mesh, with $\Delta x = \Delta z = 4$ m and a time step $\Delta t = 10^{-3}$ s. Figure 6.9 shows the vertical velocity field of the gas phase and the particle distribution above the vent after 20 s, when quasi-steady state conditions are reached. The simulation reproduces the expected behaviour of a supersonic underexpanded jet, displaying the barrel shock with a convex Mach disk, at about 320 m above the vent, which decelerates the mixture down to subsonic velocities (see Figure 6.9) and compresses the gas phase, so that the particle volumetric fraction increases by one order of magnitude across the discontinuity, as shown in Figure 6.9.

To better analyze the jet dynamics and to quantitatively compare our results with those by [97], we study the time-averaged vertical profiles along the axis of pressure, mixture density, gas vertical velocity and gas temperature, shown in Figure 6.10. The gas phase undergoes a rapid expansion from the initial pressure of 2.02×10^6 Pa to pressure values below atmospheric pressure. The minimum of the pressure is 9.1×10^3 Pa and it is reached at the height of 324 m above the vent. The ratio between Mach disk height and vent radius is 8.1 and the difference with respect to the corresponding result by [97] is around $1\,\%$. Through the normal compression shock, the gas phase returns to atmospheric value. During the expansion, as expected in supersonic flows, the gas phase accelerates up to 482 m/s and then through the shock it abruptly decelerates to a subsonic regime, with a vertical velocity around 33 m/s. During the expansion and acceleration phase, the gas decreases its temperature down to 1104 K and then warms up again by about 70 K through the Mach disk. Mixture density decreases by two orders of magnitude above the vent and then it increases by one order of magnitude through the shock. The difference in the Mach disk position with respect to the results reported in [97] is around $4\,\%$, whereas the difference in the maximum vertical velocity is around $2\,\%$.

In Case B we consider an inlet pressure ratio of $K = 5$ and a vent diameter of 20 m (Table 6.3) in order to maintain the sonic conditions at the vent. The computational domain is a box of size 200 m $\times 400$ m and we use a uniform 200×1000 mesh, with $\Delta x = 1$ m, $\Delta z = 0.4$ m and a time step $\Delta t = 5 \times 10^{-5}$ s. Figure 6.11 shows the gas vertical velocity and the particle volume fraction when the quasi-steady state configuration of the normal shock is achieved. The two-dimensional jet pattern and shape closely fit the results presented in Figure 3b by [97] and the results obtained with the multiphase model are thus in quantitative agreement with the result obtained by [97].

Parameter	Case A	Case B	Units
D_v	80	20	m
K	20	5	
w_v	150.3	150.3	m/s
T_v	1200	1200	K
ϵ_{s_1}	0.08784	0.021985	
d_{s_1}	10	10	μm
ρ_{s_1}	1000	1000	kg/m^3

Table 6.3: Inlet conditions of the inhomogeneous underexpanded jets on volcanic scale.

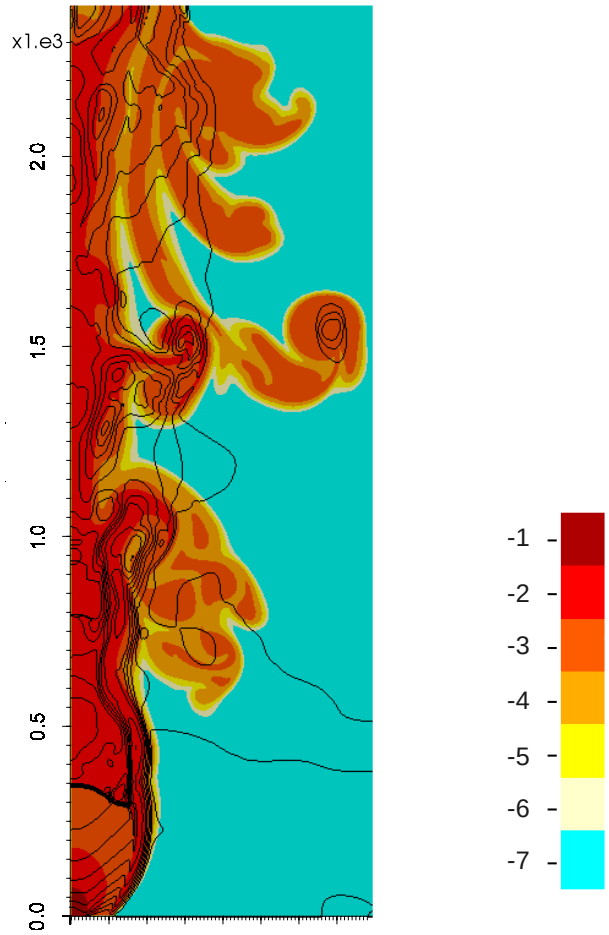

Figure 6.9: Multiphase jet on volcanic scale. Case A. $D_v = 80$ m, $K = 20$, $\epsilon_s = 0.08784$. Logarithm to the base 10 of particle volume fraction from 10^{-7} to 10^{-1} and isolines of gas vertical velocity [0:50:450] m/s. Numerical solution at $t = 20$ s obtained with second order Corner Transport Upwind FV method and θ-method time discretization.

In order to assess the importance of viscous effects on the underexpanded jet dynamics, test Case A has been repeated with the viscous multiphase model. A comparison between the viscous model and the inviscid model results is shown in Figure 6.13. It is possible to observe that, as expected from dimensional analysis, viscous terms do not affect the dynamics of the supersonic jet, and only small differences can be seen in the upper part of the jet.

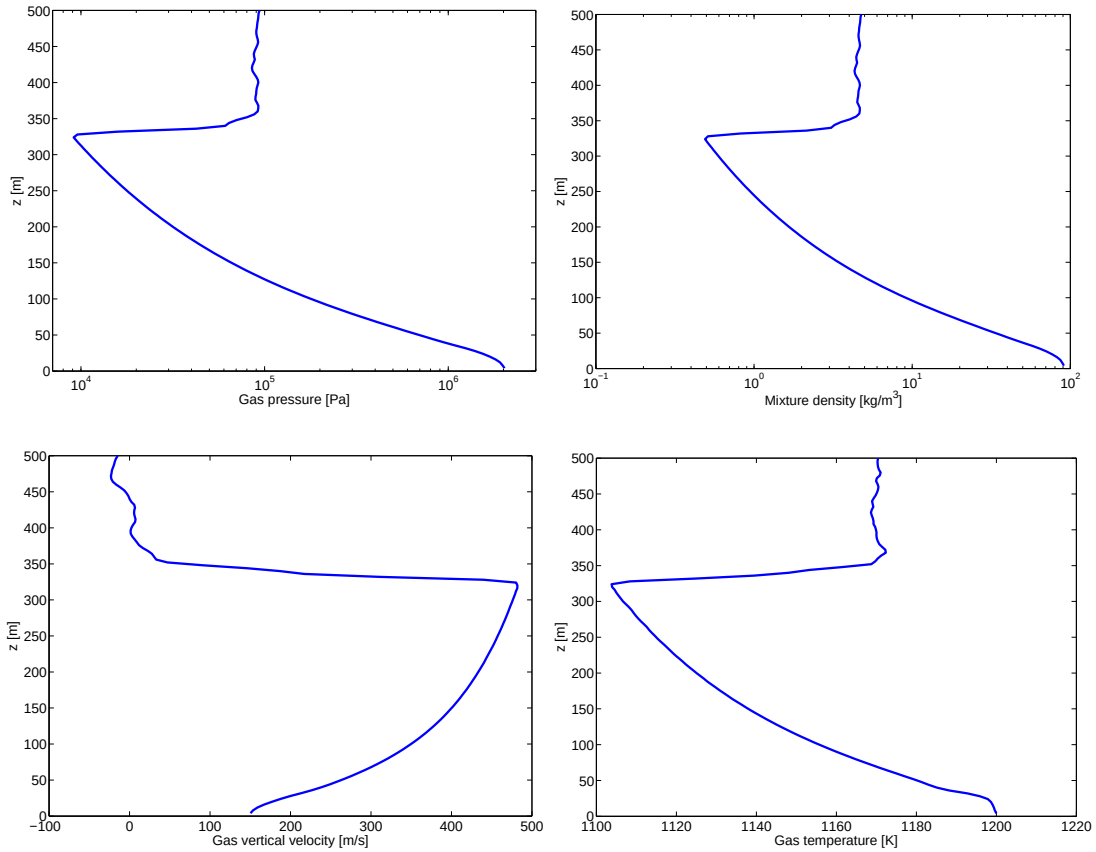

Figure 6.10: Multiphase jet on volcanic scale. Case A. $D_v = 80$ m, $K = 20$, $\epsilon_s = 0.08784$. Time-averaged axial profiles computed over the interval $[16, 20]$ s of gas pressure, mixture density, gas vertical velocity and gas temperature. Numerical solution obtained with second order Corner Transport Upwind FV method and θ-method time discretization.

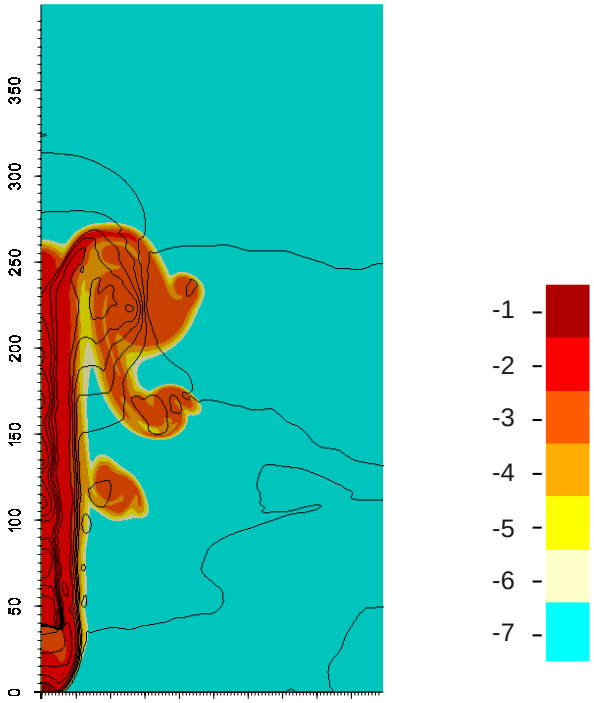

Figure 6.11: Multiphase jet on volcanic scale. Case B. $D_v = 20$ m, $K = 5$, $\epsilon_s = 0.021985$. Logarithm to the base 10 of particle volume fraction from 10^{-7} to 10^{-1} and isolines of gas vertical velocity [0:50:450] m/s. Numerical solution at $t = 2$ s obtained with second order Corner Transport Upwind FV method and θ-method time discretization.

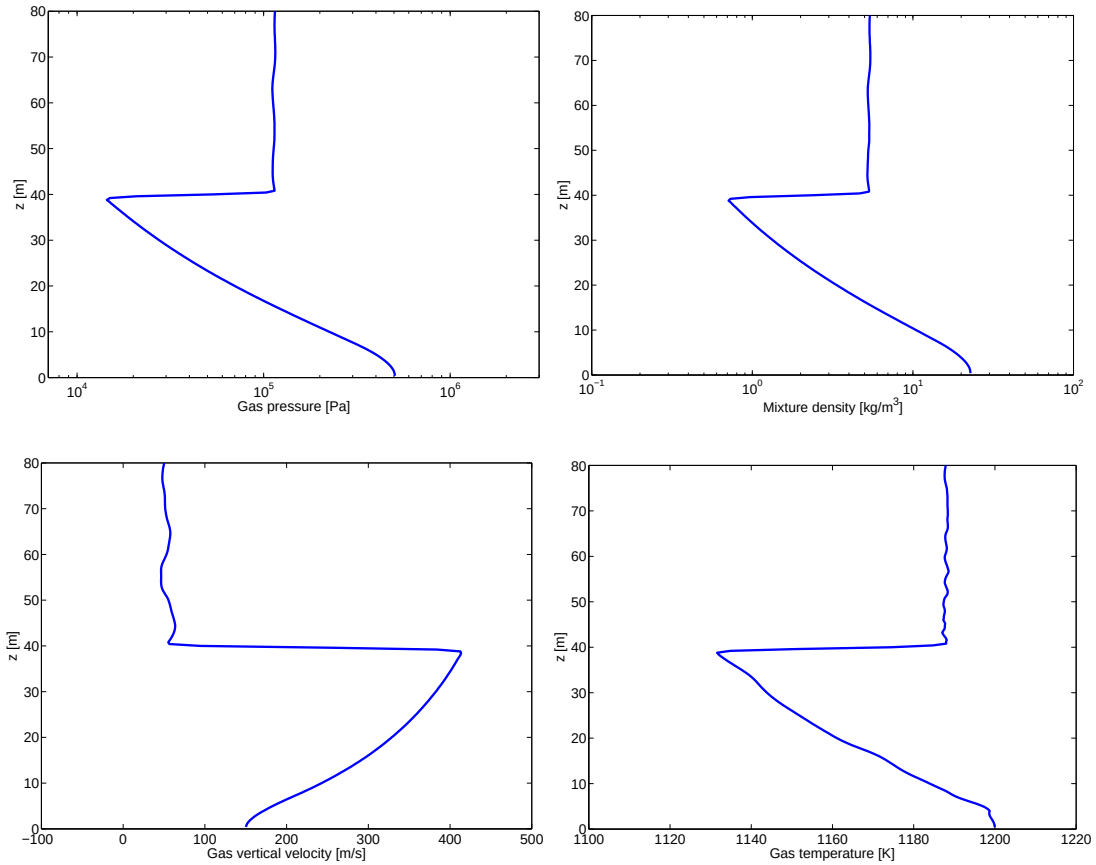

Figure 6.12: Multiphase jet on volcanic scale. Case B. $D_v = 20$ m, $K = 5$, $\epsilon_s = 0.021985$. Time-averaged axial profiles computed over the interval $[1.6, 2.0]$ s of gas pressure, mixture density, gas vertical velocity and gas temperature. Numerical solution obtained with second order Corner Transport Upwind FV method and θ-method time discretization.

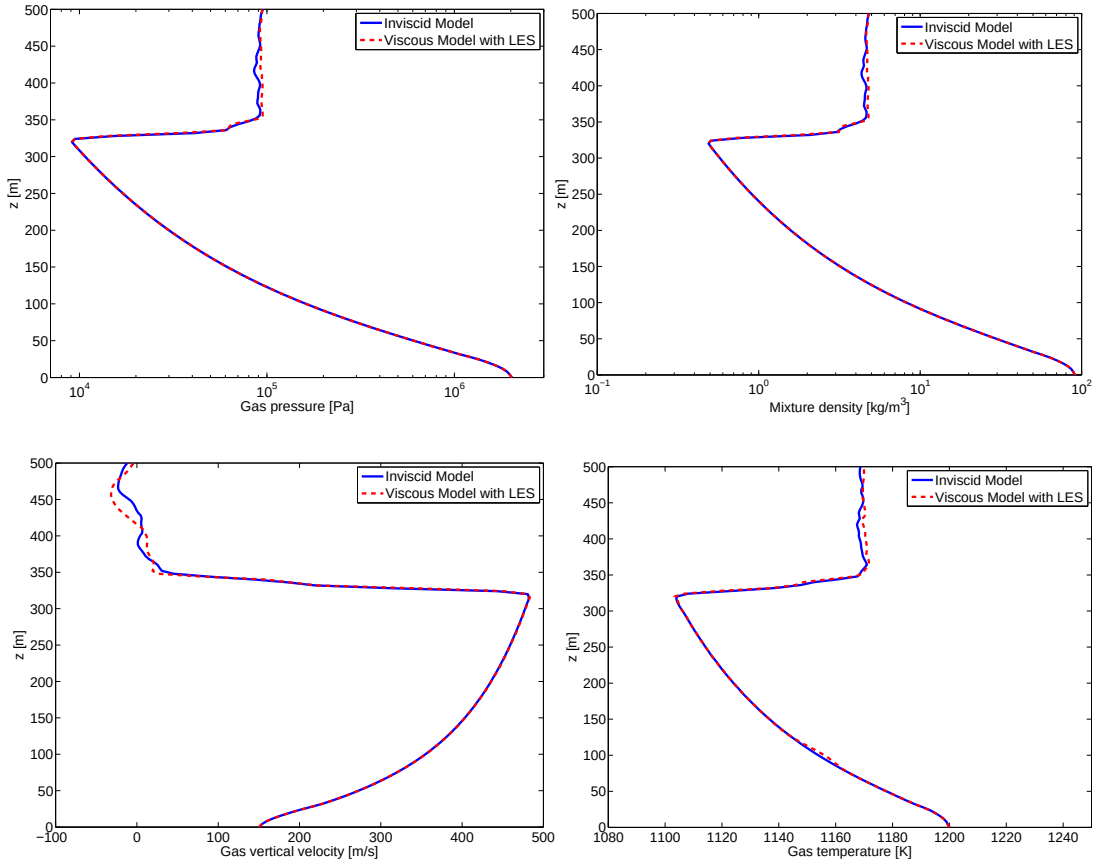

Figure 6.13: Multiphase jet on volcanic scale. Case A. $D_v = 80$ m, $K = 20$, $\epsilon_s = 0.08784$. Time-averaged axial profiles computed over the interval $[1.6, 2.0]$ s of gas pressure, mixture density, gas vertical velocity and gas temperature. Comparison between the Viscous Model with LES and the Inviscid Model. Numerical solution obtained with second order Corner Transport Upwind FV method and θ-method time discretization.

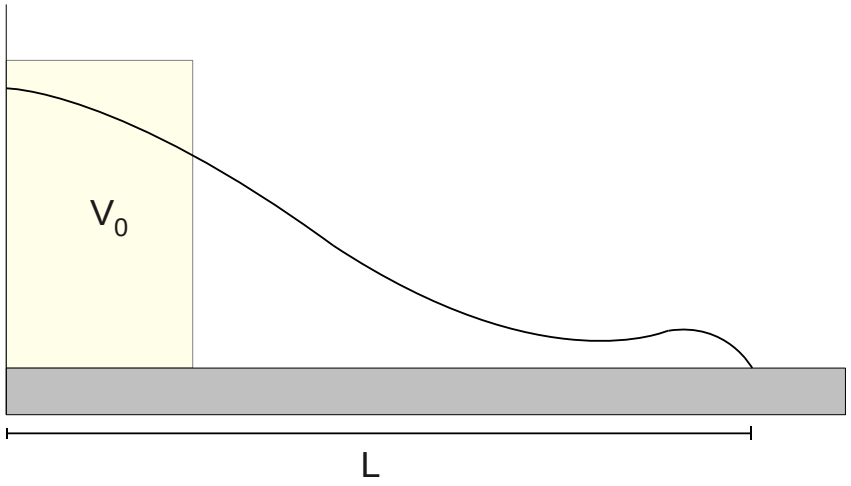

Figure 6.14: Sketch of the particle-laden gravity current test case. At time $t = 0$ s the gas–particle mixture at rest occupies the volume V_0. The mixture starts to collapse under gravitational force and flows along the horizontal solid wall. Here, L represents the front position of the density current.

6.2 Subsonic regimes

To test the FV numerical model in subsonic regimes we consider the density current test case and the collapsing jet test case.

6.2.1 Particle-driven gravity current

In this section we test the finite volume numerical model on the particle-driven gravity current problem. We consider a multiphase density current generated from the collapsing of a volume of dense gas–particle mixture, initially at rest [61], as shown in Figure 6.14. Initial conditions on the domain are reported in Table 6.4. The mixture occupies an initial volume of 500 m $\times 400$ m. The mixture is composed by dry air, with temperature $T_0 = 300$ K and pressure $1.01 \cdot 10^5$ Pa, and a volume fraction of 10^{-4} of solid particles, with diameter equal to 100 μm. Viscous terms in the multiphase equations are not neglected. The computational domain is a box with length 8 km and height 1 km. The compututational mesh is non uniform, and composed by 500×110 control volumes with maximum resolution of 5 m in the vertical direction and a uniform resolution of 20 m in the horizontal direction. At time $t = 0$ s the mixture of gas and particles starts to collapse under gravity and forms a density current that flows along the horizontal boundary. Numerical results at time $t = 300$ s are shown in Figures 6.15, 6.16 and 6.17.

To evaluate the accuracy of the model, we compare numerical results with a simple one dimensional model, which fits experimental results. For small volume fractions and almost uniform temperatures, the Boussinesq approximation can be applied to study the particle-driven gravity current. Following this approach, Halloworth at al. [61] contruct a simple box model for the motion of the gravity current. If the initial volume of the mixture is a box with volume $V_0 = L_0 H_0$, with initial solid volume fraction $\epsilon_{s,0}$, the

Parameter		Units
L_0	500	m
H_0	400	m
T_0	300	K
P_0	101325	Pa
ϵ_s	0.0001	
d_s	100	μm
ρ_s	1000	kg/m^3

Table 6.4: Initial conditions for the particle-laden gravity current test case.

evolution of the front of the current, i.e. L, is given by

$$\int_0^{L/L_{\max}} s^{1/2} \left(1 - s^{5/2}\right)^{-1} \, ds = \tau \tag{6.2}$$

where $L_{\max}$ is the maximum distance reached by the pure gas current, i.e.

$$L_{\max} = \left(\frac{5\sqrt{\epsilon_{s,0}}}{\lambda}\right)^{2/5} \tag{6.3}$$

and $\tau = \frac{t}{\bar{t}}$ is the non-dimensional time and the characteristic time $\bar{t}$ is defined as

$$\bar{t} = \frac{Fr \, \sqrt{g_s V_0 \epsilon_{s,0}}}{L_{\max}^{-3/2}}. \tag{6.4}$$

Here, the following parameters have been introduced:

$$\lambda = \frac{v_s}{\sqrt{Fr^2 g_s V_0^3}}, \tag{6.5}$$

where v_s is the settling velocity of solid particles, i.e.

$$v_s = \frac{g_s d_s^2}{18\nu_g}, \tag{6.6}$$

and g_s is the reduced gravity of particles, i.e.

$$g_s = \left| \frac{(\rho_s - \rho_{atm})}{\rho_{atm}} \, \mathbf{g} \right|. \tag{6.7}$$

Experimentally the Froude number has been estimated at 1.18. The evolution of the run out of the gravity current as a function of time obtained from Equation 6.2 with $Fr = 1.18$ and the simulated front position are shown in Figure 6.18. In particular, using the box model, the expected run out at time $t = 300$ s is 3320 m. The simulated run out at $t = 300$ s is around 3400 m, with an error of less than 3 %. We can conclude that numerical results on the particle-driven gravity test case obtained with the multiphase model are consistent with the experimental results.

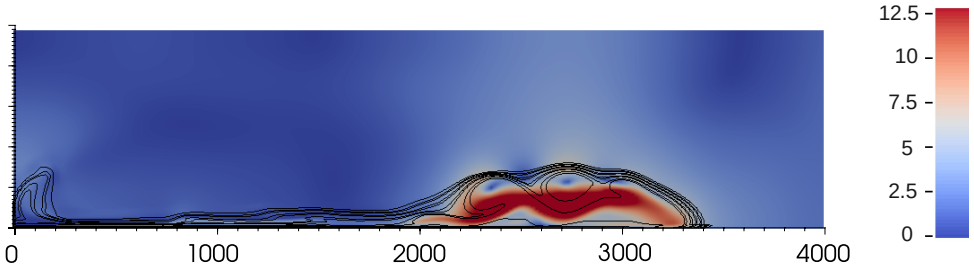

Figure 6.15: Particle-driven gravity current test case. Gas velocity magnitude from 0 to 12 m/s and isolines of logarithm to the base 10 particles volume fraction 1e[-3:-1:-9] at time $t = 300$ s. Numerical solution obtained with second order Corner Transport Upwind FV method and θ-method time discretization.

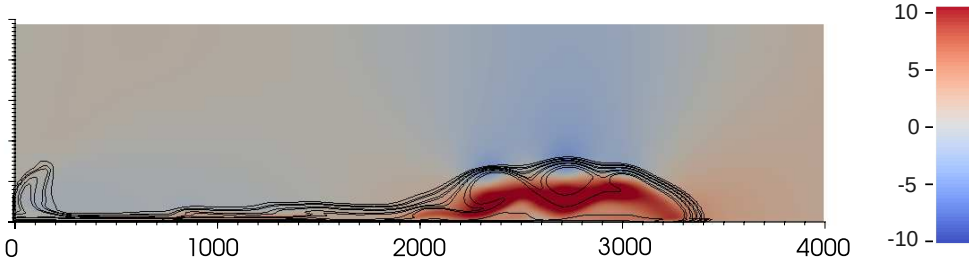

Figure 6.16: Particle-driven gravity current test case. Gas horizontal velocity from -10 to 10 m/s and isolines of logarithm to the base 10 particles volume fraction 1e[-3:-1:-9] at time $t = 300$ s. Numerical solution obtained with second order Corner Transport Upwind FV method and θ-method time discretization.

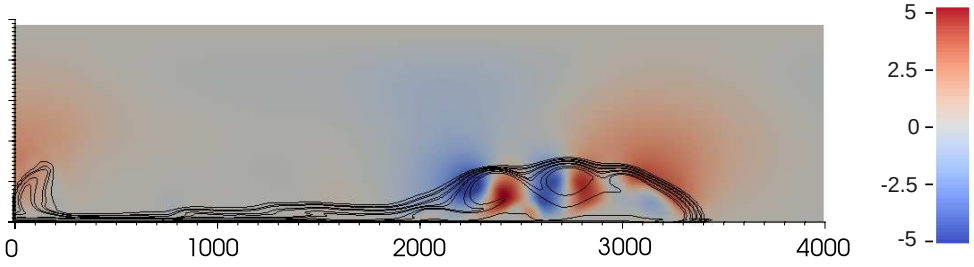

Figure 6.17: Particle-driven gravity current test case. Gas vertical velocity from -5 to 5 m/s and isolines of logarithm to the base 10 particles volume fraction 1e[-3:-1:-9] at time $t = 300$ s. Numerical solution obtained with second order Corner Transport Upwind FV method and θ-method time discretization.

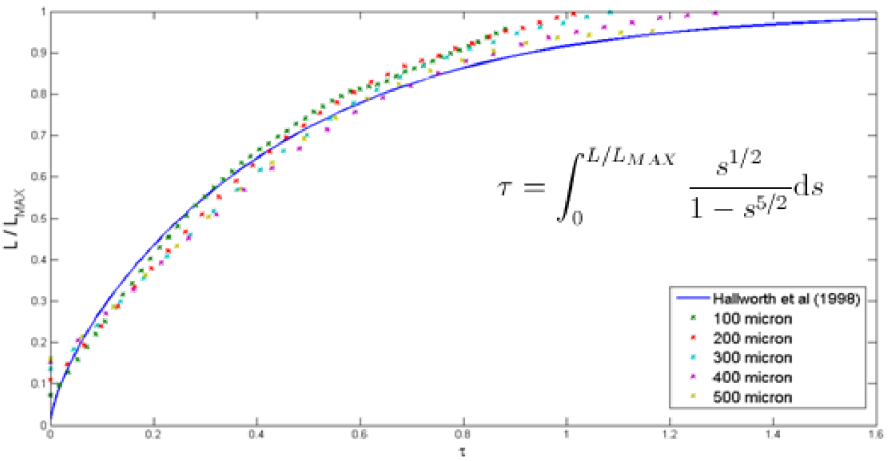

Figure 6.18: Particle-driven gravity current test case. Evolution of the gravity current front position as a function of time. Non-dimensional scaling law with $Fr = 1.18$ is compared with numerical results for different particle diameters, i.e. $d_s = 100, 200, 300, 400, 500 \mu$m.

6.2.2 Collapsing column

We consider a multiphase mixture ejected from a nozzle with subsonic speed, according to the conditions described in [90, 104]. The vent pressure is balanced with the atmospheric pressure and vent conditions are supersonic with respect to the mixture speed of sound. The mixture is considered inviscid and composed by dry air and solid particles, with diameter equal to 10 μm. For the vent initial conditions described in Table 6.5, the multiphase mixture is expected to collapse under gravitational effects and to form a density current. We compare the numerical results with the results presented in [104].

The computational domain is a box with dimensions 3000 m $\times 3000$ m. The computational mesh is composed by 300×300 control volumes ($\Delta x = 10$ m) and we use a time step $\Delta t = 0.01$ s. The computation is carried out up to the final time $t = 120$ s.

Figure 6.19 shows the evolution of the multiphase mixture at different time levels. At time $t = 10$ s, the multiphase column has reached its maximum height (about 400 m, in agreement with [104]) and starts collapsing laterally. After 25 seconds, the mixture hits the ground, forming the density current and in part flowing towards the jet. At time $t = 55$ s the mixture has run 1500 metres from the vent and part of the mixture starts rising in the atmosphere, forming buoyant plumes that are turned towards the jet by the entrainment field. In conclusion, the column height and the length of the runout of the density current are in agreement with the results presented in [104].

Parameter		Units
D_{v}	100	m
K	1	
w_v	80	m/s
T_v	1200	K
ϵ_s	0.01	
d_s	10	μm
ρ_s	2300	kg/m^3

Table 6.5: Inlet conditions for the collapsing jet test case.

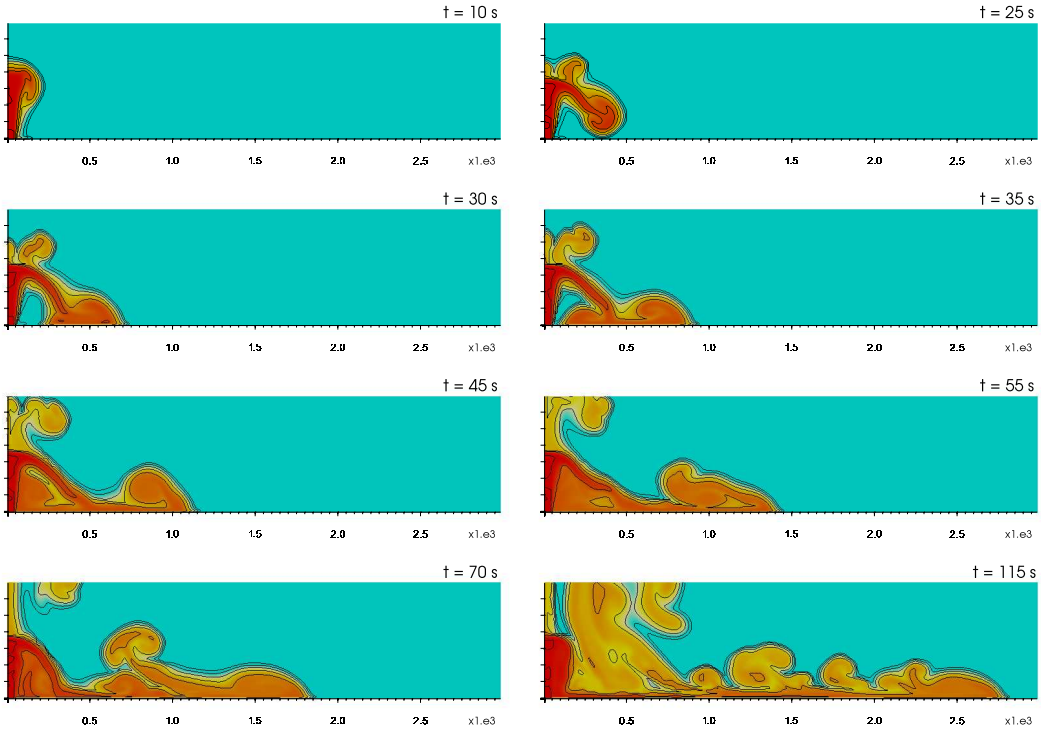

Figure 6.19: Logarithm to the base 10 of particle volume fraction and its isolines 1e[-1:-1:-8] at times $t = 10, 25, 30, 35, 45, 55, 70, 115$ s. Numerical solution obtained with second order Corner Transport Upwind FV method and θ-method time discretization.

CHAPTER 7

Validation of the discontinuous Galerkin numerical model

In this chapter, the numerical validation of the Discontinuous Galerkin approximation of the multiphase gas–particle conservation equations introduced in Chapter 2 and Chapter 4 is presented. The DG scheme with the explicit time advancing scheme has been tested on a number of one-dimensional classical benchmarks, in order to assess the accuracy in the computation of multiphase flow in both supersonic and subsonic regimes and to assess the efficiency gain related to the $p-$adaptivity algorithm. Furthermore, a comparison with respect to the finite volume approach is presented.

7.1 1D validation in the monophase regime

In this section, we test the discontinuous Galerkin numerical scheme on monophase benchmarks in order to assess the convergence properties of the scheme and the behaviour of the monotonization and p-adaptivity techniques proposed in [110, 137]. These techniques have been applied here for the first time to highly nonlinear, high Mach number regimes.

7.1.1 Linear advection test case

We consider the simple linear advection equation and we test the convergence properties of the discontinuous Galerkin numerical model. We consider the domain $[a, b] = [-1, 1]$ with periodic boundary conditions and the sinusoidal initial datum

$$c_0(x) = \sin\left(\frac{2\pi(x-a)}{b-a}\right). \tag{7.1}$$

N_K	L^2	L^∞	Dissipation	Dispersion
40	2.6647e-3	3.7512e-3	2.8524e-6	6.9845e-7
80	6.3017e-4	8.9839e-4	1.5454e-7	4.4002e-8
160	1.5329e-4	2.1969e-4	8.9449e-9	2.8049e-9
Order	2.0	2.0		

Table 7.1: Linear advection test case. Relative L^2 error, relative L^∞ error, dissipation and dispersion errors using DG scheme with $\mathbb{P}^1$ polynomials and different number of control volumes ($\Delta t = 0.001$ s).

N_K	L^2	L^∞	Dissipation	Dispersion
40	1.45e-5	6.4454e-5	2.5682e-13	1.0440e-10
80	1.81e-6	8.1700e-6	8.9067e-16	1.6353e-12
160	2.48e-7	1.1123e-6	3.2110e-18	3.0753e-14
Order	2.9	2.9		

Table 7.2: Linear advection test case. Relative L^2 error, relative L^∞ error, dissipation and dispersion errors using DG scheme with $\mathbb{P}^2$ polynomials and different number of control volumes ($\Delta t = 0.0001$ s).

The advection velocity is $u = 1$ m/s. The solution is computed until $t = 2$ s, at which the exact solution coincides with the initial datum. We consider $\mathbb{P}^1$, $\mathbb{P}^2$ and $\mathbb{P}^4$ elements on several computational grids with an increasing number of elements N_K. In all the tests, the relative L^2 and L^∞ norms are computed, that is $\|u - u_h\|_{L^2(\Omega)}/\|u\|_{L^2(\Omega)}$ and $\|u-u_h\|_{L^\infty(\Omega)}/\|u\|_{L^\infty(\Omega)}$, where u is the exact solution. We also compute the following error measures [110]:

$$\text{Dissipation error} = [\sigma(u) - \sigma(u_h)]^2 + (\bar{u} - \bar{u}_h)^2, \tag{7.2}$$

$$\text{Dispersion error} = 2\left[\sigma(u)\sigma(u_h) - \frac{1}{|\Omega|}\int_\Omega (u - \bar{u})(u_h - \bar{u_h})dx\right] \tag{7.3}$$

where

$$\sigma(u) = \sqrt{\frac{1}{|\Omega|}\int_\Omega (u - \bar{u})^2 dx}, \quad \bar{u} = \frac{1}{|\Omega|}\int_\Omega u dx. \tag{7.4}$$

It can be observed in Tables 7.1, 7.2 and 7.3 that the expected orders of accuracy in L^2 and L^∞ norms are obtained [25, 26].

N_K	L^2	L^∞	Dissipation	Dispersion
5	3.95e-5	1.93e-4	4.59e-11	7.32e-10
10	1.14e-6	6.48e-6	1.23e-14	6.43e-13
20	3.37e-8	2.08e-7	3.06e-18	4.44e-16
Order	5.1	4.9		

Table 7.3: Linear advection test case. Relative L^2 error, relative L^∞ error, dissipation and dispersion errors using DG scheme with $\mathbb{P}^4$ polynomials and different number of control volumes ($\Delta t = 0.00001$ s).

7.1.2 SOD test case

We consider the SOD benchmark test for the Euler equations, described in Table 7.4 on the domain $[-1, 1]$ m, and its solution at time $t = 0.4$ s. We solve the system of conservation equation with the DG scheme and we evaluate the behaviour of the FCT flux limiting scheme. In this test, the limiting is applied to all the equations and as limiting coefficient, the minimum between the density and the energy flux limiting coefficients is selected. To assess the monotonicity properties of the method, the maximum and minimum values of the density are reported in Table 7.5 for $\mathbb{P}^1$ elements. The numerical solution obtained with DG-NM (non monotonized) and DG-FCT schemes are shown in Figure 7.1. As it has been verified in [110] for linear problems in the framework semi-Lagrangian discontinous Galerkin methods, the FCT flux limiting guarantees the monotonicity of the mean values of the solution.

A comparison between the results obtained with the FV method on a mesh with 160 elements and with DG using $\mathbb{P}^3$ polynomials on a mesh with 40 elements is shown in Figure 7.2. The errors in the L^2 and L^∞ norms with respect to the exact solution are shown in Table 7.6. When using the same number of degrees of freedom, the DG method results to be more accurate than the FV method.

7.1.3 Shu-Osher test case

We consider the benchmark test proposed in [119] described in Table 7.7. The computational domain is $[-5, 5]$ m and the initial discontinuity is placed at $x = -4$. The solution to this problem consists in a shock ($Ma = 3$) interacting with sine waves in density. Since the solution has non trivial spatial structure, we consider this problem as a benchmark on which we can test the efficiency of the p-adaptivity algorithm presented in Section 4.2.

The domain is $[-5, 5]$ m and the solution is computed at time $t = 1.8$ s. A reference solution is computed using $\mathbb{P}^1$ elements on a mesh with $N_K = 1000$ elements. A numerical solution on a coarse ($N_K = 200$) is computed using $p-$adaptive elements. The polynomial degree can vary between 1 and 4. The solution is shown in Figure 7.3. The adapted polynomial degrees used in the last time step computation are shown in Figure 7.4, whereas the total number of degrees of freedom used at each time step is shown in Figure 7.5. Adopting a tolerance of 10^{-5} in the adaptation algorithm, we are saving more than 60% of the degrees of freedom.

7.2 1D validation in the multiphase regime

In this section, the DG numerical model is applied to the unsteady non equilibrium flow of a gas–particle mixture in a shock tube. Numerical results are compared with

Parameter	Region 1	Region 2	Units
P_g	1	0.1	Pa
ρ_g	1	0.125	kg/m^3
w_g	0	0	m/s

Table 7.4: Initial conditions for the SOD test case.

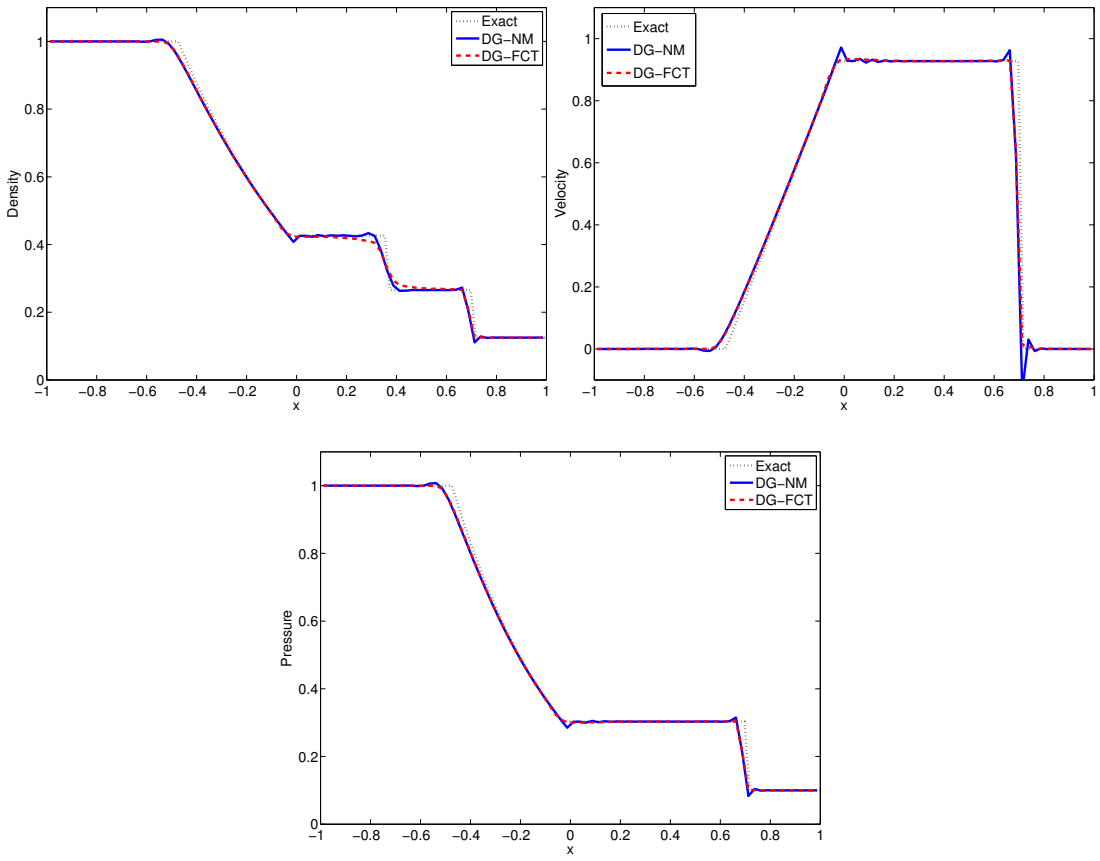

Figure 7.1: SOD test case. Comparison between the exact solution (Exact), the non monotone DG scheme (DG-NM) and the DG scheme with FCT flux limiting (DG-FCT) using $\mathbb{P}^1$ polynomials with $N_K = 80$ control volumes.

N_K	Limiter	$\max(\rho) - 1$	$\min(\rho) - 0.125$	$\max(\rho_0) - 1$	$\min(\rho_0) - 0.125$
80	None	7.0710e-3	-2.9843e-2	5.4790e-3	-1.4008e-2
80	FCT	2.1e-5	-7.675e-3	0	0
160	None	5.77e-3	-2.7977e-2	4.682e-3	-1.4078e-2
160	FCT	1.e-6	- 4.893e-3	0	0

Table 7.5: SOD test case. FCT flux limiting properties with $\mathbb{P}^1$ polynomials. Errors on the maximum and minimum values of the density ρ and on its maximum and minimum mean values ρ_0.

Method	N_K	L^2	L^∞
DG	40	[0.0137, 0.0381, 0.0125]	[0.0438, 0.1025, 0.0348]
FV	160	[0.0242, 0.1069, 0.0349]	[0.1303, 0.6158, 0.2364]

Table 7.6: SOD test case. Comparison between FV and DG-$\mathbb{P}^3$ method. Errors on the mean values of the three components of the solution.

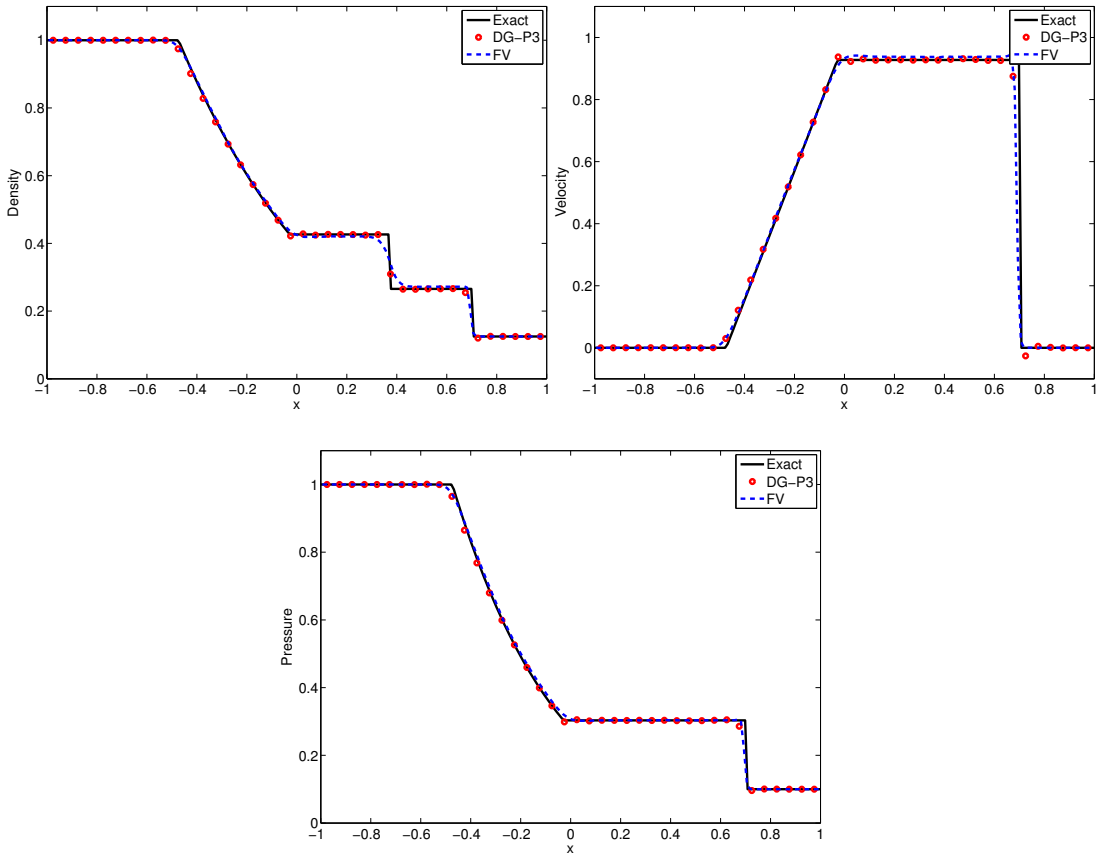

Figure 7.2: SOD test case. Comparison between the exact solution (Exact), the solution computed with DG-$\mathbb{P}^3$ and $N_K = 40$ control volumes (DG-P3) and the solution computed with second order FV method on a mesh with $N_K = 160$ elements.

Parameter	Region 1	Region 2	Units
P_g	10.33333	1	Pa
ρ_g	3.857143	$1 + 0.2\sin(5x)$	kg/m^3
w_g	2.62939	0	m/s

Table 7.7: Initial conditions for the Shu-Osher test case.

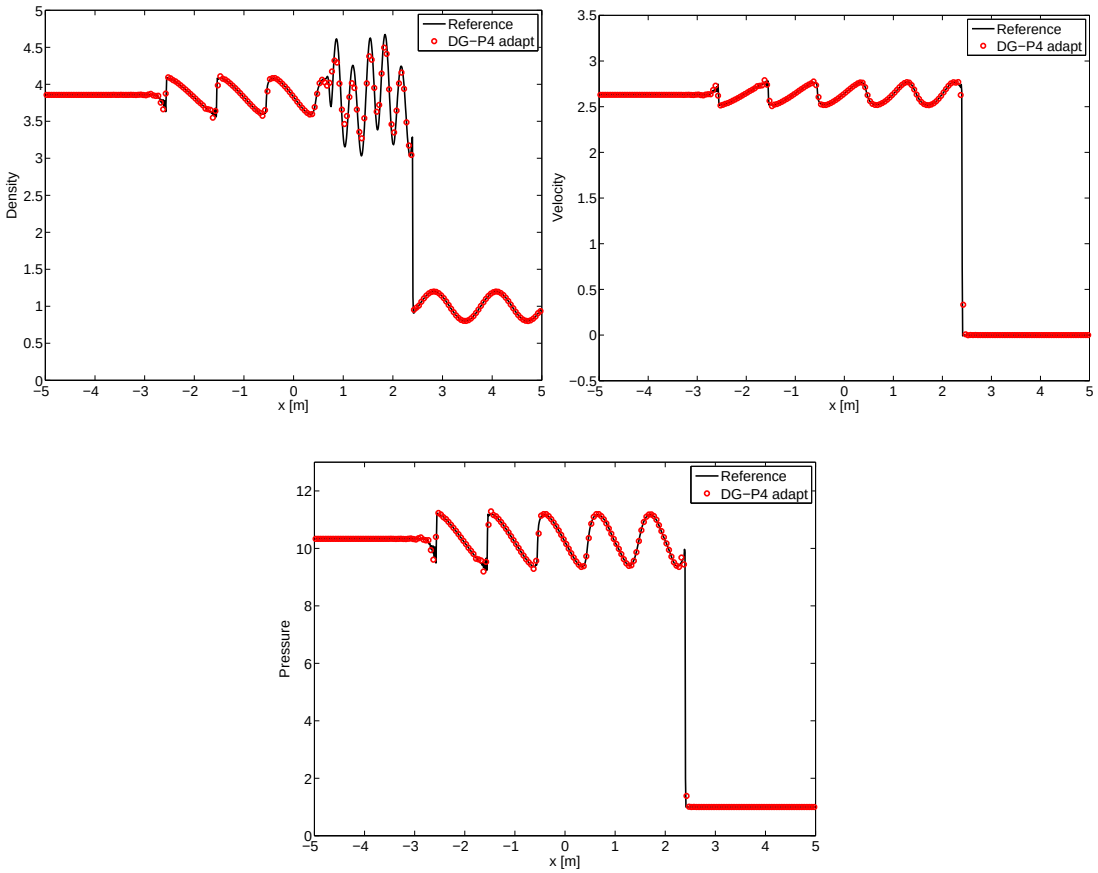

Figure 7.3: Shu-Osher test case. Evaluation of the p-adaptive algorithm. Comparison between a reference solution computed with $N_K = 1000$ elements and $\mathbb{P}^1$ polynomials and the solution computed with the p-adaptive DG scheme with $N_K = 200$ elements and $r_{max} = 4$.

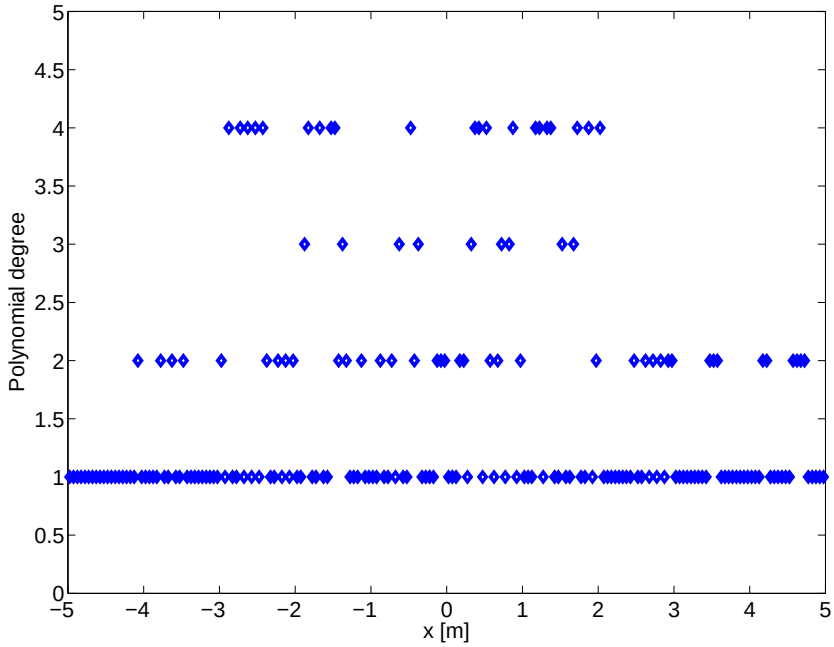

Figure 7.4: Shu-Osher test case. Evaluation of the p-adaptive algorithm. Polynomial degrees adopted on the domain during the last time step computation. Numerical solution computed with the p-adaptive DG scheme with $N_K = 200$ elements and $r_{max} = 4$.

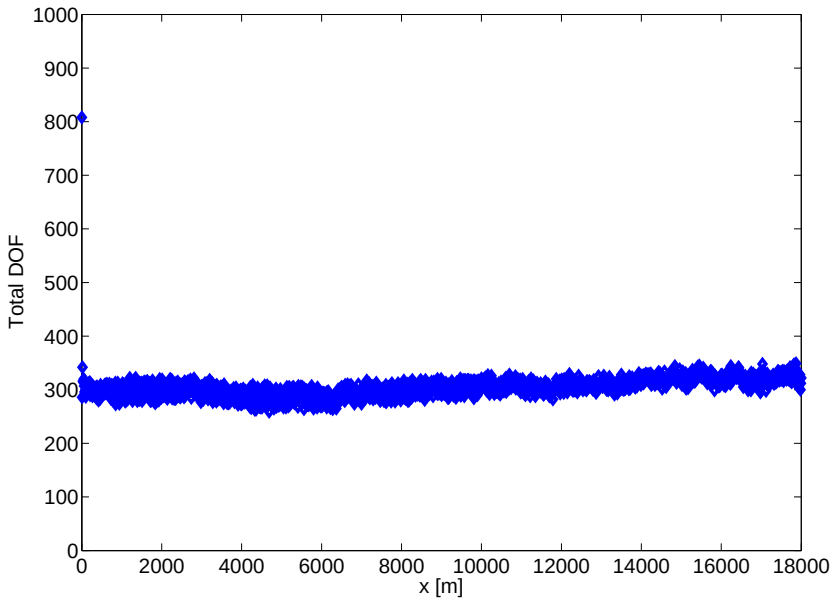

Figure 7.5: Shu-Osher test case. Evaluation of the p-adaptive algorithm. Total number of degrees of freedom adopted during the computation. Numerical solution computed with the p-adaptive DG scheme with $N_K = 200$ elements and $r_{max} = 4$.

experimental and numerical results reported in the literature.

7.2.1 Sommerfeld experiment

We present the results of some numerical computations performed under the same conditions as Sommerfeld's experiments [123]. The shock tube is divided into three parts. The high pressure section of the shock tube is occupied by pure air. The low pressure section is divided into two parts: the pure air section of length 1.0 m adjacent to the diaphragm and the region occupied by a gas–particle mixture. Solid particles have a diameter equal to 27μm, density equal to 2500 kg/m^3 and specific heat $c_{p,s} = 766$ J/Kg·K. Initial conditions for the presented test case are shown in Table 7.8.

At time $t = 0$ s, after the rupture of the diaphragm, a shock wave forms in the low pressure air region, while a rarefaction wave propagates in the high pressure section. As observed in experimental and numerical results in [89,123], the shock wave initiated in the pure gas region travels with constant speed in the gas phase until it reaches the particle cloud at time $t \simeq 2$ ms. Up to this time, the mixture on the right part of the shock tube remains at rest, whereas the gas dynamics in the left part corresponds to the solution expected for the classic Euler equations, as shown in Figure 7.6.

At time $t = 2$ ms, the shock wave starts interacting with the gas–particle mixture. The deceleration of the gas due to the interaction with the particles results in a compression of the gas, and its pressure away from the shock front raises to values higher than those in the pure gas. Thus, at $x = 0$, that is at the boundary of the particle cloud, the shock wave is partly reflected as compression wave travelling towards the left in the pure gas, as shown in Figure 7.6. The shock front, travelling through the dusty gas, is followed by a thick relaxation zone, across which velocity and temperature of the two phases equilibrate. Thus, the density and the temperature of the gas are not uniform in the neighborhood of the boundary of the particle cloud, as in the pure gas test case. Due to the heat capacity and the inertia of the particles, the velocity of the transmitted shock does not change instantaneously. A transition region develops where the shock velocity is slowly reduced to its equilibrium value, which corresponds to the speed of sound in the mixture. The equilibrium shock velocity is determined by the initial shock strength and the particle loading.

The computations have been performed using the discontinuous Galerkin approximation with the same polynomial degree on all the elements and for all the variables. It must be observed that in the solution of the multiphase equations the positivity of the macroscopic density and of the total energy has to be guaranteed in order to derive positive (and physically meaningful) drag and heat exchange coefficients. When high order polynomial approximations are adopted, this result is achieved by applying monotonization techniques, such as FCT flux limiting or minmod slope limiting. Thus, in the following simulations, either FCT or minmod limiting is always applied.

The solutions obtained with $\mathbb{P}^1$ and $\mathbb{P}^4$ elements and minmod slope limiting at time $t = 10$ ms are shown in Figure 7.7 and Figure 7.8, respectively, and compared with a reference solution obtained with the FV method. It can be observed that the solutions obtained with the two methods are in agreement as regards the gas phase, whereas the solid particles solution slightly differs. Those differences are ascribable to the different treatment of the interphase coupling terms in the two algorithm. In particular, different

linearization approaches should be tested in the explicit method described in Section 5.3.2.

The limiting properties of the minmod slope limiter and the FCT flux limiter are shown in Table 7.9. In particular, the FCT flux limiter is applied only to the mass and energy balance equations of the gas phase. When no monotonization technique is introduced, the numerical solution blows up before the end of the computation. With the FCT flux limiter, the numerical solution presents small spurious oscillations near the particle cloud boundary. Finally, the high order minmod slope limiter [9] is able to guarantee the monotonicity of the numerical solution.

The performances of the p-adaptive algorithm are evaluated by comparing the results obtained on a mesh with 200 control volumes, using $\mathbb{P}^4$ elements on the whole mesh and the p-adaptive algorithm, with maximum and minimum polynomial degrees equal to four and one, respectively. The tolerance is fixed to $2 \cdot 10^{-3}$. A reference solution is computed using $\mathbb{P}^1$ elements on a mesh with $N_K = 5000$. The numerical solutions are shown in Figure 7.9. The relative errors in L^2 norm with respect to the reference solution are shown in Table 7.10.

The computational effort reduction obtained thanks to the p-adaptive approach is evaluated with equation 4.27 and is around 54 %. The polynomial degree employed on the computational mesh during the last time step computation is shown in Figure 7.10. It can be observed that polynomials of degree one, which is the lowest degree admitted, are employed in the intervals in which the solution is constant. In the other regions, polynomials of order at least two are used to approximate the solution. In Figure 7.11, the total number of degrees of freedom employed in the computation are shown for each time step. It can be observed that, starting from the initial maximum value of 1000, in few time steps the number if degrees of freedom is reduced to about 400 and then adjusted as the numerical solution evolves in time.

Parameter	**Region 1**	**Region 2**	**Region 3**	**Units**
P_g	70000	10000	10000	Pa
T_g	280	280	280	K
w_g	0	0	0	m/s
ϵ_s	0	0	0.000019	
T_s	280	280	280	K
w_s	0	0	0	m/s

Table 7.8: Initial conditions for the Sommerfeld's shock tube experiment.

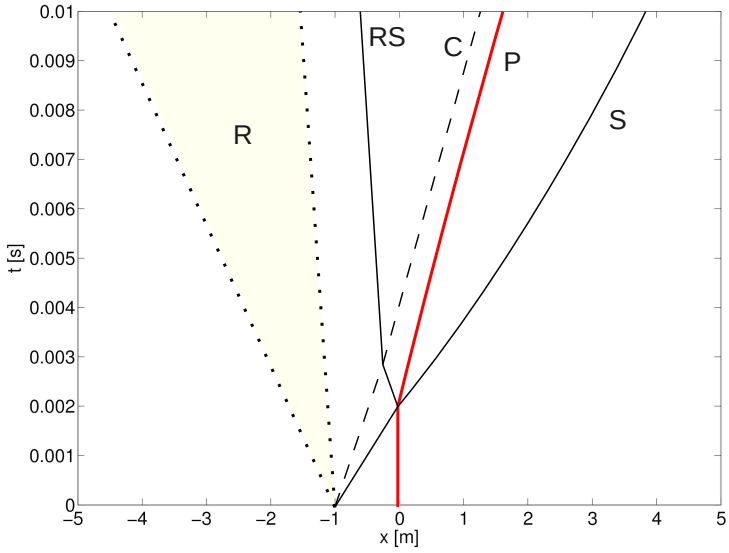

Figure 7.6: Wave diagram for the Sommerfeld's shock tube test case. In yellow, indicated with R, the rarefaction region, C is the contact wave, S the shock wave, RS the reflected shock wave and P the particle cloud front.

N_K		Limiter	$\max(\epsilon_g\rho_g) - (\epsilon_g\rho_g)^0_{\max}$	$\min(\epsilon_g\rho_g) - (\epsilon_g\rho_g)^0_{\min}$
200	DG-P4	None	-	-
500	DG-P1	FCT	0	-1.5e-5
200	DG-P4	Minmod	0	0

Table 7.9: Sommerfeld's shock tube test case. Comparison between the non-monotone DG-$\mathbb{P}^4$ scheme, the DG-$\mathbb{P}^1$ scheme with FCT flux limiting on the gas phase variables and the DG-$\mathbb{P}^4$ scheme with the minmod slope limiting techniques proposed by Biswas et al. [9].

Variable	DG-P4	DG-P4 adapt
$\epsilon_g\rho_g$	6.63e-7	6.52e-7
$\epsilon_g\rho_g u_g$	1.62e-4	1.59e-4
$\epsilon_g\rho_g E_g$	8.43e-2	8.43e-2
$\epsilon_s\rho_s$	3.12e-7	2.74e-7
$\epsilon_s\rho_s u_s$	6.79e-5	5.99e-5
$\epsilon_s\rho_s E_s$	9.44e-2	8.38e-2

Table 7.10: Sommerfeld's shock tube test case. Evaluation of the p-adaptive algorithm. Relative errors in L^2 norm with respect to a reference solution computed using DG-$\mathbb{P}^1$ with $N_K = 5000$ elements. Comparison between DG-$\mathbb{P}^4$ elements and DG-$\mathbb{P}^4$ elements with p-adaptivity.

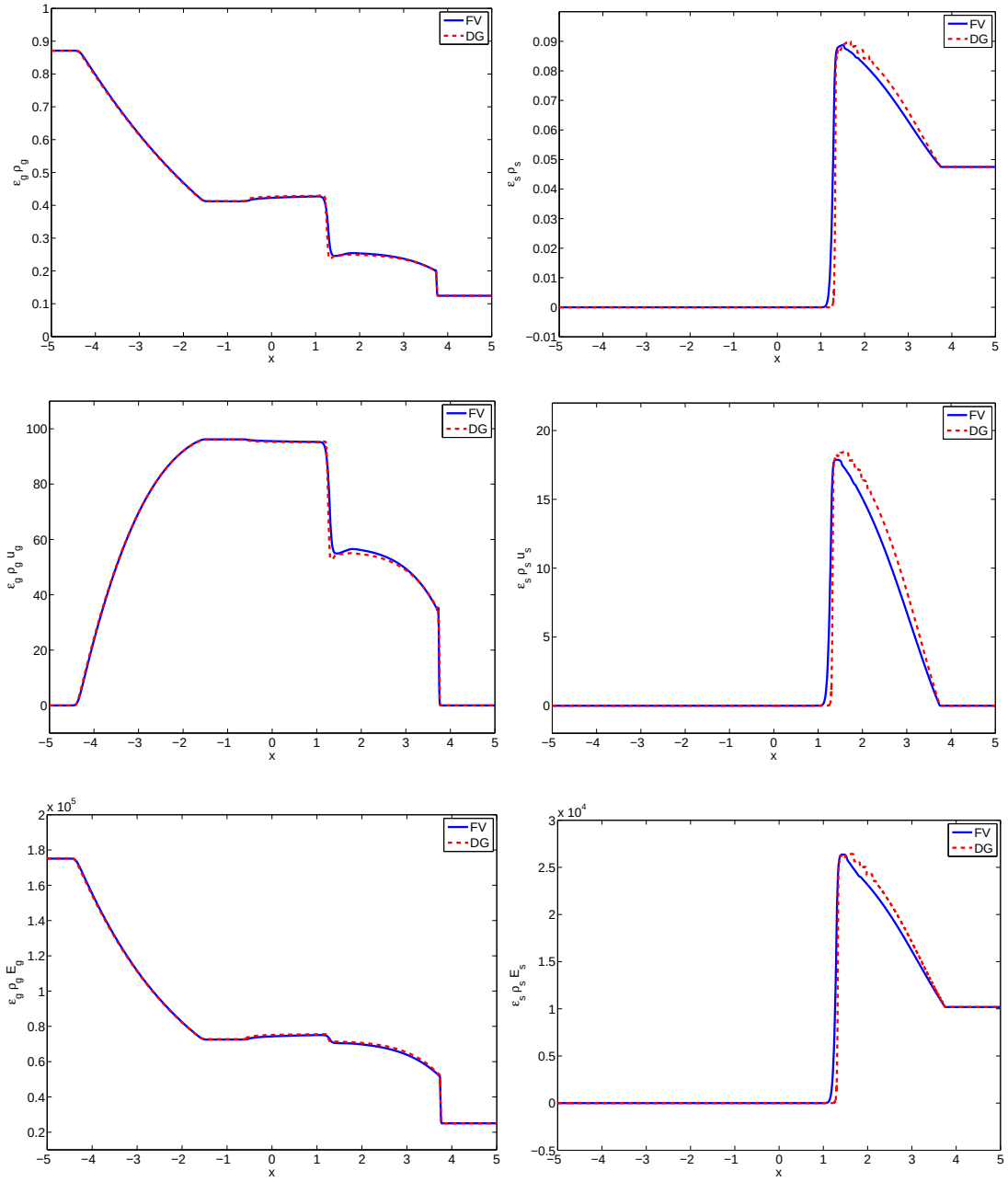

Figure 7.7: Sommerfeld's shock tube test case. Conserved variables at time $t = 10$ ms. Comparison between second order FV scheme on a computational mesh with $N_K = 1000$ elements and the DG scheme using $\mathbb{P}^1$ polynomials and $N_K = 500$ control volumes.

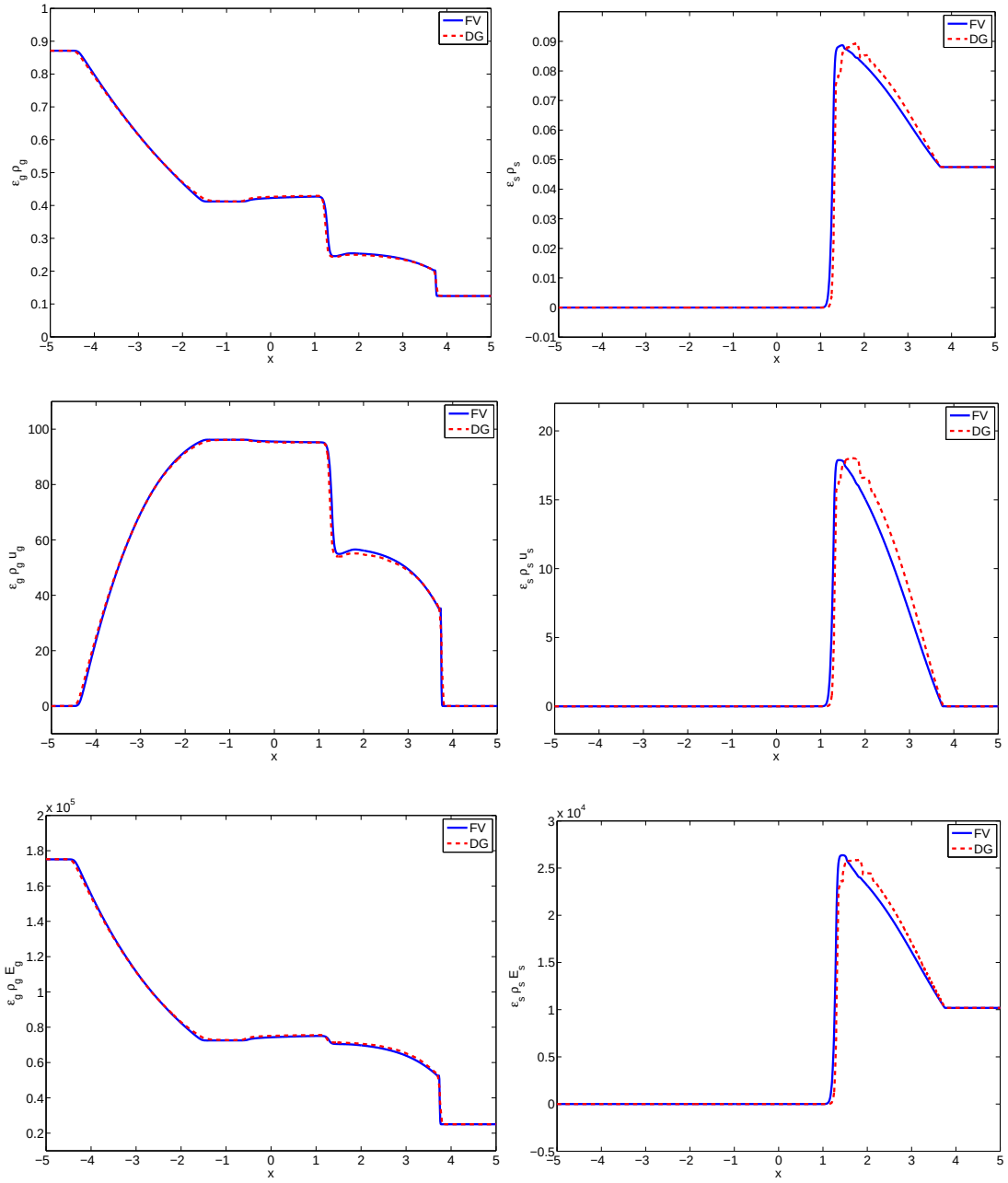

Figure 7.8: Sommerfeld's shock tube test case. Conserved variables at time $t = 10$ ms. Comparison between the second order FV scheme on a computational mesh with $N_K = 1000$ elements and the DG scheme using $\mathbb{P}^4$ polynomials and $N_K = 200$ control volumes.

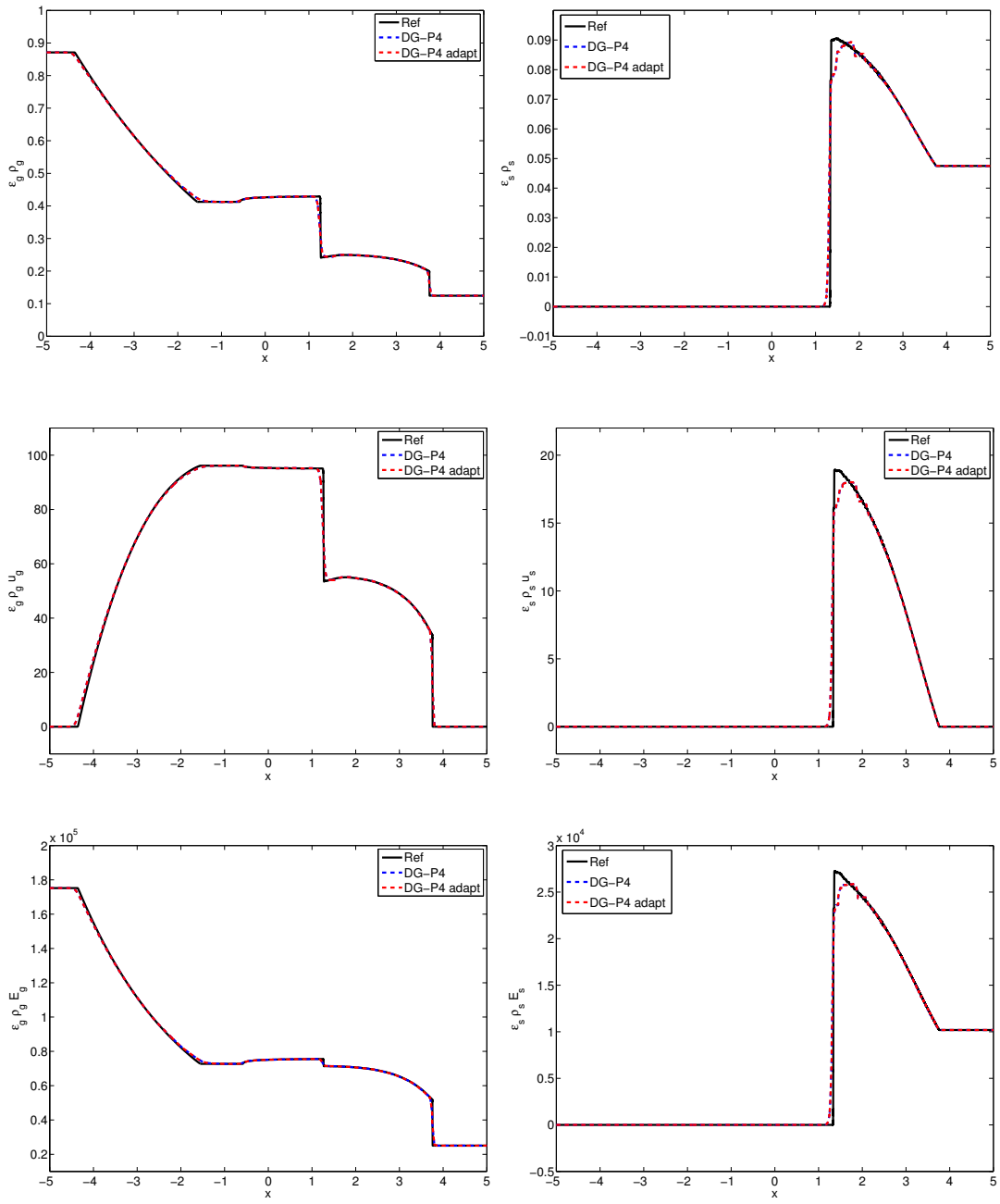

Figure 7.9: Sommerfeld's shock tube test case. Conserved variables at time $t = 10$ ms. Comparison between a reference solution computed using DG-$\mathbb{P}^1$ with $N_K = 5000$ elements (Ref), DG-$\mathbb{P}^4$ with $N_K = 200$ elements (DG-P4) and DG-$\mathbb{P}^4$ with p-adaptivity and $N_K = 200$ elements (DG-P4 adapt).

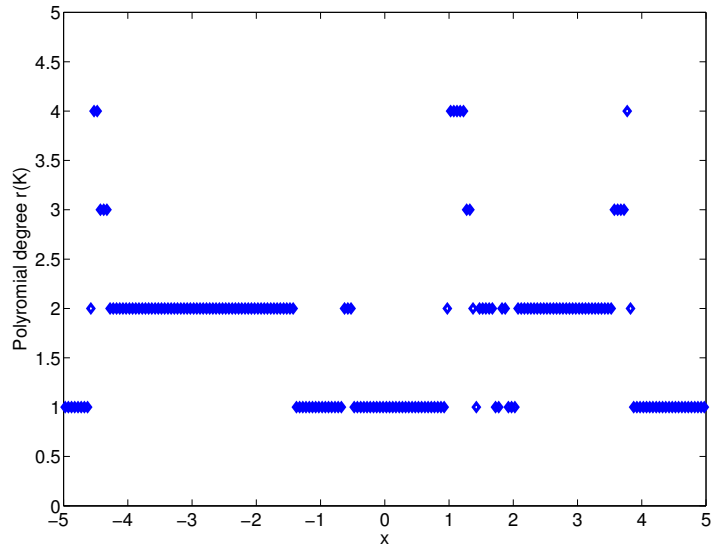

Figure 7.10: Sommerfeld's shock tube test case. Evaluation of the p-adaptive algorithm. Polynomial degrees adopted on the domain during the last time step computation. Numerical solution computed with the p-adaptive DG scheme with $N_K = 200$ elements and $r_{max} = 4$.

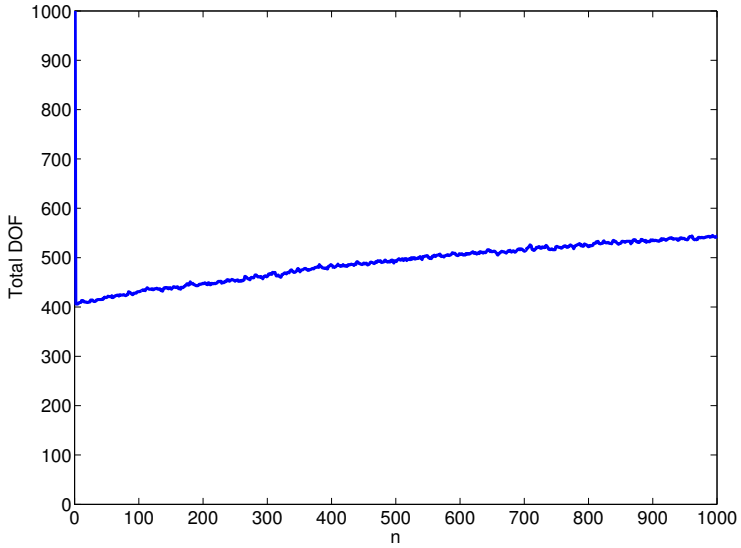

Figure 7.11: Sommerfeld's shock tube test case. Evaluation of the p-adaptive algorithm. Total number of degrees of freedom adopted during the computation. Numerical solution computed with the p-adaptive DG scheme with $N_K = 200$ elements and $r_{max} = 4$.

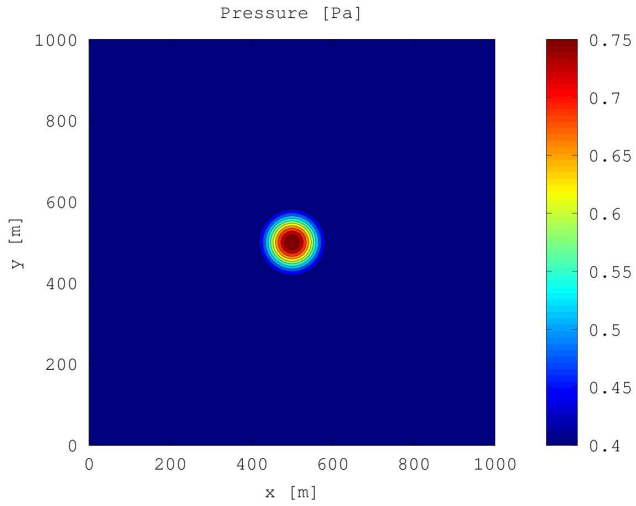

Figure 7.12: Initial pressure perturbation for the pressure wave test case.

7.3 2D validation in the monophase regime

In this section, we test the discontinuous Galerkin numerical scheme on two-dimensional monophase test case.

7.3.1 Pressure wave test case

The two-dimensional Euler equations are solved with the discontinuous Galerkin numerical scheme presented in Chapter 4. We consider a rectangular domain $[0, L]^2$, with $L = 1000$ m and an initial perturbation of the pressure in the center of the domain, as shown in Figure 7.12. The solution computed on a 100×100 mesh ($\Delta t = 0.5$ s) with polynomials of constant degree equal to 1 is shown in Figure 7.13. The solutions computed on a 50×50 mesh ($\Delta t = 0.5$ s) with $\mathbb{P}^3$ elements and with the p-adaptive scheme and maximum polynomial degree equal to 3 are shown in Figure 7.14 and Figure 7.15, respectively.

The polynomial degrees employed on the computational mesh during the first and the last time step computation is shown in Figure 7.16, whereas the fraction of degrees of freedom employed at each time step is shown in Figure 7.17. We can observe how the maximum polynomial degree is used in the region of the domain where the solution is not constant, whereas linear polynomials are employed to approximate almost constant solutions. As a consequence, in the first time steps only 30 % of the total number of degrees of freedom are used to approximate the solution. The number of degrees of freedom increases as the pressure wave expands in the domain.

7.4 2D validation in the multiphase regime

7.4.1 Pressure wave test case

The two-dimensional multiphase Euler equations are solved with the discontinuous Galerkin numerical scheme presented in Chapter 4. We consider a rectangular domain $[0, L]^2$, with $L = 1000$ m and an initial perturbation of the pressure in the center of the

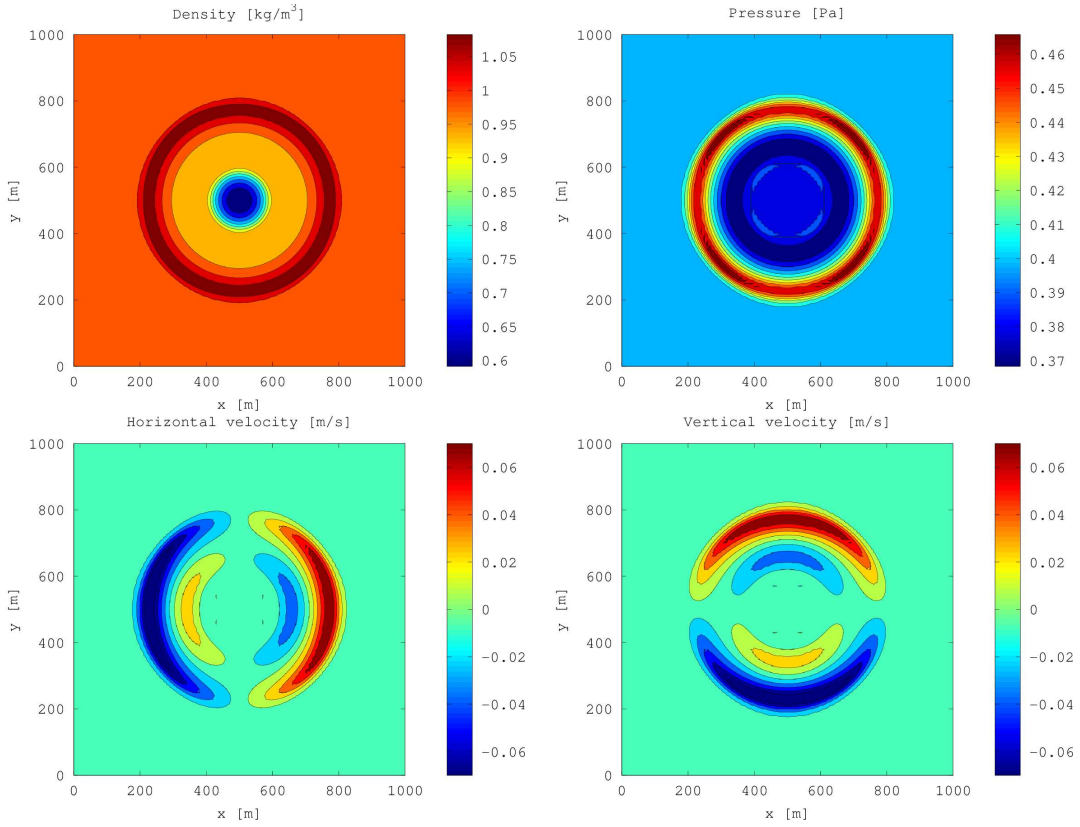

Figure 7.13: Solution computed at time $t = 300$ s with $\mathbb{P}^1$ elements on a 100×100 mesh.

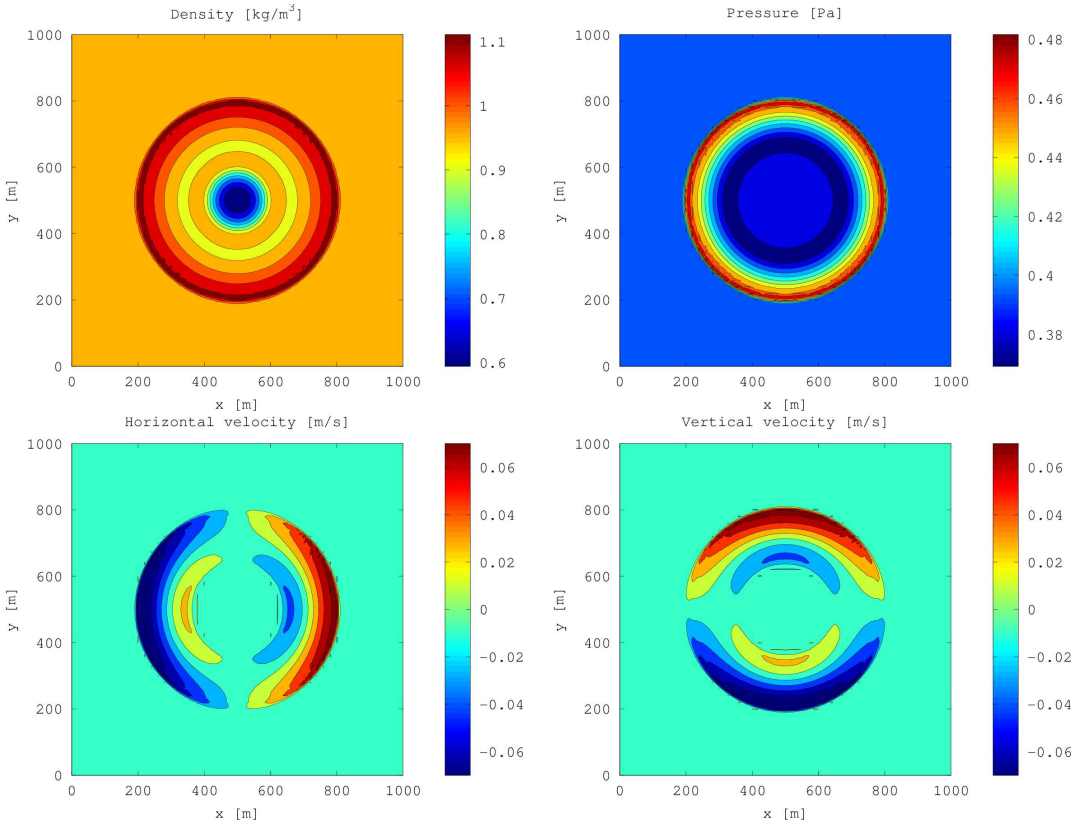

Figure 7.14: Solution computed at time $t = 300$ s with $\mathbb{P}^1$ elements on a 50×50 mesh.

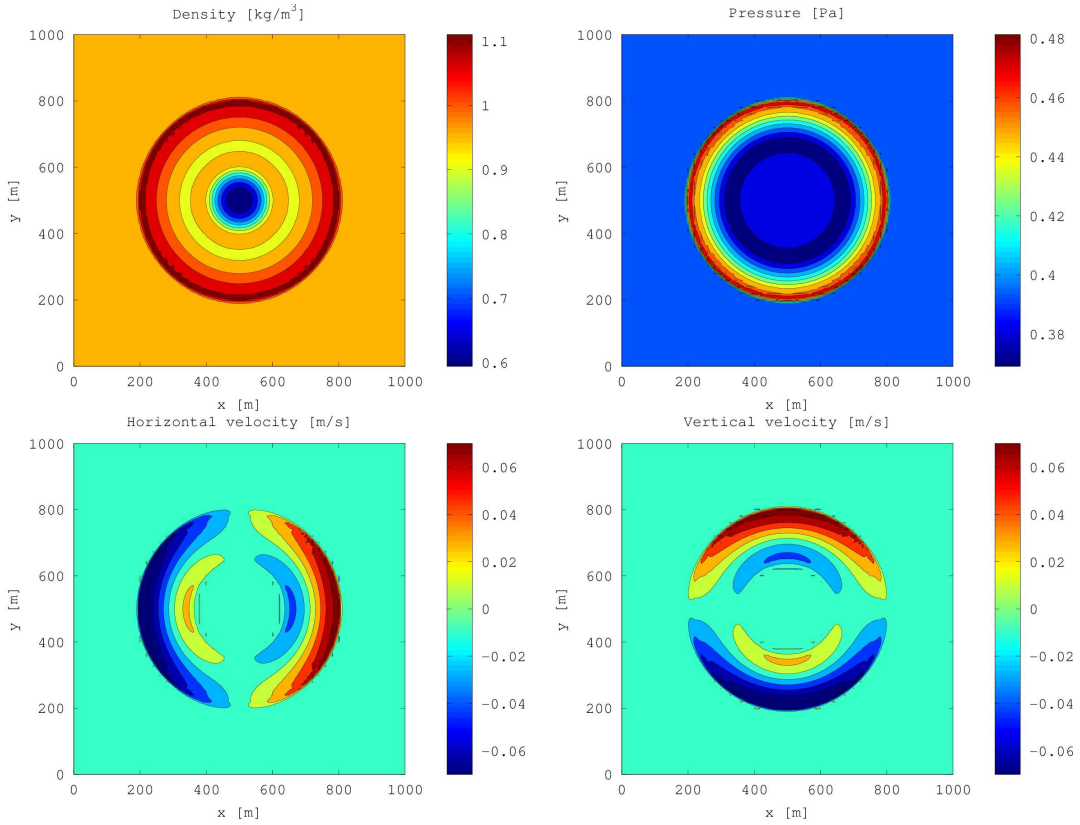

Figure 7.15: Solution computed at time $t = 300$ s with the p-adaptive scheme with maximum polynomial degree equal to 3 on a 50×50 mesh.

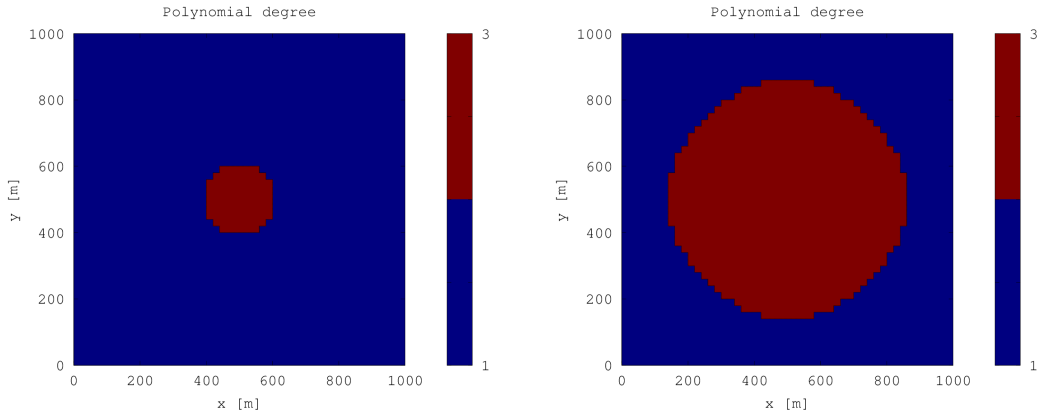

Figure 7.16: Polynomial degrees employed in the first and in the last time step computation.

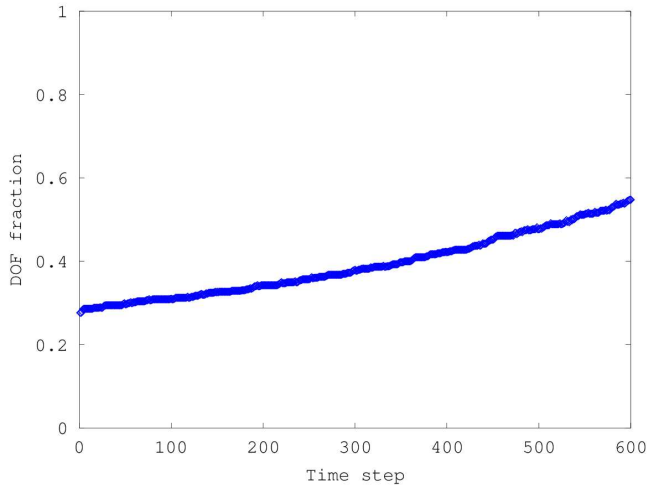

Figure 7.17: Fraction of degrees of freedom actually employed at each time step.

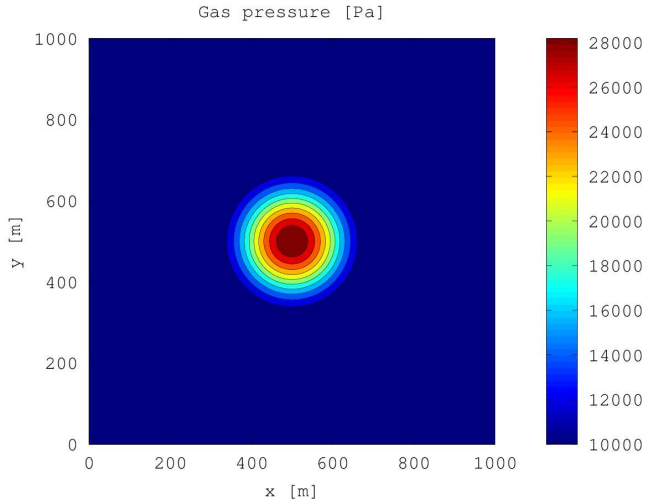

Figure 7.18: Initial pressure perturbation for the multiphase pressure wave test case.

domain, as shown in Figure 7.18. At time $t = 0$ s, a uniform concentration of particles ($\epsilon_s = 10^{-4}$) is considered in the domain. The solution at time $t = 1$ s is shown in Figure 7.19.

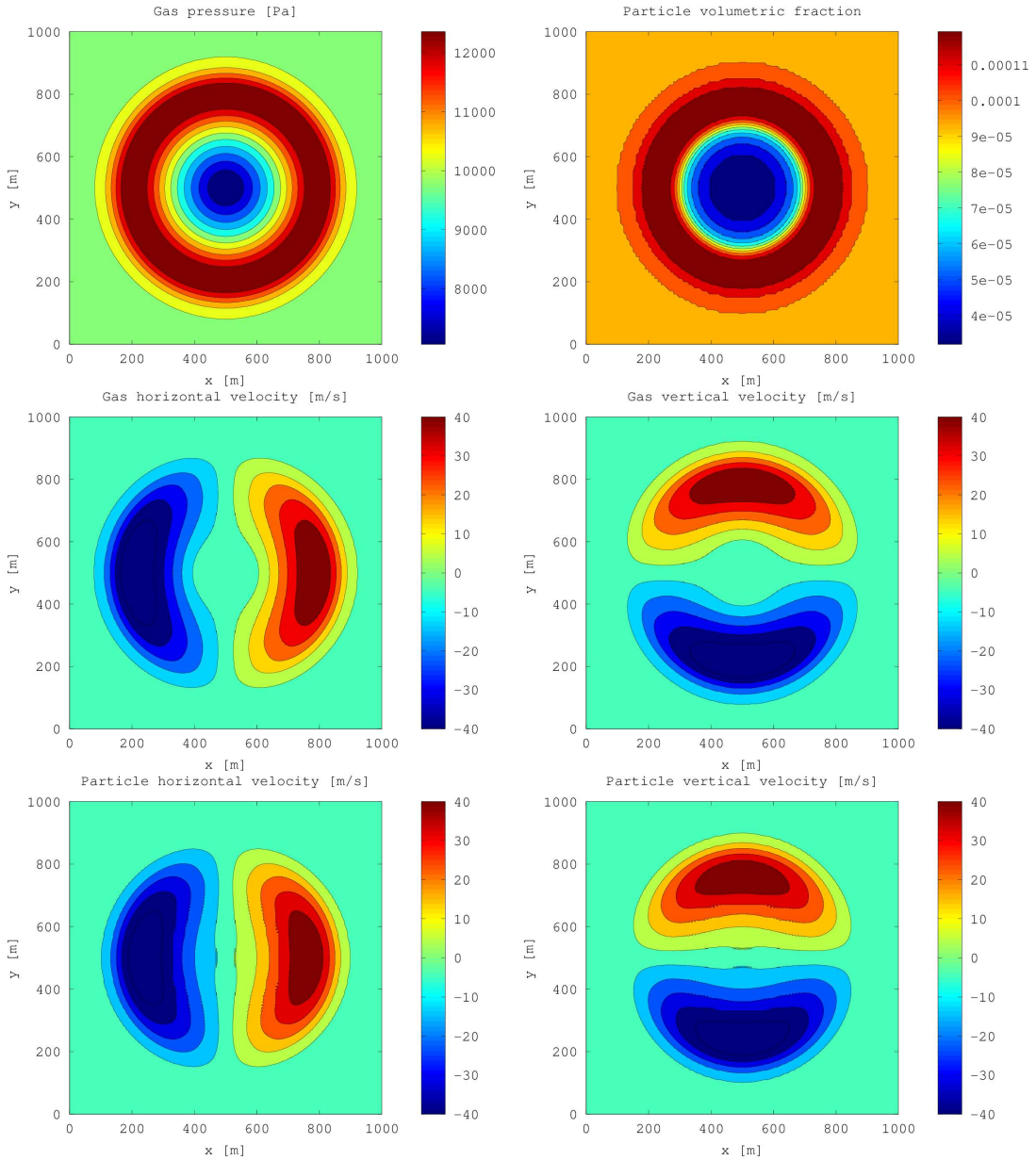

Figure 7.19: Solution computed at time $t = 1$ s with $\mathbb{P}^1$ elements on a 100×100 mesh.

CHAPTER 8

Application of the finite volume method to the analysis of gas–particle non-equilibrium effects on underexpanded volcanic jets

In Chapter 6, the dynamics of underexpanded gas–particle jets has been introduced and reproduced in order to validate the finite volume numerical model. In this chapter, the dynamics of underexpanded gas–particle jets is analyzed in depth by means of the multiphase model presented in Chapter 2. In particular, the focus will be on the non-equilibrium phenomena that take place at the volcanic scale.

The underexpanded multiphase jet problem is representative of phenomena that can be observed near the source of explosive volcanic eruptions. The explosive character of an eruption is always associated to the rapid decompression and the consequent abrupt expansion of gases in the liquid magma that rises from a magma chamber. The mixture of gases and magma fragments is injected in the atmosphere from the volcanic vent at high velocity, pressure and temperature [147]. Therefore during explosive eruptions, in the proximity of the volcanic vent, the erupted multiphase mixture can manifest the features of supersonic flows. Such initial decompression stage has been hypothesized by [75, 97, 98, 147] and evidence of it has been found by infrasonic and acoustic measurements, see e.g. [73]. Thus, in explosive volcanic eruptions, phenomena analogous to the ones described and studied in Chapter 6, i.e. underexpanded jets, can commonly take place and represent a fundamental process of the phenomenon.

A general understanding of the dynamics of supersonic volcanic jets has been achieved by assuming the mixture to be homogeneous, i.e., by assuming kinetic and thermal equilibrium between gas and particles [96, 97]. As discussed in Chapter 2, the equilibrium assumption is valid only on a restrict range of particle sizes. In this chapter, the

focus will be on the analysis of the underexpanded multiphase jet dynamics in the case of decoupled dynamics between gas and particles.

8.1 Dynamics of underexpanded volcanic jets

In this chapter, we analyse underexpanded gas–particle jets by means of the characteristic time scales of the multiphase flow, i.e. the particle relaxation time and the Mach disk formation time.

8.1.1 Particle relaxation time

The relaxation time τ_s of a particle moving with speed $\mathbf{v}_s$ in a surrounding fluid, which is flowing with velocity equal to $\mathbf{v}_g$, can be estimated from the particle momentum equation (2.14b) by assuming all the forces acting on the particle negligible except the drag force, that is

$$\frac{\partial}{\partial t}(\epsilon_s \rho_s \mathbf{v}_s) \simeq D_{g,s}(\mathbf{v}_g - \mathbf{v}_s). \tag{8.1}$$

Following [16, 72, 86], we define the particle relaxation time as

$$\tau_s = \frac{\epsilon_s \rho_s}{D_{g,s}}. \tag{8.2}$$

The particle characteristic time can be interpreted as the order of magnitude of the time needed by the particle to accelerate or decelerate to the surrounding fluid velocity, as shown in Figure 8.1. In general, after a time interval equal to $5\tau_s$, the solution $\mathbf{v}_s$ of Equation (8.1) can be considered as constant in time and equal to $\mathbf{v}_g$. In an underexpanded jet, the delay between gas and particles may occur in the rapid expansion above the vent, where the gas phase accelerates, and across the normal shock, where the gas velocity is reduced abruptly. As described in [86], an analogous thermal relaxation time can be defined starting from the energy balance equation (2.15b) and a simple analysis suggests that the time scale for thermal relaxation has the same order of magnitude as τ_s.

For dilute mixtures and low gas–particle Reynolds number, as defined in (2.45), the particle relaxation time can be computed from (8.2) and (2.43), obtaining

$$\tau_s \simeq \frac{\rho_s d_s^2}{18 \mu_g}. \tag{8.3}$$

8.1.2 Mach disk formation time

The supersonic jet process is characterized by different time scales, as discussed in [98]. Assuming steady supersonic conditions at the nozzle, the transient dynamics of the supersonic jet can be described by the formation time of the Mach disk shock τ_{Ma}, which represents the time needed by the first wave forming in the jet to reach the centerline.

An estimate of the Mach disk formation time is obtained by means of geometric considerations [98], as shown in Figure 8.2. Suppose that c is the speed of shock waves in air, $v = |\mathbf{v}_{mix}|$ is the mixture velocity at the vent. At time τ_{Ma}, the location of the normal shock is z_{Ma}, whereas the jet head is located at $z_J = v\tau_{Ma}$. The distance

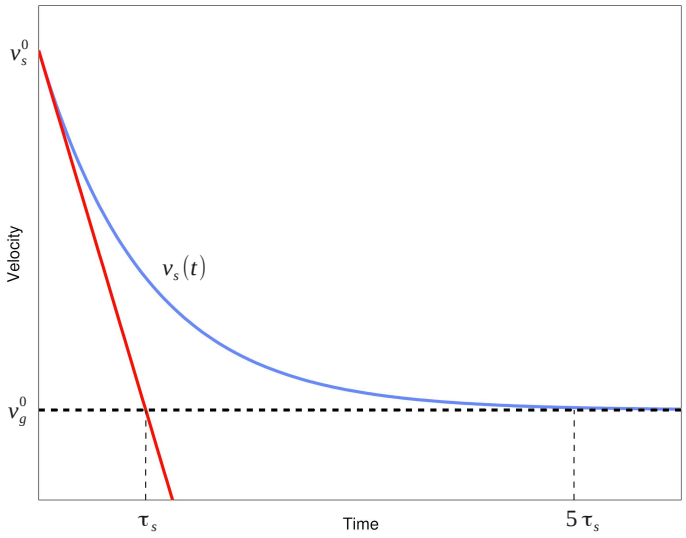

Figure 8.1: Interpretation of particle relaxation time. The blue line represents the exact solution of Equation (8.1), the red line represents its linear approximation around $t = 0$, the black line is the gas velocity. The intersection between the red and the black line defines the particle relaxation time. After $t = 5\tau_s$, we can assume that $v_s \simeq v_g$.

travelled by the shock wave in the time interval τ_{Ma} is given by $z_S = c\tau_{Ma}$. From the geometrical analysis shown in Figure 8.2, it results that

$$\frac{D}{2} = \sqrt{z_S^2 - (z_{Ma} - z_J)^2}. \tag{8.4}$$

If we assume that the first air shock and the jet head are near, we can set $z_{Ma} \simeq z_J$ and $c = c_{mix}$, where c_{mix} is the speed of sound waves in the mixture, obtaining

$$\frac{D}{2} = z_S = c_{mix}\tau_{Ma} \tag{8.5}$$

and finally

$$\tau_{Ma} = \frac{D}{2c_{mix}}, \tag{8.6}$$

where c_{mix} is defined by 2.63.

8.2 Numerical investigation

In this section, the dynamics of underexpanded gas–particle jets at the volcanic scale is studied numerically and it is analyzed by means of the characteristic time scales introduced in the previous section. First, the analysis is carried out in the case of a monodisperse mixture, by considering only one class of solid particles. The analysis is then extended to the case of bidisperse and polydisperse mixtures. In the following numerical tests, the gas phase ejected from the vent is assumed to consist of water vapor [55], whose fundamental thermodynamic properties are reported in Table 8.1.

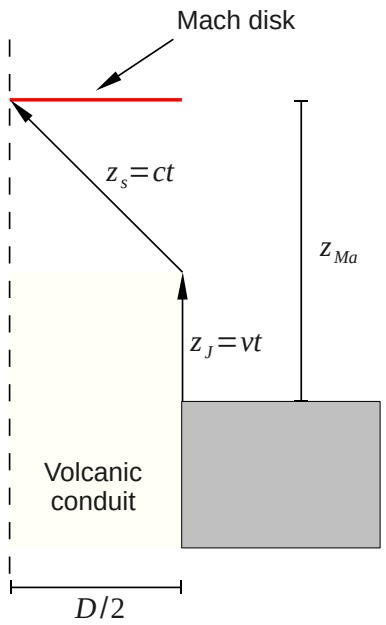

Figure 8.2: Geometrical construction of the Mach disk formation time. Here, D is the nozzle diameter, c is the speed of sound waves, v is the fluid velocity at the nozzle. z_{Ma} is the position of the standing normal shock wave, z_J is the distance covered by the fluid front at time t and z_S is the distance travelled by the shock wave in the time interval t.

Concerning solid particles, we assume a nonlinear dependence between particle diameter and particle density, $\rho_s = \rho_s(d_s)$, such as the one proposed in [10] which reproduces the typical properties of solid particulate ejected during a real volcanic eruption. The empirical relationship between particle diameter and density is shown in Figure 8.3. Other particle thermodinamic properties are reported in Table 8.2.

The mixture is ejected from a circular vent in a standard atmosphere. That is, temperature, pressure and density are taken to be stratified and the medium consists of dry air. The problem is assumed to be axisymmetric, thus the following simulations are carried out in cylindrical coordinates. Symmetry boundary conditions are imposed on the left boundary of the computational domain and non reflecting boundary conditions are imposed on the right and top boundary. On the bottom boundary, no slip conditions are imposed. As shown in Chapter 6, viscous terms have secondary effects on the dynamics of the supersonic jet, thus they are neglected in the following simulations.

Parameter	**Symbol**	**Value**	**Units**
Viscosity	μ_g	0.000013	Pa·s
Thermal conductivity	k_g	0.015	W/m·K
Molecular weight	M_{mol}	0.018	kg/mol
Specific gas constant	R_g	461.8	J/kg·K
Specific heat	$c_{p,g}$	1800	J/kg·K

Table 8.1: Water vapor properties at temperature $T = 373$ K.

8.2.1 Monodisperse mixtures

Let us consider a monodisperse mixture composed by water vapor and one class of solid particles. Two sets of vent conditions are considered, which differ for the mass flow rate M_f, defined as

$$M_f = \frac{\pi D_v^2}{4} \rho_{mix} w_{mix}, \tag{8.7}$$

where D_v is the vent diameter, ρ_{mix} and w_{mix} are the mixture density and velocity at the vent, respectively. In Case A, the mass flow rate is of the order of 10^8 kg/s, corresponding to a large Plinian volcanic eruption, whereas in Case B the mass flow rate is of the order of 10^6 kg/s, corresponding to a relatively small volcanic eruption [94]. The differences in the mass flow rates are due to different vent diameters, i.e. 80 m in Case A and 20 m in Case B, different vent pressure and different mixture density. In particular, in Case A the gas pressure and the mixture density are four times the values imposed in Case B. Vent conditions for Case A and Case B are shown in Table 8.3.

In Case A, the computational domain is a two dimensional box with dimension 800 m $\times$ 2400 m divided into 400 $\times$ 600 computational cells. The mesh size is $\Delta x = 4$m with time step $\Delta t = 10^{-3}$ s. The simulation extends up to time $t = 20$ s. In Case B, the dimension of the computational domain is 200 m $\times$ 400 m divided into 200 $\times$ 800 computational cells. The mesh size is not uniform in the two dimensions, i.e. $\Delta x = 1$ m and $\Delta z = 0.5$ m, and the time step is $\Delta t = 5 \cdot 10^{-5}$ s. The simulation extends up to time $t = 2$ s. Both in Case A and in Case B, a second order finite volume scheme in space with the implicit time advancing scheme presented in Section 5.3.1 is adopted to solve multiphase equations.

For both Case A and Case B, five different simulations are carried out with different mixture composition, but maintaining the mixture density fixed. Five different classes of solid particles, with different diameters and densities, are selected. The values of the volumetric fractions are computed in order to maintain the mixture densities fixed and are reported in Table 8.3. The mixture compositions for simulations (a)-(e) for Case A and Case B are reported in Table 8.4 and 8.5, respectively. For each class of solid particles, the values of the particle loading are shown, together with particle diameters, densities and volumetric fractions.

For Case A and Case B, the characteristic time scales are shown in Table 8.4 and Table 8.5, respectively. Since in this work the particle density is assumed to be a function of the particle diameter, the particle relaxation time can be expressed as a function of the particle diameter only:

$$\tau_s \simeq \frac{\rho_s(d_s) d_s^2}{18 \mu_g}, \tag{8.8}$$

where the gas viscosity is supposed to be constant. On the other hand, the Mach disk

Parameter	Symbol	Value	Units
Viscosity	μ_s	0.5	Pa·s
Thermal conductivity	k_s	2	W/m·K
Specific heat	$c_{p,s}$	1000	J/kg·K

Table 8.2: Solid particle thermodynamic properties.

formation time depends only slightly on the mixture composition for large values of the particle loading, which is assumed to be constant for Case A ($\beta_A = 48$) and Case B ($\beta_B = 44$). Analogously, also the Mach disk formation time can be assumed to be constant for Cases A and B and equal to 0.37 s and 0.09 s, respectively. Since the coupling between the particle dynamics and the gas dynamics depends on the difference in the characteristic time scales of the problem, the Stokes number defined as the ratio between the particle relaxation time and the Mach disk formation time is computed as a function of the particle diameter only:

$$St(d_s) = \frac{\tau_s(d_s)}{\tau_{Ma}}. \tag{8.9}$$

The functions $St_A(d_s)$ and $St_B(d_s)$ are shown in Figure 8.4, together with the reference value $St = 1$. Notice that in both Case A and Case B, test cases (a), (b), (c) are characterized by a value of St lower than one, whereas test cases (d) and (e) correspond to values of St larger than one.

Numerical results for Case A at time $t = 20$ s are shown in Figure 8.5. The logarithm to the base 10 of the particle volume fractions and the isolines of gas vertical velocity are plotted for the five test cases, corresponding to the five different particle sizes considered. Results obtained in cases (a), (b) and (c) are approximately equal. The mixture expands in the region above the vent up to 350 meters, then compresses across the normal shock wave. In case (d), the shock wave becomes weaker and finally it disappears completely in case (e). The total height of the column at $t = 20$ s slightly dependent on the class of solid particles: it is around 1500 m in case (a) and it tends to increase up to 2000 m in case (e). The structure of the lateral vortex that forms in the highest part of the jet is much more affected by mixture composition: in fact, larger particles in cases (d) and (e) tend to be ejected outward from the center of the vortex due to their larger inertia, whereas smaller particles in cases (a), (b) and (c) are uniformily distributed in the lateral vortex.

In order to understand better what is happening inside the jet, we can look at the values of the thermodynamic variables on the vertical axis of the jet in Figure 8.6. We can observe that gas pressure, mixture density, gas velocity and temperature in cases (a), (b) and (c) are almost identical. Gas pressure decreases from the initial value of $2 \cdot 10^6$ Pa to 10^4 Pa at 350 m from the vent, where the Mach disk is located. The mixture is compressed through the normal shock and reaches the equilibrium atmospheric pressure of 10^5 Pa, that remains almost constant along the upper part of the profile. Analogously, the mixture density decreases, in the expansion region, from 160 kg/m^3 down to 1 kg/m^3, then across the shock it reaches the final equilibrium value of 10 kg/m^3. The mixture is accelerated in the expansion region from the initial velocity of 150 m/s almost up to 400 m/s. Across the shock, the mixture is slowed down abruptly to subsonic speeds. Finally, gas temperature decreases from 1200 K to 1150 K in the expansion stage and then across the shock it increases up to 1180 K. In the upper part of the jet, temperature tends to decrease gradually, due to the entrainment of cold atmospheric air. In cases (a), (b) and (c) the flow above the Mach disk is unstable, due to the negative buoyancy of the compressed mixture, which causes negative vertical velocity. In some cases, this can destabilize the eruptive column causing collapse [97]. The same behaviour is observed also in the other thermodynamic variables.

In case (d) the normal shock wave becomes weaker and the maximum value of the gas velocity reached across the shock decrease to 300 $\mathrm{m/s}$. Analogously, the minimum values of gas pressure, mixture density and gas temperature increase.

The jet dynamics observed in case (e) ($St \gg 1$) is completely different from the previous test cases. First, no shock wave is forming in the core of the jet. After the initial expansion, the gas compresses gradually up to atmospheric pressure. The same smooth behaviour is also observed in the other thermodynamic quantities. Pressure and mixture density equilibrium values in the upper part of the jet coincide with the values obtained in the previous test cases. On the contrary, the equilibrium velocity in the upper part of the jet is equal to the initial velocity at the vent, i.e. 150 $\mathrm{m/s}$. Analogously, the equilibrium temperature is almost equal to the vent temperature (1190 K) and remains constant along the axis in the upper part of the jet, suggesting that entrainment processes are less efficient.

In order to understand the behaviour of solid particles in the jet as a function of their size, the differences between particle and gas velocity and temperature are shown in Figure 8.7. We observe that, in cases (a) and (b), these differences are negligible along the vertical axis of the jet. In case (c), small differences are observed near the normal shock location. In case (d), particles accumulate a delay in the expansion region, which is of the order of 10 $\mathrm{m/s}$. At 350 meters from the vent, where the gas is abruptly decelerated through the shock, particles do not decelerate immediately, but need about 50 meters to slow down to the surrounding gas velocity. Across the flow discontinuity, particles display a maximum velocity jump of 90 $\mathrm{m/s}$. A similar behaviour is observed in the temperature differences, where particles cool down slower than the gas phase in the expansion region and need 50 meters to warm up to the gas temperature above the shock. In case (e), particle dynamics is strongly decoupled from gas dynamics. In the expansion region, as the gas phase accelerates from 150 to 300 $\mathrm{m/s}$ at 200 meters from the vent, particles reach a maximum velocity delay of 35 $\mathrm{m/s}$, thus meaning that here they are moving much slower than the gas phase, due to their larger inertia. Above 200 meters, the gas phase starts to decelerate gradually, however particles do not slow down as fast as the gas phase. At 360 meters from the vent, particles are moving faster than the gas phase of about 65 $\mathrm{m/s}$. They need more than 200 meters to slow down to the equilibrium velocity. An analogous behaviour is observed in the temperature difference.

In order to explain the observed values in terms of the Stokes number St, the numerical results presented for Case A allow to formulate two preliminary hypotheses:

(H1) the Stokes number St defined as the ratio between the particle relaxation time and the Mach disk formation time is appropriate to describe the particle dynamics inside the underexpanded multiphase jet;

(H2) the decompression dynamics of the underexpanded multiphase jet is controlled by the particle Stokes number (St). In particular, for $St \ll 1$ the expected structure of an underexpanded jet, i.e. the formation of the Mach disk, is observed. On the other hand, for $St \gg 1$, the normal shock does not form.

In order to find further arguments in favour of our hypotheses, we repeat the previous analyses for Case B. In Figure 8.8 the logarithm to the base 10 of particle volume

fractions and the isolines of the gas vertical velocity are shown at time $t = 2$ s. In cases (a), (b) and (c), for which the values of the Stokes number St are 0.002, 0.02 and 0.2 respectively, the Mach disk is clearly observed at 50 meters from the vent. The volcanic column reaches about 250 meters height. On the other hand, in cases (d) and (e), that correspond to $St = 2$ and $St = 22$ respectively, the Mach disk is not forming. Moreover, the lateral vortex is collapsing due to the gravitational force. This results are a first argument in favour of the hypothesis (H2). Looking at the profiles along the vertical axis of the jet in Figure 8.9 and in Figure 8.10, we observe how in cases (a), (b) and (c) a strong shock is formed at 50 meters from the vent. Moreover, particles are coupled with the gas phase and only a strong and localized jump in the difference between particle and gas velocity is observed in case (c) at the shock location. On the contrary, in cases (d) and (e) a significant disequilibrium between gas phase and particles is observed in the expansion region and in the upper part of the volcanic column, thus supporting the hypothesis (H1).

Monodisperse jet			
Parameter	Case A	Case B	Units
D_v	80	20	m
K	20	5	
P_{atm}	101325	101325	Pa
T_{atm}	298	298	K
w_g	150	150	m/s
P_g	2026500	506625	Pa
T_g	1200	1200	K
ρ_g	3.7	0.92	kg/m^3
w_s	150	150	m/s
T_s	1200	1200	K
ρ_{mix}	161.74	40.50	kg/m^3
M_f	$1.22{\cdot}10^8$	$1.91{\cdot}10^6$	kg/s

Table 8.3: Inlet conditions for the monodisperse jet.

Monodisperse jet – Case A						
Parameter	(a)	(b)	(c)	(d)	(e)	Units
d_s	8	27	95	346	1300	μm
ρ_s	2500	2500	2052.5	1520.6	977	kg/m^3
ϵ_s	0.063324	0.063324	0.077149	0.104162	0.162391	
β	46.2	46.2	46.9	48.3	51.8	
c_{mix}	109	109	108	106	103	m/s
τ_s	0.0007	0.0078	0.0792	0.7783	7.0568	s
τ_{Ma}	0.36	0.36	0.37	0.37	0.38	s
St	0.0019	0.0212	0.2138	2.0710	18.1518	

Table 8.4: Monodisperse jet. Case A. $D_v = 80$ m, $K = 20$, $\rho_{mix} = 161.74$ kg/m^3 and $M_f = 1.22 \cdot 10^8$ kg/s. Particle properties and characteristic time scales for different values of the particle diameter.

Monodisperse jet – Case B						
Parameter	(a)	(b)	(c)	(d)	(e)	Units
d_s	4	14	45	161	607	μm
ρ_s	2500	2500	2359.4	1835	1290.2	kg/m^3
ϵ_s	0.015838	0.015838	0.016779	0.021571	0.030699	
β	44.0	44.0	44.0	44.2	44.7	
c_{mix}	112	111	111	111	110	m/s
τ_s	0.0002	0.0021	0.0204	0.2034	2.0315	s
τ_{Ma}	0.089	0.089	0.089	0.09	0.09	s
St	0.0019	0.0234	0.2276	2.2613	22.4634	

Table 8.5: Monodisperse jet. Case B. $D_v = 20$ m, $K = 5$, $\rho_{mix} = 40.5$ kg/m^3 and $M_f = 1.91 \cdot 10^6$ kg/s. Particle properties and characteristic time scales for different values of the particle diameter.

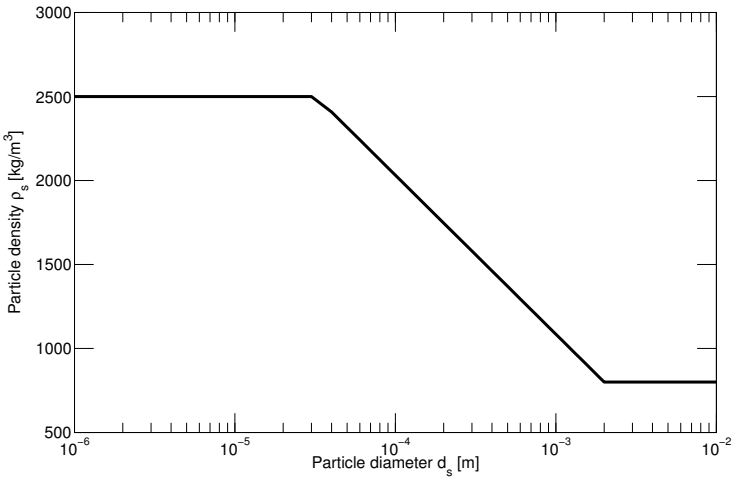

Figure 8.3: Empirical relationship between particle density ρ_s and particle diameter d_s. This relationship is assumed in all the simulations proposed in this chapter.

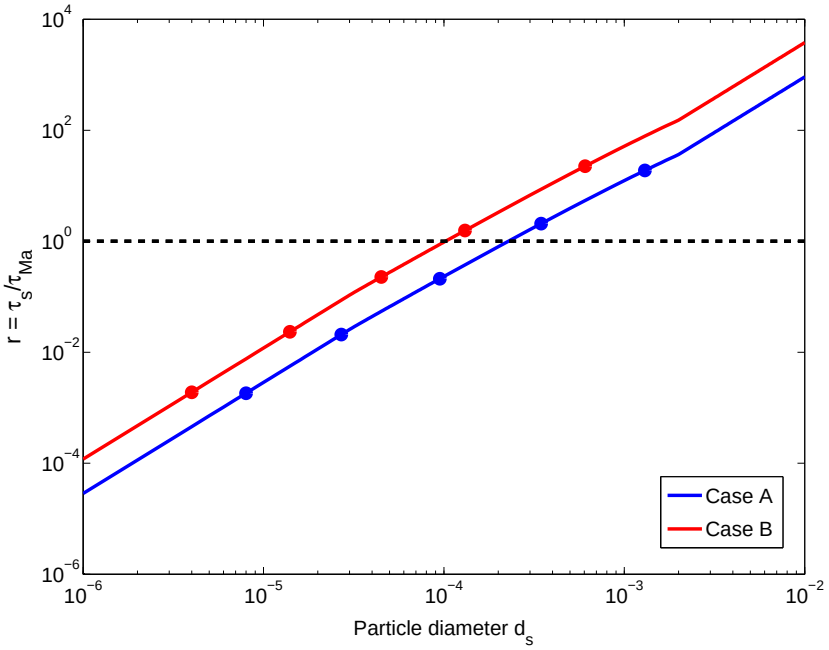

Figure 8.4: Monodisperse jet. Stokes number $St = \frac{\tau_s}{\tau_{Ma}}$ as a function of particle diameter d_s for Case A and Case B.

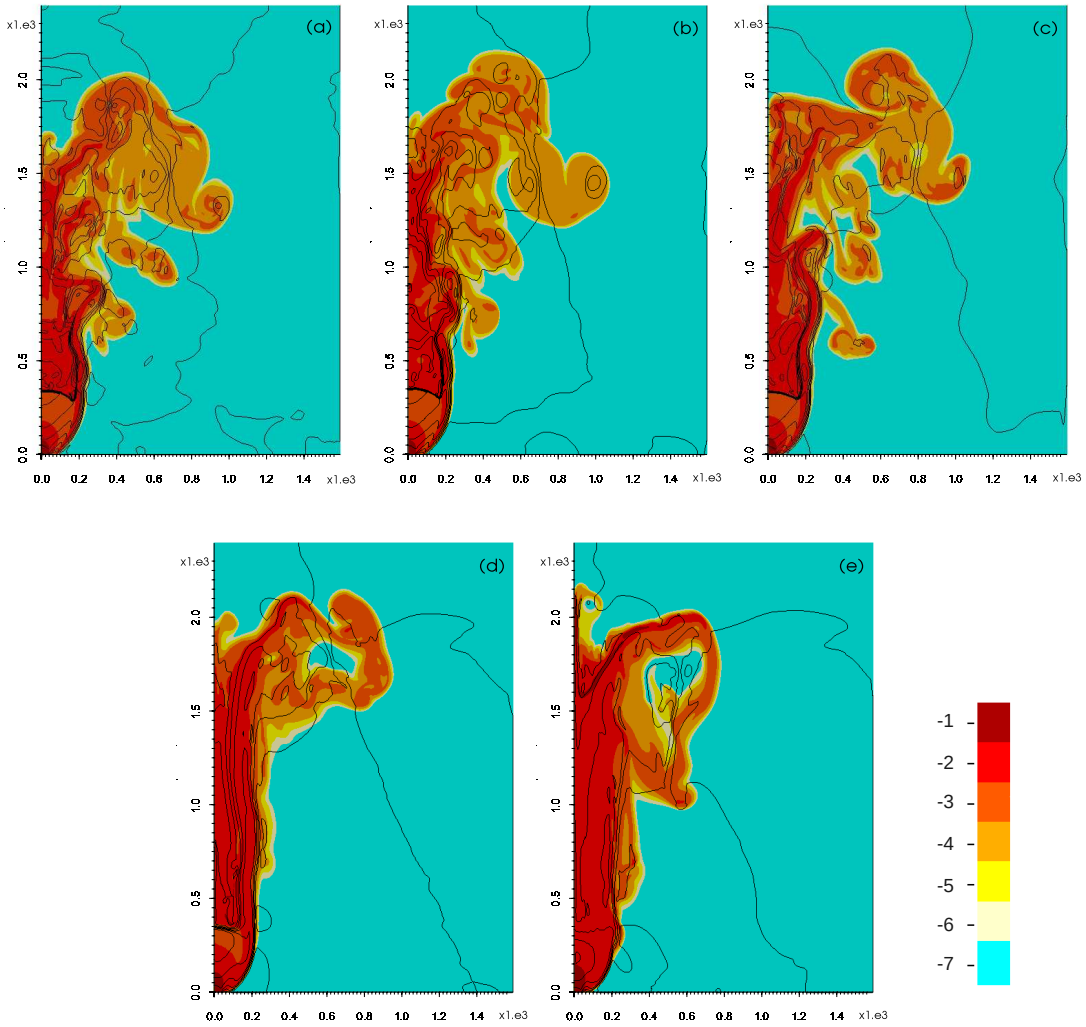

Figure 8.5: Monodisperse jet. Case A. $D_v = 80$ m, $K = 20$, $\rho_{mix} = 161.74\,\mathrm{kg/m^3}$ and $M_f = 1.22{\cdot}10^8$ kg/s. Logarithm to the base 10 of particle volume fractions from 10^{-7} to 10^{-1} and isolines of gas vertical velocity [0:50:350] m/s at time $t = 20$ s. Comparison between different values of particle diameter: **(a)** $d_s = 8$ μm, $St = 0.0019$, **(b)** $d_s = 27$ μm, $St = 0.0212$, **(c)** $d_s = 95$ μm, $St = 0.2138$, **(d)** $d_s = 346$ μm, $St = 2.071$, **(e)** $d_s = 1300$ μm, $St = 18.1518$.

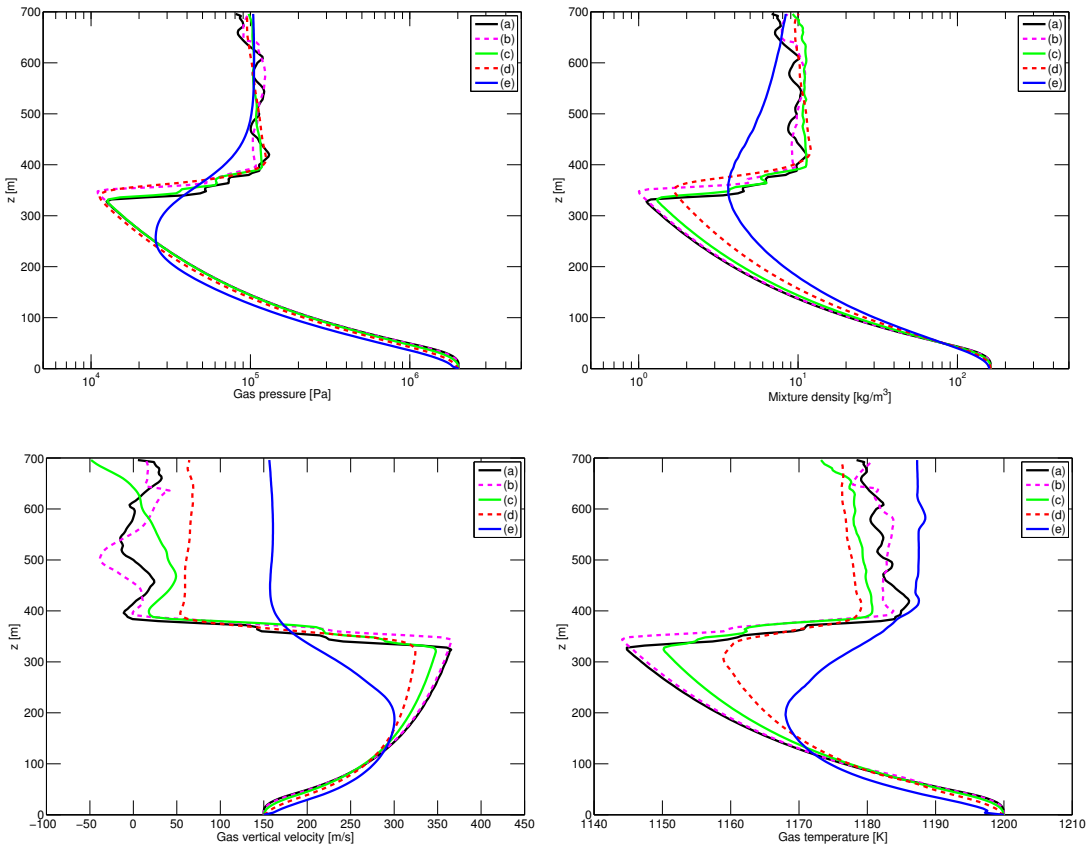

Figure 8.6: Monodisperse jet. Case A. $D_v = 80$ m, $K = 20$, $\rho_{mix} = 161.74\,\mathrm{kg/m^3}$ and $M_f = 1.22{\cdot}10^8$ kg/s. Time-averaged axial profiles computed over the interval $[16, 20]$ s of gas pressure, mixture density, gas vertical velocity and gas temperature. Comparison between different values of particle diameter: **(a)** $d_s = 8$ μm, $St = 0.0019$, **(b)** $d_s = 27$ μm, $St = 0.0212$, **(c)** $d_s = 95$ μm, $St = 0.2138$, **(d)** $d_s = 346$ μm, $St = 2.071$, **(e)** $d_s = 1300$ μm, $St = 18.1518$.

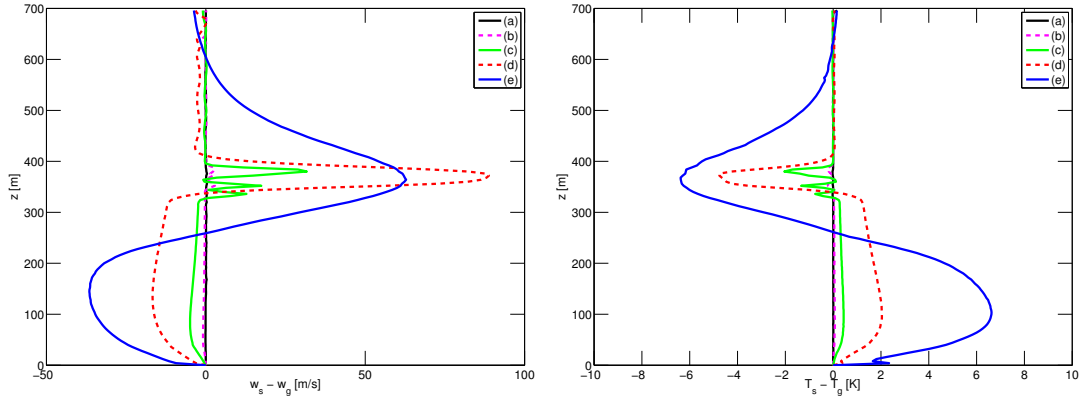

Figure 8.7: Monodisperse jet. Case A. $D_v = 80$ m, $K = 20$, $\rho_{mix} = 161.74\,\mathrm{kg/m^3}$ and $M_f = 1.22 \cdot 10^8$ kg/s. Time-averaged axial profiles computed over the interval $[16, 20]$ s of the differences between particle and gas vertical velocity and temperature. Comparison between different values of particle diameter: **(a)** $d_s = 8$ μm, $St = 0.0019$, **(b)** $d_s = 27$ μm, $St = 0.0212$, **(c)** $d_s = 95$ μm, $St = 0.2138$, **(d)** $d_s = 346$ μm, $St = 2.071$, **(e)** $d_s = 1300$ μm, $St = 18.1518$.

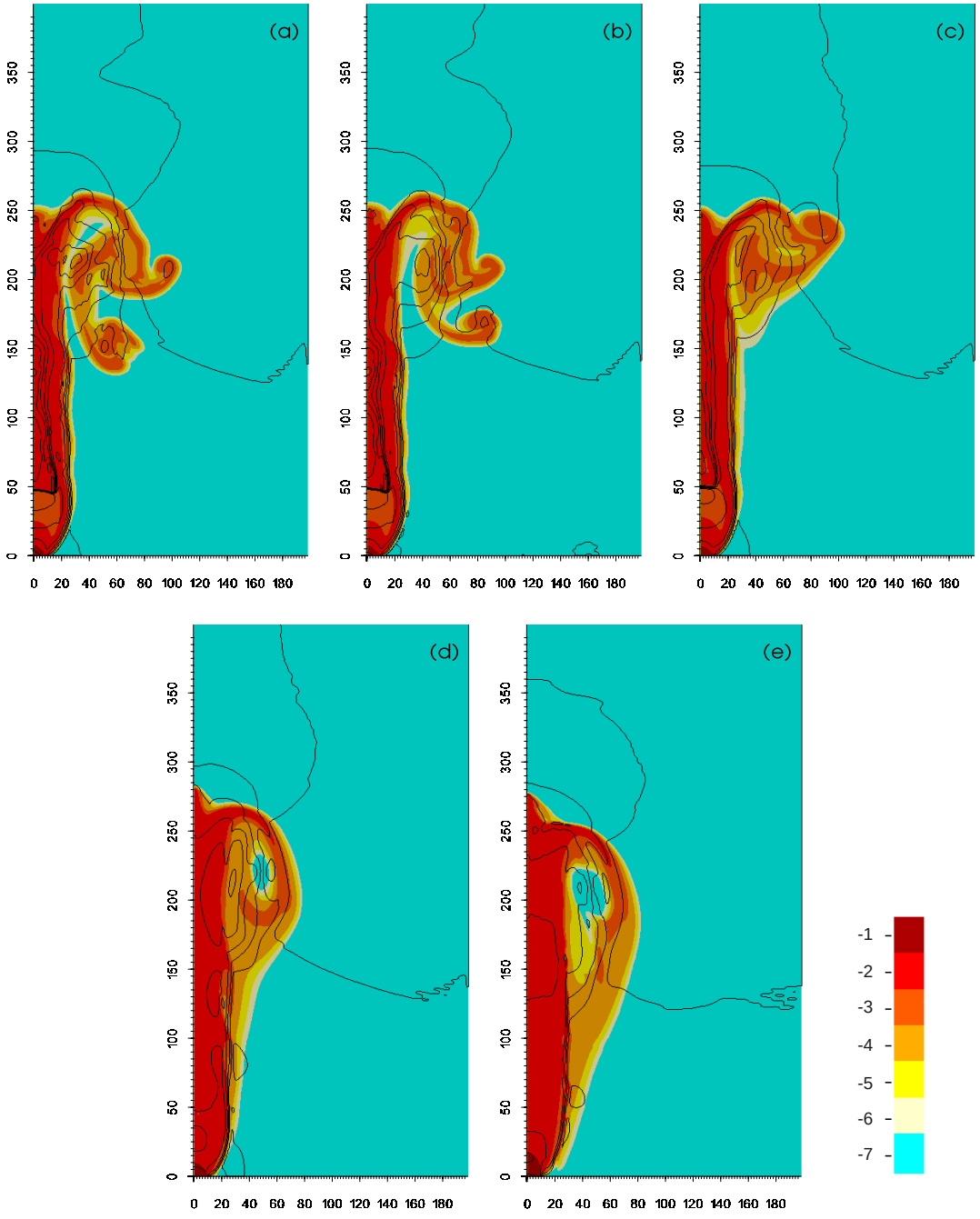

Figure 8.8: Monodisperse jet. Case B. $D_v = 20$ m, $K = 5$, $\rho_{mix} = 40.5$ kg/m^3 and $M_f = 1.91 \cdot 10^6$ kg/s. Logarithm to the base 10 of particle volume fractions from 10^{-7} to 10^{-1} and isolines of gas vertical velocity [0:50:350] m/s at time $t = 2$ s. Comparison between different values of particle diameter: **(a)** $d_s = 4$ μm, $St = 0.0019$, **(b)** $d_s = 14$ μm, $St = 0.0234$, **(c)** $d_s = 45$ μm, $St = 0.2276$, **(d)** $d_s = 161$ μm, $St = 2.2613$, **(e)** $d_s = 607$ μm, $St = 22.4634$.

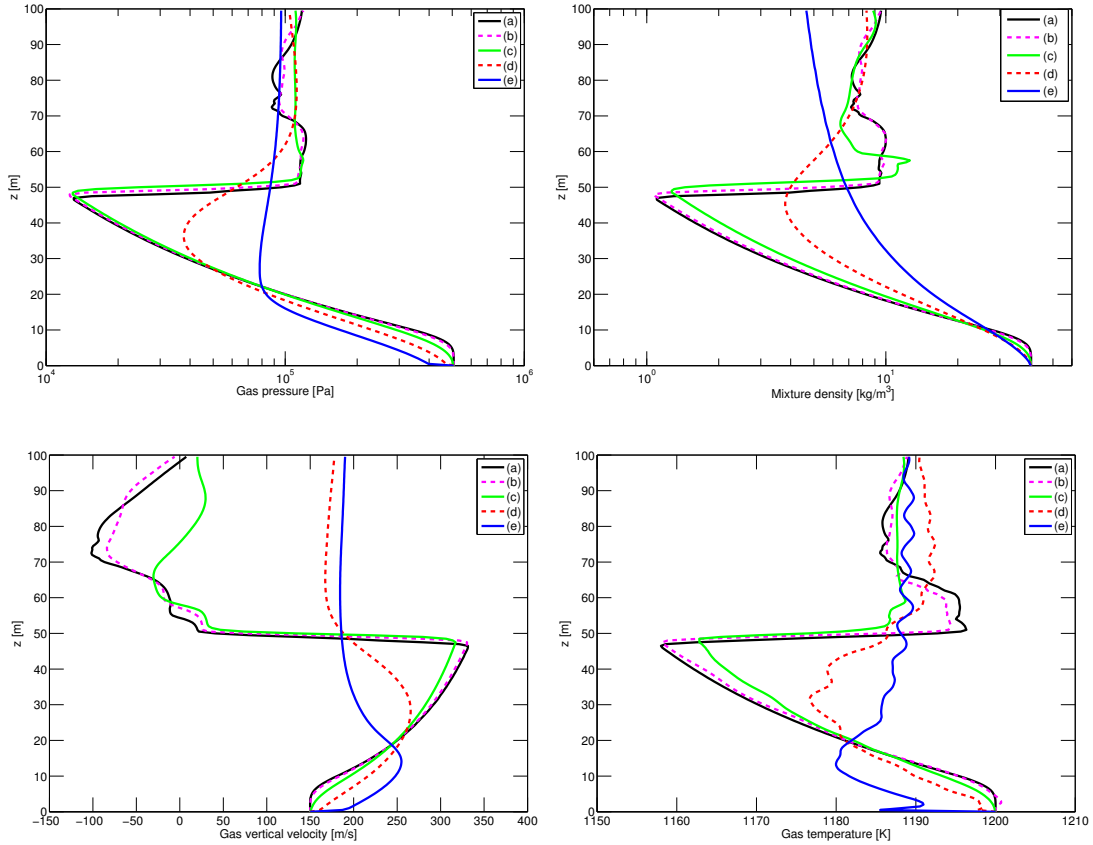

Figure 8.9: Monodisperse jet. Case B. $D_v = 20$ m, $K = 5$, $\rho_{mix} = 40.5$ kg/m^3 and $M_f = 1.91 \cdot 10^6$ kg/s. Time-averaged axial profiles computed over the interval $[1.5, 2]$ s of gas pressure, mixture density, gas vertical velocity and gas temperature. Comparison between different values of particle diameter: **(a)** $d_s = 4$ μm, $St = 0.0019$, **(b)** $d_s = 14$ μm, $St = 0.0234$, **(c)** $d_s = 45$ μm, $St = 0.2276$, **(d)** $d_s = 161$ μm, $St = 2.2613$, **(e)** $d_s = 607$ μm, $St = 22.4634$.

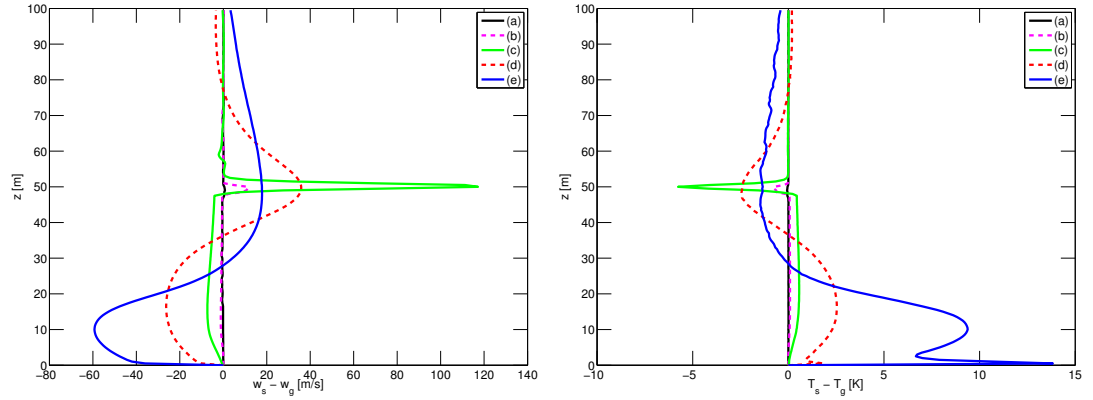

Figure 8.10: Monodisperse jet. Case B. $D_v = 20$ m, $K = 5$, $\rho_{mix} = 40.5$ kg/m^3 and $M_f = 1.91 \cdot 10^6$ kg/s. Time-averaged axial profiles computed over the interval $[1.5, 2]$ s of the differences between particle and gas vertical velocity and temperature. Comparison between different values of particle diameter: **(a)** $d_s = 4$ μm, $St = 0.0019$, **(b)** $d_s = 14$ μm, $St = 0.0234$, **(c)** $d_s = 45$ μm, $St = 0.2276$, **(d)** $d_s = 161$ μm, $St = 2.2613$, **(e)** $d_s = 607$ μm, $St = 22.4634$.

Dusty gas approximation of a monodisperse jet

Numerical experiments carried out in the previous section have shown that, for $St < 1$, particle dynamics are coupled to gas dynamics. Under this hypothesis, dusty gas models are valid and can be applied to reproduce the multiphase flow [86]. Thus, we apply the pseudogas model presented in Section 2.5 to repeat simulations (a), (b) and (c) for Case A and to compare the results obtained with the dusty model and the multiphase model. Numerical results obtained with dusty gas model for Case A, test case (b), are shown in Figures 8.11 and 8.12. Similar results have been obtained for cases (a) and (c). We can observe that the internal structure of the underexpanded multiphase jet is reproduced correctly, even if some differences between the multiphase and the dusty model results can be highlighted. In Figure 8.12 we observe how the dusty model tends to underestimate the extreme values of the thermodynamic quantities reached across the normal shock. Moreover, the equilibrium position of the normal shock obtained with the dusty model is displaced about 50 meters towards the vent. If we compare the shape of the normal shock obtained with the multiphase model (Figure 8.5b) and the dusty gas model (Figure 8.11), we observe how in the first case the shock is strongly concave downwards, whereas in the second case the shock is flattened in its central part. This difference in the shape of the shock results in the displacement of the Mach disk observed along the vertical axis of the jet.

Finally, the results obtained with the multiphase and the pseudogas models differ in the upper part of the jet. First, the height of the jet obtained with the dusty model is much larger than the one obtained with the multiphase model. Secondly, while the equilibrium vertical velocity of the mixture at time $t = 20$ s is small but positive with the multiphase model, with the dusty model it is negative, thus meaning that the mixture is already collapsing under gravitational effects. However, it is worth recalling that the particle Stokes number has been computed based on the underexpanded jet characteristic time while the multiphase coupling in the subsonic plume region may be governed by a different dynamics, implying a different definition of the Stokes number St.

In summary, for monodisperse mixtures numerical simulations overall justify the use of the pseudogas approximation for particles with $St \ll 1$. Despite some minor differences, the decompression structure of the volcanic jets is well reproduced by the dusty gas model.

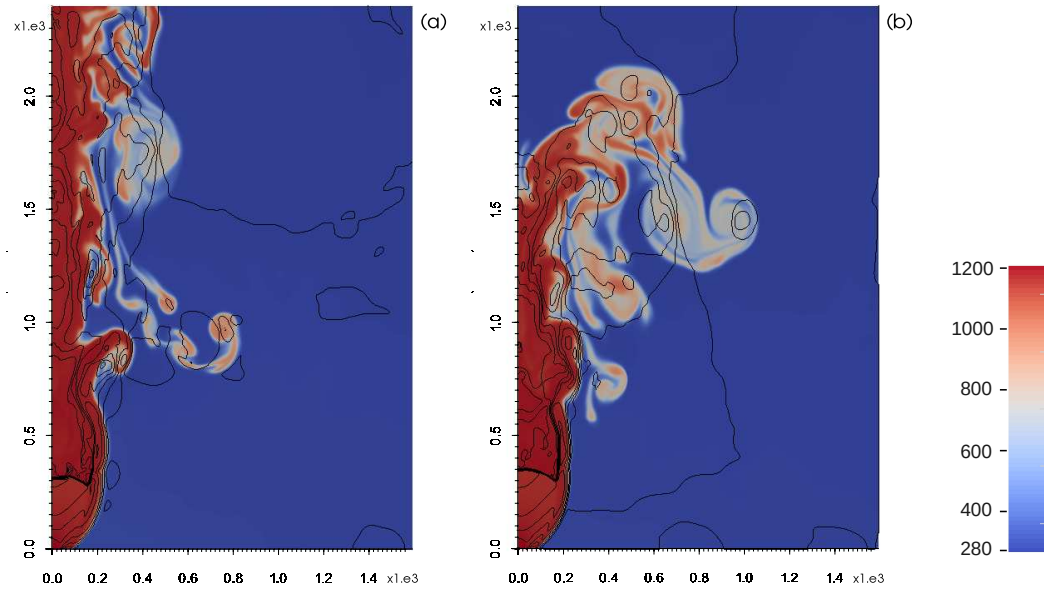

Figure 8.11: Monodisperse jet. Case A. $D_v = 80$ m, $K = 20$, $\rho_{mix} = 161.74$ kg/m^3 and $M_f = 1.22 \cdot 10^8$ kg/s. Isolines of pseudogas vertical velocity [0:50:350] m/s and mixture temperature from 280 to 1200 K at time $t = 20$ s. Comparison between **(a)** dusty model results and **(b)** multiphase model results for test **(b)** $d_s = 27$ μm, $St = 0.0212$.

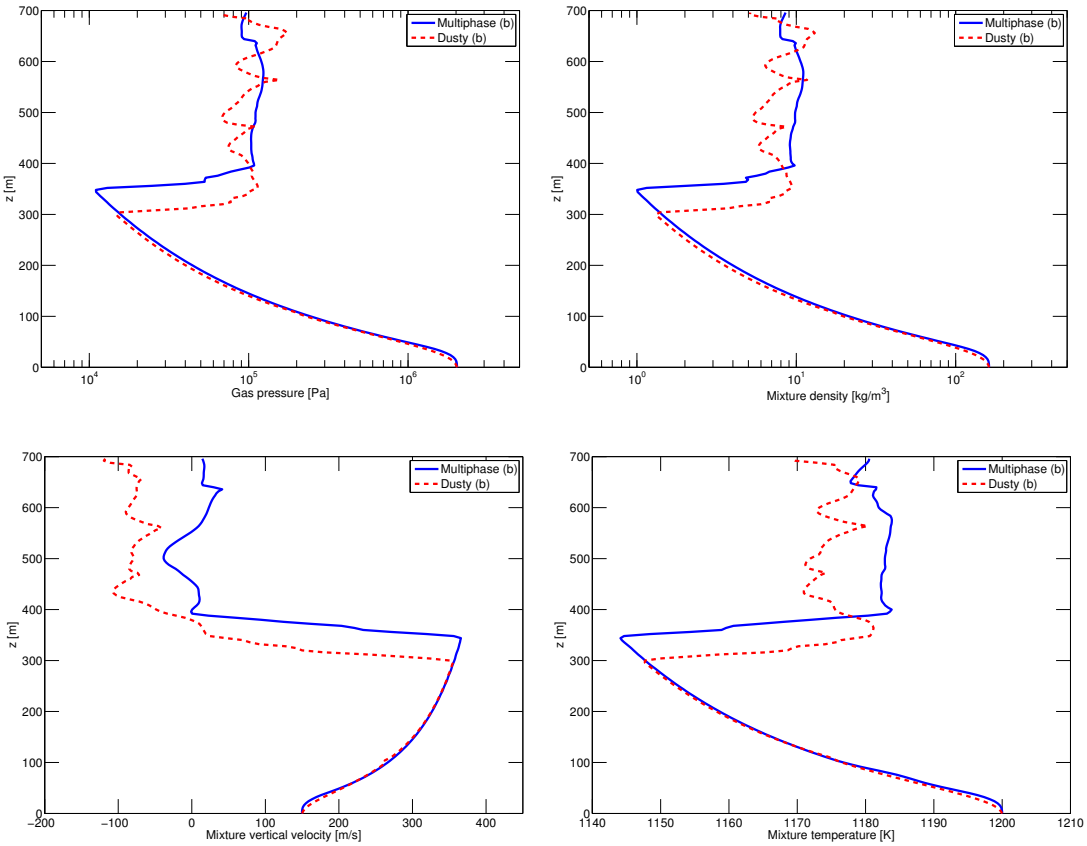

Figure 8.12: Monodisperse jet. Case A. $D_v = 80$ m, $K = 20$, $\rho_{mix} = 161.74$ kg/m^3 and $M_f = 1.22 \cdot 10^8$ kg/s. Time-averaged axial profiles computed over the interval $[16, 20]$ s of gas pressure, mixture density, mixture vertical velocity and mixture temperature. Comparison between Multiphase model results and Dusty model results for test **(b)** $d_s = 27$ μm, $St = 0.0212$.

8.2.2 Bidisperse mixtures

Let us consider a bidisperse mixture composed by water vapor and two classes of solid particles. The same vent conditions for Case A and Case B are considered, see Table 8.3, and the mixture composition is varied by maintaining the mass flow rate constant.

For Case A, three different mixture compositions are considered, as shown in Table 8.6. We consider two classes of solid particles, with diameters equal to 27μm ($\tau_{s1} = 0.00078$) and 1300 μm ($\tau_{s2} = 7.1$ s), respectively. In the three cases, the Mach disk formation time is almost constant, i.e. $\tau_{Ma} \simeq 0.38$ s. In test case (a), the volume fractions of the two classes of solid particles are comparable, i.e. $\epsilon_{s1} = 0.043755$ and $\epsilon_{s2} = 0.050184$. In case (b), the volume fraction of finer particles is reduced to $\epsilon_{s1} = 0.0045297$, whereas the concentration of coarser particle is increased up to $\epsilon_{s2} = 0.15078$. Finally, in case (c) the volume fraction of finer particles is much smaller that the one of of larger particles, i.e. $\epsilon_{s1} = 0.0001$ and $\epsilon_{s2} = 0.16213$. The Stokes number for the finer particles is equal to 0.02, thus we can assume that the first class of particles is tightly coupled to the gas phase. Larger particles have Stokes number equal to 18 and may display a different dynamics with respect to the gas phase.

Numerical results of tests (a), (b) and (c) for Case A are shown in Figure 8.14. We can observe how in cases (a) and (b) the standard structure of homogeneous underexpanded jets is observed, with the formation of the normal shock wave at 350 meters from the vent. The presence of the normal shock and its position can be clearly observed in Figure 8.15, where the axial profiles of thermodynamic quantities are shown. In case (c), instead, the Mach disk is not forming.

In order to extend the analysis carried out in the previous section for monodisperse mixtures to bidisperse mixtures, we introduce the dusty gas composed by pure water vapor and the solid particles $s1$ ($St \ll 1$), that are tightly coupled with the gas phase. Pseudogas properties can be computed as described in Section 2.5 and they are reported in Table 8.7. In particular, we account for the variation in the density, specific gas constant and dynamic viscosity (we refer to [145] for the correction of the dynamic viscosity, somehow accounting for the particle–particle drag). Larger particles $s2$ are dispersed in the pseudogas phase, forming a monodispersed mixture. We can now analyze the bidisperse mixture as a monodisperse mixture, by considering the class of solid particles $s2$ moving in a dusty gas with averaged properties. As a result, the Mach disk formation time remains unchanged, whereas the particle relaxation time $\tau_{s2,ps}$ varies as a function of the pseudogas properties (specifically, the pseudogas dynamic viscosity). In case (a), the particle characteristic time decreases to 0.006 s, in case (b) to 0.32 s and finally in case (c) it is equal to 6 s, see Table 8.7. Analogously, also the Stokes number $St_{s2,ps}$ decreases from the reference value of 18, which refers to particles $s2$ moving in the pure gas, as the concentration of particles $s1$ increases in cases (c), (b) and (a). The behaviour of $St_{s2,ps}$ as a function of the dusty gas composition, i.e. ϵ_1, is shown in Figure 8.13. From the results computed in Table 8.7 and for the hypothesis (H2), in cases (a) and (b) ($St < 1$) we expect the formation of the normal shock in the jet; on the contrary, in case (c) ($St > 1$) we do not expect the formation of the normal shock. Numerical results shown in Figures 8.14 and 8.15 confirm the validity of the analysis of bidisperse underexpaded jets based on the expression of St proposed.

The analysis carried out for test Case A has been repeated for test Case B, with three different mixture compositions, as shown in Table 8.8. Parameters of the hybrid pseudogas-multiphase model are reported in Table 8.9. As in Case A, tests (a) and (b) are characterized by a value of $St_{s2,ps}$ lower than one for particles $s2$ moving in the dusty gas, whereas in case (c) we obtain $St_{s2,ps} = 13.6$, as shown in Figure 8.13. In Figure 8.16 we observe how in cases (a) and (b) the Mach disk is forming at 50 meters from the vent, whereas in case (c) the jet does not present the normal shock. The conclusion is supported by the axial profiles of the thermodinamic quantities along the jet centerline.

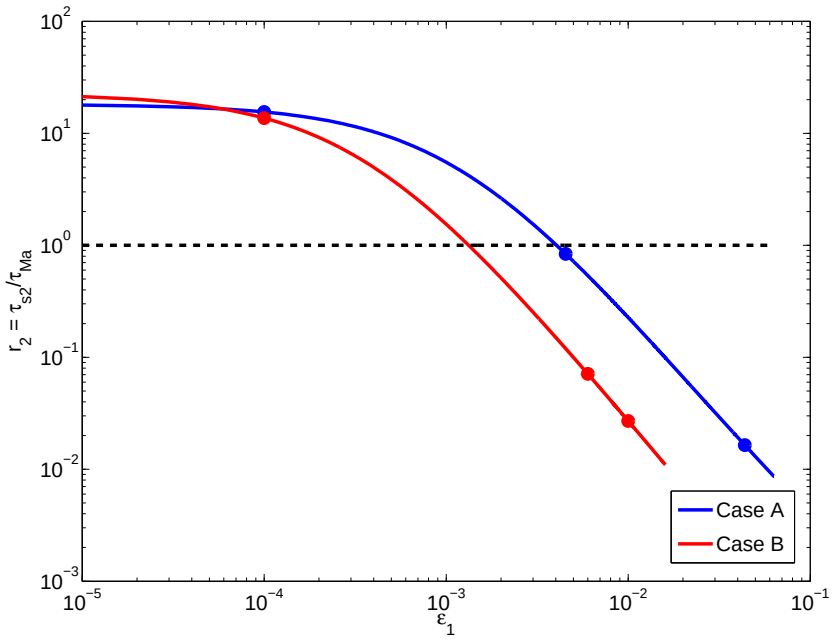

Figure 8.13: Bidisperse jet. Stokes number $St_{s2,ps} = \frac{\tau_{s2,ps}}{\tau_{Ma,ps}}$ as a function of fine particle concentration ϵ_{s1} for Case A and Case B.

Bidisperse jet – Case A				
Parameter	(a)	(b)	(c)	Units
d_{s1}	27	27	27	μm
ρ_{s1}	2500	2500	2500	kg/m^3
ϵ_{s1}	0.043755	0.0045297	0.0001	
$\%wt_{s1}$	69	7	0.16	
d_{s2}	1300	1300	1300	μm
ρ_{s2}	977	977	977	kg/m^3
ϵ_{s2}	0.050184	0.15078	0.16213	
$\%wt_{s2}$	31	93	99.84	
β	48	51	52	
c_{mix}	107	103	103	m/s
τ_{Ma}	0.37	0.38	0.39	s
τ_{s1}	0.0078	0.0078	0.0078	s
τ_{s2}	7.1	7.1	7.1	s
St_{s1}	0.021	0.02	0.02	
St_{s2}	18.9	18.2	18.1	

Table 8.6: Bidisperse jet. Case A. $D_v = 80$ m, $K = 20$, $\rho_{mix} = 161.74$ kg/m^3 and $M_f = 1.22 \cdot 10^8$ kg/s. Particle properties and characteristic time scales for different mixture composition.

Bidisperse jet – Case A – Hybrid model				
Parameter	(a)	(b)	(c)	Units
ρ_{ps}	119	17.0	3.9	kg/m^3
R_{ps}	14	99	427	J/kg·K
μ_{ps}	$1.5{\cdot}10^{-2}$	$2.8{\cdot}10^{-4}$	$1.5{\cdot}10^{-5}$	Pa·s
$c_{p,ps}$	1023	1171	1739	J/kg·K
d_{s2}	1300	1300	1300	μm
ρ_{s2}	977	977	977	kg/m^3
ϵ_{s2}	0.050184	0.15078	0.16213	
β_{ps}	0.42	10.2	47.8	
$c_{mix,ps}$	107	103	103	m/s
$\tau_{Ma,ps}$	0.37	0.38	0.39	s
$\tau_{s2,ps}$	0.006	0.32	6.0	s
$St_{s2,ps}$	0.016	0.839	15.5	

Table 8.7: Bidisperse jet. Hybrid pseudogas-multiphase model. Case A. $D_v = 80$ m, $K = 20$, $\rho_{mix} = 161.74$ kg/m^3 and $M_f = 1.22 \cdot 10^8$ kg/s. Pseudogas properties, particle properties and characteristic time scales.

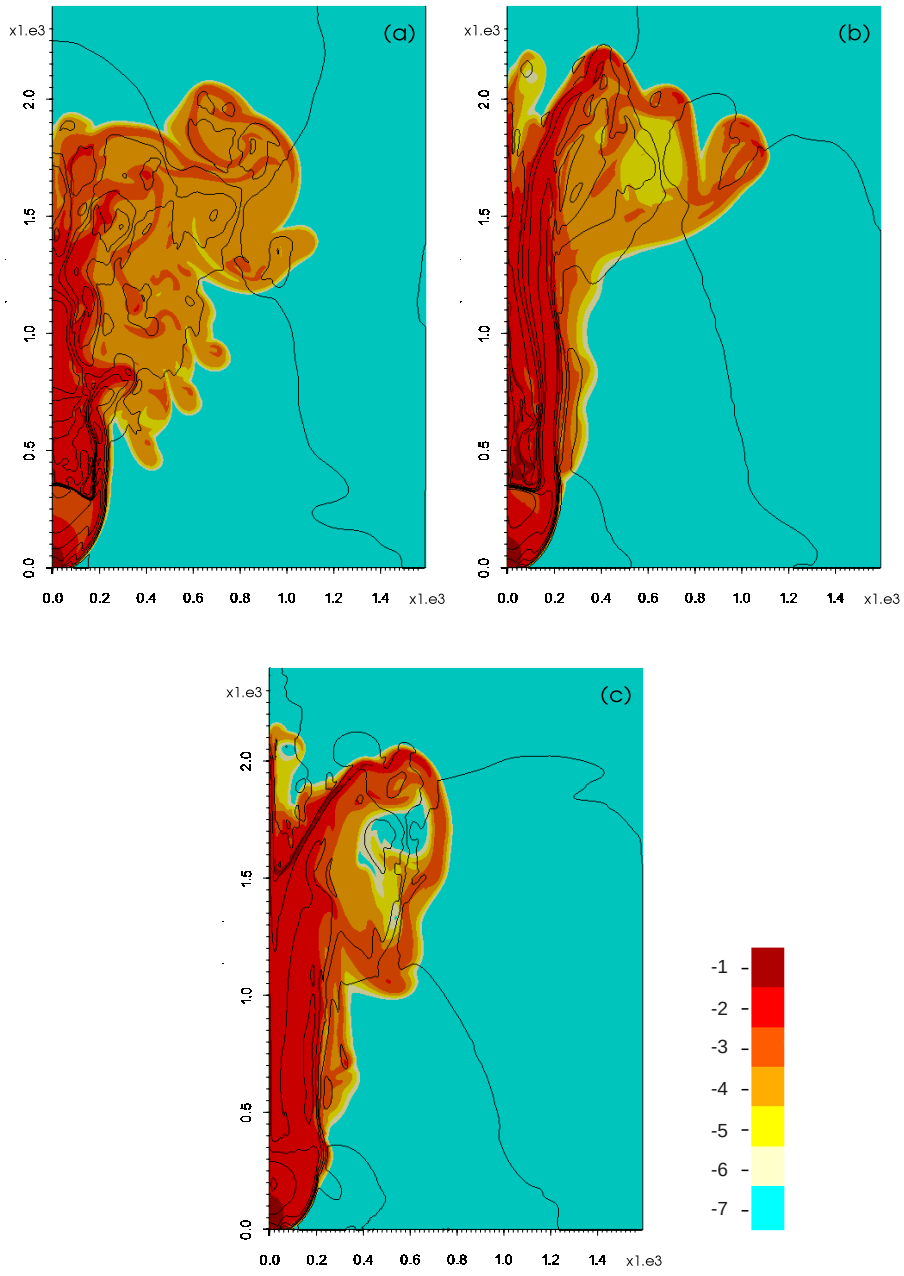

Figure 8.14: Bidisperse jet. Case A. $D_v = 80$ m, $K = 20$, $\rho_{mix} = 161.74\,\mathrm{kg/m^3}$ and $M_f = 1.22 \cdot 10^8$ kg/s. Logarithm to the base 10 of total particle volume fractions from 10^{-7} to 10^{-1} and isolines of gas vertical velocity [0:50:350] m/s at time $t = 20$ s. Comparison between different mixture composition: **(a)** $\epsilon_{s1} = 0.043755$, $\epsilon_{s2} = 0.050185$, **(b)** $\epsilon_{s1} = 0.0045297$, $\epsilon_{s2} = 0.15078$, **(c)** $\epsilon_{s1} = 0.0001$, $\epsilon_{s2} = 0.16213$.

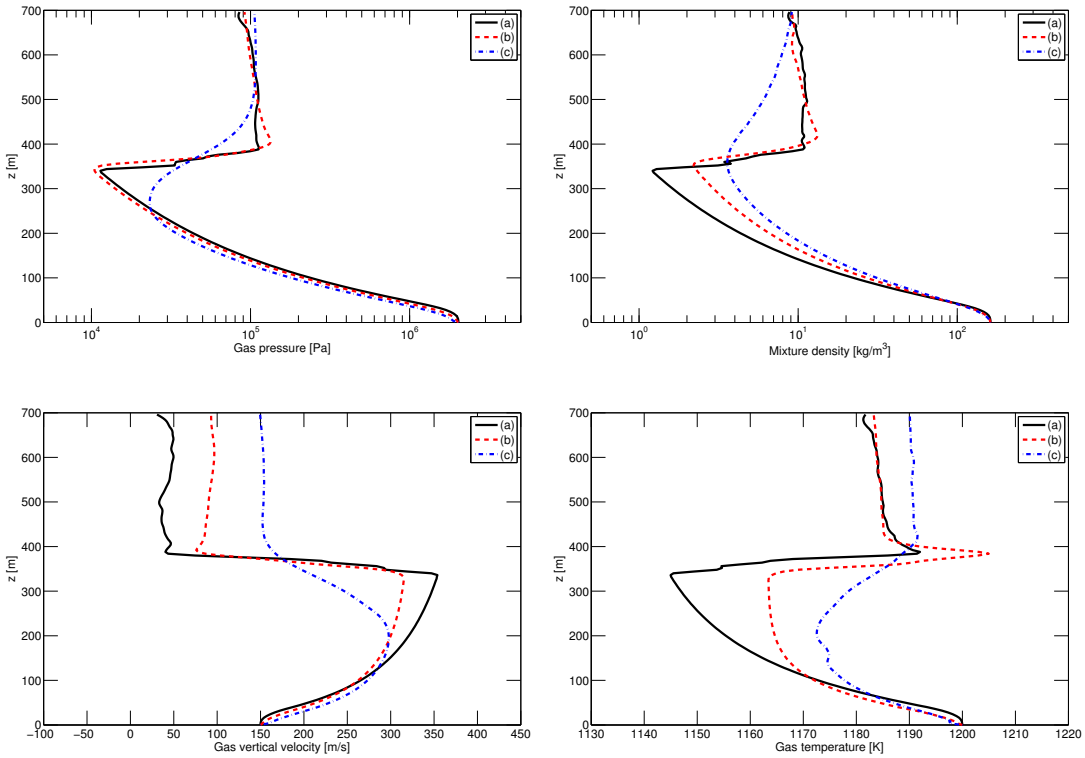

Figure 8.15: Bidisperse jet. Case A. $D_v = 80$ m, $K = 20$, $\rho_{mix} = 161.74\ \mathrm{kg/m^3}$ and $M_f = 1.22 \cdot 10^8$ kg/s. Time-averaged axial profiles computed over the interval $[16, 20]$ s of gas pressure, mixture density, gas vertical velocity and gas temperature. Comparison between different mixture composition: **(a)** $\epsilon_{s1} = 0.043755$, $\epsilon_{s2} = 0.050185$, **(b)** $\epsilon_{s1} = 0.0045297$, $\epsilon_{s2} = 0.15078$, **(c)** $\epsilon_{s1} = 0.0001$, $\epsilon_{s2} = 0.16213$.

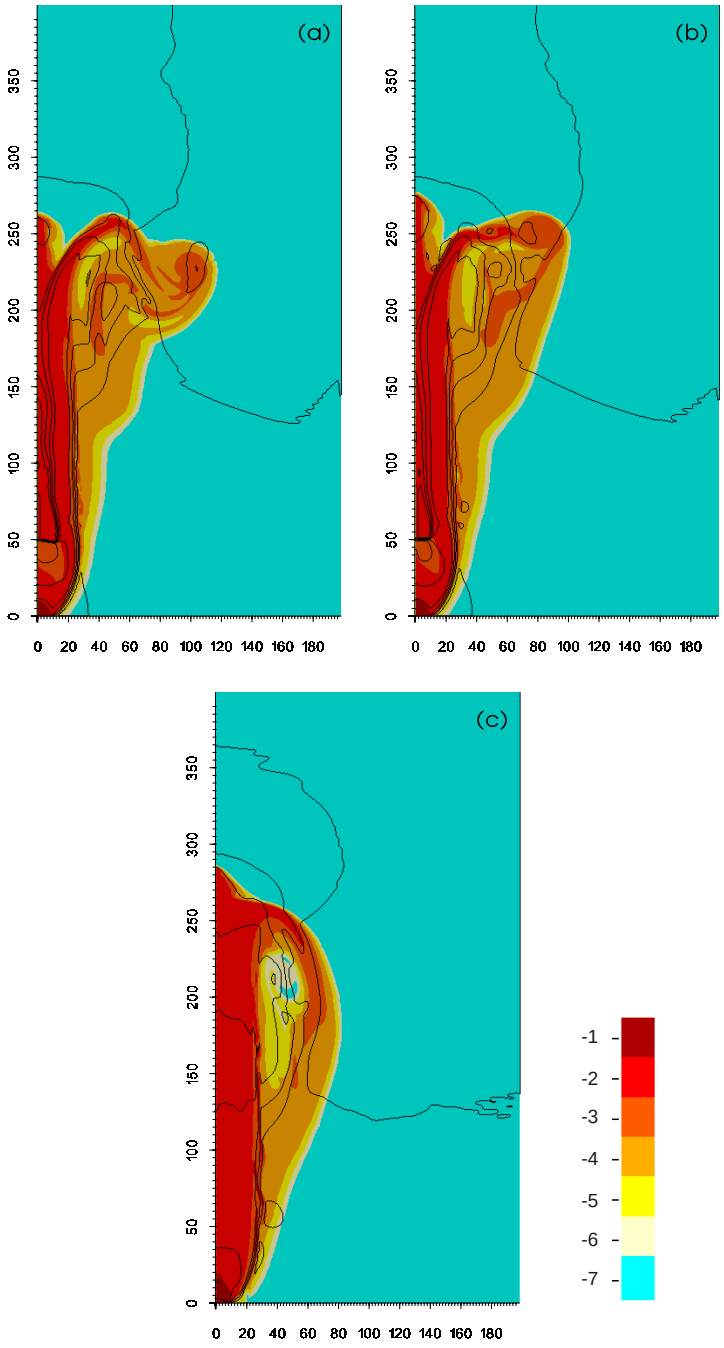

Figure 8.16: Bidisperse jet. Case B. $D_v = 20$ m, $K = 5$, $\rho_{mix} = 40.5$ kg/m^3 and $M_f = 1.91 \cdot 10^6$ kg/s. Logarithm to the base 10 of total particle volume fractions from 10^{-7} to 10^{-1} and isolines of gas vertical velocity [0:50:350] m/s at time $t = 2$ s. Comparison between different mixture composition: **(a)** $\epsilon_{s1} = 0.01$, $\epsilon_{s2} = 0.011316$, **(b)** $\epsilon_{s1} = 0.006$, $\epsilon_{s2} = 0.019069$, **(c)** $\epsilon_{s1} = 0.0001$, $\epsilon_{s2} = 0.030505$.

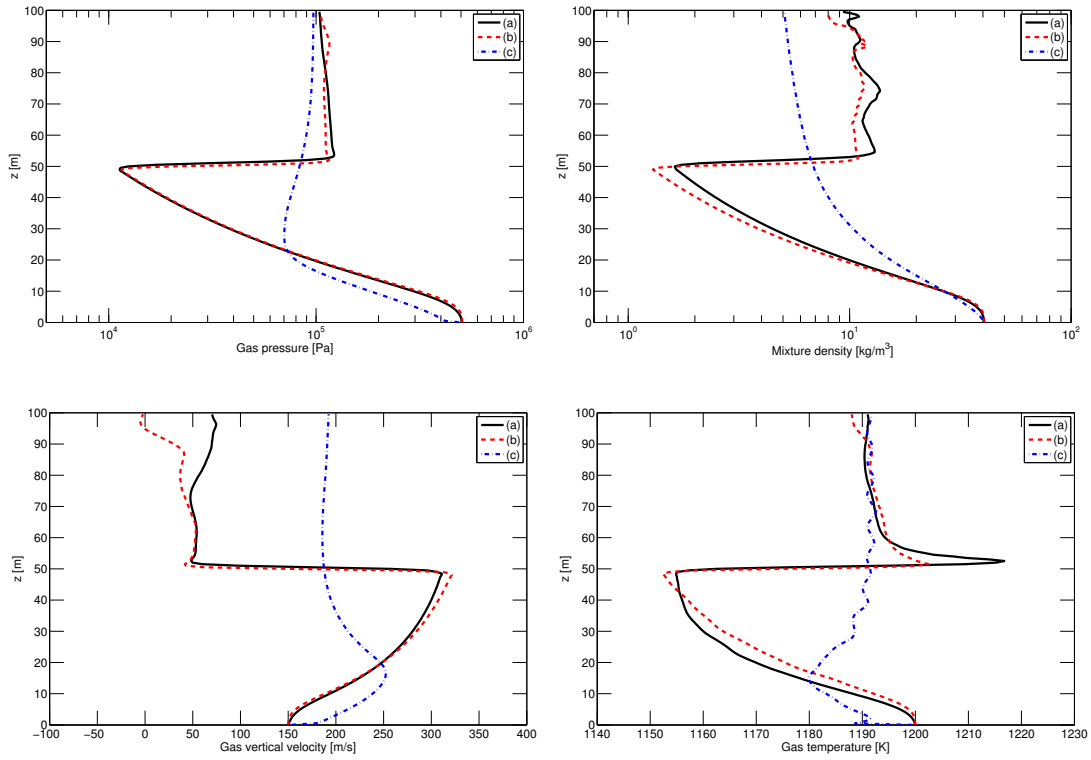

Figure 8.17: Bidisperse jet. Case B. $D_v = 20$ m, $K = 5$, $\rho_{mix} = 40.5$ kg/m^3 and $M_f = 1.91 \cdot 10^6$ kg/s. Time-averaged axial profiles computed over the interval $[1.5, 2]$ s of gas pressure, mixture density, gas vertical velocity and gas temperature. Comparison between different mixture composition: **(a)** $\epsilon_{s1} = 0.01$, $\epsilon_{s2} = 0.011316$, **(b)** $\epsilon_{s1} = 0.006$, $\epsilon_{s2} = 0.019069$, **(c)** $\epsilon_{s1} = 0.0001$, $\epsilon_{s2} = 0.030505$.

Dusty gas approximation of a bidisperse jet

Numerical simulations for bidisperse mixtures proposed in the previous section have been repeated adopting the pseudogas approach and introducing an hybrid pseudogas-multiphase model. The values of the Stokes number St with respect to the pure gas is used to classify particles. In the following simulations, the class of solid particles s_i is included in the pseudogas phase if the value of St_{s_i} is smaller than one, otherwise multiphase conservation equations for s_i are solved. In particular, in the simulations presented in this section particles $s1$ are included in the dusty gas, whereas particles $s2$ are considered as a distinct phase (see the corresponding values of St in Tables 8.6 and 8.8). Consequently, the resulting model is a hybrid pseudogas-multiphase model in which only two distinct phases are actually solved.

Numerical results for Case A are shown in Figures 8.18, 8.20 and 8.22 and Figures 8.19, 8.21 and 8.23, where a comparison between hybrid pseudogas-multiphase model and multiphase model results is proposed.

In test case (a) (Figures 8.18 and 8.19), results obtained with the hybrid model are in agreement with those obtained with the multiphase model in the decompression region. The profiles of thermodynamic quantities along the vertical axis of the jet are almost equal, as well as the location of the Mach disk and the jump of thermodynamic variables through it. As observed in the monodisperse test cases, some differences can be highlighted in the upper part of the jet, both in the height of the volcanic column and in the values of the velocity and the temperature.

In test case (b) (Figures 8.20 and 8.21) and test case (c) (Figures 8.22 and 8.23), both the structure of the decompression region and the values of the thermodynamic quantities along the axis of the jet are in good agreement and only small differences are observed in the upper part of the volcanic column. In particular, both the multiphase and the hybrid model predict the absence of the normal shock wave inside the underexpanded jet.

In order to assess the robustness of the proposed approach, the hybrid pseudogas-multiphase model has been applied to reproduce test (a), (b) and (c) for Case B. As shown in Figures 8.24, 8.26 and 8.28 and Figures 8.25, 8.27 and 8.29, numerical results obtained with the two models are in agreement and only small differences are observed in the thermodynamic quantities in the upper part of the volcanic column.

Bidisperse jet – Case B				
Parameter	(a)	(b)	(c)	Units
d_{s1}	14	14	14	μm
ρ_{s1}	2500	2500	2500	kg/m^3
ϵ_{s1}	0.01	0.006	0.0001	
$\%wt_{s1}$	63	35	0.63	
d_{s2}	607	607	607	μm
ρ_{s2}	1290.2	1290.2	1290.2	kg/m^3
ϵ_{s2}	0.011316	0.019069	0.030505	
$\%wt_{s2}$	37	65	99.37	
β	44.2	44.4	44.7	
c_{mix}	111	111	111	m/s
τ_{Ma}	0.09	0.09	0.09	s
τ_{s1}	0.002	0.002	0.002	s
τ_{s2}	2.0	2.0	2.0	s
St_{s1}	0.023	0.023	0.023	
St_{s2}	22.6	22.5	22.5	

Table 8.8: Bidisperse jet. Case B. $D_v = 20$ m, $K = 5$, $\rho_{mix} = 40.5$ kg/m^3 and $M_f = 1.91 \cdot 10^6$ kg/s. Particle properties and characteristic time scales for different mixture composition.

Bidisperse jet – Case B – Hybrid model				
Parameter	(a)	(b)	(c)	Units
ρ_{ps}	26.5	16.3	1.2	kg/m^3
R_{ps}	15.9	25.9	360.2	J/kg·K
μ_{ps}	$1.1{\cdot}10^{-2}$	$4.1{\cdot}10^{-3}$	$2.1{\cdot}10^{-5}$	Pa·s
$c_{p,ps}$	1028	1045	1624	J/kg·K
d_{s2}	607	607	607	μm
ρ_{s2}	1290.2	1290.2	1290.2	kg/m^3
ϵ_{s2}	0.011316	0.019069	0.030505	
β_{ps}	0.56	1.54	34.6	
$c_{mix,ps}$	111	111	111	m/s
$\tau_{Ma,ps}$	0.09	0.09	0.09	s
$\tau_{s2,ps}$	0.0025	0.0064	1.24	s
$St_{s2,ps}$	0.027	0.071	13.6	

Table 8.9: Bidisperse jet. Hybrid pseudogas-multiphase model. Case B. $D_v = 20$ m, $K = 5$, $\rho_{mix} = 40.5$ kg/m^3 and $M_f = 1.91 \cdot 10^6$ kg/s. Pseudogas properties, particle properties and characteristic time scales.

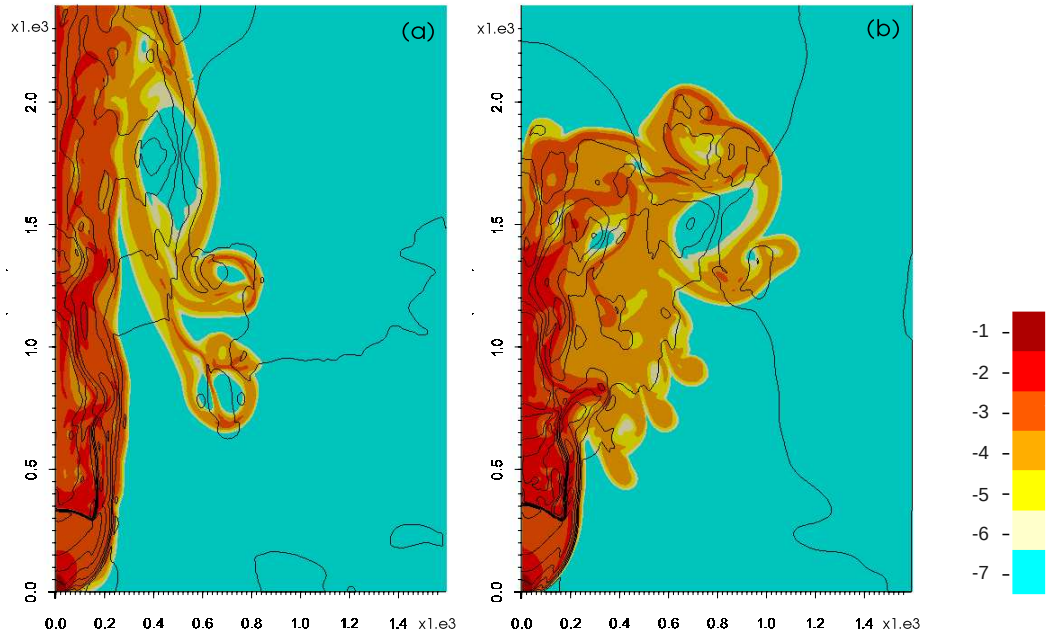

Figure 8.18: Bidisperse jet. Case A. $D_v = 80$ m, $K = 20$, $\rho_{mix} = 161.74$ kg/m^3 and $M_f = 1.22 \cdot 10^8$ kg/s. Logarithm to the base 10 of particle $s2$ volume fraction from 10^{-7} to 10^{-1} and isolines of pseudogas vertical velocity [0:50:350] m/s at time $t = 20$ s. Comparison between **(a)** hybrid pseudogas-multiphase model and **(b)** multiphase model for the test case **(a)** $St_{s2,ps} = 0.016$.

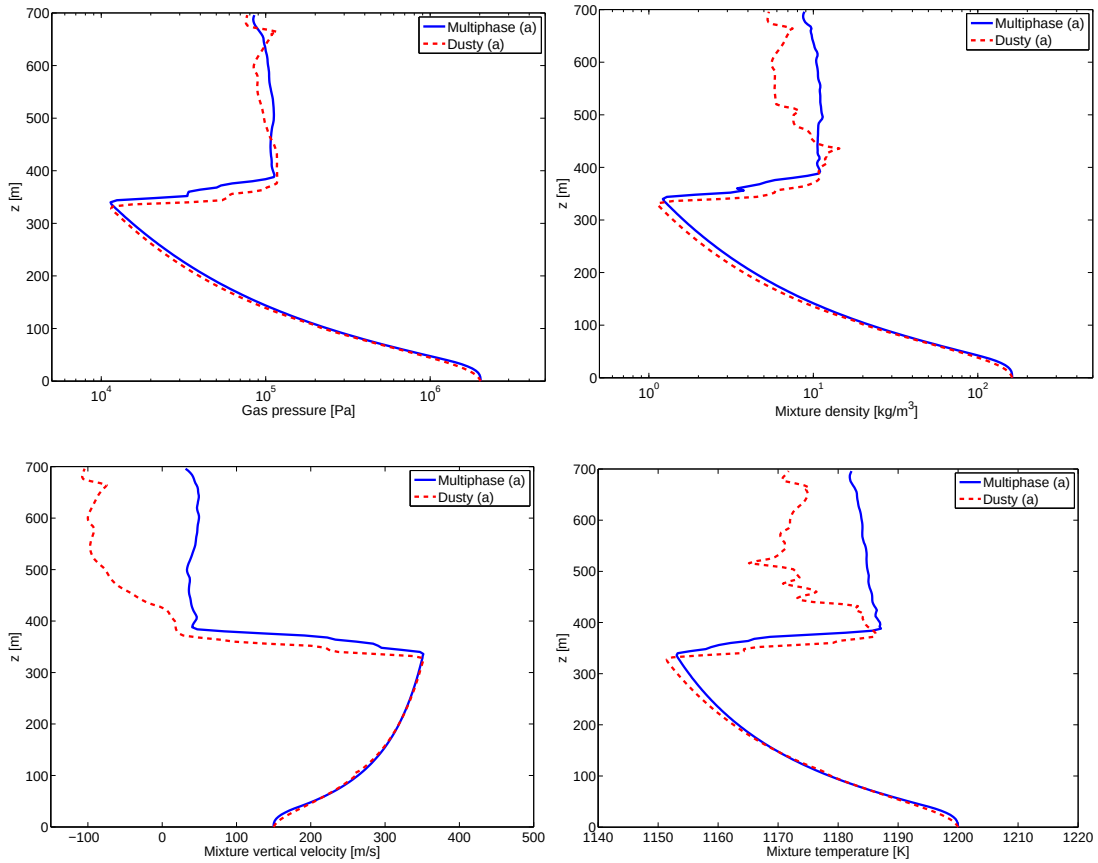

Figure 8.19: Bidisperse jet. Case A. $D_v = 80$ m, $K = 20$, $\rho_{mix} = 161.74\,\mathrm{kg/m^3}$ and $M_f = 1.22 \cdot 10^8$ kg/s. Time-averaged axial profiles computed over the interval $[16, 20]$ s of gas pressure, mixture density, mixture vertical velocity and mixture temperature. Comparison between fully multiphase model results (Multiphase) and hybrid pseudogas-multiphase model results (Dusty) for test **(a)** $St_{s2,ps} = 0.016$.

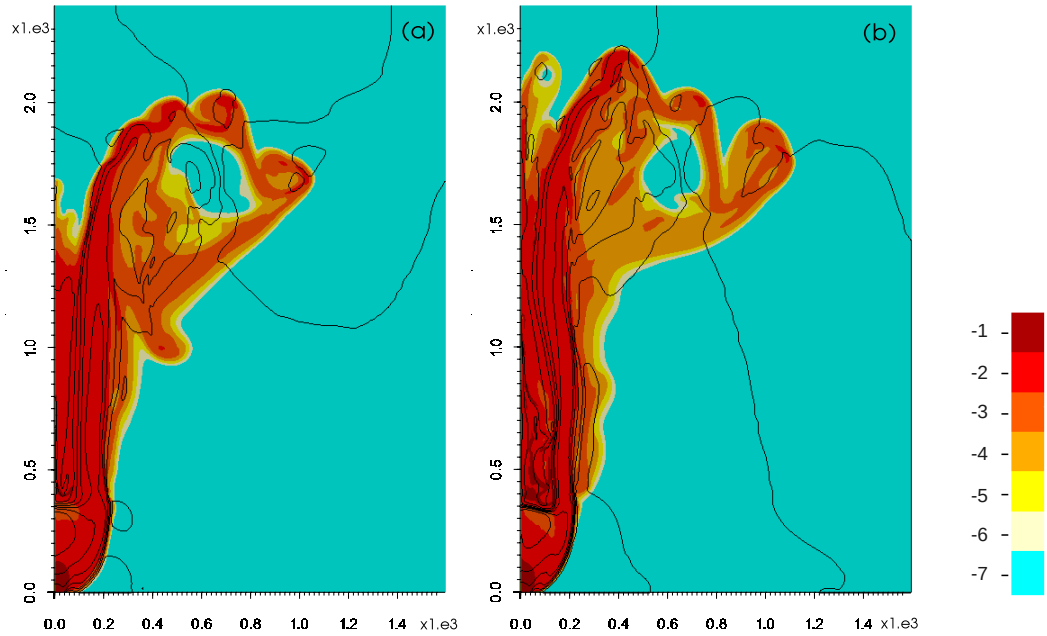

Figure 8.20: Bidisperse jet. Case A. $D_v = 80$ m, $K = 20$, $\rho_{mix} = 161.74$ kg/m^3 and $M_f = 1.22 \cdot 10^8$ kg/s. Logarithm to the base 10 of particle $s2$ volume fraction from 10^{-7} to 10^{-1} and isolines of pseudogas vertical velocity [0:50:350] m/s at time $t = 20$ s. Comparison between **(a)** hybrid pseudogas-multiphase model and **(b)** multiphase model for the test case **(b)** $St_{s2,ps} = 0.839$.

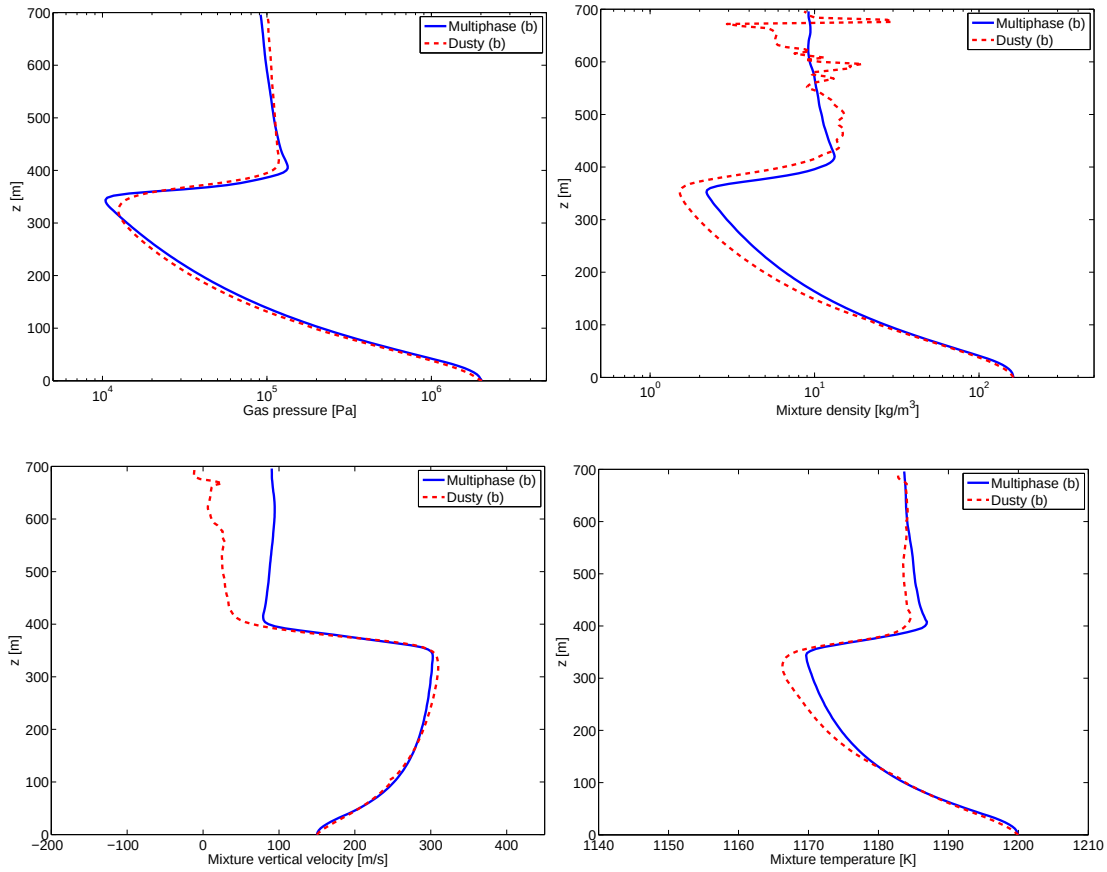

Figure 8.21: Bidisperse jet. Case A. $D_v = 80$ m, $K = 20$, $\rho_{mix} = 161.74\,\mathrm{kg/m^3}$ and $M_f = 1.22 \cdot 10^8$ kg/s. Time-averaged axial profiles computed over the interval $[16, 20]$ s of gas pressure, mixture density, mixture vertical velocity and mixture temperature. Comparison between fully multiphase model results (Multiphase) and hybrid pseudogas-multiphase model results (Dusty) for test **(b)** $St_{s2,ps} = 0.839$.

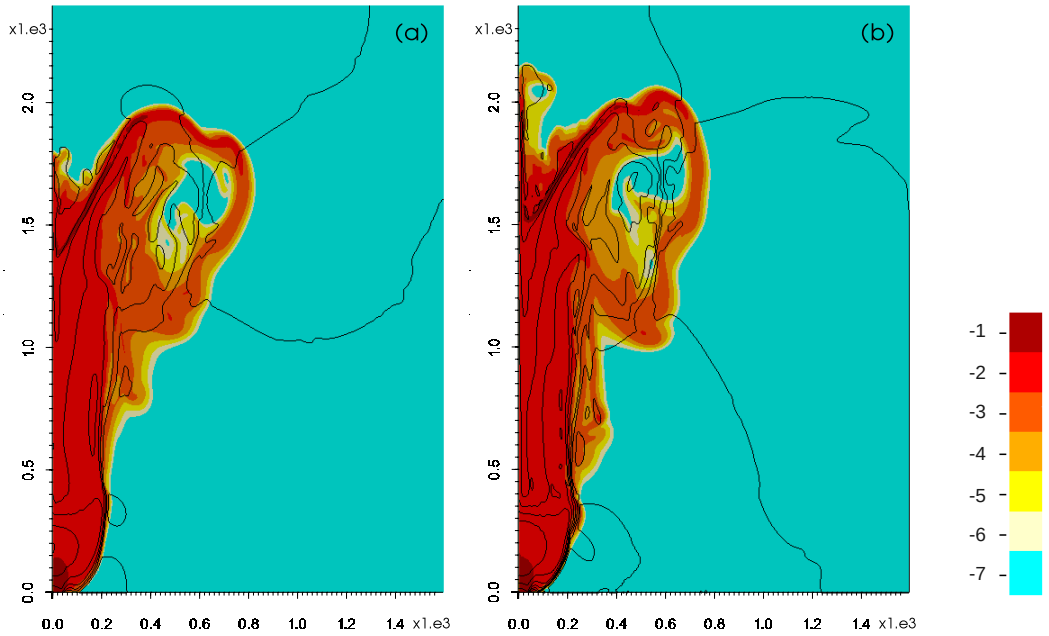

Figure 8.22: Bidisperse jet. Case A. $D_v = 80$ m, $K = 20$, $\rho_{mix} = 161.74$ kg/m^3 and $M_f = 1.22 \cdot 10^8$ kg/s. Logarithm to the base 10 of particle $s2$ volume fraction from 10^{-7} to 10^{-1} and isolines of pseudogas vertical velocity [0:50:350] m/s at time $t = 20$ s. Comparison between **(a)** hybrid pseudogas-multiphase model and **(b)** multiphase model for the test case **(c)** $St_{s2,ps} = 15.5$.

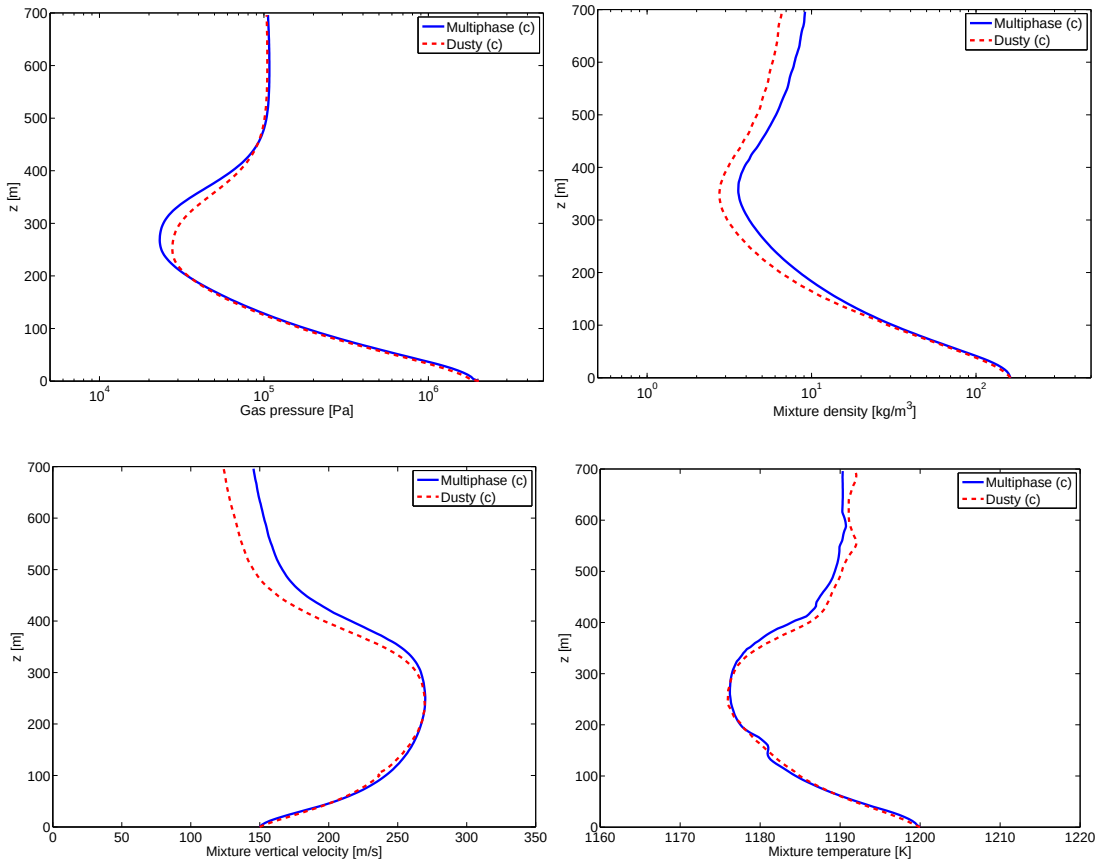

Figure 8.23: Bidisperse jet. Case A. $D_v = 80$ m, $K = 20$, $\rho_{mix} = 161.74\,\mathrm{kg/m^3}$ and $M_f = 1.22 \cdot 10^8$ kg/s. Time-averaged axial profiles computed over the interval $[16, 20]$ s of gas pressure, mixture density, mixture vertical velocity and mixture temperature. Comparison between fully multiphase model results (Multiphase) and hybrid pseudogas-multiphase model results (Dusty) for test **(c)** $St_{s2,ps} = 15.5$.

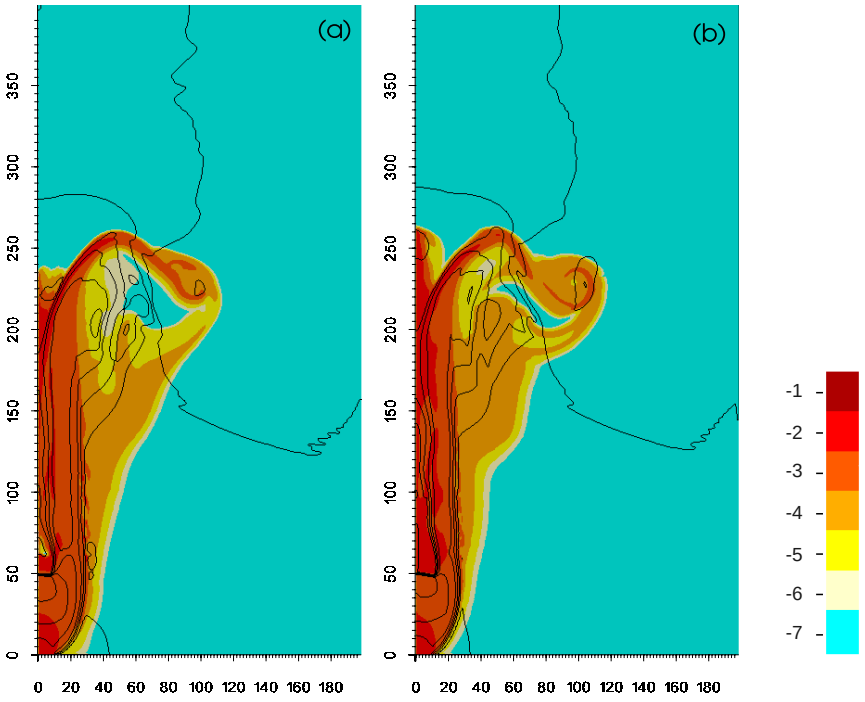

Figure 8.24: Bidisperse jet. Case B. $D_v = 20$ m, $K = 5$, $\rho_{mix} = 40.5\,\mathrm{kg/m^3}$ and $M_f = 1.91 \cdot 10^6$ kg/s. Logarithm to the base 10 of particle $s2$ volume fraction from 10^{-7} to 10^{-1} and isolines of pseudogas vertical velocity [0:50:350] m/s at time $t = 2$ s. Comparison between **(a)** hybrid pseudogas-multiphase model and **(b)** multiphase model for the test case **(a)** $St_{s2,ps} = 0.027$.

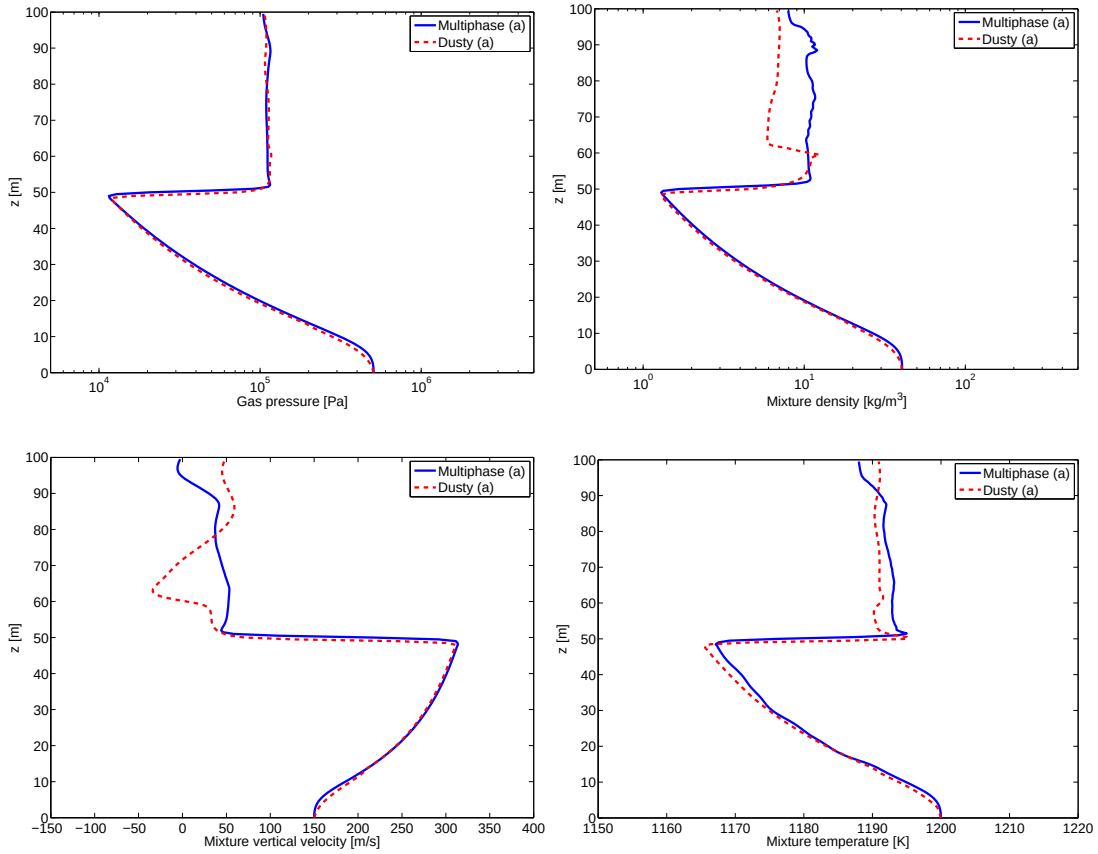

Figure 8.25: Bidisperse jet. Case B. $D_v = 20$ m, $K = 5$, $\rho_{mix} = 40.5$ kg/m^3 and $M_f = 1.91 \cdot 10^6$ kg/s. Time-averaged axial profiles computed over the interval $[1.5, 2]$ s of gas pressure, mixture density, mixture vertical velocity and mixture temperature. Comparison between fully multiphase model results (Multiphase) and hybrid pseudogas-multiphase model results (Dusty) for test **(a)** $St_{s2,ps} = 0.027$.

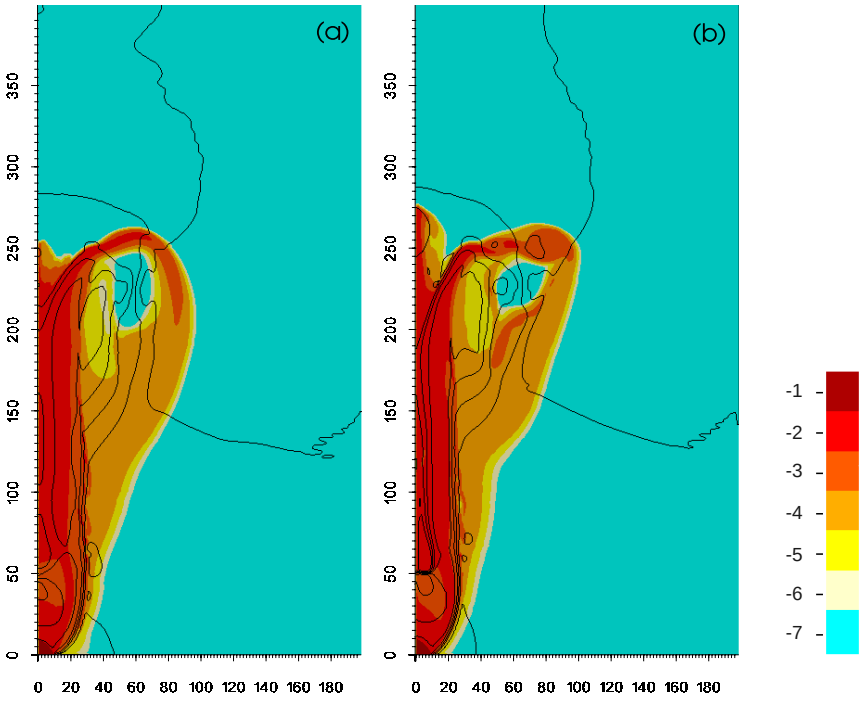

Figure 8.26: Bidisperse jet. Case B. $D_v = 20$ m, $K = 5$, $\rho_{mix} = 40.5\,\mathrm{kg/m^3}$ and $M_f = 1.91 \cdot 10^6$ kg/s. Logarithm to the base 10 of particle $s2$ volume fraction from 10^{-7} to 10^{-1} and isolines of pseudogas vertical velocity [0:50:350] m/s at time $t = 2$ s. Comparison between **(a)** hybrid pseudogas-multiphase model and **(b)** multiphase model for the test case **(b)** $St_{s2,ps} = 0.071$.

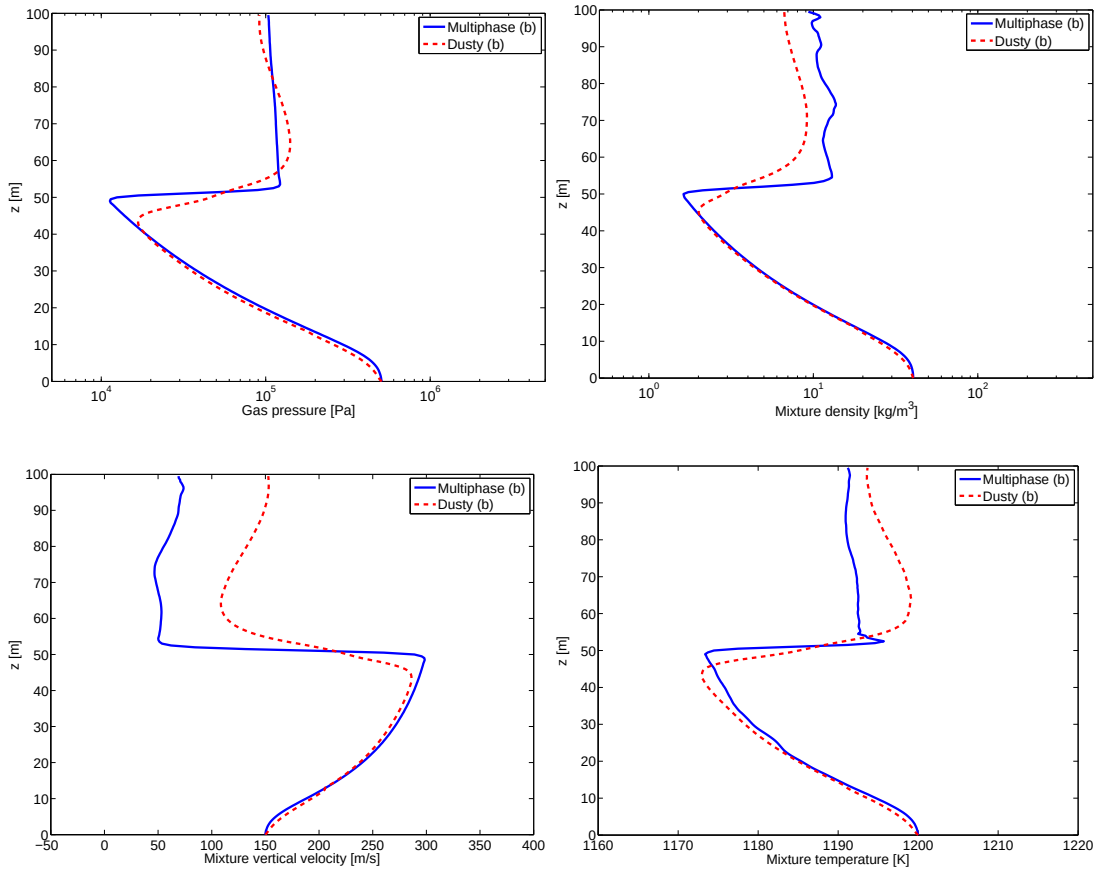

Figure 8.27: Bidisperse jet. Case B. $D_v = 20$ m, $K = 5$, $\rho_{mix} = 40.5$ kg/m^3 and $M_f = 1.91 \cdot 10^6$ kg/s. Time-averaged axial profiles computed over the interval $[1.5, 2]$ s of gas pressure, mixture density, mixture vertical velocity and mixture temperature. Comparison between fully multiphase model results (Multiphase) and hybrid pseudogas-multiphase model results (Dusty) for test **(b)** $St_{s2,ps} = 0.071$.

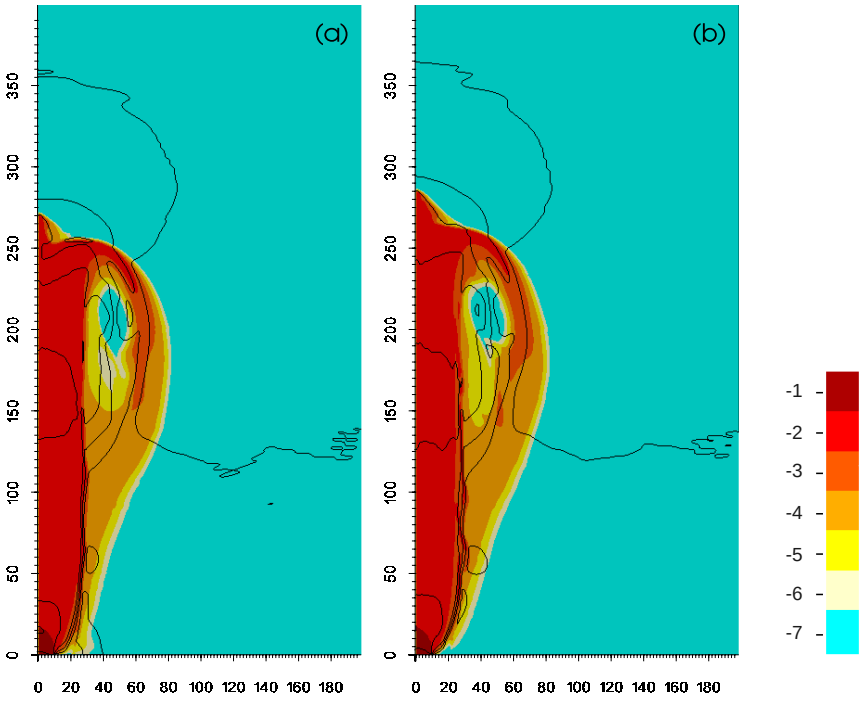

Figure 8.28: Bidisperse jet. Case B. $D_v = 20$ m, $K = 5$, $\rho_{mix} = 40.5\,\mathrm{kg/m^3}$ and $M_f = 1.91 \cdot 10^6$ kg/s. Logarithm to the base 10 of particle $s2$ volume fraction from 10^{-7} to 10^{-1} and isolines of pseudogas vertical velocity [0:50:350] m/s at time $t = 2$ s. Comparison between **(a)** hybrid pseudogas-multiphase model and **(b)** multiphase model for the test case **(c)** $St_{s2,ps} = 13.6$.

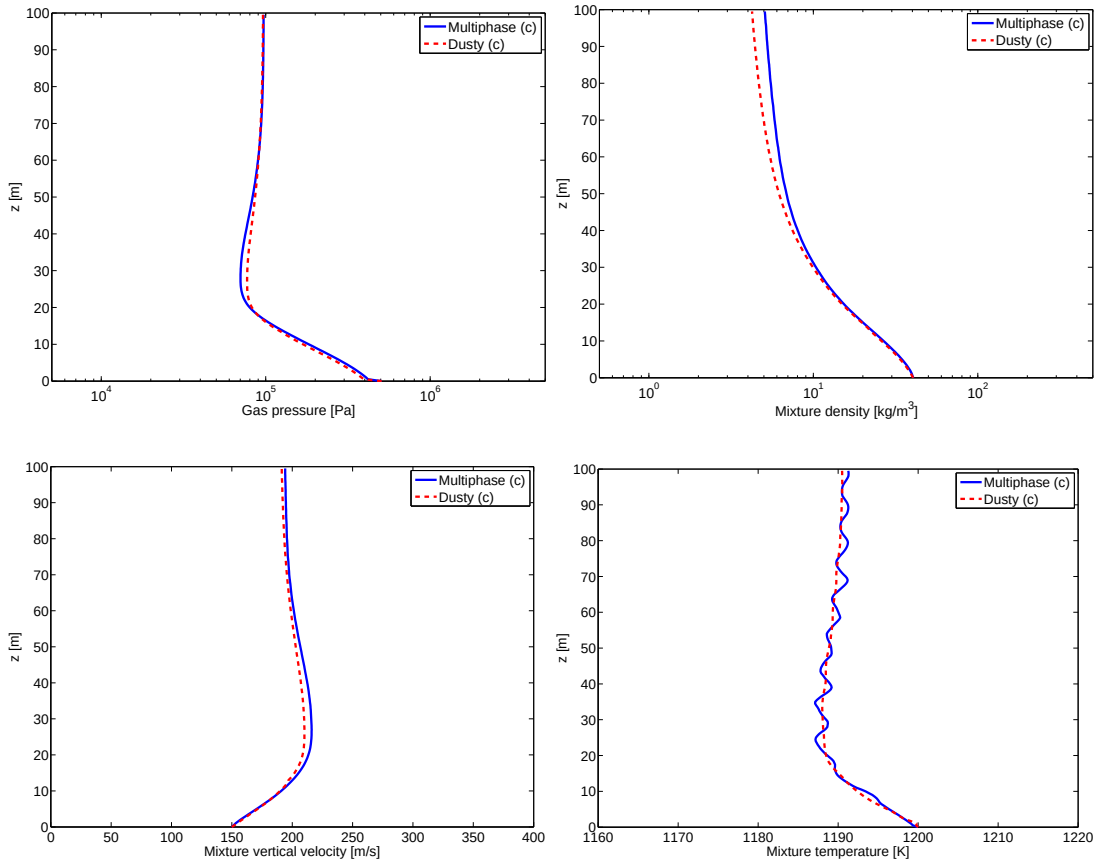

Figure 8.29: Bidisperse jet. Case B. $D_v = 20$ m, $K = 5$, $\rho_{mix} = 40.5$ kg/m^3 and $M_f = 1.91 \cdot 10^6$ kg/s. Time-averaged axial profiles computed over the time interval $[1.5, 2]$ s of gas pressure, mixture density, mixture vertical velocity and mixture temperature. Comparison between fully multiphase model results (Multiphase) and hybrid pseudogas-multiphase model results (Dusty) for test **(c)** $St_{s2,ps} = 13.6$.

Effects of particle–particle drag

Numerical results in the previous sections have shown how the analysis based on the Stokes number allows to investigate the decompression dynamics of underexpanded volcanic jets when the mixture composition changes. Following the hypothesis (H2), when the Stokes number of larger particles moving in the dusty gas is smaller than one, the Mach disk forms inside the jet, causing an abrupt change in the thermodynamic quantities. On the other hand, when the Stokes number is larger than one, the normal shock does not form.

Concerning the hypothesis (H1), i.e. the coupling between the gas phase and solid particles, we now focus on Case B (analogous results hold for Case A). In test cases (a) and (b), both finer particles $s1$ and coarser particles $s2$ have $St < 1$, thus they are expected to be tightly coupled with the gas phase. In case (c), fine particles $s1$ ($St < 1$) should be tightly coupled with the gas phase, whereas coarse particles $s2$ ($St > 1$) may display a different behaviour.

In Figure 8.30, the difference between gas and particle velocity is shown for both particles $s1$ and $s2$, in cases (a), (b) and (c). In cases (a) and (b), results are almost equal. Particles $s1$ are coupled with the gas phase in the expansion region, where only a small delay of few meters per second is observed. A strong and localized jump is observed at the shock location (50 m), where a maximum difference of about 50 m/s between particles and gas velocity is reached. Above the shock, particles equilibrate to the gas velocity in few meters.

A similar dynamics is observed for larger particles $s2$ in cases (a) and (b), even if a larger delay is reached in the expansion region (almost 20 m/s). Moreover, the maximum velocity difference through the shock is about 140 m/s. However, also for particles $s2$ only few meters are needed to equilibrate to the surrounding gas velocity.

In test case (c), both fine and coarse particles are strongly decoupled from the gas phase. Particles $s2$ accumulate a large delay in the expansion region, up to 50 m/s in the first 15 meters from the vent, where the gas phase is accelerating from 150 to 250 m/s. Then, the gas phase decelerates and particles take almost 100 m to equilibrate gradually to the gas velocity. Fine particles $s1$, which are expected to be coupled to the gas phase, display a maximum delay of 30 m/s at 15 m from the vent, and then gradually equilibrate to the gas velocity. This behaviour suggests that in case (c), where coarse particles are more abundant and only a small volume fraction of fine particles is present, particle–particle drag force has a dominant role in the mixture dynamics with respect to the gas–particle drag. Particle–particle drag effects are partly included in the pseudogas approximation introduced in the previous section through the correction on the pseudogas dynamic viscosity. Thus, the pseudogas-multiphase model describes quite well the decompression dynamics of the bidisperse underexpanded jet and reproduced correctly the Mach disk formation. However, only a fully multiphase model is able to reproduce the non-equilibrium dynamics of fine particles ascribable to the particle–particle drag. Concerning the computed Stokes number, interactions between different classes of solid particles have been considered only for larger particles through the correction on the pseudogas dynamic viscosity, but it has been neglected in the computation of St for fine particles. This approximation may explain the discrepancy between the expected behaviour of fine particles in the jet and the observed non equilibrium dynamics. An appropriate correction should be indroduced also in

the computation of the Stokes number for fine particles, when also larger particles are present in the multiphase mixture. Further investigation is thus needed in order to include particle–particle interactions in the study of both the mechanical equilibrium of the gas–particle mixture and the fluid dynamics of multiphase underexpanded jets.

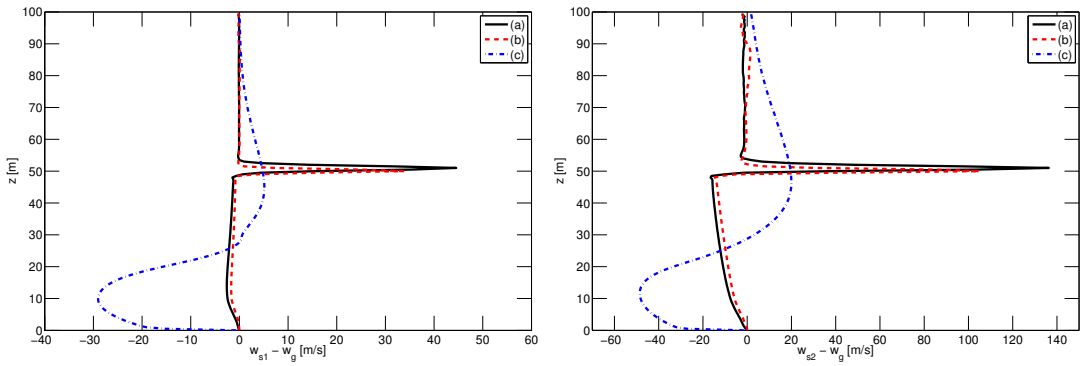

Figure 8.30: Bidisperse jet. Multiphase model. Case B. $D_v = 20$ m, $K = 5$, $\rho_{mix} = 40.5$ kg/m^3 and $M_f = 1.91 \cdot 10^6$ kg/s. Time-averaged axial profiles computed over the interval $[1.5, 2]$ s of the differences between particle and gas vertical velocity and temperature. Comparison between different mixture composition: **(a)** $St_{s2,ps} = 0.027$, **(b)** $St_{s2,ps} = 0.071$, **(c)** $St_{s2,ps} = 13.6$.

8.2.3 Polydisperse mixtures

In this section we introduce an hybrid pseudogas-multiphase model that allows to consider a mixture composed by the gaseous phase and N classes of solid particles. The multiphase model that describes the dynamics of the $N + 1$ phases is reduced to pseudogas-multiphase model in which only one pseudogas phase and only one class of solid particles are simulated.

The initial spectrum of solid particles is partitioned into two subsets with respect to the particle relaxation time. The relaxation time of each particle class is computed and compared with the Mach disk formation time by means of the Stokes number $St = \tau_s/\tau_{Ma}$. If $St_i < 1$, the class of solid particles s_i is classified as *fine*, otherwise the class is classified as *coarse*. As in the previous sections, fine particles are included, together with the pure gas, into the dusty gas phase. Coarse particles are grouped together into one single class of solid particles with averaged properties. In particular, following [79], the average coarse density is computed as:

$$\rho_C = (1 - y_{ps}) \left[\sum_{s:St_s \geq 1} \frac{y_s}{\rho_s} \right]^{-1} \tag{8.10}$$

and the average coarse diameter is computed as:

$$d_C = \left[\sum_{s:St_s \geq 1} \frac{y_s}{\rho_s} \right] \left[\sum_{s:St_s \geq 1} \frac{y_s}{\rho_s d_s} \right]^{-1} . \tag{8.11}$$

Here, y_s and y_{ps} are the mass fractions of the solid particles and the pseudogas, respectively.

We test the proposed approach on a test case representing a typical Plinian eruption, for which the total grain size distribution was assumed following Mount St. Helens 1980 data [20]. Initial conditions and eruptive parameters are the same of Case A, except for mixture composition. Vent conditions are described in Table 8.10. Solid particle distribution in terms of mass percentage is shown in Figure 8.31. In this test case, 14 classes of solid particles are considered. In Table 8.11 their properties are listed. Diameters vary from 2 μm to 16 mm and the corresponding density range is included between 800 and 2500 kg/m^3. The relaxation time and the Stokes number of each particles moving in the pure water vapor jet ($\tau_{Ma} \simeq 0.37$ s) is computed. The first 8 classes of solid particles have Stokes number smaller than one, thus they will be included, together with water vapor, in the pseudogas phase. The resulting pseudogas properties are reported in Table 8.12. The remaining 6 classes have Stokes number larger than one, thus they are included in a unique solid phase, with averaged properties. The new coarse particle s_C has diameter d_C equal to 780 μm and density ρ_C equal to 1136 kg/m^3. Using the pseudogas properties and the coarse particles averaged properties, the Mach disk formation time in the pseudogas-multiphase mixture remains almost unchanged, i.e. $\tau_{Ma} \simeq 0.37$ s. The relaxation time of particles s_C moving in the pseudogas is about $7 \cdot 10^{-4}$ s and its Stokes number is 0.0019.

The polydisperse jet is simulated with both the fully multiphase approach and the hybrid pseudogas-multiphase model. Numerical results are shown in Figure 8.32. The results obtained with the two models are in qualitative and quantitative results. The

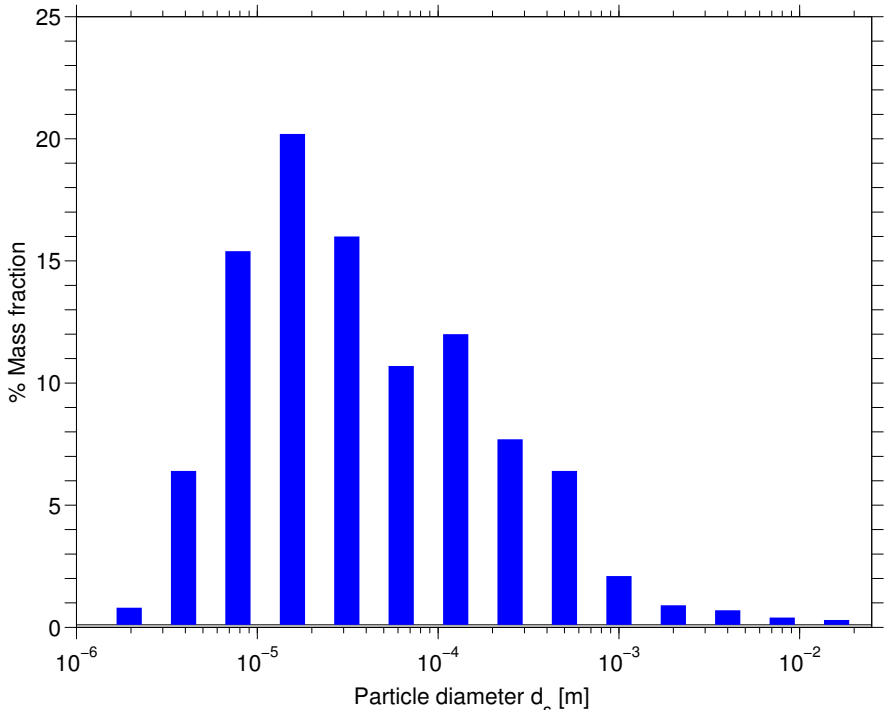

Figure 8.31: Polydisperse jet. Solid particles distribution. Mass percentage as a function of particle diameter d_s

Mach disk is located at 300 m from the vent and the volcanic column rises in the atmosphere beyond 2500 m. In Figure 8.33 the thermodynamic quantities along the vertical axis of the jet are shown for the two models. Gas pressure, mixture density and mixture velocity are in agreement and only a small difference of less than 10 K is observed in the mixture temperature.

Numerical results obtained with the hybrid pseudogas-multiphase model are consistent with the fully multiphase description and highlight the key effect of the total grain size distribution on the underexpanded jet. At the same time, the number of phases that are actually solved decreases from $N + 1$ to 2, where N is the number of particle classes, and the computational cost is drastically reduced by a factor of order N. As an example, to simulate 20 s of eruptions, the fully multiphase model ran for 272 hours on 16 parallel processors, whereas the hybrid model took only 68 hours on 8 processors. In conclusion, the hybrid pseudogas-multiphase model can effectly describe the dynamics of polydisperse underexpanded jets on the volcanic scale while reducing the computational cost of numerical simulations.

Polydisperse jet		
Parameter		Units
D_v	80	m
K	20	
P_{atm}	101325	Pa
T_{atm}	298	K
w_g	150	m/s
P_g	2026500	Pa
T_g	1200	K
ρ_g	3.7	kg/m^3
w_s	150	m/s
T_s	1200	K
ρ_{mix}	160	kg/m^3
M_f	1.2·10^8	kg/s

Table 8.10: Inlet conditions for the polydisperse jet.

Polydisperse jet					
Class	d_s (μm)	ρ_s(kg/m^3)	ϵ_s	τ_s (m/s)	St
1	2	2500.0	0.0005	$1.7 \cdot 10^{-5}$	$4.7 \cdot 10^{-5}$
2	4	2500.0	0.004	$7.0 \cdot 10^{-5}$	$1.9 \cdot 10^{-4}$
3	8	2500.0	0.0096	$2.8 \cdot 10^{-4}$	$7.6 \cdot 10^{-4}$
4	16	2500.0	0.0127	$1.1 \cdot 10^{-3}$	$3.0 \cdot 10^{-3}$
5	31	2500.0	0.01	$4.5 \cdot 10^{-3}$	$1.2 \cdot 10^{-2}$
6	63	2224.8	0.0075	$1.6 \cdot 10^{-2}$	$4.3 \cdot 10^{-2}$
7	125	1939.8	0.0097	$5.6 \cdot 10^{-2}$	$1.5 \cdot 10^{-1}$
8	250	1654.9	0.0073	$1.9 \cdot 10^{-1}$	$5.2 \cdot 10^{-1}$
9	500	1369.9	0.0073	$6.3 \cdot 10^{-1}$	1.7
10	1000	1084.9	0.003	2.0	5.4
11	2000	800.0	0.0018	5.9	$1.6 \cdot 10^{1}$
12	4000	800.0	0.0014	$2.3 \cdot 10^{1}$	$6.4 \cdot 10^{1}$
13	8000	800.0	0.0008	$9.4 \cdot 10^{1}$	$2.5 \cdot 10^{2}$
14	16000	800.0	0.0006	$3.8 \cdot 10^{2}$	$1.1 \cdot 10^{3}$

Table 8.11: Polydisperse jet. Solid particle distribution and properties. The total grain size distribution is assumed following Mount St. Helens 1980 data [20].

Polydisperse jet – Hybrid model		
Parameter		Units
ρ_{ps}	145.2	kg/m^3
R_{ps}	10.9	J/kg·K
μ_{ps}	0.0537	Pa·s
$c_{p,ps}$	1018.9	J/kg·K
d_C	780	μm
ρ_C	1136.6	kg/m^3
ϵ_C	0.0149	
β_C	0.18	
$c_{mix,ps}$	108.7	m/s
$\tau_{Ma,ps}$	0.37	s
$\tau_{C,ps}$	$7.1{\cdot}10^{-4}$	s
$St_{C,ps}$	0.0019	

Table 8.12: Polydisperse jet. Pseudogas properties, average coarse particle properties and characteristic time scales for the hybrid pseudogas-multiphase model.

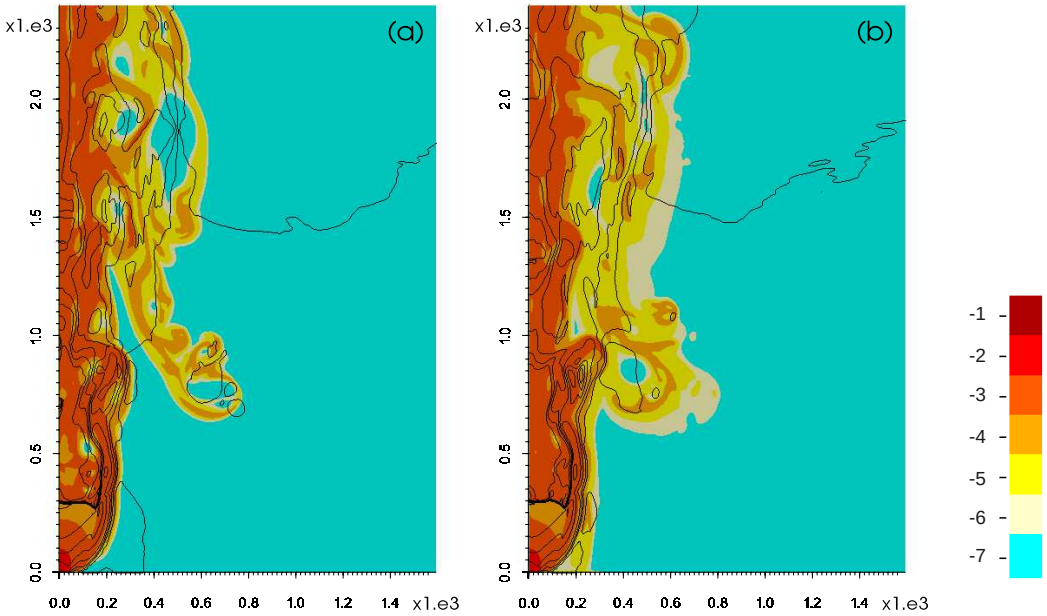

Figure 8.32: Polydisperse jet. $St_{C,ps} = 0.0019$. Comparison between **(a)** hybrid pseudogas-multiphase model and **(b)** fully multiphase model. Logarithm to the base 10 of coarse particle volume fraction from 10^{-7} to 10^{-1} and isolines of pseudogas vertical velocity ([0:50:350] m/s) at time $t = 20$ s.

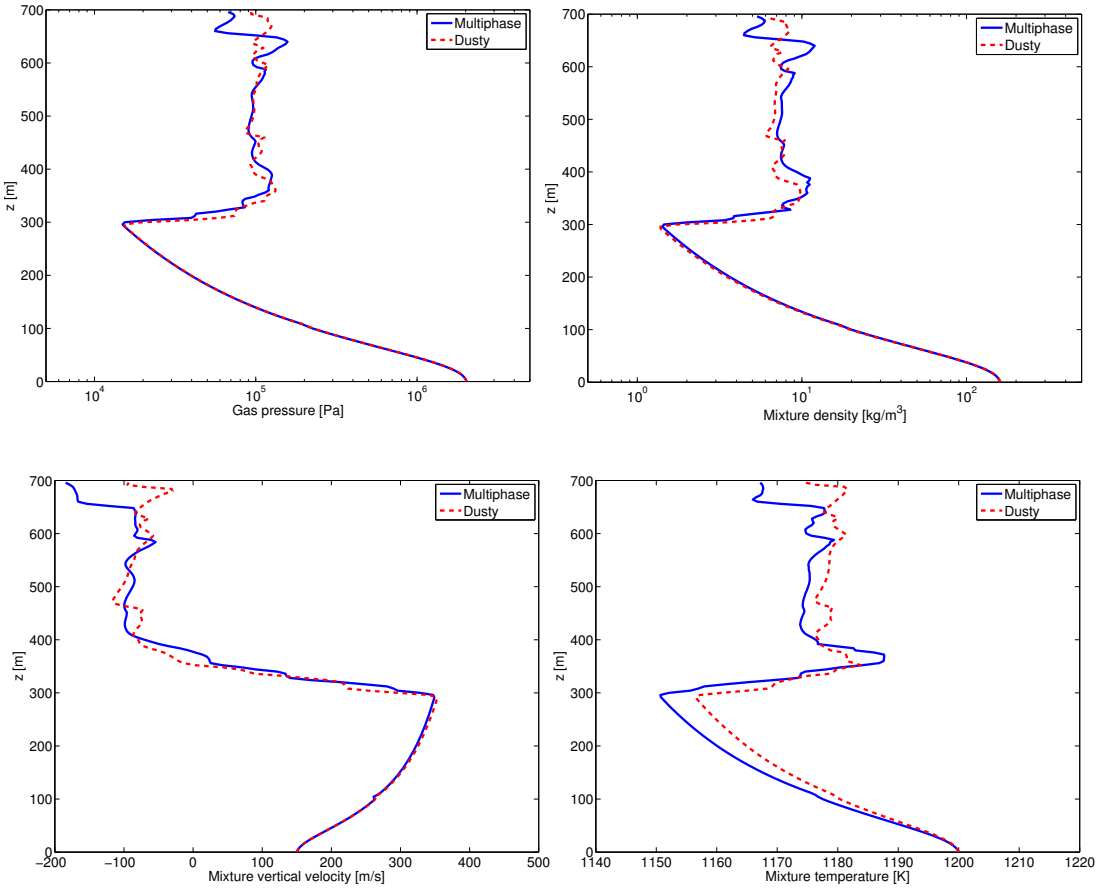

Figure 8.33: Polydisperse jet. $St_{C,ps} = 0.0019$. Time-averaged axial profiles computed over the interval $[15, 20]$ s of gas pressure, mixture density, mixture vertical velocity and mixture temperature. Comparison between fully multiphase model results (Multiphase) and hybrid pseudogas-multiphase model results (Dusty).

CHAPTER 9

Conclusions

THIS thesis has been devoted to the numerical modeling of multiphase gas–particle flows. This work has been motivated by the need of developing new and more accurate numerical tools for the simulation of explosive volcanic eruptions. However, the developed methodology and techniques are general and can be applied to the many different multiphase gas–particle flows that can be encountered in geophysical and industrial applications. In this chapter I summarize the main results achieved.

After a discussion on different approaches to the mathematical modeling of multiphase gas–particle flows, a model based on the Eulerian approach is presented for a mixture of a gaseous phase and N classes of solid particles. Appropriate closure equations are introduced, based on literature review. The dimensional analysis of the multiphase equations is carried out for significant test problems, both on the volcanic scale and the laboratory scale. In complex flow regimes, such as those encountered in natural volcanic phenomena, dimensional analysis is an effective tool to interpret numerical simulations and to reduce the physical and computational complexity of the model. The relative importance of different physical phenomena that take place in the volcanic jet and in the pyroclastic density current have been assessed. In the volcanic jet problem, we have shown that the ejected multiphase mixture can be well approximated as inviscid. Gravitational effects and dissipation due to viscous and drag forces are negligible. Compressibility effects are important and a transonic regime can be expected. Moreover, the hypothesis of equilibrium between different phases is not always valid and a fully multiphase mathematical model is needed to investigate the non-equilibrium dynamics between different phases. After the volcanic column collapse, in the pyroclastic current gravitational effects become dominant. When reproducing a multiphase jet on the laboratory scale, particle dynamics is strongly decoupled from gas dynamics.

Moreover, viscous dissipation and the work done by the drag force may play a key role in the thermodynamics of the mixture in specific flow conditions. As a consequence, the thermodynamics processes that influence the jet dynamics on the laboratory scale significantly differ from those characterizing the volcanic jet dynamics.

Two distinct numerical approximations of the multiphase flow equations are presented and validated, based on the finite volume and the discontinuous Galerkin approach. The proposed finite volume scheme achieves second order accuracy in space and time and it is validated against experimental and numerical results in both supersonic and subsonic regimes. The underexpanded jet problem on the laboratory and volcanic scale, the particle-laden gravity current and the collapsing jet problem have been taken as benchmark tests. Supersonic and subsonic regimes are well described by the finite volume scheme. The multidimensional second order spatial discretization is essential to accurately capture the shock wave pattern observed in underexpanded jets and to reduce numerical diffusion. Validation against experiments and comparison against numerical results is satisfactory.

The alternative p-adaptive discontinuous Galerkin approach allows to achieve higher accuracy, while keeping a small computational stencil and a relatively limited computational cost thanks to a p-adaptivity approach, that was originally proposed for subsonic flows and has been applied here successfully to supersonic problems. In the present work, the discontinuous Galerkin scheme is applied to solve multiphase gas–particle equations that accounts for drag and heat exchange coupling between different phases. Appropriate flux limiting and slope limiting techniques, originally introduced in the framework of scalar and linear equations, are applied to the proposed discontinuous Galerkin approximation of the multiphase flow equations. The discontinuous Galerkin approach has been tested on several benchmark problems in the one-dimensional case. In particular, monophase and multiphase shock tube test cases have been considered in order to assess the accuracy, the limiting techniques properties and the computational efficiency obtained thanks to the p-adaptive approach. We have shown that slope limiting and flux limiting techniques are essential in multiphase shock tube problems to guarantee the positivity of physical quantities, e.g. volume fractions, and the stability of the numerical solution. The p-adaptive approach is able to reduce the computational cost up to 50% by keeping a good accuracy on the numerical solution both in the monophase and in the multiphase case.

Finally, the finite volume numerical model has been applied to study the effect of gas–particle non-equilibrium on underexpanded volcanic jets by assuming monodisperse, bidisperse and polydisperse mixtures. By means of a scaling analysis based on particle Stokes numbers, i.e., the ratio between the particle relaxation time and the Mach disk formation time of the underexpanded jet, we could classify solid particulate into two categories, namely *fine* and *coarse* particles. Fine particles are tightly coupled with the gas phase and do not modify the structure of the shock wave pattern in the jet. On the contrary, coarser particles are decoupled from the gas phase and strongly influence the jet decompression structure, including the intensity, shape and position of the Mach disk. Depending on the mass ratio between fine ($St \ll 1$) and coarse ($St \gg 1$)

particles, the jet flow pattern can dramatically change, leading to the obliteration of the Mach disk structure. On the basis of the results of the time scale analysis, an hybrid pseudogas-multiphase model is proposed, in which fine particles and the gas phase are modeled together as a pseudogas with average thermodynamics properties, whereas coarse particles are grouped together into a representative class of solid particles with average properties. Numerical results confirm the validity of the hybrid approach for the simulation of monodisperse, bidisperse and polydisperse underexpanded jets and highlight the key effect of the total grain size distribution on the jet phase and on the overall stability properties of the eruptive column.

The general approach adopted in the model formulation and in the proposed numerical approximations allows, with the support of an appropriate dimensional analysis, to extend the present work to other geophysical or industrial applications.

List of Figures

List of Tables

Bibliography

[1] A.A. Amsden and F.H. Harlow. Numerical calculation of almost incompressible flows. *Journal of Computational Physics*, 3:80–93, 1968.

[2] D. Arnold, F. Brezzi, B. Cockburn, and L. Marini. Unified analysis of discontinuous Galerkin methods for elliptic problems. *SIAM Journal on Numerical Analysis*, 39:1749–1779, 2002.

[3] S. Balachandar and J.K. Eaton. Turbulent dispersed multiphase flow. *Annual Review of Fluid Mechanics*, 42:111–133, 2010.

[4] T. Barth and M. Ohlberger. *Finite volume methods: foundation and analysis*. John Wiley and Sons, Ltd, 2004.

[5] F. Bassi and S. Rebay. High-order accurate discontinuous finite element method for the numerical solution of the compressible navier-stokes equations. *Journal of Computational Physics*, 131:267–279, 1997.

[6] F. Bassi and S. Rebay. High-order accurate discontinuous finite element solution of the 2d Euler equations. *Journal of Computational Physics*, 138:251–285, 1997.

[7] G.K. Batchelor. *An introduction to fluid dynamics*. Cambridge University Press, 1967.

[8] C.E. Baumann and J.T. Oden. A discontinuous hp finite element method for convection-diffusion problems. *Computer Methods in Applied Mechanics and Engineering*, 31:311–341, 1999.

[9] R. Biswas, K.D. Devine, and J.E. Flaherty. Parallel, adaptive finite element methods for conservation laws. *Applied Numerical Mathematics*, 14:255–283, 1994.

[10] C. Bonadonna and J.C. Phillips. Sedimentation from strong volcanic plumes. *Journal of Geophysical Research*, 108(B7):2340, 2003.

[11] L. Bonaventura and T. Ringler. Analysis of discrete shallow-water models on geodesic Delaunay grids with C-type staggering. *Monthly Weather Review*, 133:2351–2373, 2005.

[12] D.L. Book, J.B. Boris, and K. Hain. Flux-corrected transport II: generalization of the method. *Journal of Computational Physics*, 18(3):248–283, 1975.

[13] J.B. Boris and D.L. Book. Flux-corrected transport III: minimal-error FCT algorithms. *Journal of Computational Physics*, 20(4):397–431, 1976.

[14] J.P. Boris and D.L. Book. Flux-corrected transport. I. SHASTA, a fluid transport algorithm that works. *Journal of Computational Physics*, 11:38–69, 1973.

[15] C.E. Brennen. *Fundamentals of multiphase flows*. Cambridge University Press, 2005.

[16] A. Burgisser and G.W. Bergantz. Reconciling pyroclastic flow and surge: the multiphase physics of pyroclastic density currents. *Earth and Planet Science Letters*, 202:405–418, 2002.

[17] C.S. Campbell and C.E. Brennen. Computer simulation of granular shear flows. *Journal of Fluid Mechanics*, 151:167–188, 1985.

[18] C. Canuto, M.Y. Hussaini, A. Quarteroni, and T.A. Zang. *Spectral methods*. Springer, 2006.

[19] S. Carcano, L. Bonaventura, T. Esposti Ongaro, and A. Neri. A semi-implicit, second-order-accurate numerical model for multiphase underexpanded volcanic jets. *Geoscientific Model Development*, 6:1905–1924, 2013.

[20] S.N. Carey and H. Sigurdsson. Influence of particle aggregation on deposition of distal tephra from the May 18, 1980, eruption of mount st. helens volcano. *Journal of Geophysical Research*, 87(B8):7061–7072, 1982.

[21] G.F. Carrier. Shock waves in a dusty gas. *Journal of Fluid Mechanics*, 4:376–382, 1958.

[22] G. Chavent and B. Cockburn. The local projection p^0–p^1 discontinuous Galerkin finite element method for scalar conservation laws. *Mathematical Modeling and Numerical Analysis*, 23:565–592, 1989.

[23] B. Cockburn, S. Hou, and C.W. Shu. The Runge-Kutta local projection discontinuous Galerkin finite element method for conservation laws IV: the multidimensional case. *Mathematics of Computation*, 54(190):545–581, 1990.

[24] B. Cockburn and S.Y. Lin. TVB Runge-Kutta local projection discontinuous Galerkin finite element method for conservation laws III: one dymensional systems. *Journal of Computational Physics*, 84:90–113, 1989.

[25] B. Cockburn and C.-W. Shu. TVB Runge-Kutta local projection discontinuous Galerkin finite element method for conservation laws II: general framework. *Mathematics of Computation*, 52(186):411–435, 1989.

[26] B. Cockburn and C.-W. Shu. The Runge-Kutta local projection $p1$ discontinuous Galerkin finite element method for scalar conservation laws. *Mathematical Modeling and Numerical Analysis*, 25:337–361, 1991.

[27] B. Cockburn and C.-W. Shu. The Runge-Kutta discontinuous Galerkin method for conservation laws V. *Journal of Computational Physics*, 141:198–224, 1998.

[28] P. Colella. Multidimensional upwind methods for hyperbolic conservation laws. *Journal of Computational Physics*, 87:171–200, 1990.

[29] J. Crank and P. Nicolson. A practical method for numerical evaluation of solutions of partial differential equations of the heat-conduction type. *Proceedings of the Cambridge Philosophical Society*, 43(1):50–67, 1947.

[30] C.T. Crowe, M. Sommerfeld, and Y. Tsuji. *Multiphase flows with droplets and particles*. Boca Raton, FL: CRC Press, 1998.

[31] P.A. Cundall and O.D.L Stack. A discrete numerical model for granular assemblies. *Geotechnique*, 29:47–65, 1979.

[32] S. Dartevelle, W.I. Rose, J. Stix, K. Kelfoun, and J.W. Vallance. Numerical modeling of geophysical granular flows: 2. Computer simulations of Plinian clouds and pyroclastic flows and surges. *Geochemistry, Geophysics, Geosystems*, 5, Q08004, 2004.

[33] M. de'Michieli Vitturi, A. Neri, S. Lo Savio, and E. Boschi. Lagrangian modeling of large volcanic particles: application to Vulcanian explosions. *Journal of Geophysical Research B: Solid Earth*, 115(B08206), 2010.

[34] F. Dobran, A. Neri, and G. Macedonio. Numerical simulation of collapsing volcanic columns. *Journal of Geophysical Research*, 98(B3):4231–4259, 1993.

[35] D.M. Doronzo, J. Martí, R. Sulpizio, and P. Dellino. Aerodynamics of stratovolcanoes during multiphase processes. *Journal of Geophysical Research*, 117, B01207, 2012.

[36] D.R. Durran. *Numerical methods for wave equations in geophysical fluid dynamics*. Springer, 1999.

[37] C.T. Crowe (ed). *Multiphase flow handbook*. CRC Press, 2005.

[38] B. Einfeldt. On Godunov-type methods for gas dynamics. *SIAM Journal on Numerical Analysis*, 25(2):294–318, 1988.

[39] B. Engquist and S. Osher. One sided difference approximations for nonlinear conservation laws. *Mathematics of Computation*, 36(154):321–351, 1981.

[40] S. Ergun. Fluid flow through packed colums. *Chemical Engineering Progress*, 48:89–94, 1952.

[41] C. Eskilsson. An hp-adaptive discontinuous Galerkin method for shallow water flows. *International Journal for Numerical Methods in Fluids*, 67:1605–1623, 2011.

[42] T. Esposti Ongaro, C. Cavazzoni, G. Erbacci, A. Neri, and M.V. Salvetti. A parallel multiphase flow code for the 3D simulation of explosive volcanic eruptions. *Parallel Computing*, 33:541–560, 2007.

[43] T. Esposti Ongaro, A.B. Clarke, A. Neri, B. Voight, and C. Widiwijayanti. Fluid dynamic of the 1997 Boxing Day volcanic blast on Montserrat, West Indies. *Journal of Geophysical Research B: Solid Earth*, 113(3):B03211, 2008.

[44] T. Esposti Ongaro, A.B. Clarke, B. Voight, A. Neri, and C. Widiwijayanti. Multiphase flow dynamics of pyroclastic density currents during May 18, 1980 lateral blast of Mount St. Helens. *Journal of Geophysical Research B: Solid Earth*, 117(6):B06208, 2012.

[45] T. Esposti Ongaro, A. Neri, G. Menconi, M. de'Michieli Vitturi, P. Marianelli, C. Cavazzoni, G. Erbacci, and P.J. Baxter. Transient 3D numerical simulations of column collapse and pyroclastic density current scenarios at Vesuvius. *Journal of Volcanology and Geothermal Research*, 178:378–396, 2008.

[46] Z.-G. Feng and E.E. Michaelides. A numerical study on the transient heat transfer from a sphere at high Reynolds and Péclet numbers. *International Journal of Heat and Mass Transfer*, 43:219–229, 2000.

[47] J.E. Flaherty and P. K. Moore. Integrated space-time adaptive hp-refinement methods for parabolic systems. *Applied Numerical Mathematics*, 16:317–341, 1995.

[48] M. Germano, U. Piomelli, P. Moin, and W. Cabot. A dynamic subgrid-scale eddy viscosity model. *Physics of Fluids A*, 3(7):1760–1765, 1991.

[49] D. Gidaspow. *Multiphase flow and fluidization: continuum and kinetic theory descriptions*. Academic Press, San Diego, USA, 1994.

[50] D. Gidaspow and B. Ettahadieh. Fluidization in two-dimensional beds with a jet. 2. Hydrodynamics modeling. *Industrial and Engineering Chemistry Fundamentals*, 22:183–201, 1983.

[51] D. Gidaspow and L. Huilin. Collisional viscosity of FCC particles in a CFB. *AIChE Journal*, 12:2503–2510, 1996.

[52] E. Godlewski and P.-A. Reviart. *Hyperbolic systems of conservation laws*. Ellipses, 1991.

[53] S.K. Godunov. A finite difference method for the computation of discontinuous solution of the equations of fluid dynamics. *Matematicheskii Sbornik*, 1(1):1–10, 1000.

[54] S.K. Godunov. Reminiscences about difference schemes. *Journal of Computational Physics*, 153:6–25, 1999.

[55] H.M. Gonnermann and M. Manga. The fluid mechanics inside a volcano. *Annual Review of Fluid Mechanics*, 39:321–356, 2007.

[56] S. Gottlieb and C.-W. Shu. Total variation diminishing Runge-Kutta schemes. *Mathematics of Computation*, 67(221):73–85, 1998.

[57] H.-F. Graf, M. Herzog, J.M. Oberhuber, and C. Textor. Effect of environmental conditions on volcanic plume rise. *Journal of Geophysical Research*, 104(D20):24309–24320, 1999.

[58] E.S. Gross, V. Casulli, L. Bonaventura, and J.R. Koseff. A semi-implicit method for vertical transport in multidimensional models. *International Journal for Numerical Methods in Fluids*, 28:157–186, 1998.

[59] M.T. Gudmundsson, R. Pedersen, K. Vogfjörd, B. Thorbjarnardóttir, S. Jakobsdóttir, and M.J. Roberts. Eruptions of Eyjafjallajökull Volcano, Iceland. *Eos, Transactions American Geophysical Union*, 91(21):190–191, 2010.

[60] D.J. Gunn. Transfer of heat or mass to particles in fixed and fluidized beds. *International Journal of Heat and Mass Transfer*, 21:467–476, 1978.

[61] M.A. Hallworth, A.J. Hogg, and H.E. Huppert. Effects of external flow on compositional and particle gravity currents. *Journal of Fluid Mechanics*, 359:109–142, 1998.

[62] H.C. Hamaker. The London–Van der Waals' attraction between spheroid particles. *Physica*, 4:1058, 1937.

[63] F.H. Harlow and A.A. Amsden. Numerical calculation of multiphase fluid flow. *Journal of Computational Physics*, 17, 1975.

[64] F.H. Harlow and J.E. Welch. Numerical calculation of time-dependent viscous incompressible flow of fluid with free surface. *Physics of Fluids*, 8:2182–2189, 1965.

[65] A. Harten, P.D. Lax, and B. van Leer. On upstream differencing and Godunov-type schemes for hyperbolic conservation laws. *SIAM Review*, 25(1):35–61, 1983.

[66] C. Hirsch. *Numerical computation of internal and external flows. Volume 1. Fundamentals of computational fluid dynamics*. Elsevier, 2007.

[67] P. Houston and B. Süli. A note on the design of hp-adaptive finite element methods for elliptic partial differential equations. *Computed methods in applied mechanics and engineering*, 194:229–243, 2005.

[68] C. Hsu. *A curvilinear-coordinate method for momentum, heat and mass transfer in domains of irregular geometry*. PhD thesis, University of Minnesota, 1981.

[69] J. Hudson and D. Harris. A high resolution scheme for Eulerian gas-solid two-phase isentropic flow. *Journal of Computational Physics*, 216:494–525, 2006.

[70] C.T. Jacobs, G.S. Collins, M.D. Piggott, S.C. Kramer, and C.R.G. Wilson. Multiphase flow modelling of volcanic ash particle settling in water usign adaptive unstructured meshes. *Geophysical Journal International*, 192:647–665, 2012.

[71] J.Dufek and G.W. Bergantz. Dynamics and deposits generated by the Kos Plateau Tuff eruption: Controls of basal particle loss on pyroclastic flow transport. *Geochemistry, Geophysics, Geosystems*, 8, Q12007, 2007.

[72] J.Dufek and G.W. Bergantz. Suspended load and bed-load transport of particle-laden gravity currents: the role of particle-bed interaction. *Theroetical and Computational Fluid Dynamics*, 21(2):119–145, 2007.

[73] J.B. Johnson. Generation and propagation of infrasonic airwaves from volcanic explosions. *Journal of Volcanology and Geothermal Research*, 121:1–14, 2003.

[74] M. Jones, R.S.J. Sparks, and P.J. Valdes. The climatic impact of supervolcanic ash blankets. *Climate Dynamics*, 29:553–564, 2007.

[75] S.W. Kieffer. *Factors governing the structure of volcanic jets*, pages 143–157. Boyd, F.R. (ed), National Academy Press, Washington, 1984.

[76] W. Kim and S. Menon. A new dynamic one-equation subgrid-scale model for large eddy simulation. In *33rd Aerospace Sciences Meeting and Exhibit*, Reno, NV, 1995.

[77] D. Kröner. *Numerical schemes for conservation laws*. Wiley-Teubner, 1997.

[78] S.N. Kruzcov. First order quasilinear equations in several independent variables. *Matematicheskii Sbornik*, 10:217–243, 1970.

[79] D. Kunii and O. Levenspiel. *Fluidization Engineering*. Butterworth-Heinemann, 1991.

[80] H.L. Langhaar. *Dimensional analysis and theory of models*. John Wiley and Sons, Ltd, 1951.

[81] P.D. Lax and B. Wendroff. System of conservation laws. *Communications on Pure and Applied Mathematics*, 13:217–237, 1960.

[82] B. Van Leer. Toward the ultimate conservative scheme, II. Monotonicity and conservation combined in a second order scheme. *Journal of Computational Physics*, 14:361–370, 1974.

[83] R.J. LeVeque. High-resolution conservative algorithms for advection in incompressible flow. *SIAM Journal on Numerical Analysis*, 33(2):627–665, 1996.

[84] C.H. Lewis and D.J. Carlson. Normal shock location in underexpanded gas and gas particle jets. *AIAA Journal*, 2:776–777, 1964.

[85] R. Löhner, K. Morgan, J. Peraire, and M. Vahdati. Finite element flux-corrected transport (FEM-FCT) for the Euler and Navier-Stokes equations. *International Journal for Numerical Methods in Fluids*, 7:1093–1109, 1989.

[86] F.E. Marble. Dynamics of dusty gases. *Annual Review of Fluid Mechanics*, 2:397–446, 1970.

[87] J.H. Masliyah and N. Epstein. Numerical study of steady flow past spheroids. *Journal of Fluid Mechanics*, 44:493–512, 1970.

[88] S. Matsumoto and S. Saito. On the mechanism of suspensions in horizontal pneumatic conveying: Monte Carlo simulation based on the irregular bouncing model. *Journal of Chemical Engineering of Japan*, 3:83, 1970.

[89] H. Miura. Decay of shock waves in a dusty-gas shock tube. *Fluid Dynamics Research*, 6:251–259, 1990.

[90] A. Neri and F. Dobran. Influence of eruption parameters on the thermofluid dynamics of collapsing columns. *Journal of Geophysical Research*, 99:11833–11857, 1994.

[91] A. Neri, T. Esposti Ongaro, G. Macedonio, and D. Gidaspow. Multiparticle simulation of collapsing volcanic columns and pyroclastic flow. *Journal of Geophysical Research*, 108(B4):2202, 2003.

[92] A. Neri, T. Esposti Ongaro, G. Menconi, M. de'Michieli Vitturi, C. Cavazzoni, G. Erbacci, and P.J. Baxter. 4D simulation of explosive eruption dynamics at Vesuvius. *Parallel Computing*, 33:541–560, 2007.

[93] A. Neri and G. Macedonio. Physical modeling of collapsing volcanic columns and pyroclastic flows. In *Monitoring and mitigation of volcano hazards*, pages 389–427, Berlin-Heidelberg, Germany, 1996. Springer-Verlag.

[94] C.G. Newhall and S. Self. The Volcanic Explosivity Index (VEI): and estimate of explosive magnitude for historical volcanism. *Journal of Geophysical Research*, 87(C2):1231–1238, 1982.

[95] J.M. Oberhuber, M. Herzog, H.-F. Graf, and K. Schwanke. Volcanic plume simulation on large scales. *Journal of Volcanology and Geothermal Research*, 87:29–53, 1998.

[96] D.E. Ogden, G.A. Glatzmaier, and K.H. Wohletz. Effects of vent overpressure on buoyant eruption columns: implications for plume stability. *Earth and Planet Science Letters*, 268:283–292, 2008.

[97] D.E. Ogden, K.H. Wohletz, G.A. Glatzmaier, and E.E. Brodsky. Numerical simulations of volcanic jets: importance of vent overpressure. *Journal of Geophysical Research*, 113(2), B02204, 2008.

[98] M.M. Orescanin, J.M. Austin, and S.W. Kieffer. Unsteady high-pressure flow experiments with applications to explosive volcanic eruptions. *Journal of Geophysical Research*, 115(6), B06206, 2010.

[99] N. Oreskes, K. Shrader-Frechette, and K. Belitz. Verification, validation, and confirmation of numerical models in the Earth Sciences. *Science*, 263:641–646, 1994.

[100] C.W. Oseen. Uber den Goltigkeitsbereich der Stokesschen Widerstandsformel. *Arkiv f´or Matematik, Astronomi och Fysik*, 9(19), 1913.

[101] S. Osher and F. Solomon. Upwind difference schemes for hyperbolic conservation laws. *Mathematics of Computation*, 38(158):339–374, 1982.

[102] E. A. Parfitt and L. Wilson. *Fundamentals of Physical Volcanology*. Blackwell Publishing, Malden, USA, 2008.

[103] S.V. Patankar. *Numerical heat transfer and fluid flow*. Hemisphere Publishing Corporation, New York, USA, 1980.

[104] M. Pelanti and R.J. LeVeque. High-resolution finite volume methods for dusty gas jets and plumes. *SIAM Journal on Scientific Computing*, 28:1335–1360, 2006.

[105] C. Prakash. *A finite element method for predicting flow through ducts with arbitrary cross sections*. PhD thesis, University of Minnesota, 1981.

[106] . Quarteroni, R. Sacco, and F. Saleri. *Numerical mathematics*. Springer, 2007.

[107] W.E. Ranz and W.R. Marshall. Evaporation from drops. *Chemical Engineering Progress*, 48:141–146, 1952.

[108] W.H. Reed and T.R. Hill. Triangular mesh methods for the neutron transport equation. Los alamos scientific laboratory report, LA-UR-73-479, 1973.

[109] J.F. Remacle, J.E. Flaherty, and M. S. Shephard. An adaptive discontinuous galerkin technique with an orthogonal basis applied to compressible flow problems. *SIAM Review*, 45(1):53–72, 2003.

[110] M. Restelli, L. Bonaventura, and R. Sacco. A semi-Lagrangian discontinuous Galerkin method for scalar advection by incompressible flows. *Journal of Computational Physics*, 216:195–215, 2006.

[111] C.M. Rhie. *A numerical study of the flow past an isolated airfoil with separation*. PhD thesis, University of Illinois, Urbana-Champaign, 1981.

[112] B. Rivière, M.F. Wheeler, and V. Girault. Improved energy estimates for interior penalty, contrained and discontinuous Galerkin methods for elliptic problems. *Computational Geosciences*, 3:337–360, 1999.

[113] P.L. Roe. Approximate Riemann solvers, parameter vectors, and difference schemes. *Journal of Computational Physics*, 43:357–372, 1981.

[114] P.L. Roe and J. Pike. *Efficient construction and utilization of approximate Riemann solutions*. North-Holland, 1984.

[115] G. Rudinges and A. Chang. Analysis of non-steady two-phase flow. *Physics of Fluids*, 7:1747–1754, 1964.

[116] V.V. Rusanov. Calculation of interaction of non-steady shock waves with obstacles. *USSR Computational Mathematics and Mathematical Physics*, 1:267–279, 1961.

[117] S. Saltzman. An unsplit 3D upwind method for hyperbolic conservation laws. *Journal of Computational Physics*, 115:153–168, 1993.

[118] L. Schiller and A. Nauman. Uber die grundlegende Berechnung bei der Schwekraftaufbereitung. *Vereines Deutscher Inggenieure*, 44:318–320, 1933.

[119] C.-W. Shu. Efficient implementation of essentially non-oscillatory shock-capturing schemes II. *Journal of Computational Physics*, 83:32–78, 1989.

[120] C.-W. Shu. A survey of strong stability preserving high order time discretizations. *Estep, D. and Tavener, S. Collected Lectures on the Preservation of Stability under Discretization SIAM*, pages 51–65, 2002.

[121] C.-W. Shu and S. Osher. Efficient implementation of essentially non-oscillatory shock-capturing schemes. *Journal of Computational Physics*, 77:439–471, 1988.

[122] J. Smagorinsky. General circulation experiments with the primitive equations. *Monthly Weather Review*, 91(3):99–164, 1963.

[123] M. Sommerfeld. The unsteadiness of shock waves propagating through gas–particle mixtures. *Experiments in Fluids*, 3:197–206, 1985.

[124] M. Sommerfeld. The structure of particle-laden, underexpanded free jets. *Shock waves*, 3:299–311, 1994.

[125] R.S.J. Sparks, M.I. Bursik, S.N. Carey, J.S. Gilbert, L.S. Glaze, H. Sigurdsson, and A.W. Woods. *Volcanic Plumes*. John Wiley, New York, 1997.

[126] G. Strang. On the construction and comparison of different splitting schemes. *SIAM Journal on Numerical Analysis*, 5:392–402, 1968.

[127] Y.J. Suzuki and T. Koyaguchi. Numerical determination of the efficiency of entrainment in volcanic eruption columns. 37(5), L05302, 2010.

[128] Y.J. Suzuki, T. Koyaguchi, M. Ogawa, and I. Hachisu. A numerical study of turbulent mixing in eruption clouds using a three-dimensional fluid dynamics model. *Journal of Geophysical Research*, 110(8), B08201, 2005.

[129] P. Sweby. High resolution schemes using flux-limiters for hyperbolic conservation laws. *SIAM Journal on Numerical Analysis*, 21:995–1011, 1984.

[130] M. Syamlal. Multiphase hydrodynamics of gas-solid flow. Ph.d. thesis, Illinois Institute of Technology, Chicago, Illinois, USA, 1985.

[131] M. Syamlal. Mfix documentation: numerical technique. Technical report, U.S. Department of energy, Office of fossil energy, Federal Energy Technology Center, Morgantown, West Virginia, USA, January 1998.

[132] M. Syamlal and T.J. O'Brien. Simulation of granular layer inversion in liquidized beds. *International Journal of Multiphase Flow*, 14:473–481, 1988.

[133] M. Syamlal, W. Rogers, and T.J. O'Brien. Mfix documentation: technical note. Technical report, U.S. Department of energy, Office of fossil energy, Morgantown Energy Technology Center, Morgantown, West Virginia, USA, December 1993.

[134] M. Todesco, A. Neri, T. Esposti Ongaro, P. Papale, G. Macedonio, R. Santacroce, and A. Longo. Pyroclastic flow hazard assessment at Vesuvius (Italy) by using numerical modeling. 1. Large-scale dynamics. *Bulletin of Volcanology*, 64:155–177, 2002.

[135] E.F. Toro, M. Spruce, and W. Speares. Restoration of the contact surface in the HLL-Riemann solver. *Shock waves*, 4:25–34, 1992.

[136] Y. Tsuji, N.-Y. Shen, and Y. Morikawa. Lagrangian simulation of dilute gas-solid flows in a horizontal pipe. *Advanced Powder Technology*, 2:63, 1991.

[137] G. Tumolo, L. Bonaventura, and M. Restelli. A semi-implicit, semi-Lagrangian, p-adaptive discontinuous Galerkin method for the shallow water equation. *Journal of Computational Physics*, 232(1):46–67, 2013.

[138] G.A. Valentine and K.H. Wohletz. Numerical models of Plinian eruption columns and pyroclastic flows. *Journal of Geophysical Research*, 94:1867–1887, 1989.

[139] M.W. Vance, K.D. Squires, and O. Simonin. Properties of the particle velocity field in gas-solid turbulent channel flow. *Physics of Fluids*, 18:063302, 2006.

[140] H. Wadell. Sphericity and roundness of rock particles. *Journal of Geology*, 41:310–331, 1933.

[141] C.Y. Wen and Y.H. Yu. Mechanics of fluidization. *Chemical Engineering Progress Symposium Series*, 62:100, 1966.

[142] M.F. Wheeler. An elliptic collocation finite-element method with interior penalties. *SIAM Journal on Numerical Analysis*, 15:152–161, 1978.

[143] S. Whitaker. Forced convection heat transfer correlations for flow in pipes past flat plates, single cylinders, single spheres, and for flow in packed beds and tubes bundles. *AIChE Journal*, 18:361–371, 1972.

[144] L. Wilson. Explosive volcanic eruptions – III – Plinian eruption columns. 45:543–556, 1976.

[145] K.H. Wohletz. *Pyroclastic surges and compressible two-phase flow*, pages 247–312. A. Freundt (ed.), Elsevier, Amsterdam, 1998.

[146] A.W. Woods. The dynamics and thermodynamics of eruption columns. *Bulletin of Volcanology*, 50(3):169–193, 1988.

[147] A.W. Woods. The dynamics of explosive volcanic eruptions. *Reviews of Geophysics*, 33(4):495–530, 1995.

[148] Y. Yamamoto, M. Potthoff, T. Tanaka, T. Kajishima, and Y. Tsuji. Large eddy simulation of turbulent gas-particle flow in a vertical channel: effect of considering interparticle collisions. *Journal of Fluid Mechanics*, 442:303–334, 2001.

[149] D. You and P. Moin. A dynamic global-coefficient subgrid-scale eddy-viscosity model for large-eddy simulation in complex geometries. *Physics of Fluids*, 19(6):065110, 2007.

[150] S. Zalesak. Fully multidimensional Flux Corrected Transport algorithms for fluids. *Journal of Computational Physics*, 31:335–362, 1979.